UNIVERSIDAD COMPLUTENSE DE MADRID

FACULTAD DE CIENCIAS QUÍMICAS

Departamento de Ciencia de los Materiales
e Ingeniería Metalúrgica

TESIS DOCTORAL

Estudio y optimización del proceso de soldadura por fricción batida (FSW) de materiales compuestos de matriz metálica (MMC) con elevado contenido de refuerzo

MEMORIA PARA OPTAR AL GRADO DE DOCTOR

PRESENTADA POR

Florencia Cioffi

Directores

Gaspar González Doncel
Ricardo Fernández Serrano

Madrid, 2017

UNIVERSIDAD COMPLUTENSE DE MADRID
FACULTAD DE CIENCIAS QUÍMICAS
DEPARTAMENTO DE CIENCIA DE LOS MATERIALES E INGENIERÍA METALÚRGICA

ESTUDIO Y OPTIMIZACIÓN DEL PROCESO DE SOLDADURA POR FRICCIÓN BATIDA (FSW) DE MATERIALES COMPUESTOS DE MATRIZ METÁLICA (MMC) CON ELEVADO CONTENIDO DE REFUERZO

Memoria para optar al grado de Doctor en Ciencias Químicas

FLORENCIA CIOFFI

Directores:
GASPAR GONZÁLEZ DONCEL
RICARDO FERNÁNDEZ SERRANO

DEPARTAMENTO DE METALURGIA FÍSICA
CENTRO NACIONAL DE INVESTIGACIONES METALÚRGICAS
CONSEJO SUPERIOR DE INVESTIGACIONES CIENTÍFICAS
Madrid, 2016

"La duda es uno de los nombres
de la inteligencia."

"Que otros se jacten de las
páginas que han escrito; a mí me
enorgullecen las que he leído."

JORGE LUIS BORGES (1899-1986)

AGRADECIMIENTOS

En primer lugar quiero agradecer al Ministerio de Economía y Competitividad que a través del proyecto MAT-09-09545 y la beca FPI BES-2010-030247 financió la investigación que condujo a esta Tesis.

En segundo lugar, a toda la gente que trabaja en el CENIM quienes me acogieron desde el primer día y me hicieron sentir como en casa. En especial a mis directores Gaspar y Ricardo, por haber confiado en mí desde el otro lado del océano cuando sólo habíamos hablado unas cuantas veces por teléfono, por todo el tiempo y esfuerzo que dedicaron en estos años de trabajo juntos, por su paciencia y predisposición. También a Joaquín porque nuestras discusiones me motivaban a ir hasta el fondo del problema y por hacer las horas de microscopio más amenas.

Agradezco las colaboraciones con el grupo de soldadura por FSW de AIMEN, con el CIEMAT, con Zhan Chen durante mi estancia en la Auckland University of Technology y con el grupo de Sistemas adaptivos y bioinspirados de la Universidad Complutense de Madrid.

Por supuesto agradezco también a mis amigos del CENIM, porque muchas veces la hora de la comida salvaba un día en que todo lo experimental salía mal. A Judi, Alberto, Edu y Elvi, por las risas y por poner la oreja.

A mis amigos de Madrid que fueron testigos de esta etapa, al punto de poder explicar de qué se trata mi Tesis, aunque no se dediquen a nada que tenga que ver con la ciencia de materiales.

A mi familia y amigos en Argentina, por apoyarme siempre y alentarme a conseguir mis objetivos. Porque cuando veo que los lleno de orgullo se me recargan las pilas. En especial le agradezco a mi mamá, por su empatía y humildad, de las que todavía me queda mucho por aprender.

A Gloria y Eu por acogerme y hacerme sentir parte de la familia, por toda su ayuda y apoyo en este tiempo.

A Paco por su eterna paciencia e incondicional aliento, por devolverme la cordura las veces que fuera necesario. No lo podría haber hecho sin ti.

ÍNDICE

RESUMEN

La soldadura por fricción batida (FSW, del inglés *Friction Stir Welding*) es una técnica que, por ser en estado sólido, resulta interesante para unir compuestos de matriz metálica (MMC, del inglés *Metal Matrix Composite*). Especialmente aquellos que presentan excelentes propiedades mecánicas pero se consideran «no soldables» por técnicas tradicionales de fusión.

La principal aplicación de la soldadura por FSW se encuentra en aleaciones de aluminio. A pesar de que en la última década se ha extendido el uso a otros materiales (aceros, aleaciones de titanio, polímeros, etc.) la principal fuente de conocimiento sobre el proceso de FSW sigue siendo el campo de las aleaciones de aluminio.

En la implementación del proceso de FSW en los MMC con alto contenido de refuerzo surgen nuevas dificultades relacionadas con la presencia de partículas cerámicas en el material. Por un lado, la mayor resistencia al flujo plástico de estos materiales dificulta la deformación plástica severa que ocurre durante la soldadura por FSW. Por otro lado, la presencia de partículas cerámicas abrasivas hace que la resistencia al desgaste de las herramientas de FSW utilizadas en aleaciones de aluminio no sea suficiente para realizar el proceso de manera reproducible. Por lo tanto, se deben utilizar herramientas con formas simples y fabricadas en materiales resistentes al desgaste (e. g. WC-Co). A su vez, los parámetros del proceso se ven condicionados por la utilización de dichas herramientas; de tal manera que se reduce la ventana de condiciones que permite obtener uniones sin defectos macroscópicos. Además, muchas de las estrategias comúnmente utilizadas para la eliminación de defectos en uniones de aleaciones de aluminio pierden validez cuando se aplican a los MMCs.

Por lo tanto, las dificultades que surgen de la aplicación de la soldadura por FSW a los compuestos de este trabajo requieren de un estudio específico. Ya que éstas no pueden ser superadas simplemente aplicando los conocimientos adquiridos para aleaciones de aluminio. En este trabajo se proponen estrategias de eliminación de defectos basadas en la utilización de herramientas no roscadas y resistentes al desgaste. Inclusive, una de estas estrategias saca provecho de la asimetría del flujo de material característico del FSW, para hacer que las zonas críticas de la soldadura reciban mayor nivel de deformación.

Otro de los factores que condiciona la capacidad de soldeo de estos materiales compuestos mediante FSW es la presencia de tensiones residuales. Sin pretender abordar la problemática en toda su complejidad, se acomete el estudio del efecto del carácter termotratable de la matriz en la determinación de estas tensiones para un caso más

sencillo: una unión realizada en aleación termotratable sin refuerzo cerámico. La dificultad que presentan las aleaciones termotratables, en comparación con el resto, reside en que su espaciado de red cambia con la cantidad y naturaleza de los elementos de aleación que se encuentran en solución solida en la red, es decir con el estado de precipitación del material. Este hecho dificulta enormemente el cálculo de las tensiones residuales mediante técnicas de difracción, para el cual el espaciado de red es un parámetro clave.

A partir del planteamiento, estudio y superación de dichas dificultades se espera lograr extender la aplicación de la técnica de FSW en estos materiales. Y por lo tanto, que los mismos puedan utilizarse en aplicaciones estructurales en las que haya piezas soldadas.

ABSTRACT (ENGLISH)

INTRODUCTION

Metal matrix composites (MMC) with high content of reinforcing particles have excellent specific mechanical properties. Therefore, they are an alternative to traditional metal alloys in structural applications in which weight is a key factor.

The industrial production of these materials has been improved, to the point that, nowadays, producing flawless plates or blocks with homogeneous distribution of ceramic particles is a fact. However, the use of these materials is not as broad as it could be expected from their outstanding mechanical properties. This is mainly due to the difficulty of the second processing operations, specially the joining.

When applying traditional fusion welding techniques to MMC, several problems arise: the particles react with the molten metal producing brittle compounds, and, also, they move in the liquid forming agglomerates. Both of these changes deteriorate the mechanical properties of the material. This is why MMC are considered unweldable by fusion methods.

Friction stir welding (FSW) is a solid-state process that, by severe plastic deformation, can join a number of different materials. In particular, the initial and main use of this technique is in aluminum alloys. Therefore, after more than twenty years since its invention, the process is in a very advance stage for these materials. Applications can be found in the transport, aerospace, automotive and electronics markets.

However, the use of this knowledge for the implementation of FSW in MMC is not straight-forward. Applying the technique to MMC brings new challenges to the process, such us:

- severe wear of the welding non-consumable tool,
- difficulties in the elimination of defects,
- restricted choice of welding conditions.

Consequently, in order to reach a broad use of FSW in MMC and, therefore, expand the application of these materials to welded structures, further studies are needed. These studies must address and overcome the challenges of the process, taking into a count the differences between MMC and aluminum alloys.

The body of this thesis is constituted by four scientific publications. In each of them, different present challenges of the FSW are boarded with the common objective of

optimizing the mechanical response of the welds. Some of these challenges are related to the optimization of welding conditions; others to the determination of residual stress in the joints; most of them, regard the optimization of the joints strength, and also, the use of new strategies to eliminate defects.

MATERIALS AND EXPERIMENTAL METHODS

The characteristics of the aluminum alloy and composite plates used in this thesis can be summarized as follows:

Material	Thickness (mm)	Direction of welding	Temper
25%SiC/2124Al	15	Perpendicular to forging direction	T6
	8	Perpendicular to forging direction	T1
17%SiC/2124Al	8	Perpendicular to forging direction	T1
2024 Al	8	Perpendicular to cold rolling direction	T351
	10	Perpendicular to cold rolling direction	T6

The heat-treatable alloy and metal matrix of the MMC correspond to aerospace grades. The composites were manufactured by powder-metallurgy routes and contained homogeneously distributed fine (2-3 μm) SiC particles. The plates were electro discharge machined from blocks (composites) or plates (alloys). The thickness range in the plates is above the average of the FSW works found in the literature which makes the welding process more challenging.

Different kinds of welding tools were used, including MP159 alloy threaded tools and WC-Co tools of much simpler shapes. In most cases a PDS-4 Intelligent Stir FSW machine from MTS was used for welding, but also adapted milling machines were utilized.

The microstructural characterization of the welds and base materials includes optical microscopy and scanning electron microscopy. As per the study of the mechanical properties, tensile tests, compressive tests, high temperature torsion tests and, micro-hardness indentations were carried out. Also residual stress profiles were determined using data collected by neutron diffraction measurements and analytical and computational tools.

RESULTS

The most important results of this thesis are:

- Thick 25%SiC/2124Al composite plates (15 mm) can be welded by FSW using two passes, one on each side of the plates.
- 25%SiC/2124Al composite can reach 97% joint efficiency ($UTS_{weld}/UTS_{base\ material}$ *100) by FSW.
- Dissimilar composite-alloy FSW joints can be obtained with joint efficiencies of up to 90%.
- A severe wear is observed in MP159 tool, starting on the thread and following in the section of the pin next to the shoulder. When using WC-Co unthreaded tools no wear is appreciated.
- To eliminate the tunnel defect, when using a metallic threaded tool, raising the rotational speed is an effective strategy. Instead, when using unthreaded harder WC-Co tools, rotational and advancing speeds need to be low to maximize the material transport and avoid tunnel defects.
- The reinforcement particles distribution in the stir zone is always more homogeneous than in the base material. The advancing side of stir zone has the most homogenous distribution of particles of the joint.
- The asymmetrical nature of the material flow within the stir zone can be used to apply more or less deformation to the joint line, by changing the lateral off-set. The contact area between the materials coming from each plate is more thoroughly deformed as the lateral off-set changes from the advancing side to the retreating side; within the extent of the stir zone.
- A diagonal set-up in which the joint line and the tool path form a small angle (5-15°) can be used to determine suitable combinations of lateral off-set with other welding parameters such us advancing speed, rotation speed and tilt angle.
- A difference between tensile and compressive strength was observed, which indicates that: microscopic residual stresses are developed during the cooling down of the joint after the welding process and, the stirring process imposed by the FSW does not damage the matrix-particle interface.
- The residual stresses developed in thick age-hardenable aluminum joints are very hard to determine properly by diffraction methods, due to the difficulty to establish the unstressed lattice parameter profiles. Using equilibrium conditions, detailed neutron diffraction measurements and multi-objective evolutionary

algorithms, the residual stress profiles can be determined for the three principal directions.

- The fracture location in tensile test does not always coincide with the lowest hardness section of the joint.

DISCUSION

In general, to approach the FSW of composites such us the ones studied in this thesis, it is useful to take advantage of the previous findings regarding other materials. In particular, the broadest and most advanced application of FSW is in aluminum alloys. But some of the principles that apply to those materials are not valid in the case of composites with high content of reinforcement. For example, while using complex profile tools allows faster and better mixed FSW joints in aluminum alloys, it worsens the wear phenomenon in composites. Therefore, new studies need to be carried out to overcome the specific problematic that arise when joining by FSW composite materials.

Such is the case of the use of wear resistant tools. These tools, of ceramic nature and simple profiles, have a low material transport associated to them. This implies that the welding parameter window, in which sound joints are obtained, becomes much smaller than that of aluminum alloys (complex profile metallic tools). In general, low rotational speeds and low advancing speeds are necessary to avoid tunnel defects. Such welding conditions favor the material transport by raising the friction coefficient of the tool/material system.

In a smaller scale, to eliminate microscopic defects appearing in the joint line it is recommended to apply a simple grinding treatment to the lateral surfaces of the plates and to use lateral off-sets into the retreating side. In this way, the presence of oxides and contaminants is minimized and the amount of deformation that the joint line goes through is maximized.

The precipitation state, on which depend the mechanical properties of heat treatable aluminum alloys, changes due to the thermo-mechanical process introduced by the FSW. Since the deformation and temperature that the material goes through is not uniform across the weld, each portion of the joint has a different precipitation state. In the case of composites, the particle distribution also changes in the stir zone. In addition, defects play an important role in the strength of a joint. Therefore, the mechanical response of the joint as a whole is constituted by all of these somewhat different materials. The relative

importance of these factors can be determined by conducting tensile tests of the whole joint and complementing their results with detailed hardness measurements.

In a similar way to the mechanical properties, the residual stresses present in the joint plate will vary from one point to the other. And, so will the unstressed lattice parameter, d_0, value, which is essential when determining the residual stresses by diffraction methods. The here proposed method is of great importance, since it avoids measuring the d_0 profile and, therefore minimizes the experimental errors.

CONCLUSIONS

The most important conclusions of this thesis are as follows:

1.- The presence of reinforcement particles in the composites greatly affects the FSW process, by hindering the direct application of much of the know-how previously obtained for aluminum alloys.

2.- It is possible to weld by FSW aluminum matrix composites with high content of reinforcement, and to obtain joints with high strength, in a repeatable and trustable way. It is also possible to weld this kind of composites to a monolithic alloy (dissimilar welds).

3.-The parameter window in which these materials can be welded is very narrow, and is located at lower rotational and advancing speeds than the aluminum alloys one.

3.- By using detailed diffraction measurements, equilibrium conditions and genetic algorithms, is it possible to calculate the residual stresses in aluminum alloy plates joint by FSW, without the need of measuring the unstressed lattice parameter profile. This method can be applied to composite materials with heat-treatable matrix. In the later case, also the microscopic stresses associated with the presence of ceramic particles have to be taken into a count.

1. INTRODUCCIÓN

1.1. Materiales compuestos de matriz metálica

Los materiales compuestos de matriz metálica (MMC, del inglés *Metal Matrix Composite*) están formados generalmente por una aleación ligera como aluminio, magnesio u, ocasionalmente, titanio, reforzada con partículas, whiskers o fibras de materiales cerámicos. La adición del refuerzo proporciona unas propiedades especiales al compuesto resultante que lo diferencia de las aleaciones convencionales. La gama de propiedades que pueden ofrecer los materiales compuestos es muy amplia y dependerá de varios factores como son: las propiedades de la matriz, la composición, forma, orientación y volumen del refuerzo y finalmente, la ruta de fabricación del material compuesto. De estos factores también depende el coste final del material, Tabla 1. Por ejemplo, los compuestos con refuerzos discontinuos hasta el 30-40% en volumen pueden fabricarse utilizando métodos tradicionales de procesado de aleaciones sin un excesivo sobrecoste, mientras que aquellos con fibras continuas o volúmenes muy altos de refuerzo necesitan métodos de fabricación específicos como la infiltración en fase líquida (liquid metal infiltration) o la deposición por plasma (plasma spraying) y su coste es mucho mayor que el de las aleaciones.

MMC type	*Properties Strength*	*Young's modulus*	*High temperature properties*	*Wear*	*Expansion coefficient*	*Costs*
mineral wool: MMC	*	*	**	**	*	medium
discontinuous reinforced MMC	**	**	*	***	**	low
long fiber reinforced MMC: C fibers	**	**	**	*	***	high
other fibers	***	***	***	*	**	high

Tabla 1. Descripción cualitativa de las propiedades y coste de distintos materiales compuestos de matriz metálica en función del tipo de refuerzo [1].

Reforzar materiales metálicos puede tener objetivos muy distintos en función de la aplicación. Por ejemplo, el refuerzo de metales ligeros encuentra muchas aplicaciones en áreas donde la reducción de peso es una prioridad. En estos casos los objetivos se centran en mantener el nivel de prestaciones exigido en el diseño del componente disminuyendo su peso, por ejemplo en cuanto a: módulo elástico, límite elástico, resistencia a altas temperaturas o corrosión, resistencia al choque térmico, etc. Otras aplicaciones se

encuentran en el área de los materiales funcionales, donde los objetivos son más variados: disminución de la expansión térmica, absorción de radiación (partículas subatómicas) por el refuerzo, aumento de la conductividad térmica, etc.

A pesar de la amplia gama de posibles aplicaciones y de los esfuerzos de la comunidad científica y tecnológica desde hace más de 30 años, los MMC siguen sin ser materiales ampliamente utilizados. Los problemas en la producción y procesado, sumado al elevado coste de las operaciones secundarias, hacen que estos materiales sólo se utilicen en aplicaciones donde el coste no es un condicionante importante, como por ejemplo, componentes de automóviles de alta gama o de motores de avión.

Además, las dificultades para realizar los procesados secundarios como el conformado, el corte, el mecanizado y la unión en los compuestos de matriz metálica, reducen de manera drástica la gama de componentes existentes en el mercado.

En general las técnicas convencionales de unión utilizadas en materiales metálicos podrán ser adaptadas para el uso en MMC con ciertas limitaciones dependiendo de los siguientes factores:

- Cantidad y tipo de refuerzo. A mayor volumen de refuerzo, más difícil es adaptar una técnica convencional. Es más fácil soldar MMCs con refuerzo discontinuo que con refuerzo continuo.
- Temperatura de fusión de la matriz metálica. El contacto prolongado de la matriz metálica líquida con el refuerzo puede conducir a reacciones químicas indeseadas en la intercara que a su vez se aceleran al aumentar las temperaturas del proceso. Por lo tanto, en casos en que ésta incompatibilidad exista, las soldaduras con fusión no podrán ser adaptadas a los MMC.
- El manejo y control de la energía térmica. Aquellas técnicas que puedan controlar el nivel de aporte térmico y mantenerlo bajo serán las que mejor se adapten a los MMC.

En la Figura 1, se resumen distintas técnicas de unión normalmente utilizadas en materiales metálicos. En la tabla se evalúa cualitativamente la aplicabilidad de cada técnica al caso de los MMC.

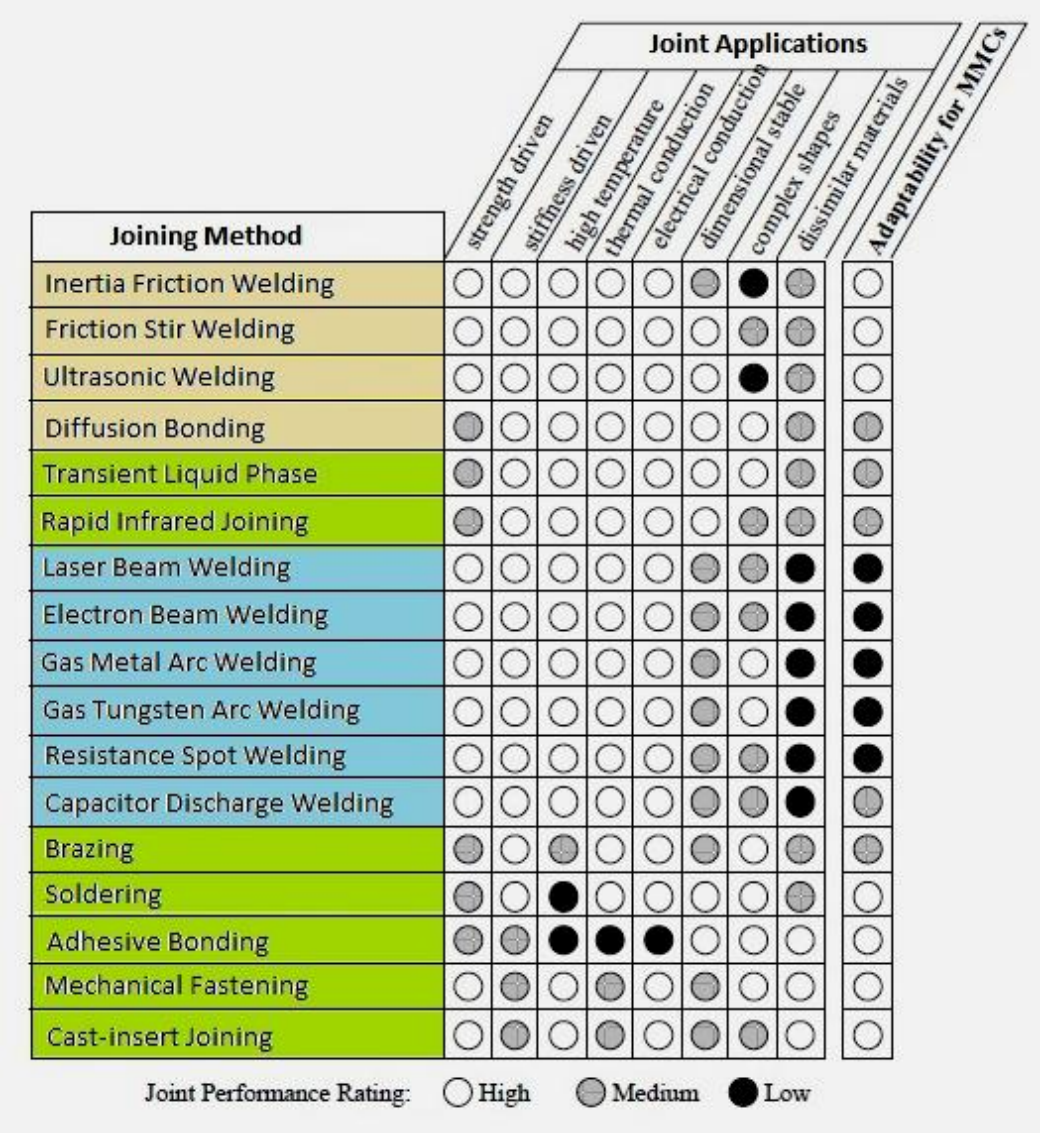

Figura 1. Aplicabilidad de los métodos de unión de materiales metálicos a los MMC [2]. Métodos en estado sólido (beige), métodos de fusión (azul) y otros métodos (verde).

Si bien existen muchos tipos de MMC, y las limitaciones de las técnicas de soldadura varían según el caso, en general se puede concluir que las soldaduras en estado sólido y otros procesos de baja temperatura se adaptan mejor a la unión de estos materiales que las técnicas de fusión. En este trabajo se abordará la aplicación de la técnica de soldadura por fricción batida, FSW a la unión de MMC con alto contenido de partículas cerámicas. Los conceptos básicos de la técnica y el grado de conocimiento y experiencia actual se describirán en el apartado 1.2 del documento, al igual que las particularidades de su aplicación al caso de los MMC.

1.1.1. Los MMC con alto contenido de partículas cerámicas

La adición de partículas de tamaño micrométrico a aleaciones ligeras como las de aluminio, hace que la dureza, el módulo de Young, el límite elástico, la resistencia a rotura y la resistencia al desgaste aumenten, y que el coeficiente de expansión térmica disminuya. Lamentablemente, la ductilidad del material y su tenacidad a la fractura también disminuyen. El orden de magnitud de estos cambios dependerá de la microestructura del compuesto. Que a su vez depende del volumen, tamaño y naturaleza de las partículas que se agregue y de la ruta de fabricación que se elija.

Los refuerzos más comúnmente utilizados y algunas de sus propiedades se detallan la Tabla 2.

Reinforcement	*Saffil (Al_2O_3)*	*SiC particle*	*Al_2O_3 particle*
crystal structure	δ-Al_2O_3	hexagonal	hexagonal
density (g cm^{-3})	3.3	3.2	3.9
average diameter (μm)	3.0	variable	variable
length (μm)	ca. 150	–	–
Mohs hardness	7.0	9.7	9.0
strength (MPa)	2000	–	–
Young's Modulus (GPa)	300	200–300	380

Tabla 2. Propiedades de refuerzos discontinuos más comúnmente utilizados en compuestos de aluminio [3].

Las partículas de SiC son las que aportan mayor dureza y menor densidad y son por lo tanto las más interesantes desde el punto de vista tecnológico para reforzar aleaciones ligeras.

Además, los mecanismos de refuerzo de este tipo de materiales compuestos se ven incrementados al utilizar partículas de tamaño pequeño para un contenido de refuerzo dado, ya que la superficie de contacto entre la matriz y el refuerzo es mayor.

La fabricación de MMCs con alto contenido de refuerzo (≥15%) supone un reto importante, entre otros motivos porque es difícil evitar la aglomeración de partículas (no es fácil conseguir una distribución suficientemente homogénea del refuerzo). Entre los distintos métodos de fabricación de estos MMC, los que involucran una vía pulvimetalúrgica consiguen la distribución de partículas más homogénea, de manera que permiten alcanzar volúmenes de refuerzo de hasta un 40% [3]. Además, mediante la utilización de una ruta pulvimetalúrgica, en comparación con los procesos de colada, la matriz adquiere una estructura de grano mucho más fina, el límite elástico del compuesto aumenta, su módulo de Young se mantiene alto (hasta 760 MPa y 125GPa, respectivamente) y el coeficiente de expansión térmica presenta un valor bajo

(aproximadamente $17x10^{-6}$ K^{-1}). Es importante mencionar, además, que la pérdida de ductilidad y tenacidad con respecto a las aleaciones, es menor en compuestos pulvimetalúrgicos que en compuestos colados [3].

En particular, los materiales utilizados en el presente trabajo contienen un alto volumen de partículas de SiC (17 y 25%) de pequeño tamaño (2-3μm), además han sido fabricados por vía pulvimetálurgica y poseen una matriz termotratable de altas prestaciones mecánicas (2124Al) utilizada habitualmente en aplicaciones aeroespaciales. Esto les confiere propiedades específicas superiores a los materiales metálicos estructurales tradicionales. En la Figura 2 se compara el módulo elástico específico de distintos materiales compuestos y materiales estructurales tradicionales. Es en ésta propiedad en dónde se aprecian las mayores diferencias a favor de los compuestos.

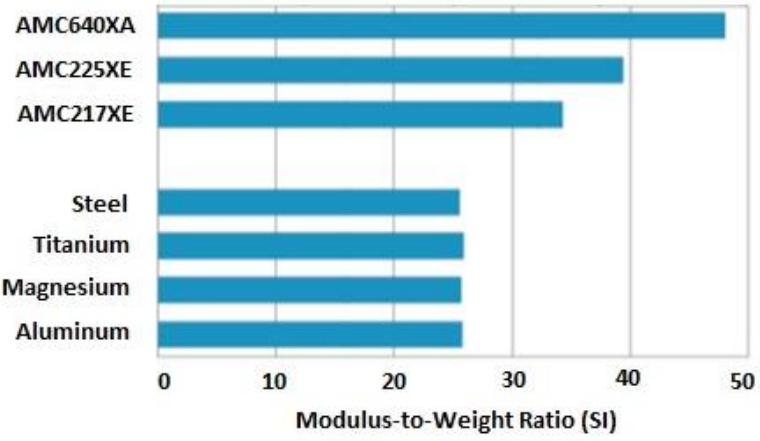

Figura 2. Relación módulo elástico/peso de MMC pulvimetálurgicos y materiales estructurales tradicionales [4].

A tenor de esta mejora de propiedades, los MMC se presentan como una alternativa prometedora a las aleaciones convencionales en una amplia gama de aplicaciones estructurales de altas prestaciones como se muestra a continuación [5-10]:

Mercado aeroespacial y de defensa

- Componentes de motores de aeronaves [11] (Álabes de guía en turbina de salida, motor: Pratt&Whitney 4xxx-series, Boeing 777)
- Estructura de aeronaves
- Tren de aterrizaje [12]
- Componentes de naves espaciales (tren de aterrizaje de Space Shuttle Orbiter [13])

Figura 3. Aeronave Boeing 777. Detalle del componente de la turbina fabricado en material compuesto (alabe guía de salida).

Mercado automotriz

- Pernos de pistones
- Camisas de cilindros [14] (Honda en los motores modelos: B21A1, H22A and H23A, F20C, F22C y C32B. Porshe: en los modelos Boxster y 911. Toyota modelo Matrix)
- Barra de transmisión (General motors Corvette, Ford Crown Victoria)

Figura 4. Ejemplos de aplicaciones de materiales compuestos en la industria automotriz, en componentes del sistema de transmisión. Arriba: Corvette (izquierda) y barra de transmisión del GM Corvette (derecha). Abajo: Ford Crown Victoria

- Tren de válvulas del motor
- Componentes del chasis
- Discos y tambores de freno [15] (Porsche Boxster y 911, Lotus Elise, Volkswagen Lupo, Toyota RAV-4EV, Chrysler Plymouth Prowler, General motors: EV-1, Precept e Impact, Ford Prodigy)

Figura 5. Ejemplos de aplicaciones de materiales compuestos en la industria automotriz (frenos). Arriba: detalle rueda Porsche (izquierda), Lotus Elise (centro) y colocación de disco de freno. Abajo: Toyota RAV-4EV (izquierda), disco y camisa de freno (centro) y Volkswagen Lupo (derecha).

- Tren de propulsión
- Suspensión
- Refuerzo localizado en bloque del motor y pistones [16] (Porsche Boxster y 911, Ferrari, Toyota Celica)

Figura 6. Ejemplos de aplicaciones de materiales compuestos en la industria automotriz (motor). Arriba: Toyota Celica (izquierda), bloque del motor (centro) y detalle de zona localmente reforzada con MMC. Abajo: motor Ferrari (izquierda), detalle de pistón con camisa reforzada (centro) y prototipo de camisa de cilindro (derecha).

Figura 7. Aplicaciones de MMC en discos de freno de trenes. Copenhagen metro (izquierda), discos de freno de A359/SiC/20p (centro) y discos colocados en el tren (derecha).

1.2. El proceso de soldadura por la técnica de fricción batida, *Friction Stir Welding*

Desde su invención en 1991 [17] en The Welding Intitute (TWI), en Reino Unido, el proceso de *Friction Stir Welding* (FSW) ha pasado de ser una técnica prometedora a convertirse en la actualidad en un proceso con diversas aplicaciones industriales y a gran escala. Empresas, centros de investigación y universidades, han invertido importantes esfuerzos y recursos en la investigación y el desarrollo de esta tecnología desde entonces. Un hecho que da cuenta de su importancia es la existencia de congresos enteramente dedicados a su estudio. Hacia finales de 2007 el TWI había emitido 200 licencias para el uso del proceso y se habían aceptado 1900 solicitudes de patente relacionadas con aplicaciones del proceso de FSW [18].

A diferencia de las soldaduras tradicionales, en el proceso de FSW no se produce fusión; los materiales se unen en estado sólido por un proceso de deformación plástica severa. En este factor radica el principal motivo de su utilización, ya que al no producirse fusión, muchos de los defectos provenientes de la presencia de fase líquida (porosidad, microestructura de solidificación desde fase líquida, fisuras, etc.) se evitan. Así es como, gracias a este método, materiales que se consideraban no soldables han ampliado sus aplicaciones.

Si bien el proceso ha evolucionado mucho desde sus comienzos y hoy en día existen muchas variantes [19-22], el denominador común del mismo se puede describir mediante el esquema de la Figura 8:

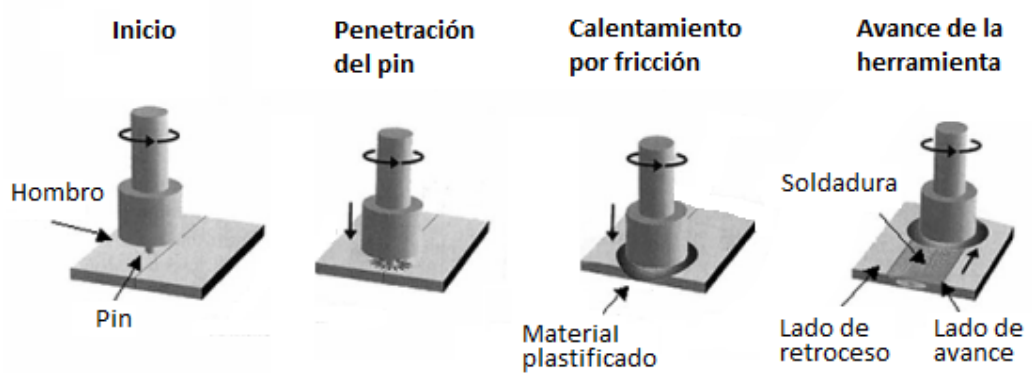

Figura 8. Esquema del proceso de *Friction Stir Welding*.

En una primera etapa, la herramienta gira mientras se introduce lentamente en el material. Las formas de las herramientas son muy diversas, pero en general cuentan con una parte de diámetro más pequeño (pin o punzón) que penetra en el material a soldar y otra concéntrica de diámetro mayor (hombro) que no penetra. Cuando el hombro entra en contacto con el material, la fricción entre las superficies produce un aumento de temperatura que facilita el flujo plástico del material. Entonces, la herramienta comienza a avanzar hasta completar la soldadura.

El proceso es de naturaleza asimétrica. Se llama lado de avance a aquel en que coinciden el sentido de la velocidad de avance y el de la velocidad tangencial de la herramienta. El opuesto es el llamado lado de retroceso. Como se indica en el esquema de la Figura 8. Se puede interpretar el proceso de FSW como una extrusión [23, 24], en la que el material está constreñido por el punzón a un lado, el hombro en la superficie superior y el material frío en el resto. Prácticamente la totalidad del material transportado por la herramienta pasa por el lado de retroceso, siguiendo el sentido de giro. De esta manera se rellena el hueco dejado por la herramienta al avanzar.

Durante la formación de la unión, el material está sujeto a grandes deformaciones y elevadas velocidades de deformación; mayores que las típicas de procesos de conformado de metales como la laminación o la extrusión. Si bien existe consenso en que la temperatura máxima no supera la temperatura de fusión del material, su valor exacto es difícil de concretar, más allá de que pertenece a un rango que en aleaciones de aluminio va de 425 a 500°C [25, 26].

Hoy en día existen muchas alternativas que permiten diversas configuraciones; desde las básicas (a tope, a solape y por puntos) hasta otras muy complejas (trayectorias curvas, recorridos automatizados, en atmosfera controlada, bajo el agua, etc.) [27-31].

Los principales parámetros del proceso de FSW son: la velocidad de giro (w), la velocidad de avance (v), el esfuerzo de forja (P) y el ángulo de inclinación de la herramienta. Según

las distintas combinaciones de parámetros se producirán distintos aportes energéticos y distinto flujo del material. Lo que es importante destacar es que los valores que adquieren estos parámetros no son universales sino que deberán ajustarse para cada sistema de trabajo: material + herramienta.

Las ventajas de la técnica de FSW frente a los métodos de soldadura tradicionales son:

- No se produce fusión: ventajas microestructurales (afino de grano y se evitan microestructuras de solidificación) y ventajas técnicas (no se producen salpicaduras ni goteo y las distorsiones se reducen).
- Es fácilmente automatizable y reproducible, no depende de la habilidad del operario.
- No hay aporte de material y la herramienta es no consumible.
- Es más limpio, no se producen humos, ni radiación.
- Permite soldar materiales no soldables por otras técnicas.
- No requiere mecanizados posteriores.
- Consigue menores pérdidas de propiedades mecánicas respecto a la resistencia del material base.
- La energía que requiere el proceso es menor que la soldadura por arco con gas inerte [32].
- Las velocidades de soldeo son competitivas con los procesos de fusión, especialmente en espesores grandes donde mediante la técnica de FSW se puede realizar la unión en una sola pasada.

1.2.1 Aplicaciones

A día de hoy, no hay duda de que el proceso de FSW para soldar aleaciones de aluminio ha alcanzado una madurez suficiente como para competir con métodos tradicionales. Además ha extendido el uso y aplicaciones de ciertos materiales, especialmente aluminios de las series 2xxx y 7xxx de gran importancia para la industria aeroespacial.

Las aplicaciones actuales van desde trenes de alta velocidad [33] y cruceros [34], Figura 9, plataformas de lanzamiento aeroespacial y tanques de combustible para cohetes [35-37], Figura 10, a componentes de coches deportivos como el Mazda Rx-8 Figura 11 a [38], o los últimos modelos de iMac [39], Figura 11 c.

Figura 9. Aplicaciones de la soldadura por FSW en el transporte. Arriba: el crucero 'Seven Seas Navigator' contiene en su superestructura numerosas soldaduras realizadas por FSW [40]. El «Super Liner Ogasaware» ha sido reportado como el mayor barco construido utilizando FSW por Mitsui Engineering and Shipbuilding en Japón [34]. Centro: en la red de trenes de alta velocidad de China se utiliza la tecnología Powerstir-FSW para soldar paneles de 30 metros de largo que forman el cuerpo de los vagones. El tren de alta velocidad construido por Hitachi contiene soldaduras realizadas por FSW en los paneles del techo y los costados de los vagones [41]. Abajo: el avión a reacción «Elipse 500» contiene soldaduras a solape realizadas por FSW para unir ventanas, esqueleto y fuselaje [42].

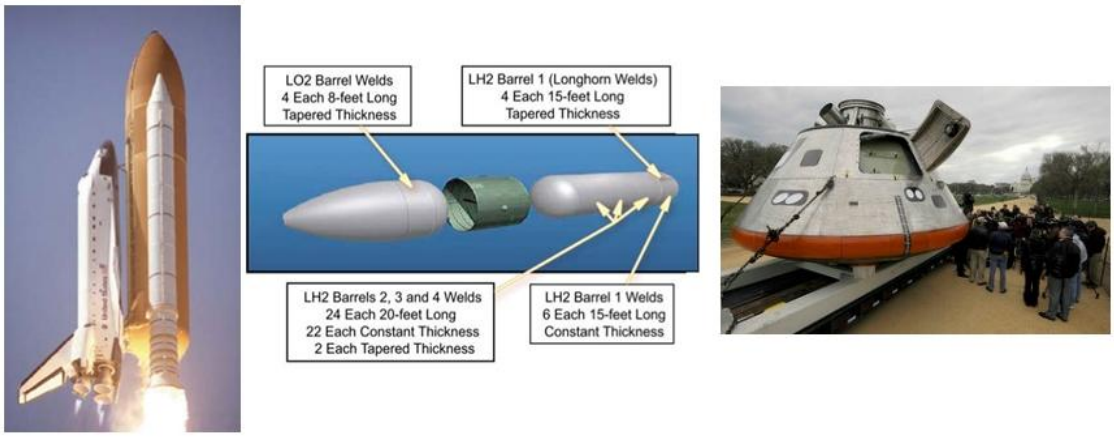

Figura 10. Aplicaciones aeroespaciales. Izquierda: el tanque de combustible de la lanzadera espacial contiene varias soldaduras realizadas por FSW en una aleación de la serie 8xxx (detalle en el centro) [35, 37]. Derecha: dos de las secciones del módulo de tripulación del Orion Spacecraft de la NASA están unidas por una soldadura FSW [43].

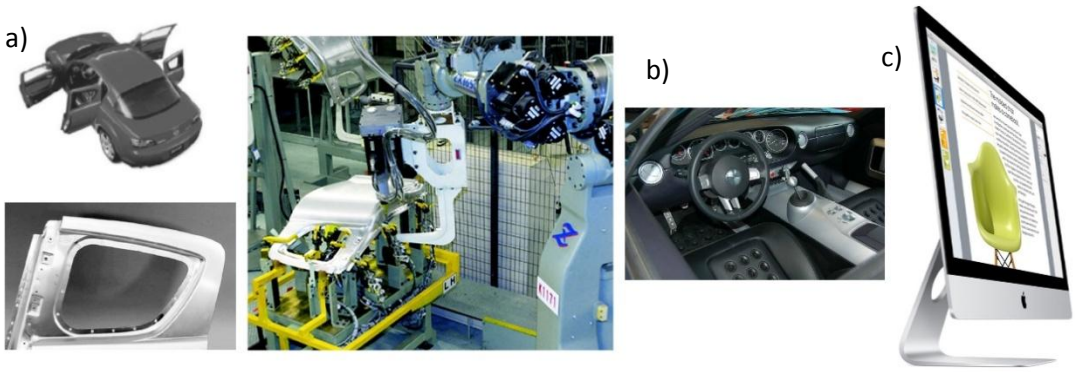

Figura 11. Aplicaciones en el mercado masivo. a) El automóvil Mazda RX-8 lleva soldadura FSW por puntos en la puerta trasera, robot automático soldando estas piezas [44]. b) En la construcción del Ford GT se utiliza la técnica de FSW para soldar el túnel central [43] c) En el nuevo iMac se utiliza FSW para unir las partes trasera y delantera del ordenador [39].

1.2.2. Estado del arte de la soldadura por FSW

La utilización más inmediata de la soldadura por FSW desde su inicio ha sido en aleaciones de aluminio por dos motivos principales: primero, estas aleaciones eran consideradas no soldables ya que pierden sus propiedades mecánicas al soldarse por métodos que impliquen fusión, y segundo, su gran ductilidad facilita los procesados por deformación severa. Les siguieron las aleaciones de magnesio [45, 46] y de cobre [47, 48]. Luego, se amplió la investigación a materiales con puntos de fusión más altos como aleaciones de titanio [49, 50], aceros [51-53], e incluso superaleaciones [54-56]. Además, se han publicado diversos trabajos que combinan estos materiales en uniones disimilares [57-61]. Finalmente, en comparación con las aleaciones de aluminio, el proceso de FSW de materiales compuestos de matriz metálica se encuentra muy poco estudiado [62]. En la sección 1.2.2 se realizará una revisión del estado del arte en lo que refiere a la aplicabilidad del proceso de FSW en materiales compuestos.

En el campo de las aleaciones de aluminio es donde el proceso de soldadura mediante FSW se encuentra más desarrollado, de ello da cuenta la gran cantidad de aplicaciones enumeradas en la sección anterior 1.2.1. El conocimiento adquirido se encuentra descrito en multitud de patentes y publicaciones científicas. Las patentes se centran principalmente en modificaciones del proceso y el diseño de herramientas [27], como por ejemplo las herramientas bobina, que incluyen un segundo hombro en la parte inferior de la herramienta y permiten un calentamiento más uniforme a través del espesor [63], y la soldadura por FSW auto-soportada [64] que adapta el proceso a aquellos casos en que no es posible colocar una placa de apoyo.

Las publicaciones científicas cubren prácticamente la totalidad de los aspectos del proceso. Entre ellas, en esta revisión del estado del arte de la técnica de FSW, se han

seleccionado las que se relacionan de forma más cercana a los temas de esta tesis: microestructura y propiedades mecánicas de la unión resultante.

1.2.2.1 Flujo de material y diseño de herramientas

El estudio del flujo de material durante el proceso de FSW despertó el interés de la comunidad científica desde el comienzo del uso de la técnica. A grandes rasgos se pueden dividir los trabajos realizados en tres grupos, según la estrategia utilizada para estudiar el flujo: a partir de fundamentos teóricos y observaciones microestructurales, mediante el uso de trazadores y por medio de simulación por elementos finitos. A continuación, se describen los principales hallazgos de cada grupo.

1. **A partir de fundamentos teóricos de la mecánica de fluidos y observaciones microestructurales** [24, 65, 66]. La principal ventaja de este tipo de estudios es la simplicidad y el carácter general de sus descripciones. Muchos de los modelos dentro de este grupo no alcanzan a revelar los detalles del flujo de material ya que utilizan grandes simplificaciones, pero permiten explicar ciertos aspectos de las uniones resultantes. En particular, las distintas zonas microestructurales y la formación de defectos.

   Uno de los modelos más aceptados es el de Nunes [24, 65, 67]. En dicho modelo, se describe el flujo de material en el proceso de FSW mediante la combinación de tres tipos de flujos incompresibles para formar dos corrientes de material distintas. La primera, llamada corriente de vórtice, está formada por el material que entra en contacto con el punzón y cuyo campo de velocidades viene impuesto por la rosca. Y la segunda, llamada corriente directa, es más simple y sólo pasa alrededor del punzón sin girar. Entonces, el material de la corriente de vórtice sufre un nivel más severo de deformación, incluso puede que gire con el punzón por más de una vuelta. Las características geométricas de la herramienta condicionaran la magnitud de estas corrientes; una rosca profunda provocará una corriente de vórtice de mayor volumen que una rosca superficial. En la Figura 12, se muestran los esquemas de las corrientes modelizados por Nunes y micrografías que las evidencian experimentalmente en una unión disimilar perteneciente a este trabajo. Es interesante destacar que la unión de la figura, se realizó con una herramienta cónica lisa. Esto indica que la corriente de vórtice existe a pesar de la ausencia de rosca.

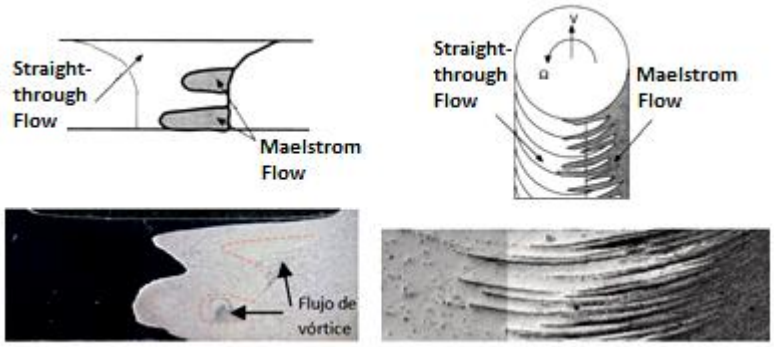

Figura 12. Esquemas de las dos corrientes del modelo de Nunes «straight through flow» o corriente directa y «maelstrom flow» o corriente de vórtice [65] (arriba). Evidencias experimentales de dichas corrientes en micrografías de uniones disimilares de 2024Al y 17%SiC/2124Al (abajo).

Otro modelo interesante para comprender el proceso de FSW es el de Arbegast [66]. En este modelo, se interpreta el proceso de FSW en cinco etapas, Figura 13, asemejando cada una de ellas a un tratamiento termomecánico: precalentamiento, deformación inicial, extrusión, forja y enfriamiento.

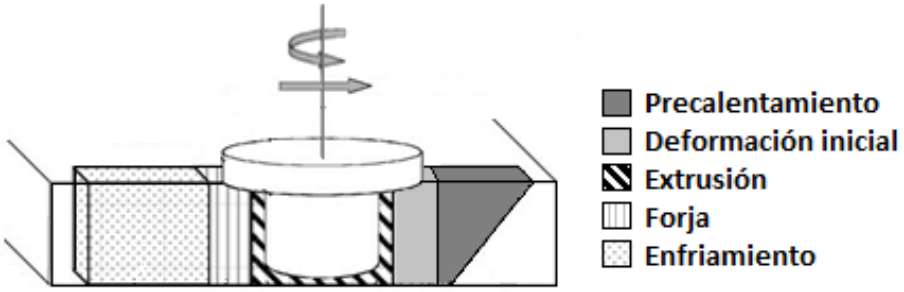

Figura 13. Esquema del modelo de Arbegast que interpreta el proceso de soldadura por FSW como una serie de sucesivos tratamientos termomecánicos [66].

Según este modelo, el calor generado por la herramienta al girar precalienta el material a soldar. Al acercarse la herramienta, el material entra en la zona de deformación inicial en la que el metal es forzado a moverse hacia el hombro y luego hacia abajo hasta entrar en la zona de extrusión. En ésta, el giro de la herramienta hace que el material se deforme y transporte hacia atrás, rellenando el espacio dejado por la herramienta. En la siguiente etapa, la parte trasera del hombro presiona el material que sale de la zona de extrusión y lo forja. Finalmente, al alejarse el punzón, el material se enfría progresivamente.

Este modelo no explica el transporte de material, pero puede servir para explicar algunos defectos en términos de parámetros del proceso. Por ejemplo, un defecto

volumétrico dentro de la unión se puede explicar como una falta de forja que hace que el material no se una completamente tras el paso del punzón.

2. **Mediante la utilización de trazadores** [24, 68-72]. Los trazadores pueden ser partículas, láminas o alambres de un material de distinta naturaleza del que se va a soldar, que permanece discernible de éste después del proceso de FSW. Mediante estudios metalográficos de las uniones, es posible determinar la posición de los trazadores y deducir la trayectoria que han seguido durante el proceso.
   De los estudios con trazadores destacan las siguientes observaciones:
   - El flujo parece ser ordenado, sólo algunas porciones de material son empujadas hacia abajo por la rosca, el resto simplemente gira alrededor del punzón de adelante a atrás [24, 70-72]. El flujo no es turbulento.
   - Existen diferencias entre el camino que sigue el material en el lado de avance y aquel que sigue el material en el lado de retroceso [73]. El flujo es asimétrico.
   - El material del centro es empujado hacia arriba y luego hacia abajo, mientras que el material en el lado de retroceso apenas cambia su posición en profundidad [70, 73].
   - Parte del material puede girar varias vueltas con la herramienta [74].

3. **Mediante simulación por elementos finitos** [75-78]. Las modelizaciones por elementos finitos, como las mostradas en la Figura 14, cubren un amplio rango de condiciones, desde simples modelos en dos dimensiones con herramientas lisas, a complejas simulaciones en tres dimensiones que incluyen condiciones de contacto variables, herramientas roscadas, etc.

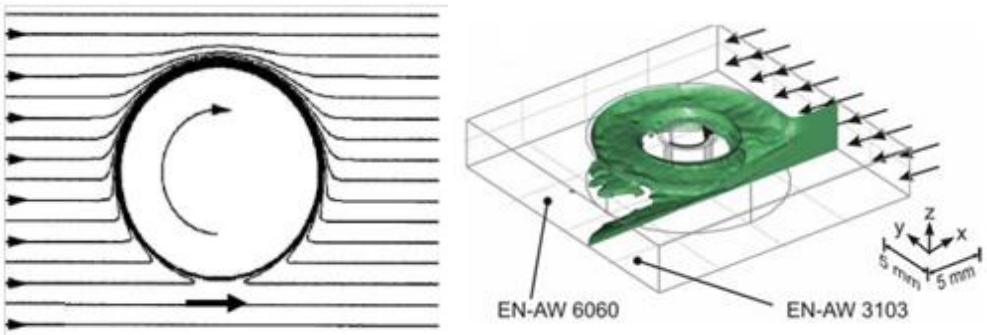

Figura 14. Modelado del flujo de material en el proceso de FSW mediante simulación por elementos finitos. Líneas de flujo en dos dimensiones (izquierda) [75] y superficie de contacto de materiales disimilares (derecha) [78].

La simulación del flujo tridimensional completo es uno de los desafíos actuales de la investigación en FSW. La complejidad no sólo radica en los factores geométricos sino en la sensibilidad del flujo de material a las condiciones de contacto, temperatura y velocidad de deformación. Además, existe un gran desconocimiento de las condiciones a las que realmente está sujeto el material durante el proceso.

En los últimos años, los modelos teóricos y los puramente experimentales (a partir de trazadores) van cediendo paso a la modelización por elementos finitos. Los programas de simulación son cada vez más amigables y potentes, lo que ha extendido su uso de manera muy importante. Además, su coste es menor respecto a la investigación experimental. A pesar de este panorama, las pruebas experimentales siguen siendo el único método fiable de contrastar los resultados obtenidos por simulación, por lo tanto, es importante mantener un balance entre estos dos métodos de estudio que permita la retroalimentación y el avance del conocimiento del flujo de material.

Los resultados experimentales y el estudio del flujo han servido para marcar las tendencias en cuanto al diseño de herramientas. Por ejemplo, se ha demostrado la importancia de tener una componente vertical en el flujo, por lo tanto se han incorporado roscas y muescas helicoidales a las herramientas [79]. También se han diseñado herramientas específicas atendiendo a las necesidades del flujo. Por ejemplo, la herramienta TrifluteMX® consigue barrer un volumen mayor que una herramienta cónica lisa y produce una zona batida de bordes más paralelos que su antecesora Whorl® [80], de este modo se disminuyen las diferencias a través del espesor. Otro ejemplo es la herramienta Flared-Triflute® diseñada para producir una zona batida más ancha, especialmente útil para uniones por solape.

1.2.2.2 Generación de calor y distribución de temperatura

Al igual que los estudios relativos al flujo de material, los estudios referidos a la generación de calor y distribución de temperaturas en el proceso de FSW, se pueden agrupar en tres categorías: aquellos que utilizan fundamentos teóricos junto con observaciones microestructurales, los puramente experimentales (en lugar de trazadores se utilizan termopares) y los de simulación por elementos finitos. En la Figura 15 se recogen dos ejemplos extraídos de la literatura.

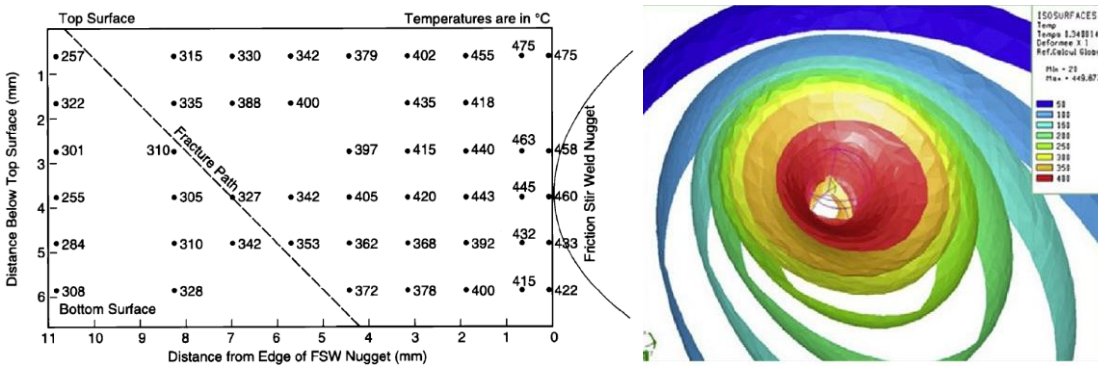

Figura 15. Distribución de temperaturas máximas en zonas cercanas al punzón de soldaduras por FSW en aluminio. Medidas experimentales obtenidas mediante termopares embebidos en el material (izquierda) [25] y valores obtenidos por simulación mediante elementos finitos (derecha)[81].

Existe consenso en cuanto a que los fenómenos de generación de calor en el proceso de FSW son dos: la fricción y la deformación plástica. Dependiendo de las condiciones de contacto entre la herramienta y el material, la contribución de cada una de estas fuentes de calor sobre el total cambia. Aunque en todos los casos el calor generado por deformación es menor que el generado por fricción; se ha estimado su valor entre el 2% [82] y el 20% [76] del total. Estudios experimentales han mostrado que la mayor generación de calor ocurre en la zona de contacto con el hombro [83, 84]. Y al igual que ocurre con el flujo de material, el campo de temperaturas es asimétrico con valores máximos levemente mayores en el lado de retroceso [85].

En el caso de aleaciones termotratables, el estado de precipitación es función de la historia térmica del material. Por este motivo, se han utilizado las curvas de envejecimiento de algunas de estas aleaciones de aluminio para deducir, por comparación con la microestructura, las temperaturas máximas del proceso. Éstas se encuentran entre 425 y 500°C.

Los estudios con termopares embebidos en el material, han permitido obtener mapas del campo de temperaturas en la unión [25, 83, 84, 86]. Los mapas de temperatura muestran dos gradientes: en la dirección normal, las temperaturas máximas se encuentran junto al hombro y descienden al atravesar el espesor; y en la dirección transversal, descienden al alejarse del centro de la soldadura hacia los lados. Además, las medidas sugieren que la región cerca del punzón es prácticamente isotérmica y que la temperatura máxima podría ocurrir en la zona ubicada entre el material que gira con el punzón y el material circundante [84].

Por otro lado, se ha sugerido que existe un mecanismo de estabilización de la temperatura que podría ser la razón por la que el material no llega a fundir. Al aumentar la temperatura del metal, su resistencia al flujo plástico disminuye, por lo tanto el par necesario

disminuye y el calor impartido al material por deformación también disminuye. Esto provoca que la temperatura del material baje y su resistencia al flujo plástico vuelva a aumentar [75]. De este modo, el calor y el par se estabilizan entre sí.

1.2.2.3. Zonas microestructurales

Las propiedades de una soldadura realizada mediante FSW vienen dadas por su microestructura. Ésta, a su vez, depende del material de partida, del ciclo termomecánico impuesto por los parámetros del proceso y de la herramienta utilizada. Por lo tanto, es lógico, que para soldar un material dado, se elijan la herramienta y los parámetros del proceso que den como resultado la microestructura óptima en función de las propiedades buscadas.

En una unión realizada por FSW existen cuatro zonas microestructurales. Dichas zonas pueden ser más o menos fáciles de identificar según el material.

1-. Se considera material base (MB) a aquel material que conserva la microestructura de partida, es decir que no ha sido afectado por el ciclo termomecánico.

2-. Contiguo al MB se encuentra la zona afectada térmicamente (HAZ, del inglés *Heat Affected Zone*) en la que, como su nombre indica, el tiempo que el material ha estado a alta temperatura ha sido suficiente para modificar la microestructura. Cabe destacar que muchas veces los cambios en el estado de precipitación de esta zona son difícilmente detectables por microscopía electrónica de barrido (SEM, del inglés scanning electron microscopy), por lo tanto se suele recurrir a ensayos de microdureza para determinar la extensión de la HAZ.

3-. Siguiendo hacia el centro de la soldadura, se encuentra la zona termomecánicamente afectada (TMAZ del inglés *Thermo-Mechanically Affected Zone*) en la que el de la deformación, se suma al efecto de la temperatura.

4-. Finalmente, en el centro se encuentra el *nugget* o zona recristalizada (NZ del inglés *Nugget Zone*). En ella la deformación y temperatura han sido suficientes para que se produzca la recristalización del material y la estructura de grano del MB se pierda completamente.

Por definición, la NZ forma parte de la TMAZ que a su vez forma parte de la HAZ. Pero se suele llamar a las zonas por el criterio más restrictivo para poder identificarlas, Figura 16.

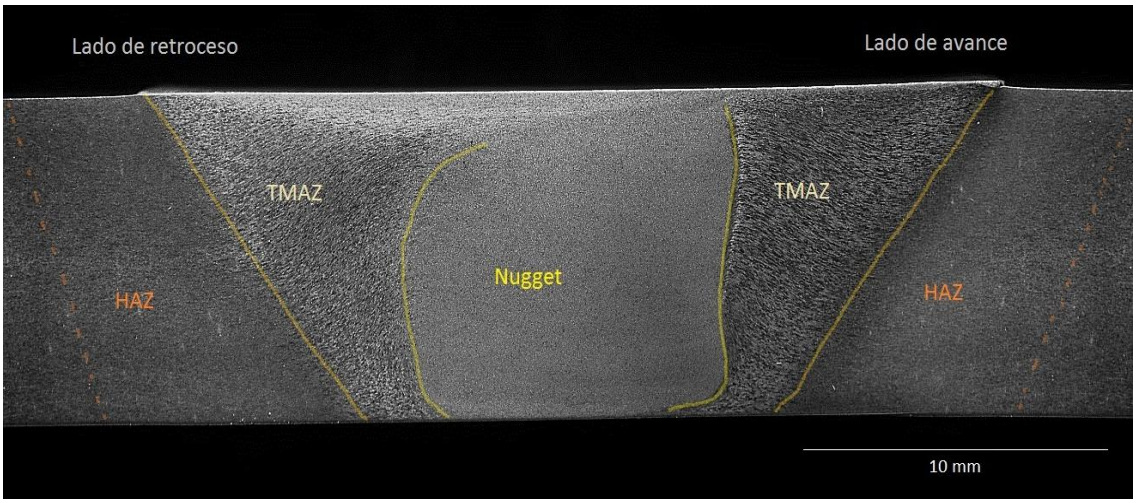

Figura 16. Macrografía de un corte transversal de una soldadura por FSW en 7075Al. Sobre ella se marcaron los límites de las zonas microestructurales características [87].

1.2.2.4. Propiedades mecánicas

El estudio de las propiedades mecánicas de las uniones mediante FSW es de suma importancia para identificar posibles aplicaciones y, llegado el caso, para el diseño de componentes. Existen numerosos trabajos que relacionan microestructura con propiedades mecánicas, en especial mediante medidas de microdureza.

En el caso de aleaciones de aluminio termotratables (series 2xxx, 6xxx, 7xxx y 8xxx) el perfil de durezas en secciones transversales a la unión tiene una gran complejidad ya que tanto la deformación como la evolución de la precipitación afectan a la dureza del material. En cambio, en aleaciones no termotratables (series 1xxx, 3xxx, 4xxx y 5xxx), el segundo factor no existe. En la Figura 17, extraída de la revisión realizada por Threadhill et al.[32], se muestran esquemas de los perfiles típicos de dureza según el tipo de aleación de aluminio y su estado termomecánico de partida.

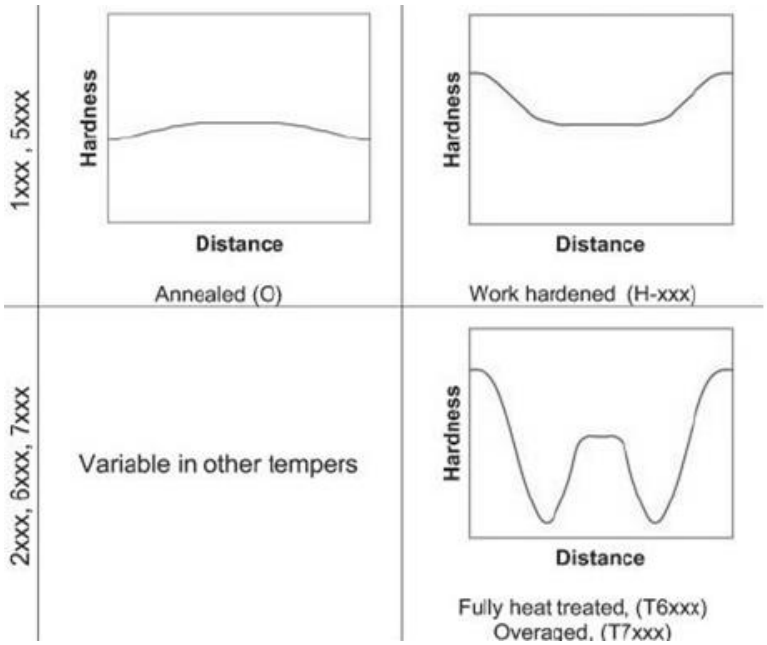

Figura 17. Esquemas representativos del perfil genérico de dureza en secciones transversales a la soldadura para distintos tipos de aleaciones de aluminio [32].

Los perfiles descritos en la Figura 17 tienen una explicación microestructural. Por ejemplo, en el caso de aleaciones termotratables, el estado de máxima dureza del material de partida se pierde en la HAZ por sobreenvejecimiento y se recupera parcialmente en la TMAZ y NZ debido al endurecimiento por deformación y al afino de grano, respectivamente, dando como resultado la típica forma de w. Además de la descripción experimental de la dureza, basada en la microestructura, se han realizado varios estudios de modelización de la evolución de la microestructura y la dureza en aluminios termotratables se ha modelado en varios estudios [88-91].

Existen pocos que cuantifiquen el detrimento introducido por los distintos tipos de defectos en las propiedades mecánicas de la unión, en comparación con la cantidad de estudios que relacionan microestructura con durezas. Este hecho es debido a que habitualmente los defectos macroscópicos son considerados como inadmisibles en las uniones soldadas. Sin embargo, la presencia de defectos microscópicos puede ser igual de perjudicial. En este trabajo se ha estudiado el detrimento que introducen algunos defectos concretos en las propiedades mecánicas de la unión mediante FSW de MMC con alto porcentaje de partículas de SiC.

En relación a los resultados de los ensayos de tracción, es difícil encontrar tendencias globales dado el gran número de materiales de partida (composición, estado termomecánico, espesor, etc.), combinaciones de parámetros y herramientas. Aún así se consideran como generales los siguientes resultados [32]:

- En aleaciones termotratables (2xxx, 6xxx y 7xxx) la resistencia a la tracción suele ser igual o levemente mayor a la del MB cuando se parte del estado sobreenvejecido. En cambio, no suele superar el 90% cuando se parte de aleaciones en estado T6 o T7.
- La ductilidad deja de ser uniforme y se concentra en las zonas de menor dureza, en conjunto suele disminuir.
- La fractura puede ocurrir en el lado de avance o de retroceso indistintamente, aunque para un mismo sistema (material + herramienta) suele coincidir en uno de los dos.
- En aleaciones no termotratables endurecidas por deformación la fractura suele ocurrir en el centro de la unión, donde la dureza es mínima.
- Si éstas últimas se encuentran recocidas la perdida de propiedades mecánicas es mínima.

Por último, las aleaciones de aluminio soldadas por FSW se suelen utilizar en aplicaciones en las que la tenacidad a la fractura no es el condicionante principal. Sin embargo, existen áreas dónde puede ser un factor crítico, como por ejemplo, las aplicaciones criogénicas. Los resultados reportados coinciden en que el *nugget* típicamente presenta una mayor tenacidad que el MB [92, 93], pero aún es necesario extender estos estudios al resto de zonas microestructurales.

1.2.2.5. Tensiones residuales

Las tensiones residuales, TR, se generan en los materiales debido a diferentes procesos térmicos, mecánicos y termomecánicos no homogéneos, como pueden ser procesos de mecanizado, conformado o tratamientos térmicos. Durante los procesos de soldadura se suelen generar TR de magnitud significativa, que dan lugar a una degradación de la integridad estructural y del rendimiento de los componentes en servicio. Cuando se combina el efecto de las tensiones residuales con las cargas aplicadas en servicio se puede producir un fallo imprevisto en la estructura soldada, si aquellas no se habían tenido en cuenta en el diseño. Además las TR pueden afectar el comportamiento a fatiga, la tenacidad y la resistencia a la corrosión de las uniones soldadas. Por todos estos motivos, el estudio de la distribución y magnitud de las TR en las soldaduras es de gran importancia.

Existen diversos métodos para determinar las tensiones residuales en un componente, técnicas destructivas, como por ejemplo técnicas del agujero ciego o «hole drilling», de seccionamiento como el método de contorno o «contour method», y técnicas no

destructivas, como las basadas en difracción de rayos X, radiación sincrotrón o neutrones [94]. En el esquema de la Figura 18 se comparan distintas técnicas en cuanto a su profundidad de penetración y su carácter destructivo.

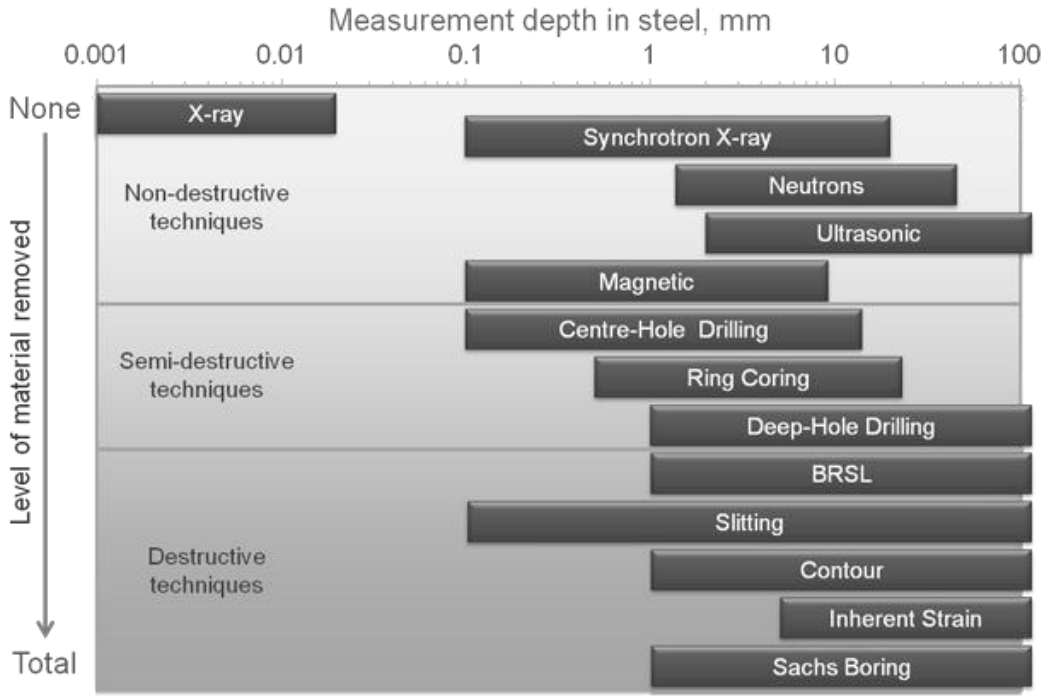

Figura 18. Representación de las distintas técnicas para determinar tensiones residuales según la capacidad de penetración en el material y su carácter destructivo [95].

Las técnicas destructivas son las más convencionales y se basan en un mismo proceso, la relajación: se mecaniza un trozo de la pieza de forma que se elimina material de forma controlada y se relajan las tensiones residuales. El análisis de las tensiones comienza con la medición de las dimensiones del material, o el componente o pieza, antes y después del mecanizado. A partir de estas medidas se calculan las deformaciones y finalmente, utilizando las constantes elásticas del material, se calculan las tensiones.

Por ejemplo, en la técnica de agujero ciego o «hole drilling» se perfora la pieza (el diámetro y profundidad del agujero varía según el experimento) y se mide la deformación utilizando galgas extensométricas de roseta. De modo similar, el método de contorno consiste en el mecanizado de una sección plana del componente, mediante la medida del contorno de la probeta se pueden calcular las tensiones residuales perpendiculares a dicha sección.

En cuanto a las técnicas no destructivas, destaca la difracción. La medición de TR mediante difracción de radiaciones penetrantes, ya sea de neutrones o rayos x, se basa en la ley de Bragg. Éstas técnicas utilizan la expansión o contracción de los planos en la red cristalina como extensómetro dentro del material [96]. De este modo, se determinan las TR a partir

de cambios en la distancia interplanar dentro del material. Los neutrones tienen una gran capacidad de penetración en la mayoría de los materiales metálicos, lo que los convierte en una buena herramienta para hacer mediciones en soldaduras de gran espesor.

En la literatura existen numerosos trabajos que abordan el estudio de las TR en uniones por FSW de aleaciones de aluminio [97]. Entre la diversidad de técnicas empleadas y materiales estudiados, existe acuerdo en que los valores máximos que se alcanzan son menores que en soldaduras por fusión. También coinciden en que la componente longitudinal (paralela a la dirección de soldadura) presenta la mayor variación de las tres: con máximos en la HAZ (tracción), valores menores en el *nugget* y mínimos en el MB (compresión). En la Figura 19 se muestra un resumen de distintos estudios recogidos de la literatura por Woo et al.

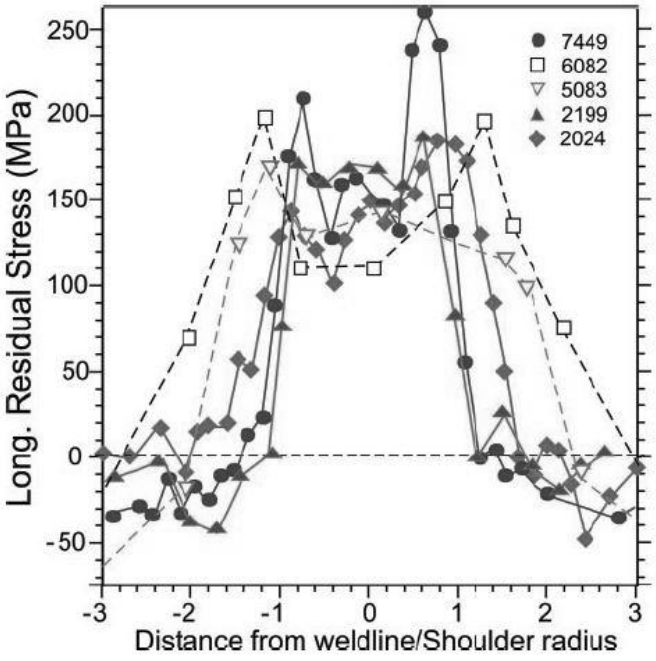

Figura 19. Perfil de tensiones residuales longitudinales normalizado según el diámetro del hombro de la herramienta para distintas aleaciones de aluminio [32].

A pesar del gran avance que se ha realizado en la caracterización de tensiones residuales en soldaduras por FSW de materiales metálicos, existen puntos en los que se necesita reforzar el conocimiento:

- En general el estado de tensiones en una soldadura es triaxial. En muchos casos se asumen estados biaxiales de tensión plana para simplificar los cálculos y reducir el tiempo de medida. Pero este procedimiento sólo es válido en chapas muy finas, de lo contrario puede conducir a grandes errores.
- Muchas medidas se realizan sobre una parte del material extraída de la soldadura. Es importante tener en cuenta que el proceso de extracción relaja las

TR si la pieza sobre la que se mide no es lo suficientemente grande. Existe un criterio según el cual la muestra a medir debe contener una soldadura de longitud al menos 8 veces el diámetro de la herramienta [98, 99] para que ésta retenga un 90% de las TR.

- Otra carencia en la mayoría los trabajos reportados es la falta de medidas en profundidad. Es sabido que el campo de deformación que produce la soldadura por FSW cambia a través del espesor. Por lo tanto, también es importante caracterizar las TR en esta dirección.
- En las técnicas de difracción, el establecimiento del parámetro de referencia d_0 o espaciado interplanar sin tensiones (relajado), conlleva habitualmente muchas dificultades experimentales. El uso de muestras en forma de polvo queda limitada a casos en que la microestructura del componente que se quiere medir es conocida y se puede reproducir.
- Una alternativa que se suele utilizar para obtener el valor de referencia, d_0, son las medidas realizadas sobre una muestra tipo peine extraída de la soldadura, Figura 20. En este caso, los pelos de la muestra peine deben ser lo suficientemente pequeños para que las TR se relajen completamente, de lo contrario se provocaría una subestimación en los cálculos. Además, un aspecto a destacar del uso de muestras peine, es que la extracción de dichas muestra hace que el método de medida deje de ser no destructivo.

Figura 20. Muestra peine extraída de forma transversal a una de las soldaduras de esta Tesis realizada por FSW en dos pasadas sobre chapas de 25%SiC/2124Al de 15 mm de espesor.

1.2.2.6. Otras propiedades: Fatiga y corrosión

En general el comportamiento a fatiga de las uniones realizadas por FSW supera aquel de las soldaduras por fusión [100, 101]. Se atribuye esta diferencia al afino microestructural característico del proceso de FSW. El inicio de la grieta normalmente está asociado a alguna singularidad geométrica que concentra las tensiones en la superficie superior de la unión (rebaba, reducción de espesor debajo del hombro, etc.) [102]. En aquellos casos en los que estas singularidades han sido mecanizadas, la grieta generalmente comienza en la

región de menor resistencia. Las TR pueden jugar un papel significativo en el comportamiento a fatiga [103-106], sin embargo muchas veces su efecto se elimina al mecanizar especímenes de ensayo pequeños [98].

Cuando los efectos superficiales se eliminan (uniones mecanizadas), los tres factores que dominan el comportamiento a fatiga son: las TR, la microestructura y los defectos. Debido a la falta de estudios que reporten la interacción de estos factores en las uniones por FSW [32] se destaca la dificultad de establecer tendencias en su comportamiento a fatiga.

Por otro lado, es sabido que la microestructura es un factor importante en la determinación del comportamiento frente a la corrosión de las aleaciones de aluminio [107]. El proceso termomecánico severo que impone el FSW afina la estructura de grano y altera la distribución de la precipitación, particularmente cerca de los bordes de grano. La Tabla 3 muestra un resumen de las observaciones recogidas de la literatura por Threadgill [32] en relación a la corrosión.

Alloy	Corroding zone	Mechanism	Test
2024	TMAZ	Exfoliation	ASTM G34
	Nugget	Pitting/blistering	
	Nugget	Intergranular/pitting (150 μm)	Immersion ($NaCl + H_2O_2$)
	HAZ/parent	Pitting to 150 μm	
	HAZ	Intergranular	Immersion (NaCl)
	Nugget and HAZ	Intergranular attack (low rotation spends in nugget/high speeds predominantly HAZ))	Gel visualisation and Immersion ($NaCL + H_2O_2$)
	Nugget/HAZ Parent	Passive Pitting	Poarisation curves and ellectrochemical impedance spectroscopy in NaCl
2219	Parent	Slight pitting at bottom of nugget, overall better than parent	Immersion (NaCl)
2139	Parent	Pitting + intergranular	Immersion ($NaCl + H_2O_2$)
2195	No preference	Even pitting across sample or weld better than parent	Immersion (NaCl)
5083	Parent	Welds show lower pitting tendency	EXCO (KCl, KNO_3, HNO_3)
5456	Nugget	Preferential to advancing side	Immersion (phosphoric acid)
6082		Even pitting across sample	Immersion (NaCl+ acetic acid)
6013	Parent	Intergranular corrosion	Immersion (NaCl)
7010	HAZ	Intergranular corrosion	Immersion (NaCl)
7050	Nugget, TMAZ/HAZ	Intergranular corrosion	Immersion tests in NaCl solution
7075	HAZ	Intergranular	Immersion ($NaCl–KNO_3–HNO_3$)
	HAZ		Immersion
	HAZ		Pitting potential cell
	TMAZ/HAZ boundary		Salt spray
7108	TMAZ	Localised intergranular corrosion	ASTM G34 EXCO
7150	TMAZ		Immersion

Tabla 3. Resumen de los distintos comportamientos frente a la corrosión de uniones realizadas por FSW en aleaciones de aluminio [32].

En general, la determinación del comportamiento frente a la corrosión en las uniones por FSW sigue siendo un desafío. Esto se debe a la complejidad de la microestructura y a la variedad de posibles mecanismos.

1.2.3. La soldadura de los MMC mediante la técnica de FSW

Hoy en día la fabricación de los MMC se considera bastante madura como para ser económicamente competitiva en sectores tecnológicos de alto valor añadido. Así, las rutas pulvimetalúrgicas permiten la adición de un alto volumen de refuerzo y una distribución muy homogénea. En cambio, la soldadura de este tipo de materiales, especialmente aquellos con alto contenido de refuerzo, sigue siendo problemática y es una de las razones que frena su utilización masiva.

La soldadura por métodos tradicionales puede provocar los siguientes defectos:

- Porosidad en la zona de fusión.
- Descomposición química de las partículas o reacción con la matriz líquida, que da lugar a compuestos indeseados.
- Deterioro de la intercara matriz/partícula debido a la formación de fases frágiles o a la falta de mojabilidad de las partículas.
- Formación de fisuras.
- Microestructura de solidificación desde la fase líquida (colada).
- Aglomeración de las partículas de refuerzo.

La mayoría de estos problemas, surgen de la presencia de una fase líquida en la soldadura, es por este motivo que los procesos de soldadura en estado sólido se presentan como alternativas muy prometedoras para la unión de MMC. Existen cuatro técnicas dentro de este grupo: la soldadura por ultrasonidos, la unión por difusión o «diffusion bonding», la soldadura por fricción y la soldadura por fricción batida (FSW) descrita en detalle en la sección 1.2.2.

La soldadura por ultrasonidos produce la unión mediante la aplicación de vibraciones a alta frecuencia en las superficies a soldar sujetas firmemente. En comparación con la soldadura por fricción y la soldadura por fricción batida, la deformación que introduce este proceso por vibración es muy pequeña y localizada. Por ello, esta técnica se suele utilizar en la soldadura de cables y pequeños filamentos, no de componentes estructurales.

La unión por difusión es un proceso en que los materiales se ponen en contacto dentro de una cámara térmica en condiciones de vacío. La unión se forma por la acción de la difusión atómica. Es decir, los átomos de cada superficie se mueven hasta llenar el espacio que exista entre ellas. Muchas veces se utiliza una pequeña lámina de un material similar y compatible que se coloca entre los materiales a soldar para agilizar el proceso. Aun en esta variante, los tiempos del proceso son muy largos, la preparación de las superficies debe

ser cuidadosa (pulido) y el tamaño de las piezas a unir queda limitado por el tamaño de la cámara térmica.

La soldadura por fricción utiliza el rozamiento por movimiento relativo entre los cuerpos a soldar para generar calor y producir una región de material reblandecido en la zona de contacto. Existen dos configuraciones: una en la que las dos partes a unir se mueven y otra en la que una de las partes se mantiene fija (en ambos casos hay movimiento relativo entre los dos componentes). También existen variantes rotacionales y lineales, según sea el tipo de movimiento realizado por las piezas a soldar. En todos los casos se producen rebabas del material plastificado en la superficie de la soldadura por la presión impuesta, Figura 21. Aunque esta técnica ha logrado unir algunos MMC [108, 109], la forma de las piezas que permite soldar está muy limitada y su sujeción puede ser problemática. Además, las rebabas requieren operaciones de mecanizado posteriores a la soldadura.

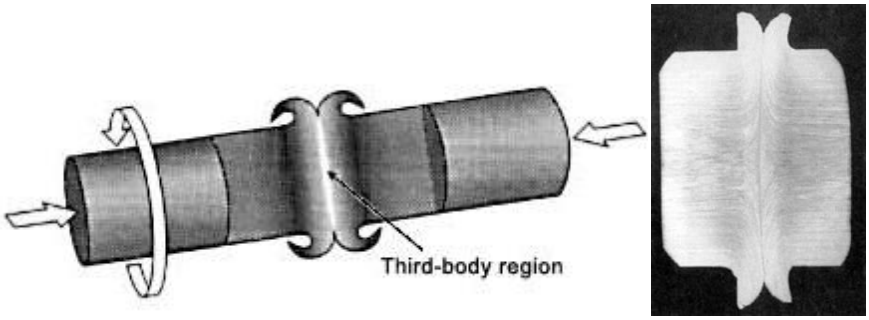

Figura 21. Soldadura por fricción. Izquierda: esquema del proceso [110]. Derecha: macrografía de una sección longitudinal de una soldadura en compuesto [111].

Entre las técnicas de soldadura en estado sólido, la que mejor se adapta a la unión de componentes estructurales de MMC con alta carga de refuerzo discontinuo es la soldadura por fricción batida. Su velocidad es compatible con la de los procesos industriales. La preparación de las superficies es simple, el volumen de material deformado permite que se suelden piezas con fines estructurales, la geometría es relativamente versátil y no hay limitación de tamaño.

Estudios de soldadura por FSW en MMC aseguran que no se producen reacciones químicas desfavorables entre las partículas y la matriz [62]. Esto se debe a que el ciclo térmico es menos severo que en soldaduras por fusión porque las temperaturas alcanzadas y el tiempo de proceso son menores. Por esta técnica, se han conseguido uniones sin defectos volumétricos [112-123]. Además, los trabajos coinciden en que se logra una distribución más homogénea del refuerzo en el *nugget* [112, 115, 122, 123]. Sin embargo, han surgido problemáticas nuevas, entre las que se destaca: el excesivo desgaste de las herramientas

ocasionado por las partículas de refuerzo [114, 117, 118, 120, 121, 124], y la limitación de las condiciones en las que se obtienen uniones sin defectos [113]. Es por este motivo, que la aplicación de la técnica de FSW a compuestos con alta carga de refuerzo se encuentra en una fase inicial en comparación con las aleaciones sin reforzar. Se necesita superar las dificultades técnicas propias de este campo, en particular eliminar el desgaste de las herramientas y ahondar en la relación parámetros-defectos. Una vez superadas estas dificultades, el siguiente paso es la caracterización de las uniones, especialmente en aquellos aspectos que tengan que ver con las aplicaciones estructurales (propiedades mecánicas, tenacidad a la fractura, tensiones residuales, comportamiento a fatiga, etc.). De modo que se logre un proceso repetible, fiable y robusto que pueda dar lugar a más aplicaciones y a mayor escala.

2. OBJETIVOS

Los objetivos de esta tesis se enmarcan dentro de una estrategia global para eliminar las causas que dificultan la utilización de los MMC con alta carga de refuerzo en aplicaciones que requieran uniones soldadas. Conseguir superar dichas dificultades permitiría ampliar el campo de utilización de estos materiales y beneficiarse de sus excelentes propiedades mecánicas específicas. Para ello, es necesario profundizar en el estudio del proceso de FSW de MMC, única técnica de soldadura capaz de abordar estos objetivos.

En particular, uno de los objetivos de este trabajo de tesis es optimizar el proceso de soldadura mediante la técnica de FSW en compuestos de matriz de aluminio aeroespacial (serie 2xxx) reforzados con alto contenido de partículas de SiC para obtener uniones con una adecuada resistencia mecánica. La bondad de las uniones resultantes se determinará mediante su eficiencia de junta.

Para lograr dicho objetivo, se utilizará como punto de partida el conocimiento que se tiene de las aleaciones de aluminio puesto que el proceso de FSW ha sido muy estudiado en estos materiales. A partir de ello, se analizará la validez de estos conocimientos para el caso de los materiales compuestos estudiados en este trabajo.

En paralelo, se estudiarán las problemáticas específicas que surgen en el proceso de FSW de este tipo de materiales: las debidas tanto a la naturaleza termotratable de la matriz, como a la presencia de partículas cerámicas.

3. PUBLICACIONES

Publicaciones incluidas en este trabajo de tesis:

3.1. F. Cioffi, R. Fernández, D. Gesto, P. Rey, D. Verdera, G. González-Doncel, "*Friction stir welding of thick plates of aluminum alloy matrix composite with a high volume fraction of ceramic reinforcement*", Composites A, 54 (2013) 117–123. **(FI=2.744)**

3.2. F. Cioffi, J. Ibañez, R. Fernández, G. González-Doncel, "*The effect of lateral off-set on the tensile strength and fracture of dissimilar Friction Stir Welds, 2024Al alloy and 17%SiC/2124Al composite"*, Materials and Design, 65 (2015) 438–446. **(FI=2.913)**

3.3. F. Cioffi, J. Ibañez-Ulargui, R. Fernández, D. Verdera, G. González-Doncel, "*Influence of friction stir welding parameters on the mechanical performance of 25%SiC/2124Al composite joints conducted with an un-threaded WC-Co tool*", enviada a Journal of Materials Science. **(FI=2.371)**

3.4. F. Cioffi, J.I. Hidalgo, R. Fernández, T. Pirling, B. Fernández, D. Gesto, I. Puente Orench, P. Rey, G. González-Doncel, "*Analysis of the unstressed lattice spacing, d0, for the determination of the residual stress in a friction stir welded plate of an age-hardenable aluminum alloy – Use of equilibrium conditions and a genetic algorithm*", Acta Materialia, 74 (2014) 189–199. **(FI=3.941)**

Además en el Anexo 1 se incluye una publicación realizada durante el trabajo de investigación doctoral que se enfoca en el aspecto computacional de aplicar Algoritmos Evolutivos a la determinación de las tensiones residuales en uniones por FSW de aluminios termotratables.

- J. I. Hidalgo, R. Fernandez, J. M. Colmenar, F.Cioffi, J. L. Risco-Martin, G. Gonzalez-Doncel, "*Using Evolutionary Algorithms to determine the residual stress profile across welds of age-hardenable aluminum alloys*", Applied Soft Computing Journal (2015). **(FI=2.81)**

Composites: Part A 54 (2013) 117–123

Contents lists available at ScienceDirect

Composites: Part A

journal homepage: www.elsevier.com/locate/compositesa

Friction stir welding of thick plates of aluminum alloy matrix composite with a high volume fraction of ceramic reinforcement

F. Cioffi [a], R. Fernández [a], D. Gesto [b], P. Rey [c], D. Verdera [b], G. González-Doncel [a,*]

[a] Centro Nacional de Investigaciones Metalúrgicas (CENIM) CSIC, Av. de Gregorio del Amo, 8, E-28040 Madrid, Spain
[b] Centro Tecnológico AIMEN, Planta de Tecnologías de Unión, C/Relva n° 27, E-36410 O Porriño, Spain
[c] Centro Tecnológico AIMEN, Área de Materiales y Procesos de Fabricación, C/Relva n° 27, E-36410 O Porriño, Spain

ARTICLE INFO

Article history:
Received 27 March 2013
Accepted 20 July 2013
Available online 27 July 2013

Keywords:
A. Metal matrix composites (MMCs)
B. Mechanical properties
B. Microstructures
E. Joints/joining

ABSTRACT

The microstructure and mechanical properties of joints conducted by friction stir welding, FSW, at different rotational speeds in thick plates of a composite material with a high volume fraction of reinforcement, namely 2124Al/25vol%SiC_p, are studied. Original particle-free regions vanish during the stirring process, leading to a homogeneous particle distribution. Occasional breakage of some large particles occurs. Tunnel defects appear at low rpm, and disappear at high rotational speeds. The size of the thermo mechanically affected zone, TMAZ, increases with increasing rpm. Ductility of the welds in the range of 10–15% is achieved in compression tests whereas a rather brittle behavior is obtained in tension. A strength difference, SD, effect between compression and tensile test is obtained. This accounts for the little detrimental effect of the FSW process on the matrix–reinforcement interface. The SD effect is attributed to the presence of a microscopic residual stress.

1. Introduction

Discontinuously reinforced aluminum alloy metal matrix composites (MMCs), with ceramic particles in the range of 10–25 vol%, are known to exhibit higher Young modulus and strength [1,2], better wear resistance [3,4] and better high temperature properties than the corresponding monolithic alloys [5,6]. These improvements are accompanied by a very small increase in density, which makes these composites very attractive structural materials for many applications in the automotive and aerospace industries [3,7–9]. Furthermore, a noteworthy factor that makes them very attractive from the technological point of view relies in that their preparation takes advantage of conventional fabrication procedures used for monolithic alloys (casting, powder metallurgy, rolling, extrusion...). This implies limited modifications of already existing metal manufacturing plants and, hence, potential reduced cost in materials preparation in comparison, for example, to continuously reinforced composites [10,11].

The technological advantages of these materials, however, have not been yet fully exploited and their use is still restricted to very specific applications. Several reasons are usually suggested to explain this delay: it is believed that secondary operations such as welding [12,13], machining [14] and/or forging (extrusion, rolling,...) [15,16] involved in the manufacture of components imply difficulties which impede a massive use of these materials [12,14]. In particular, conventional fusion joining techniques present important drawbacks such as: reinforcement–matrix reactions; segregation of the reinforcement; high viscosity of the melt compared with that of the un-reinforced alloy; porosity derived from the occluded gas, and additional problems associated with the different coefficients of thermal expansion and conductivities between metal and ceramic particles [12,13, 17].

On the contrary, friction stir welding (FSW) is revealed as a promising alternative to the conventional methods to join MMCs [18–23]. The specific characteristics of this relatively new joining method are extensively described elsewhere [18,24–26]. Their advantages rely on a very unique characteristic: melting of the parent metal does not occur. As a consequence, the process is not detrimental for the original distribution of the ceramic particles. In fact, it can, instead, help to improve its homogeneity [27,28] As a drawback, however, it has been shown that the FSW parameters in these composites become more critical than for the corresponding un-reinforced alloys, and tunnel defects in the thermo mechanically affected zone, TMAZ, may easily appear [29]. Further efforts are, therefore, needed to understand the influence of the FSW process variables on the final microstructure in the joints of these composites.

In this work, the potentiality of this technique to joint plates of aluminum matrix composites with an elevated amount of reinforcement and high thickness is investigated: specifically, a 15 mm thick plate of 2124Al/25vol%SiC_p composite has been

* Corresponding author. Tel.: +34 915538900x337.
E-mail address: ggd@cenim.csic.es (G. González-Doncel).

studied. Taking advantage of the versatility of this technique the weld was conducted in two passes, one on each side of the plate, using a pin which length was about half of the plate thickness. To the best of these authors knowledge, no published work reports welds in plates of aluminum matrix composites of thickness above 8 mm [28,30,31]. Furthermore, joints of composites with a reinforcement content above 20% in volume have been rarely conducted using this technique [21,28,29,32,33]. In particular, the present study is focused on the microstructure and the mechanical properties of the composite joints obtained with different rotational speeds.

2. Materials and experimental details

The composite material studied was 2124Al/25vol%SiC_p in the form of a 15 mm thick plate and denoted as AMC225xe by the supplier: Aerospace Metal Composites, AMC, UK. This composite is a high quality aerospace material produced by a proprietary powder metallurgy route and forged to the final thickness. The average SiC particle size is of about 2 μm.

The initial plate was sectioned in several pieces, with no extra care on the preparation of the surface edges to be joined: just a usual finishing from the mill was conducted to eliminate defects from the cuts. The pieces were heat treated to T6 condition. This consisted of a solution treatment at 530 °C for 2 h followed by quenching in oil bath at 20 °C and subsequent annealing at 160 °C for 18 h.

The welds have been carried out in two runs, one on each side of the plates, taking advantage of the PDS-4 Intelligent Stir FSW machine from MTS located in AIMEN. Both the advancing and the retreating sides coincide in the two runs. A 2-piece fix tool with a threaded pin (length of 7.62 mm) which included three ground flats was used. The shoulder diameter was slightly above 20 mm while the pin diameter varied from 7.95 to 6.35 mm. The internal face of the shoulder was not flat, but inclined 7° to create a conical surface. The shoulder and the pin were made on H13 steel (48 HRc) and MP159 alloy, respectively. Both the advancing and the retreating sides coincide in the two runs. Welds were conducted in the composite at increasing rotational speeds, namely: 300, 550, and 800 rpm, holding the advancing speed at 75 mm/min and a tilt angle of 1.5°. For security reasons, the machine operated under position control, trying to achieve the same force from the shoulder (about 8.5 kN). For this purpose, a slight change in the vertical tool position was required since different rotational speeds imply different heat inputs, different plastic behaviors of the material, and, hence, slightly different forces. In this manner, the variable of rotational speed is isolated, maintaining the remaining parameters nearly constant in the three experiments. Tool wear occurs during FSW of this composite [29,32]. This could be appreciated from the appearance of the pin at beginning and the end of each run (of approximately 250 mm total length). Therefore, the pin used in the welds performed at 300 and 550 rpm was replaced for a new one in the weld conducted at 800 rpm, the most severe wearing conditions.

The metallographic sections of the welds were prepared by conventional procedures. These involved grinding in successively finer sandpaper and polishing down to 1 μm diamond paste. In some cases, also etching with a solution of 0.5% HF in water was employed. Microstructural characterization was carried out using optical microscopy, OM, and scanning electron microscopy, SEM. Observations were carried out both before and after etching.

Ultra-micro hardness was measured using an automatic Berkovich indenter and a load of 300 mN on a transverse section of the weld conducted at 800 rpm, the one where no tunnel defects appeared. These measurements were done with the aim of distinguishing the different regions of the weld.

Finally, tensile and compression test have been conducted to evaluate the influence of the rotational speed on the mechanical properties of the joints. For this purpose, tensile specimens were machined with the tensile direction perpendicular to the welding direction such that the tunnel defects in the nugget were avoided. The samples were small, with a gauge length of 15 mm and a diameter of 2.5 mm, and threaded heads. The gauge length of these samples covered different microstructural regions developed in the welds. Tests were conducted at $1 \times 10^{-3}\,s^{-1}$ of initial strain rate. Due to the heat input provided by the stirring process, the precipitation state after welding will differ from that imposed by the initial T6 condition. For this reason, evaluation of the mechanical properties in the as processed and after a subsequent T6 conditions is required. As it will be shown, the ulterior T6 treatment accentuated the dispersion of the tensile behavior of the welds, leading frequently to a brittle behavior. Therefore, the compressive behavior of the welds was also evaluated in the as processed conditions. Compression samples were machined in the shape of small cylinders, of 3 mm in gauge diameter and 5 mm in length, with the same orientation as the tensile samples. For comparison, tensile and compression specimens machined from the base material (T6 condition) were also tested. The fracture surfaces of the tensile samples were observed using SEM and longitudinal cross sections were also observed by OM to identify the position of the fracture with respect to the weld center or the different microstructural zones.

3. Results and discussion

The microstructure of the composite shows a homogeneous distribution of the SiC ceramic particles if observed at low magnification. At high magnification, however, particle-free areas in the form of elongated regions and some particle agglomerates along parallel bands are visible, Fig. 1. The size of the particle-free areas ranges from 20 to 250 μm of length and 3–15 μm of width, and are uniformly distributed throughout the base material. The horizontal alignment of the particle-free regions, Fig. 1, is a consequence of the cold forging process used to reduce material thickness. Despite the severe deformation induced by this process, it seems that

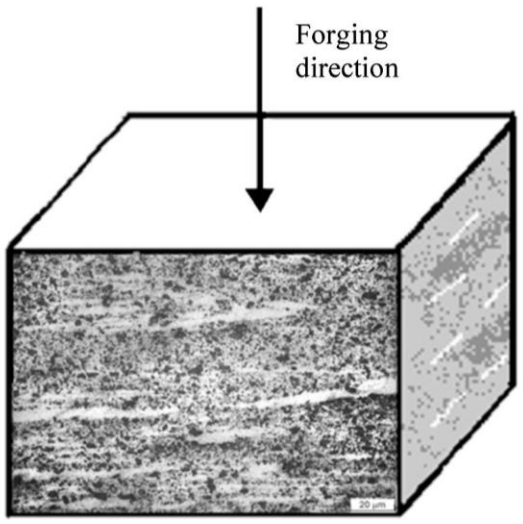

Fig. 1. Microstructure of 2124Al/25vol%SiC_p composite material showing the reinforcement free zones and their orientation with respect to the forging direction. (Lateral view is a schematic representation constructed to complete the image).

neither SiC particles cracking (breakage of large particles was rarely observed) nor matrix-particle detachment has occurred.

The superficial aspect of the joints at the three rotational speeds is shown in Fig. 2. The surface presented pores at the lowest speed, 300 rpm, which is characteristic of too cold processing conditions [34]. Excessive flash and penetration of the tool shoulder, however, occurs at the highest rotational speed, 800 rpm. The different surface appearance could be also related to a different vertical plunge rather than only to a direct effect of the increasing rotational speed. A compromise, with no surface pores or flashing, is attained at the intermediate speed, 550 rpm. Although the vertical force was similar in all three cases, material softening becomes more significant with increasing rotational speed, in agreement with other authors [35,36]. On the other hand, tunnel defects, which are clearly visible at 300 rpm, do not appear at 800 rpm, as it is seen in the overview of Fig. 3, where transverse metallographic sections of the three welds are illustrated. These observations suggest that the optimal rotational speed for this composite, namely no tunnel defects and no superficial flaws, should lie between 550 and 800 rpm.

Other microstructural changes resulting from FSW can be also appreciated from the scheme of Fig. 3. In the three joints the TMAZ can be easily distinguished from the un-deformed region (heat affected zone, HAZ, and base material, BM) due to a noticeable difference in particle distribution: more homogeneous in the TMAZ than in the HAZ and BM. Furthermore, and as it is generally observed, the boundary between the TMAZ and the HAZ, delimited by dotted lines in Fig. 3, is sharper in the advancing than in the retreating side. This can be seen in more detail in Fig. 4: the stirring process causes full particle homogenization in the TMAZ and the particle-free regions, Fig. 1, disappear, in agreement with other investigations [27,28]. It is not possible to delimit the HAZ from the BM since the particle distribution is similar in both regions and the microstructural changes occurring in the alloy matrix such as grain growth, and of course precipitation, are not appreciated by OM or SEM.

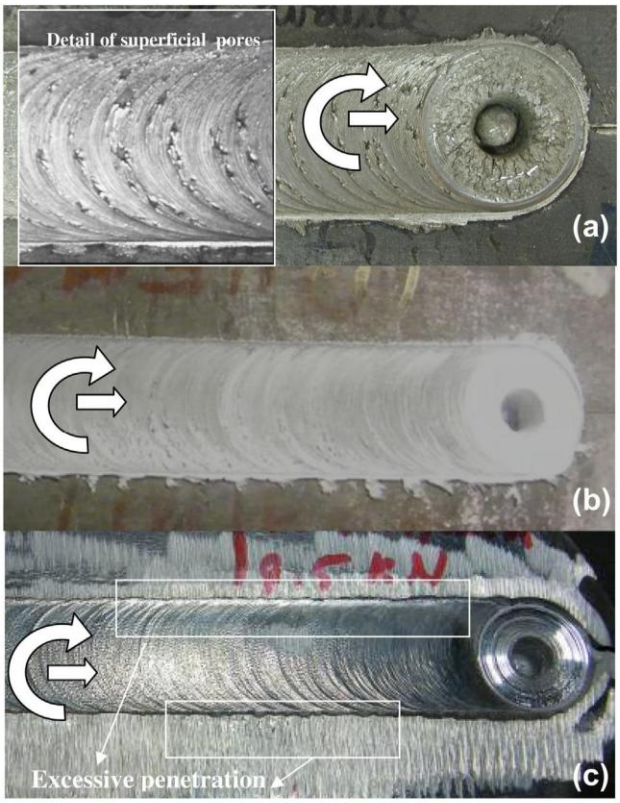

Fig. 2. Superficial aspect of the joints at the three rotational speeds: (a) 300, (b) 550 and (c) 800 rpm. White arrows indicate rotation and advance direction of the tool. (For interpretation of the references to color in this figure legend, the reader is referred to the web version of this article.)

The results of the ultra-micro hardness tests measurements are summarized in the plot of Fig. 5, which shows the hardness profile across the mid-region of the plate welded at 800 rpm. From the BM to the center of the weld, the same tendency can be observed in the advancing and retreating sides: firstly, a progressive decrease in hardness occurs and, after a minimum is reached, an increase in hardness takes place up to a value similar to that of the BM. The boundary between the TMAZ and the HAZ, revealed by OM, is indicated as solid vertical lines. As can be seen, no sign of hardness variation associated with a different particle distribution is detected across the weld in this boundary. This is an indication that this difference does not affect the hardness of this material. Instead, the precipitation state seems to greatly change the hardness of the material in the different zones. So is the case of the HAZ, in which the temperature rise imposed by the FSW process is a function of the distance to the weld center, and therefore the precipitation state will vary from the T6 condition in the BM to different over-aged states. Though a well defined BM-HAZ border is not observed, it can be considered as the position in which the hardness starts to decrease: roughly at 22 mm from the center of the weld in the advancing side. Hardness measurements on the retreating side, however, did not cover the complete HAZ, but it is evident that it extends more than in the advancing side. This is in agreement with the asymmetrical nature of this welding process and the more diffuse TMAZ–HAZ boundary in the retreating side than in the advancing one, Fig. 4.

The hardness data were not useful to distinguish between the nugget zone, NZ, and the TMAZ. The maximum value, obtained in the weld center, is similar to that of the BM, indicated in the plot as a dotted horizontal line. This suggests that the severe plastic deformation occurring in this region is not deleterious for the metal–ceramic interface.

The size and shape of the TMAZ varies for the different joints. It increases its cross sectional area from 119 mm^2 to 155 mm^2 and to 164 mm^2 at 300, 550, and 800 rpm, respectively. It becomes wider in the middle and goes from a bell to a trapezium shape as the rotational speed increases. This variation is a consequence of the temperature rise in the material caused by increasing the rotational speed. In other words, the heat transferred to the material rises producing more softening and an enlarged deformed region; i.e., a broader TMAZ.

Large tunnel defects, clearly visible to the naked eye, are developed in both runs at 300 rpm near to the advancing side of the TMAZ, Fig. 3a). The tunnel defect in the first pass is elongated and vertically aligned; whereas the one in the second pass is round shaped and its cross sectional area is approximately 30% smaller (see detail of Fig. 3a). As rotational speed increases (550 rpm) the size of the defect diminishes, and it appears only on the second run of the weld. Contrarily to the alignment of the tunnel defects formed at 300 rpm, the tunnel defect was elongated in the horizontal direction and located towards the bottom advancing side of the TMAZ (see detail of Fig. 3b). The differences between size/shape of the tunnel defects developed in the first and second pass of the welds must be a consequence of the microstructural modifications resulting from the thermal treatment suffered during the first pass.

Finally, at 800 rpm no tunnel defects are visible. In summary, these experiments show that with increasing rotational speed the probability that tunnel defects appear diminishes. This tendency can be understood bearing in mind energetic considerations: an increase of the rotational speed will provide more energy into the material, which implies an increase of the heat input, and,

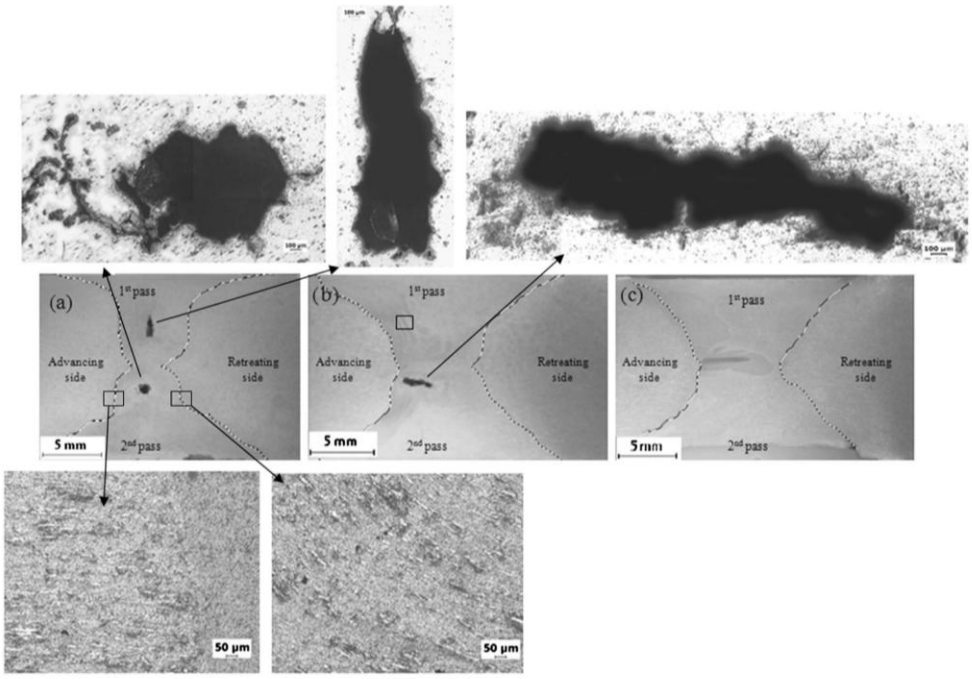

Fig. 3. Transverse section of the joints conducted at: (a) 300 rpm, (b) 550 rpm, and (c) 800 rpm. Detail of tunnel defects and TMAZ–HAZ limits are also shown.

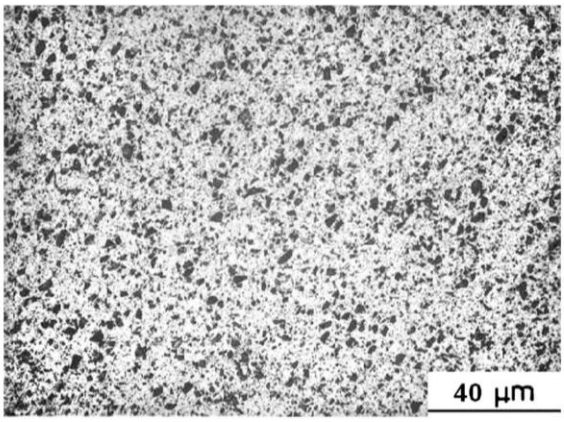

Fig. 4. Micrograph of the advancing side of the TMAZ of material welded at 550 rpm.

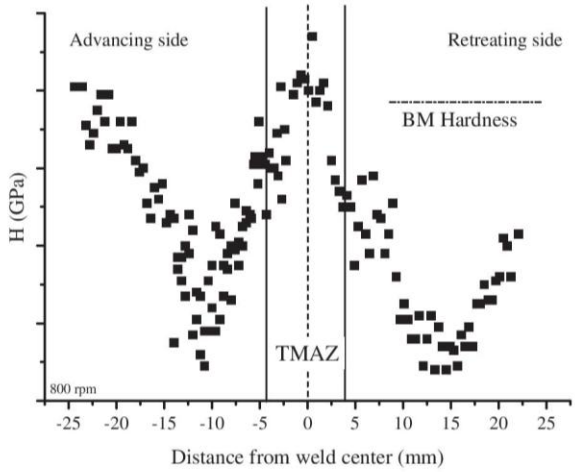

Fig. 5. Hardness profile across the composite weld (mid-region) conducted at 800 rpm. The error is of ±0.2 GPa.

hence, an increase of temperature. The higher the temperature the easier the plastic flow will be for the joining process, which restricts the appearance of tunnel defects. Another plausible factor promoting the appearance of these tunnel defects is the presence of a microscopic residual stress, RS, inherent to these composites [37]. This stress is positive in the matrix and, to equilibrate it, negative in the reinforcement. To investigate this hypothesis, however, a detailed study of the RS present in the welds is needed. This study is beyond the scope of this investigation, and is now under progress.

In the border of the TMAZ, the high strain makes the horizontal bands align parallel to the maximum shear stress direction and appear angled, Fig. 3. From the center of the TMAZ to the advancing side limit of the HAZ the material undergoes severe plastic deformation and shows a more homogeneous distribution of the reinforcement in comparison with that in the base material, irrespectively of tool rotational speed, Fig. 4. Due to the high percentage of SiC and the small particle size it is very difficult to define the grain boundaries of the matrix alloy. This makes it impossible to distinguish the NZ within the TMAZ. Another feature common to the three welds is a dark zone located on the advancing side of the TMAZ that coincides with the highest strain region [38]. Flow patterns studies [39,40] report that the material on the advancing side rotates and flows driven by the tool pin. Therefore, this portion of material is highly deformed and sloughs off behind the pin in arc-shaped features. On the other hand, material on the retreating front side does not rotate with the pin, is less deformed, and fills in the rest of the space. This suggests that the observed dark bands correspond to material that was originally on the advancing side, entered into a zone that rotated and advanced with the tool pin and flowed as above described. In particular, the sample welded at 550 rpm presents regions of banded microstructure alternating light and dark bands located towards the advancing side of the TMAZ, Fig. 6. This banded microstructure was reported before in

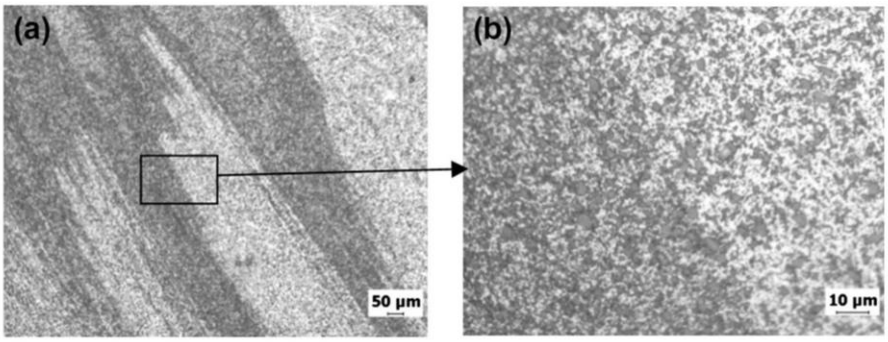

Fig. 6. Detail of the bands formed at the advancing side of the TMAZ of the first pass in the composite welded at 550 rpm, after etching with HF 0.5%.

MMCs [28, 41]. A similar phenomenon was observed in the sample welded at 800 rpm, but in this case there is also one central horizontal dark region, located in the intersection of the two passes starting on the advancing side and extended to more than half the width of the TMAZ, Fig. 3c).

The fact that the dark regions coincide with severe plastic deformed zones could suggest that the difference in contrast is due to a different concentration of fine particles, being higher in these zones [28]. Only a small number of cracked particles were found and the distribution of particle sizes was similar for both the light and dark bands shown in Fig. 6: only large particles, above 10 μm^2, were fractured, as reported in other investigations [27,41–44]. However, particle damage with change of shape, such as break-up of corners and sharp edges of large particles, cannot be discarded. Therefore, the difference between the dark and light bands is not in the particles size or distribution but in the surrounding aluminum matrix [41]. This is similar to the so called "onion rings" phenomenon, characteristic of FSW in aluminum alloys. Recent publication [39] shows that this zone etches differently as the different thermo-mechanical histories would lead to different dislocations densities and/or dynamic recrystallization in the aluminum alloy matrix. This phenomenon could also explain the differences found between the contrast zones shown in Fig. 6.

The mechanical properties resulting from the tensile and compressive tests are summarized in Table 1. The tensile yield stress (at 0.2%) in the welds in the as-processed condition ranges from 61% to 66% of the base material (of about 650 MPa). However, the plastic tensile elongation was rather small, below that of the base material, which was of only about 5%. Nevertheless, a rather scattered behavior from the repeated tests conducted in each condition was obtained. This scatter accounts for the influence of the defects or flaws arising during the FSW process and for the fact that the gauge length covered different regions of the welds. Probably due to the limited tensile elongation, no substantial differences in the strain hardening behavior with respect the base material was observed and a clear dependence with rotational speed could not be deduced. After the subsequent T6 treatment, some increase of the yield strength was obtained in some samples, but the initial scatter of the plastic flow behavior increased. In fact, failure in many cases occurred without significant plastic deformation. It could be inferred that this T6 treatment magnifies the detrimental effects of the microscopic defects produced during the FSW process. Probably, these defects develop mainly at the metal–ceramic interface, which are sites where stress concentration takes place leading to premature failure. All tensile samples failed in the TMAZ of the advancing side, as shown in Fig. 7, which corresponds to a sample machined from the weld processed at 300 rpm.

Table 1
Summary of tensile and compression test results.

	Mechanical properties			
	Sample	σ_{02} (Mpa)	σ_{max} (Mpa)	e_{max} (%)
Tensile	300	421.4	543.9	1.9
	550	406.6	552.4	2.6
	800	435.4	442.8	0.3
	BM	657.3	741.9	5.3
	300 + T6	438.2	438.2	0.2
	550 + T6	478.8	642.1	2.9
	800 + T6	–	254.8	0.1
Compresive	300	503.9	769.8	17.1
	550	516.9	832.9	18.0
	800	550.0	840.6	15.7
	BM	600.2	846.2	15.9

The compressive behavior of the welds also led to some scatter in the stress–strain curves for the three rotational speeds, although a considerable plastic deformation, in the range of 15–18%, was observed in all cases. This behavior is summarized in the plot of Fig. 8, where the plastic flow behavior at each rotational speed is summarized. For comparison, the compressive behavior of the BM is also shown. In all cases, compressive failure occurred by brittle shear, at some 45° with respect the compressive axes direction, with no sign of barreling despite the large deformation achieved. As seen from the figure, the flow strength increases with the rotational speed, and the plastic deformation is similar to that of the BM. The increase of plastic strength with rotational speed shown in Fig. 8, however, cannot be taken as aconclusive result since the scatter in the stress–strain curves also increased. Due to the detrimental effect of the ulterior T6 treatment observed from the tensile tests, no compression tests were conducted after this treatment. It is relevant that the compressive behavior of the welds is very similar to that of the BM. This indicates, in agreement with the hardness value in the TMAZ, Fig. 5, that no sign of damage appears in the metal–ceramic interface despite the severe plastic deformation that this zone has underwent.

It is finally worth mentioning the lower tensile strength achieved in all cases if compared with the compressive strength of the welds, Table 1. Due to the scatter of the results under both modes of testing, this difference varied in the range of 60–160 MPa. In the BM, the difference was of about 120 MPa, which is within the above range. This compressive-tensile strength difference, SD, is consistent with previous studies of these authors [37] where a similar behavior was observed in 6061Al-15vol%SiC_p composites obtained by a powder metallurgical route. The different compressive-tensile behavior was attributed to the presence of the above mentioned microscopic residual stress of these composites. The extent of the compressive-tensile SD accounts mainly for the magnitude of the internal stress reached, whichis related with the aspect ratio and amount of reinforcing particles as well as with the aluminum alloy matrix strength. The possible effect of decohesion at particle–matrix interfaces when tensile tests are conducted, however, should not be disregarded. This phenomenon, active in

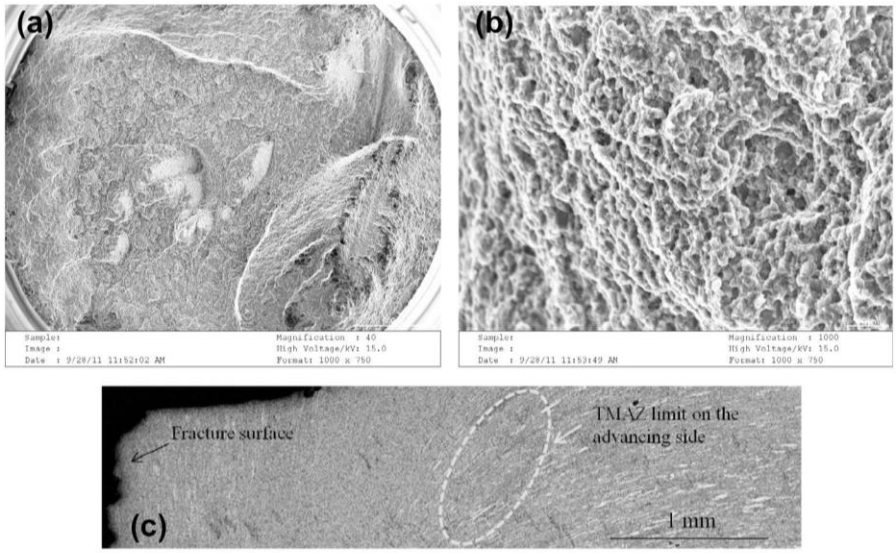

Fig. 7. SEM micrographs at: (a) low and (b) high magnification of the fracture surface of the material welded at 300 rpm. (c) OM micrographs of the transverse section of a tensile tested sample showing the position of the fracture surface with respect to the microstructural zones of the weld.

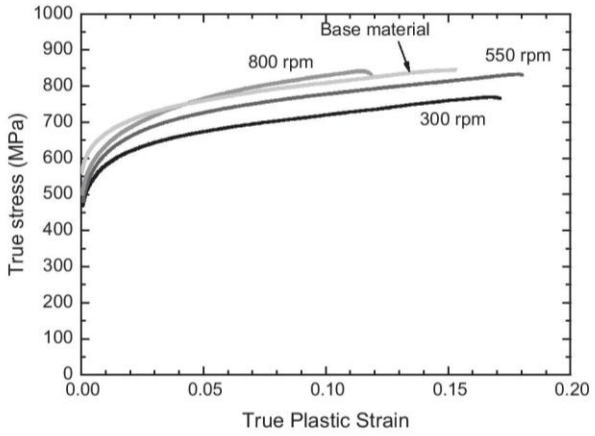

Fig. 8. True stress vs. true plastic strain curves of the welds in compressive mode. The stress–strain curve of the original 2124Al/25vol%SiC_p composite (base material) is also shown for comparison.

tensile but not in compression mode [45], can lead to a lower tensile yield strength and has been considered the responsible of the SD effect in composites based on commercial magnesium–lithium alloy LA-141 (14.1 wt% Li and 1.5 wt% Al) reinforced by 10%, 20%, and 30% boron particles [46]. The fact that similar compressive-tensile strength difference results in the welds and in the base material indicates that the severe plastic flow occurring during the FSW process is not detrimental for the adherence between matrix and reinforcement. As a consequence, the loadtransfer mechanism is still active when the material undergoes mechanical loads in the welded region.

4. Summary and conclusions

In the present work, the influence of tool rotational speed on the microstructure developed in thick plates of a large amount of reinforcement of 2124Al/25vol%SiC_p composite joints produced by FSW and the resulting mechanical properties has been investigated. The joints were conducted in two passes, one on each side of the plate, with a pin which length was half of the plate thickness. The followings are the main conclusions that can be drawn from the study:

(1) A homogenization of the initial SiC particle distribution of the composite occurs, irrespectively of rotational speed. The resulting particle distribution is similar for the three rotational speeds. The TMAZ, however, is larger the higher the rotational speed.
(2) The resulting surface appearance of the welded region also depends on rotational speed: pores are observed at the lowest one, 300 rpm. On the contrary, excessive flash and penetration of the tool shoulder appears at the highest one, 800 rpm. At 550 rpm, a compromise, with restricted surface pores and chip removal, results. Different surface appearance could be also a consequence of the pin vertical position on the plate.
(3) Large tunnel defects appear at the lowest rotational speed. With increasing speed the magnitude of this type of flaw decreases, and at the highest speed, 800 rpm, no tunnel defects appear.
(4) The hardness profile across a transverse section of the joint conducted at 800 rpm, revealed the extension of the HAZ to be asymmetrical with respect to the weld center, and helped define the BM-HAZ border. The highest values correspond to the center of the weld and are similar to the BM hardness; the lowest values correspond to the HAZs.
(5) Good ductility, in the range of 10–15%, is achieved in compressive mode whereas in tension failure occurred below 2% plastic elongation. Fracture always occurred in a brittle manner. Material strength in the welds was similar to that of the base material. A strength difference, SD, effect between compressive and tensile test was obtained. This indicates that the severe plastic deformation produced during the FSW process is not detrimental for the matrix–reinforcement interface. The SD effect is attributed to the presence of a microscopic residual stress.

Acknowledgements

Projects MAT-05-0527 and MAT-09-09545 from MICINN, Spain and PIE 200960I076 from CSIC, Spain.

References

[1] Christman T, Needleman A, Suresh S. Acta Metall 1989;37:3029.
[2] Harris SJ. New light alloys. AGARD Lecture Series 1990;144:1.
[3] Aghajanian MK, Anderson CA, Wiener RJ, Rosing BR. SAE international congress and exposition. Detroit. Michigan; 1–7, 1995.
[4] Chawla KK. Structure and properties of composites. New York: VCH Publishers Inc.; 1993.
[5] González-Doncel G, Sherby OD. Acta Metall Mater 1993;41:2797.
[6] Fernández R, González-Doncel G. Acta Mater 2008;56:2549.
[7] Rohatgi P. JOM 1991;43:10.
[8] Koczak MJ, Khatri SC, Allison JE, Bader MG. Fundamentals of metal matrix composites. Boston: Butterworth-Heinemann; 1993.
[9] Howes MAH. JOM 1986;38:28.
[10] Klimowicz TF. JOM 1994;46:49.
[11] Lloyd DJ. Int Mater Rev 1994;39(1):1.
[12] Minak G, Ceschini L, Boromei I, Ponte M. Int J Fatigue 2010;32(1):218.
[13] Feng AH, Ma ZY. Scripta Mater 2007;57:1113.
[14] Andrewes CJE, Feng HY, Lau WM. J Mater Process Technol 2000;102:25.
[15] Wagener HW, Wolf J. J Mater Process Technol 1993;37:253.
[16] Li JH, Li CF. J Mater Process Technol 2004;151:302–6.
[17] Storjohann D, Barabash OM, David SA, Sklad PS, Bloom EE, Babu SS. Metall Mater Trans A 2005;36(11):3237.
[18] Mishra RS, Ma ZY. Mater Sci Eng R 2005;50:1.
[19] Lee JA, Carter RW, Ding J. MSFC Center Directoŕs Discretionary Fund Final Report. Project N°.98-09; NASA.
[20] Dalkilic S, Biallas G. In: 6th International symposium on friction stir welding. Quebec, Canada; 10–13 October 2006.
[21] Fernandez GJ, Murr LE. Mater Charact 2004;52:65.
[22] Wert JA. Scripta Mater 2003;49:607.
[23] Marzoli L, Von Stombeck A, Dos Santos JF, Gambaro C, Volpone ML, Rizzuto E. 29th convegno nazionale AIM. Italy: Modena; 2002.
[24] Thomas WM. International Patent Application no. PCT/GB92/02203 and GB Patent Application no.9125978.8, US Patent no. 5460, 317; December, 1991.
[25] Dawes C, Thomas W. TWI Bullet 1995;6:124.
[26] Ellis M, Strangwood M. TWI Bullet 1995;6:138.
[27] Amirizad M, Kokabi AH, Abbasi Gharacheh M, Sarrafi R, Shalchi B, Azizieh M. Mater Lett 2006;60:565.
[28] Uzun H. Mater Des 2007;28:1440.
[29] Gesto D, Ferreira-Barragáns S, Rey P, Fernández R, González-Doncel G. In: 8th Friction stir welding symposium. Germany; 2010.
[30] Feng AH, Xiao BL, Ma ZY. Mater Sci Eng A 2008;497:515.
[31] Ma ZY, Feng AH, Xiao BL, Fan JZ, Shi LK. Mater Sci Forum 2007;539–543:3814.
[32] Prado RA, Murr LE, Shindo DJ, Soto KF. Scripta Mater 2001;45:75.
[33] Shindo DJ, Rivera AR, Murr LE. J Mater Sci 2002;37:4999.
[34] Lohwasser D, Chen Z. Friction stir welding: from basics to applications. UK: Woodhead Publishing Limited; 2010.
[35] Elangovan K, Balasubramanian V. Mater Sci Eng A 2007;459:7.
[36] Balasubramanian V. Mater Sci Eng A 2008;480:397.
[37] Fernández R, Bruno G, González-Doncel G. Acta Mater 2004;52:5471.
[38] Heurtier P, Jones MJ, Desrayaud C, Driver JH, Montheillet F, Allehaux D. J Mater Process Technol 2006;171:348.
[39] Guerra M, Schmidt C, McClure JC, Murr LE, Nunes AC. Mater Charact 2003;49:95.
[40] Li Ying, Murr LE, McClure JC. Mater Sci Eng A 1999;271:213.
[41] Cavaliere P. Composites A 2005;36:1657.
[42] Ceschini L, Boromei I, Minak G, Morri A, Tarterini F. Composites A 2007;38:1200.
[43] Ceschini L, Boromei I, Minak G, Morri A, Tarterini F. Compos Sci Technol 2007;67:605.
[44] Marzoli LM, Strombeck Av. Compos Sci Technol 2006;66:363.
[45] Olsen RJ, Ansell GS. Trans ASM 1969;62:711.
[46] Whalen RT, González-Doncel G, Robinson SL, Sherby OD. Scripta Metall 1989;23:13.

Materials and Design 65 (2015) 438–446

Contents lists available at ScienceDirect

Materials and Design

journal homepage: www.elsevier.com/locate/matdes

The effect of lateral off-set on the tensile strength and fracture of dissimilar friction stir welds, 2024Al alloy and 17%SiC/2124Al composite

Florencia Cioffi *, Joaquín Ibáñez, Ricardo Fernández, Gaspar González-Doncel

Centro Nacional de Investigaciones Metalúrgicas (CENIM) C.S.I.C., Av. de Gregorio del Amo 8, E-28040 Madrid, Spain

ARTICLE INFO

Article history:
Received 23 March 2014
Accepted 15 September 2014

Keywords:
Dissimilar Friction Stir Welding
Non-ferrous metals and alloys
Metal matrix composites
Mechanical properties
Weld interface

ABSTRACT

Welding a high quality aluminum matrix discontinuously reinforced composite is a difficult task and can be expensive. Joining the composite to a commercial aluminum alloy can reduce costs by only using the expensive material where it is needed. The solid state process Friction Stir Welding, FSW, is a promising alternative to fusion welding techniques since it can avoid the problems related to the molten metal and its solidification. We study the effect of the lateral off-set on the strength and fracture location in welds of 8 mm thick 2024Al alloy and 17%SiC/2124Al composite. We used a novelty diagonal set up to adjust the rotational and welding speed, and to select the three lateral off-sets for straight welds. The lateral off-set determines the amount of plastic deformation that the plates' contact surface undergoes. Therefore, it affects the shape and bonding quality of the alloy-composite boundary, which determines the strength of these welds. The highest joint efficiency (90% of 2024Al-T351) was obtained for the centered off-set, which had the most resistant boundary. However, the results suggest that a joint with an off-set of around 1.5 mm into the retreating side could exceed the efficiency obtained.

1. Introduction

Joining high quality metal matrix composites (MMCs) to conventional monolithic alloys is of great interest since it would allow the use of the more expensive composite material only where its properties are needed. In this way the costs could be reduced and the applications of MMCs would become wider. As it is known, these materials have higher specific strength, higher Young's modulus and better wear resistance than monolithic alloys [1]. In spite of all these advantages, the applications of MMCs are not as much as expected. The reason for this is, not only their higher cost but, also the difficulty they present during different secondary processes-an important one among them is welding. Using fusion welding techniques brings problems such as porosity and chemical reaction of the molten matrix with the reinforcing particles, which deteriorate the mechanical properties of the material. On the contrary, Friction Stir Welding (FSW) prevents these problems since no melting occurs during the process. Therefore, FSW is a promising alternative method to join MMCs [2,3] and conduct dissimilar welds [4].

In particular, several dissimilar FSW joints have been studied before: two different aluminum alloys [5,6], aluminum and magnesium [7], aluminum and steel [8,9], aluminum and titanium [10], and aluminum and MMCs [11–15]. In the last group, Wert et al. [11] studied the microstructure of 2024Al to 20%Al_2O_3/2014Al friction stir welds, concluding that the extent of the mixing was favored when the MMC was placed in the advancing side. Dalkilic et al. [12] observed the same as Wert et al. but found that even though the mixing was better, placing the composite in the advancing side resulted in a lower strength. Guo et al. [13] pointed the importance of carefully studying the lateral off-set of dissimilar MMC-Al FSW joints since the window of parameters to produce a sound weld can be very narrow, especially when using an unthreaded tool. Xiao et al. [14] used a lateral off-set into the alloy to reduce wear and found that the joint efficiency dropped 45% with respect to the joint without off-set. Finally, Sharifitabar et al. [15] studied the effect of conducting welds in one and two passes on the microstructure and hardness.

The objective of this study was: to evaluate the effect of the lateral off-set in the microstructural characteristics of the alloy-composite boundary (2024Al and17%SiC/2124Al) and to correlate the differences with the mechanical properties of the joints. In a more general way, we attempted to improve the mechanical properties of the joints by using a lateral off-set different from

* Corresponding author. Tel.: +34 91 5538900 (210).
E-mail address: flo@cenim.csic.es (F. Cioffi).

http://dx.doi.org/10.1016/j.matdes.2014.09.042
0261-3069/

the traditional centered one. For the present work, a WC–Co wear resistant tool with no thread was used. Therefore, tool wear was negligible. One important novelty of the present work is the design of a diagonal setup that allows scanning different lateral off-sets in one weld.

2. Experimental methods

The composite material used in this study was fabricated by Aerospace Metal Composites, AMC, UK by a powder metallurgy route, using a high quality aerospace grade aluminum alloy (2124Al) as matrix and 17% in volume of ultra-fine silicon carbide particles (2–3 μm) [16]. The 275 × 110 × 8 mm^3 plates used in the welds were electro discharge cut from a 275 × 220 × 32 mm^3 block naturally aged after high temperature forging. The aluminum alloy plates used were cut from a 2024Al-T351 alloy from Alustock, Spain, the final thickness of 8 mm was given by the rolling process. Both composite and alloy plates were friction stir welded in the as received condition.

The friction stir welds were carried out in a conventional milling machine, Fig. 1a). The tool used was specially selected to avoid wear caused by the composite. The WC–Co one piece tool with conical smooth/unthreaded pin and concave shoulder showed no wear after several meters of welding. The shoulder diameter, pin diameter, and length were 19, 9–8, and 6.8 mm respectively. The tool tilt angle was 3° and the alloy was always placed in the retreating side.

To investigate appropriate parameters for the welding process four diagonal joints were carried out varying the rotational and advancing speed, Table 1.

The plates were fixed so that the contact surface of the plates formed a 9° angle with respect to the tool path, Fig. 1b. The plunging was done in the alloy with the edge of the tool shoulder aligned with the contact surface of the plates. The weld finished when the retreating edge of the tool shoulder was aligned with the contact surface of the plates.

The transverse cuts made in the diagonal welds were ground and polished using diamond paste up to 1 μm. The examination under optical microscope (OM) allowed establishing the combination of FSW parameters and lateral off-sets to be used in the subsequent straight welds.

Transverse sections, for macro and microstructural studies and micro-hardness tests, were extracted from the straight welds and prepared in the same way as those extracted from the diagonal ones. X-ray Diffraction microanalysis was also performed in these samples.

Three parallel lines of micro-hardness measurements across the weld (at approximately 2, 4, and 6 mm from the top surface of the plate) were performed in each sample following ASTM: E384 standard, with 2 mm between indentations covering a total of around 60 mm. The profiles were called top, center, and bottom. The load was 1 kg and the loading time 10 s.

Also, dog-bone tensile samples were machined from the plates, perpendicular to the weld direction, with 60 mm gauge length and 12.5 mm width; in this way, the mechanical response of the whole joint was evaluated. Tests to fracture were performed at $5 \times 10^{-4}\ s^{-1}$, using a 10 T SERVOSIS™ tensile test machine and a 25 mm gauge length extensometer, in accordance with standard ASTM: E8/E8M.

The fracture surface of the samples was observed under the Scanning Electron Microscope (SEM). Also metallographic sections parallel to the tensile direction were ground and polished to be examined by SEM.

3. Results

3.1. Welding parameter optimization with diagonal setup

The diagonal welding parameters are summarized in Table 1. The rotational speed, w, decreased from 1000 rpm in weld D1 to 500 rpm in weld D2; while keeping the rest of parameters constant. The superficial aspect was improved since the flash diminished and the channel disappeared, but a tunnel defect appeared. Further reducing w to 250 rpm in weld D3, reduced the size of the tunnel defect. Finally, reducing the advancing speed to 20 mm/min resulted in a sound weld, D4, with no tunnel in the central section of the welded plate. The metallographic cuts along D4 showed that when the contact surface of the two materials was outside of the tool pin path, little mixing occurred. Furthermore, when the lateral off-set exceeded 2.5 mm in the alloy side, tunnel defects appeared in the advancing lower corner of the stir zone (SZ). These observations allowed choosing the three lateral off-sets for the straight welds: SComp (2.5 mm into the composite), SCenter (no off-set) and SAlloy (2.5 mm into the alloy). Since the pin diameter varied from 9 to 8 mm, it is warranted that the contact surface alloy-composite entered the SZ in the straight welds.

3.2. Macro and microstructure of straight welds

Fig. 2 shows the transverse cuts of the straight welds. As expected, the SZ in each weld is different: in SComp it contains a majority of composite material, whereas in SAlloy and SCenter of aluminum (having the latest a more even proportion of both). An abrupt change in contrast under the OM is appreciated. The two materials remain easy to discern and the alloy-composite boundary is clear. But its shape changes from a simple zig-zag in SComp to a more intricate one in SAlloy. This change implies that the length of the alloy-composite boundary (L) increases as we move

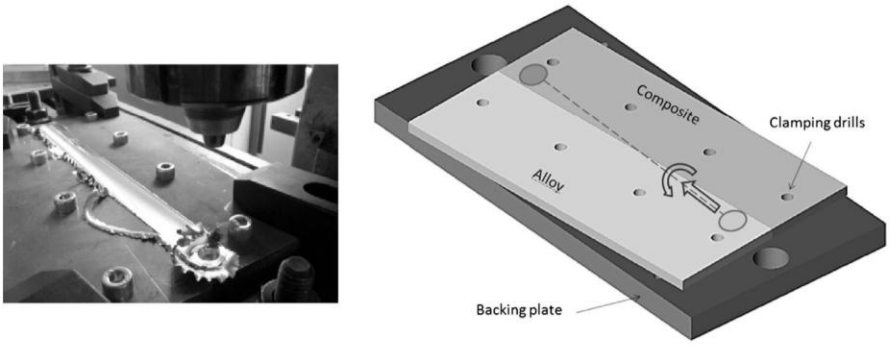

Fig. 1. Experimental setup used for the diagonal friction stir weld, (a) photograph of weld D2 and (b) scheme.

Table 1
Process parameters and observations for the diagonal friction stir welds. The tilt angle was 3° in all welds.

	Rotational speed, w (rpm)	Advancing speed, v (mm/min)	Remarks
D1	1000	28	Big channel and excessive flash
D2	500	28	Lack of penetration in the beginning and tunnel (smaller as it advances)
D3	250	28	Good general appearance, small tunnel defect in the beginning section
D4	250	20	Good general appearance, no tunnel defect found in the central section

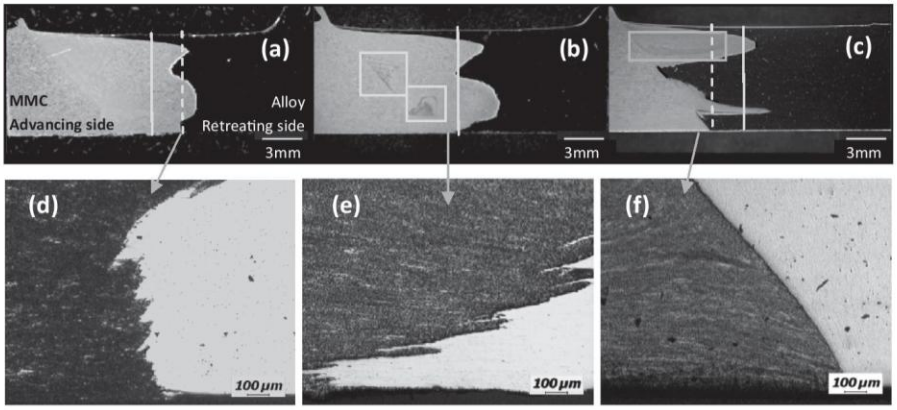

Fig. 2. Metallographic sections of straight welds conducted at 250 rpm and 20 mm/min (a) SComp, (b) SCenter and (c) SAlloy. Solid lines represent the position of the tool axe and dashed lines represent the position of the contact surface of the plates before welding. White boxes mark concentrically periodic shapes. (d)–(f) show details of the boundaries. The difference in contrast between (a)–(c) and (d), (e) is due to the instruments used to take them, but the composite is always on the left.

from off-sets in the advancing side to the retreating side ($L_{SComp} < L_{SCenter} < L_{SAlloy}$).

In was observed in all welds that in the upper region there was always aluminum (narrow regions in the top surfaces, Fig. 2). The shoulder-induced shear forces, which are highest in the back region due to the tool tilting, transported the alloy to the advancing side. Furthermore, the bottom region presented the least mixing. This is because the tool pin did not reach so far into the plates.

In the three welds, the material that appears most thoroughly stirred and mixed occupies the advancing side of the Thermo-mechanically Affected Zone (TMAZ), next to the limit with the Heat Affected Zone (HAZ). In this region the distribution of SiC particles is very homogeneous. Also, in SCenter and SAlloy small portions of alloy appear mixed with the composite forming a concentric shape, boxes in Fig. 2b and c, similar to the "onion rings" typical of FSW joints [17].

At higher magnification, the composite in the SZ presents a very homogenous distribution of SiC particles and precipitates (mainly Al_2CuMg and Al_2Cu, typical of 2124Al) Fig. 3a and b. As a consequence of the FSW induced dynamic recrystallization process [18], the alloy grain structure changed from an elongated shape (typical of cold rolled metals), to a finer equiaxed one, Fig. 3c–e.

Finally, the observation under SEM of the alloy-composite boundary showed that the materials are mixed to an extent of a few hundred microns. In Fig. 4 small portions of each material appear intercalated. So what seemed to be an abrupt boundary, is not so when observed at high magnification. Furthermore, no oxides were detected by XRD microanalysis in this area.

3.3. Mechanical properties

Fig. 5 presents the microhardness profiles for the three welds at three depths: top, center, and bottom. They have some common characteristics: The hardness is similar in both base materials (BM), in spite of the presence of the reinforcing particles in the composite. The composite maintains the hardness level of the BM until it reaches the near HAZ where it rises, from an average value of 120 HV1 to around 135 HV1. In the alloy instead, we observe an increase, from 123 HV1 in the BM to 135 HV1 in the far HAZ, followed by a significant drop, down to 85 HV1, in the near HAZ and a final rise in the TMAZ and SZ, but it does not reach the BM hardness. Also, the HAZ in the alloy is larger than in the composite. The minimum hardness always corresponds to the alloy HAZ. It is a 71% of the alloy BM hardness in SComp, 66% in SCenter, and 68% in SAlloy.

There are some differences between the through-thickness hardness profiles for each weld: the hardness loss in the alloy HAZ is the smallest in the bottom profiles and the highest in the top. Also, the distance from the weld center of the minimum and maximum values changes.

Table 2 summarizes the tensile tests results. The elongation to failure was small in all cases: around 0.1%, 1–2.5%, and 0.2% in Scomp, SCenter, and SAlloy, respectively. The ultimate tensile strength (UTS) was 65% of that of the alloy BM [19] in Scomp, 66% in SAlloy, but a remarkable 90% in SCenter. The fracture of SComp occurred by crack propagation through the alloy-composite boundary, Fig. 6a. SCenter shows, Fig. 6b, two different fracture modes: either by crack propagation through the boundary, similar to SComp, or through the composite BM. Finally, fracture in SAlloy Fig. 6c, began in the bottom surface detaching the two materials up to approximately 1 mm into the sample, then the load kept rising until the crack run straight through the two materials, perpendicular to the tensile direction (referred to as center in Table 2).

From a macroscopic point of view, the fact that fracture occurs by crack propagation along the alloy-composite boundary suggests a simple detachment phenomenon. However, the microscopic examination under the SEM of the fractured samples (longitudinal sections) of SComp and SCenter shows that these are not cases of detachment, Fig. 7a and b. In some areas a fine layer of composite was adhered to the alloy and in others the opposite phenomenon was observed. SAlloy shows a detachment zone in the bottom region, Fig. 7c, followed by a flat fracture which runs through both materials, Fig. 6c. Near the fracture surface, we see that the big precipitates in the alloy fractured perpendicular to the tensile

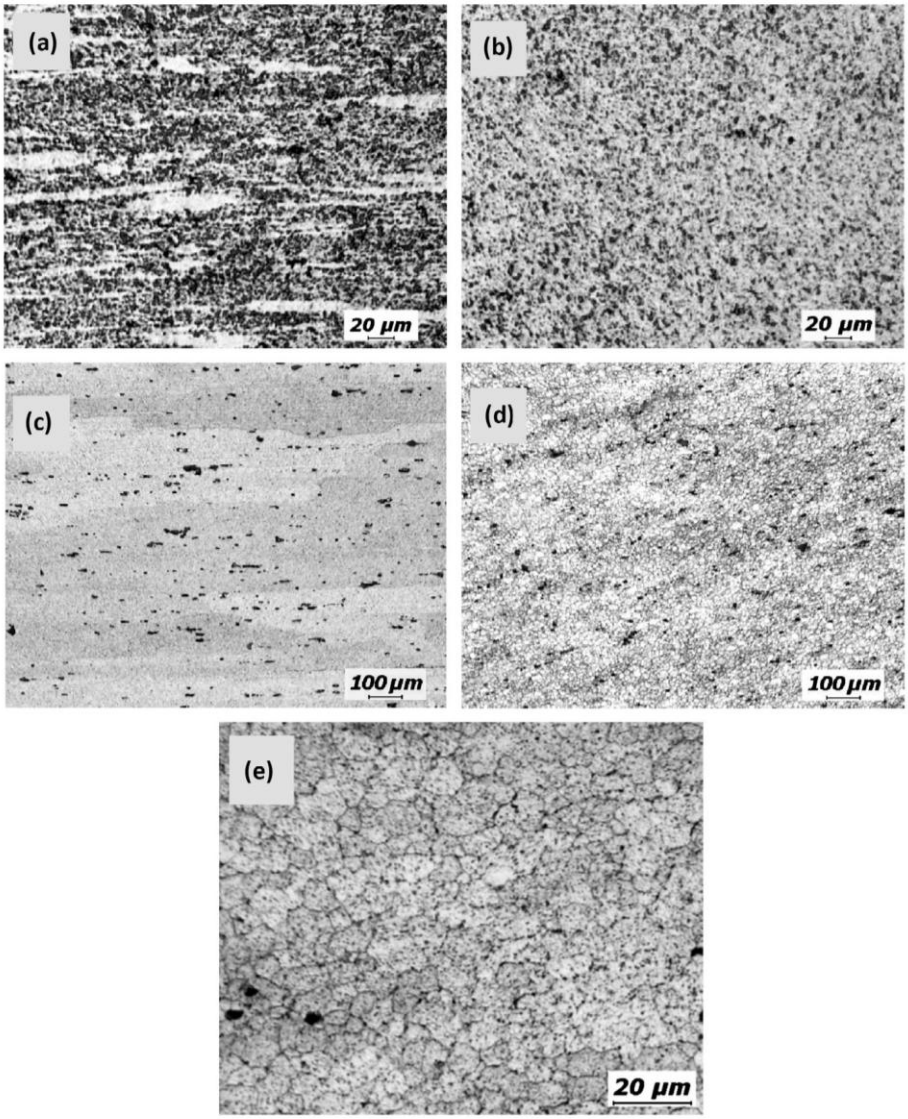

Fig. 3. Optical microscope images showing the refinement occurred in the microstructure of both materials due to the FSW. The particle distribution in the composite becomes more homogeneous due to the stir deformation: (a) composite BM and (b) composite SZ. The grain structure in the alloy changes to a finer and equiaxial one: (c) alloy BM and (d) alloy SZ. A higher magnification of the alloy stir zone shows its fine grain structure (e).

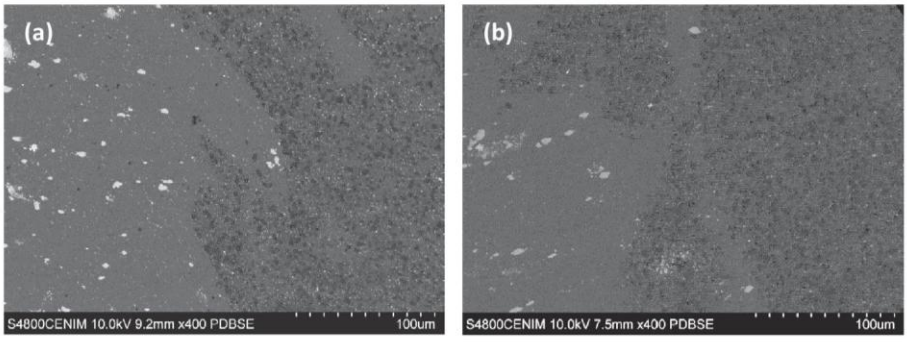

Fig. 4. SEM images of metallographic sections in Fig. 2, showing examples of the boundaries and how intricate there are in (a) SComp and (b) SCenter.

direction (see arrows in Fig. 7). Instead, the SiC particles in the composite did not break: crack propagated through the surrounding matrix. Further examination of the fracture surfaces, Fig. 8, confirms the presence of dimples revealing nucleation, growth, and coalescence of microvoids, a consequence of local plastic deformation.

The two steps of the fracture mode of SAlloy, described above, are confirmed by the analysis of its fracture surfaces, Fig. 9. The

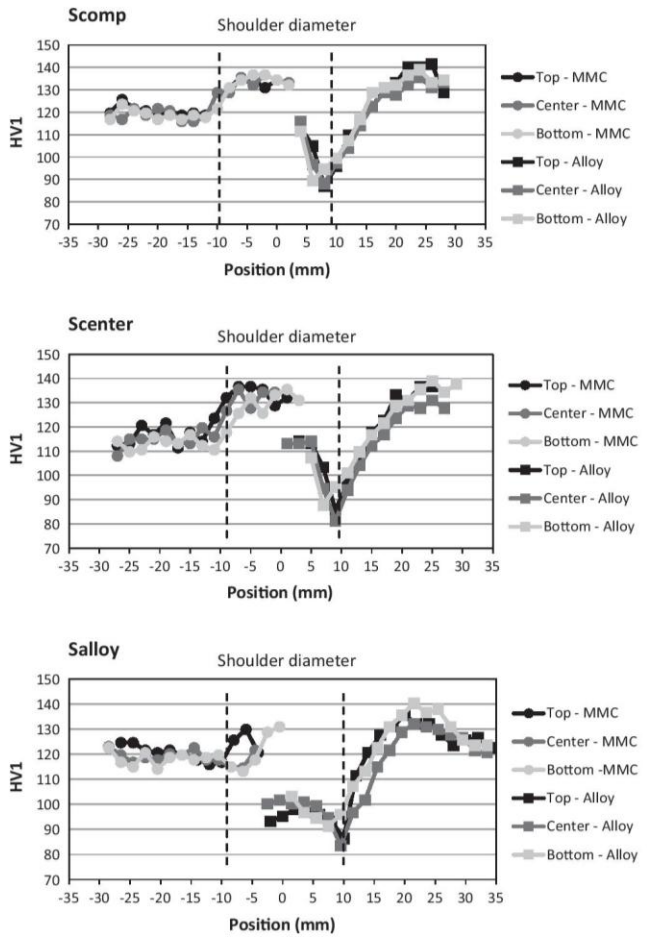

Fig. 5. Microhardness profiles across the straight welds at three depths. The error in the measurements is ±2 HV1.

differences between the two stages are evident: in the bottom region, no sign of deformation is present; in the adjacent region, microvoids can be observed.

4. Discussion

4.1. Diagonal welds

In the present work we used a novel FSW diagonal setup to join 2024Al and 17%SiC/2124Al. In this way, we could scan different lateral off-sets in one weld. The main concern that may arise when implementing this setup is the difference between a diagonal weld at certain point and a straight weld with the equivalent off-set. In the diagonal welds the amount of alloy and composite in front of the pin changes as the tool advances. Therefore, since the cavity formed at the trailing edge is filled with material coming from the front edge, there is an off-set difference between these two zones. This difference is approximately equal to the change in off-set when advancing 8.5 mm (the pin average diameter). However, the results in the present work show that this difference is not an impediment for using the diagonal welds as a guide to select parameters for straight welds.

It would be interesting to use the diagonal setup in other similar and dissimilar FSW joints such as [6–9,13,20–22], to study the influence of lateral off-set on the microstructure and mechanical properties.

4.2. Stir zone microstructure with the different lateral off-sets

As it is known, the material flow in FSW is asymmetric and rather complex [23]. Depending on the position of a certain volume of material with respect to the tool axe, its transport path will vary. Consequently, it will experience a different amount of deformation. Several studies [23–25] have concluded that the material in the advancing side of the SZ is more thoroughly deformed than the one in the retreating side. This difference is due to the asymmetry of the material flow. In the advancing side the material is stirred: it enters the tool pin current and is transported for a number of turns before being deposited in the trailing edge [25]. While the material in the retreating side is extruded: it enters the straight-throw current and it is simply transported from the front edge to the trailing edge. This was confirmed by the results of this study: the material in the advancing side of the SZ shows sings of being more thoroughly deformed than the material in the retreating side, Fig. 2.

One important feature within the SZ of the dissimilar joints of this study is the boundary. The differences observed in the boundaries of the straight joints are due to the material flow. In Scomp, the material around the plates contact surface is positioned in the retreating side with respect to the tool axe. Therefore, its boundary is formed by material that followed the straight-throw current and was poorly deformed. The opposite occurs in SAlloy, in which the boundary is formed by material in the advancing side that entered the tool pin current and was thoroughly deformed. As expected, SCenter is an intermediate case between SComp and SAlloy. This means that as the lateral off-set changes from the retreating side to the advancing side, the boundary becomes more intricate in shape because it went through more deformation. In agreement with a previous MMC-Alloy FSW study [13] and other dissimilar FSW studies [5,7,9].

Table 2
Tensile tests results for straight welds.

Sample	Tensile elongation (%)	UTS (MPa)	Fracture location
Scomp-4	0.13	235.8	Boundary Al/MMC
Scomp-6	0.09	255.9	Boundary Al/MMC
Scomp-7	0.09	280.6	Boundary Al/MMC
SCenter-2	2.31	337.4	Boundary Al/MMC
SCenter-3	1.51	362.2	Boundary Al/MMC
SCenter-4	2.19	349.5	Boundary Al/MMC
SCenter-5	1.36	358.7	MMC base material
SCenter-7	1.11	354.5	MMC base material
SCenter-8	1.51	365.4	Boundary Al/MMC
SAlloy-2	0.26	239.0	Center
SAlloy-3	0.18	250.2	Center
SAlloy-4	0.28	270.8	Center
SAlloy-5	0.27	274.3	Center
SAlloy-reduced thickness	7.32	363.5	HAZ alloy

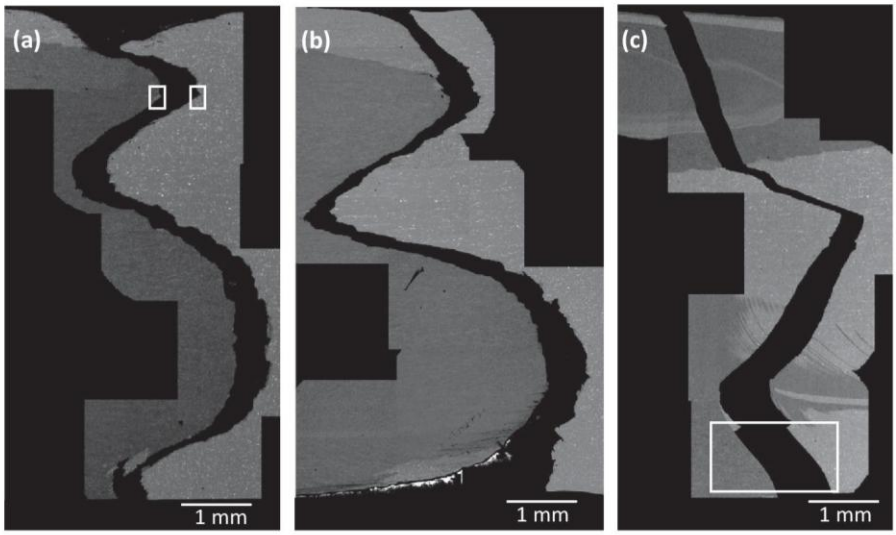

Fig. 6. Metallographic sections of fractured tensile samples. Montage of several low magnification SEM images (a) SComp-7, (b) SCenter-8 and (c) SAlloy-2.

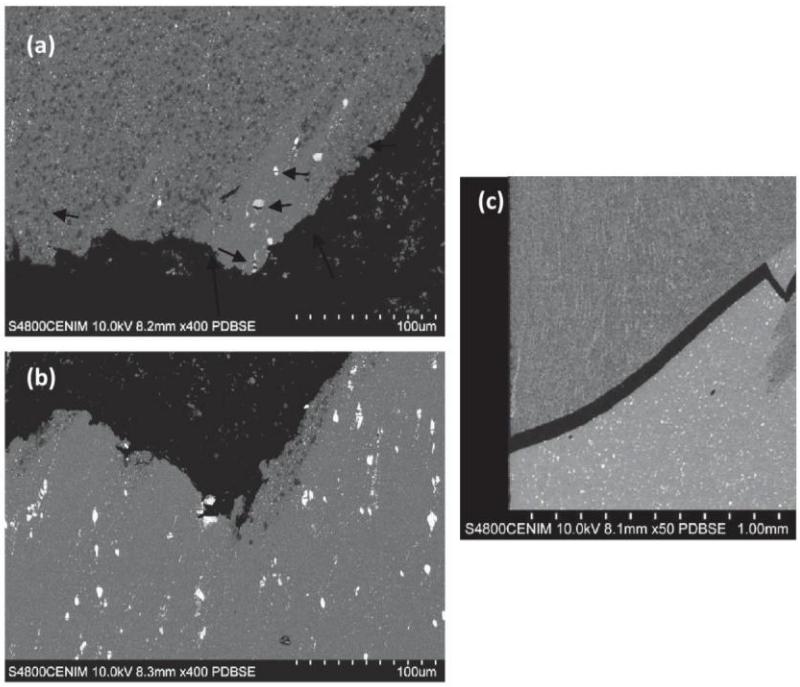

Fig. 7. SEM images of metallographic sections of fractured tensile sample SComp-7 (a) and (b) and SAlloy-2 (c) corresponding to the areas marked with boxes on Fig. 6(a) and (c). Black arrows in (a) and (b) point at precipitates in the alloy that broke perpendicular to the tensile direction (vertical).

In terms of material flow, the bottom zone is different to the rest of the SZ. Since the pin does not reach so far into the plates, the tool pin current is absent in this zone. Therefore, the material is not stirred. Instead, passes from the front edge to the trailing edge through the retreating side, in a similar way to the straight through current. As a result, in the bottom, the material is more deformed in the retreating side than in the advancing side. This is the opposite to the rest of the SZ.

In this way, the asymmetry of the material flow makes the lateral off-set a key factor to determine the amount of deformation in the boundary; and thus, its shape and bonding quality. The desirable boundary would be the most thoroughly deformed. But, as mentioned, the upper and bottom regions of the SZ behave in opposite ways. Therefore, the selection of the most appropriate lateral off-set is not straight forward.

4.3. Mechanical properties and fracture with the different lateral off-sets

The hardness profiles of the straight welds are similar in shape, as explained in the results section. Also, the absolute maximum and minimum hardness' values are similar irrespectively of the lateral off set, and these values are located at the same distance from the joint center.

The increase in hardness observed in the composite near HAZ accounts for a change in the precipitation state of the matrix.

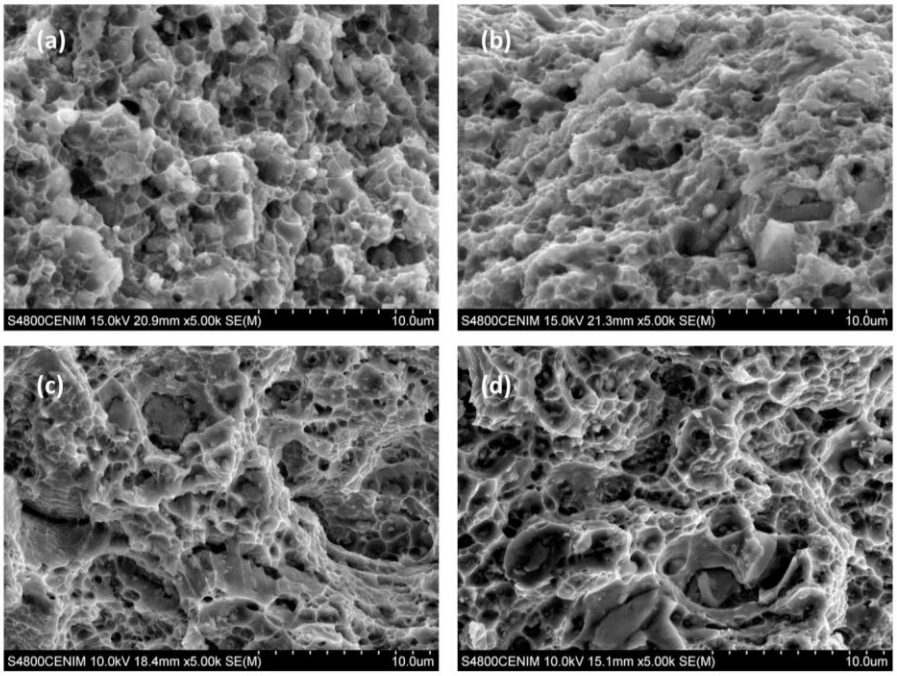

Fig. 8. SEM images of the fracture surfaces of tensile samples: (a) SComp-7 composite side, (b) SComp-7 alloy side, (c) SCenter-8 composite side and (d) SCcenter-8 alloy side. The aluminum matrix appears deformed showing microvoids, which are bigger and deeper in the SCenter sample (it is a sign that greater plastic deformation occurred before the fracture).

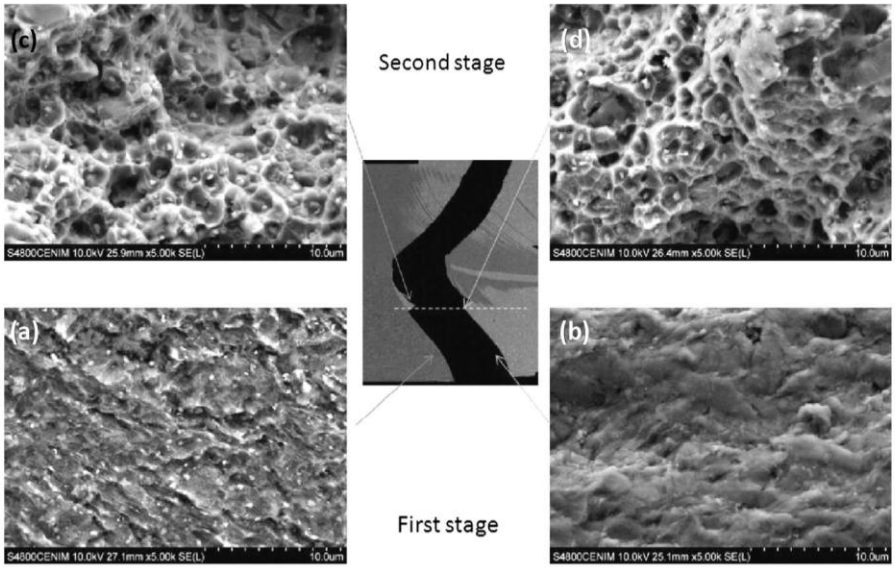

Fig. 9. SEM images of the fracture surfaces of tensile sample SAlloy-4 (a) and (b) correspond to the first stage of the fracture: flat surface associated with a brittle behavior, (c) and (d) correspond to the beginning of the second stage: precipitates and deep microvoids appear on both sides of the fracture that runs through the alloy.

According to the plates' thermo-mechanical history, a slow cooling rate is expected, leading to an overaged condition in the plates. The hardness profiles indicate that solutionizing temperature (around 493 °C [26]) is only reached from the near HAZ to the center. In the TMAZ and SZ, the stir effect is added to the heat effect, giving as a result a further increase in hardness. This is due to the microstructure refinement and particle distribution homogenization.

According to previous studies [27], part of the alloying elements in the alloy BM may remain as Guinier-Preston zones due to the fast cooling rate that the plates underwent after the rolling process. This precipitation state evolves with a lower temperature rise than the over aged state; as it is revealed by the extension of the alloy HAZ (broader in the alloy). The hardness profiles indicate that a moderate increase in temperature has a positive effect on the hardness (far HAZ), but increasing the temperature further makes the precipitation evolve into an overaged state (near HAZ). In the alloy TMAZ, part of this hardness decrease is compensated by strain hardening. And finally, in the center of the SZ the grain refinement results in a further increase of hardness with respect to the HAZ. The shape of the microhardness profiles coincides with that reported in previous studies in 2024Al-T351 [27–30]. Finally, the similar hardness of both BMs indicates that the presence of the

SiC is not sufficient to compensate the low hardness of the over-aged matrix.

The differences between the through-thickness profiles for each weld have to do with the shape of the alloy-composite boundary and with the temperature distribution in the joint. As it is known, the highest temperatures during FSW occur near the tool shoulder [31]. And the bottom surface in contact with the backing plate is the coldest region and the fastest to cool down after the process [23]. This explains that, in the bottom region, the hardness loss is the smallest. Furthermore, since the HAZ is narrower, the minimum is always closer to the center of the weld [28]. In the same way, the hardness rise in the composite starts closest to the center of the joint in the bottom profile.

Regarding the tensile properties, Guo et al. [13] observed no difference between the UTS of a joint with 0.8 mm off-set into the advancing side and one with centered set-up. Instead, in the present study, the tensile resistance of the weld changes greatly with different lateral off-sets. SComp and SAlloy show a 27% UTS loss with respect to the usual centered set-up (SCenter), and an even more significant reduction in elongation, Table 2. The higher elongation of SCenter with respect to SComp is in accordance with the much deeper microvoids, Fig. 8.

In previous dissimilar MMC-Al alloy FSW publications, Xiao et al. [14] also obtained the best results for the null off-set configuration, getting up to 85% of the 2024Al-T3 UTS. Dalkilic et al. [12] reached 72% efficiency in 25%SiC/2124Al to 2024Al-T3 joints using a centered set up. This means that the 90% UTS that we obtained for SCenter is, as far as we know, the highest efficiency ever reached for a FSW dissimilar joint of SiC reinforced Al MMC and aluminum alloy. All of these studies [11–15] observed that the dissimilar materials remain easy to discern, though the joints carried out with threaded pin tools [12,14,15] presented better mixing.

The two main factors that affect the tensile strength are: (1) the shape of the alloy-composite boundary and (2) the bonding quality. The first determines the extension of alloy-composite contact and the orientation of this surface (the highest shear stress in a uniaxial tensile test forms a 45° angle with the tensile direction). In this way, we can expect that a more intricate boundary, which implies a bigger contact area and lower angle with the tensile direction, should result in a stronger joint. In addition to this, the bonding quality in the boundary will be given by the extent of the alloy-composite mixing and the possible presence of oxides or microscopic defects.

The mechanical behavior of the dissimilar joints can be interpreted as the response of a chain made up of different materials, or links, which undergo iso-stress conditions. In this way, the chain (joint) will fail through its weakest link. One could expect fracture to occur in the area with lowest hardness, in which case the fracture location would be the alloy HAZ in all joints. But that was not the case.

The weakest link in SComp is the alloy-composite boundary, where fracture occurred in all samples. In SCenter, the weakest link is either the boundary or the composite BM; since samples broke in either location at similar stress levels. Because the resistance of SCenter is higher than in SComp, the boundary is stronger in SCenter. The difference lies in its shape: in SCenter the boundary is 33% larger and the angle that forms with the tensile direction is in average smaller.

The case of SAlloy is more complex. As described in the results section, the fracture occurs in two steps. This suggests that the tensile strength of the weakest link varies through the thickness of the sample. In the first stage of the fracture, the crack runs along the boundary (approximately 1 mm from the bottom surface), revealing that this is the weakest region of the link. But the fracture mode in the second stage suggests that the boundary in the remaining section is stronger. The fracture surface shows these differences, Fig. 9. In the bottom region the materials simply detached from each other (Fig. 7c) and no material adherence was found in the fracture surfaces, Fig. 8a and b. The bonding in this section is the weakest because the tool pin does not reach so far into the plates. So, while the upper section is heavily stirred; the bottom section is barely deformed. In the second stage, the fracture progressed through the center of the joint probably because the bottom area was detached in the first stage and acted as a stress concentrator for the second stage.

To probe this, we machined a reduced thickness tensile sample (6.8 mm thick), removing the bottom section. The results of the tensile test are in Table 2 (SAlloy-Reduced thickness). The sample fractured through the alloy HAZ (lowest hardness value), demonstrating that this would be the weakest link of the upper section of the joint. Furthermore, this sample had a much ductile behavior than the whole joint and the UTS increased a 40% (becomes equal to or higher than that of SCenter).

It is worth mentioning that, in spite of the hardness changes that the FSW process introduces in the material (including the considerable drop in the alloy HAZ); the joints tensile resistance was ultimately determined by the alloy-composite boundary shape and microstructure. A similar result was observed by Dalkilic et al. [12]: although the hardness minimum was at the 2024Al HAZ, the fracture occurred in the alloy-composite boundary.

The lateral off-set greatly influences the tensile strength of the alloy-composite boundary and, therefore, the fracture location of the joint. As the off-set changes from advancing side to the retreating side, the upper section of the boundary becomes more intricate and, as explained, more resistant. At the same time, the bonding quality of the lower section of the boundary becomes poorer and, therefore, weaker.

5. Conclusions

From the present study the following conclusions can be drawn:

- The diagonal setup probed to be an efficient way to find the appropriate welding parameters for a range of lateral off-sets.
- The lateral off-set greatly influences the fracture location and resistance of the dissimilar friction stir welds, by affecting the shape and bonding quality of the alloy-composite boundary.
- The highest tensile resistance corresponds to the traditional centered set-up (90% joint efficiency). However, a lateral off-set of around 1.5 mm into the alloy and a slightly deeper plunging could overtake the resistance of the traditional centered setup, by improving the bonding quality in the bottom section of the alloy-composite boundary.
- The strength of the weld is more affected by the strength of the alloy-composite boundary than by the changes in hardness induced by the FSW process.
- The lateral off-set could be used as a parameter to improve the resistance of, not only dissimilar MMC-Alloy joints, but also friction stir welds of other materials. Because it changes the amount of deformation that the joint line goes through. However, further research is needed.

Acknowledgements

Support from Project MAT-09-09545 and the PhD grant BES-2010-030247 for one of the authors (F.C.) from MINECO, is acknowledged. The support for the short stay in the Auckland University of Technology (AUT) EEBB-I-2012-03889 from MINECO, is recognized. The help and advice from Professor Zhan Chen

during the stay in AUT, is sincerely appreciated. Finally, the help from David Verdera from AIMEN, Spain, is recognized.

References

[1] Ibrahim IA, Mohamed FA, Lavernia EJ. Particulate reinforced metal matrix composites – a review (Review). J Mater Sci 1991;26(5):1137–56.
[2] Storjohann D, Barabash OM, Babu SS, David SA, Sklad PS, Bloom EE. Fusion and friction stir welding of aluminum–metal–matrix composites. Metall Mater Trans A 2005;36A:3237–47.
[3] Guo J, Gougeon P, Nadeau F, Chen X-G. Joining of AA1100-16 vol.%B4C metal matrix composite using laser welding and friction stir welding. Can Metall Q 2012;51(3):277–83.
[4] Murr LE. A review of FSW research on dissimilar metal and alloy systems. J Mater Eng Perform 2010;19:1071–89.
[5] Scialpi A, De Giorgi M, De Filippis LAC, Nobile R, Panella FW. Mechanical analysis of ultra-thin friction stir welding joined sheets with dissimilar and similar materials. Mater Des 2008;29:928–36.
[6] Ghosh M, Kumar K, Kailas SV, Ray AK. Optimization of friction stir welding parameters for dissimilar aluminum alloys. Mater Des 2010;31:3033–7.
[7] Liang Z, Chen K, Wang X, Yao J, Yang Q, Zhang L, et al. Effect of tool offset and tool rotational speed on enhancing mechanical property of Al/Mg dissimilar FSW joints. Metallurgy Mater Trans A 2013;44A:3721–31.
[8] Lee WB, Schmuecker M, Alfaro Mercardo U, Biallas G, Jung S. Interfacial reaction in steel–aluminum joints made by friction stir welding. Scripta Mater 2006;44:355–8.
[9] Dehghani M, Amadeh A, Akbari Mousavi SAA. Investigations on the effects of friction stir welding parameters on intermetallic and defect formation in joining aluminum alloy to mild steel. Mater Des 2013;49:433–41.
[10] Chen YC, Nakata K. Microstructural characterization and mechanical properties in friction stir welding of aluminum and titanium dissimilar alloys. Mater Des 2009;30:469–74.
[11] Wert J. Microstructures of friction stir weld joints between an aluminium-base metal matrix composite and a monolithic aluminium alloy. Scripta Mater 2003;49:607–12.
[12] Dalkilic S, Biallas G. FSW joints of an aluminium base metal matrix composite and a monolithic aluminium alloy. In: Proceeding of 6th international symposium on friction stir welding, 10–13th of October 2006, Canada.
[13] Guo J, Gougeon P, Chen XG. Microstructure evolution and mechanical properties of dissimilar friction stir welded joints between AA1100-B4C MMC and AA6063 alloy. Mater Sci Eng A 2012;553:149–56.
[14] Xiao BL, Wang D, Bi J, Zhang Z, Ma ZY. Friction stir welding of SiCp/Al composite and 2024 Al alloy. Mater Sci Forum 2010;638–642:1500–5.
[15] Sharifitabar M, Nami H. Microstructures of dissimilar friction stir welded joints between 2024-T4 aluminum alloy and Al/Mg2Si metal matrix cast composite. Compos B 2011;42:2004–12.
[16] Materion, SupremEX® AMC217XE. <http://materion.com/Products/CompositesCompoundsCeramics/MetalMatrixComposites/AluminumSiliconCarbide/SupremEXAMC217XE.aspx> [accessed 14.08.14].
[17] Krishnan KN. On the formation of onion rings in friction stir welds. Mater Sci Eng A 2002;327:246–51.
[18] McNelley TR, Swaminathan S, Su JQ. Recrystallization mechanisms during friction stir welding/processing of aluminum alloys. Scripta Mater 2008;58:349–54.
[19] Properties and selection: nonferrous alloys and special-purpose materials, vol. 2, Metals Handbook. 10th ed. ASM International; 1990. p. 272.
[20] Song Z, Nakata K, Wu A, Liao J, Zhou L. Influence of probe offset distance on interfacial microstructure and mechanical properties of friction stir butt welded joint of Ti6Al4V and A6061 dissimilar alloys. Mater Des 2014;57:269–78.
[21] Li B, Zhang Z, Shen Y, Hu W, Luo L. Dissimilar friction stir welding of Ti–6Al–4V alloy and aluminum alloy employing a modified butt joint configuration: Influences of process variables on the weld interfaces and tensile properties. Mater Des 2014;53:838–48.
[22] Li B, Shen Y. A feasibility research on friction stir welding of a new-typed lap–butt joint of dissimilar Al alloys. Mater Des 2012;34:725–31.
[23] Schneider JA. Temperature distribution and resulting metal flow. In: Mishra RS, Mahoney MW, editors. Friction stir welding and processing. Ohio: ASM International; 2007. p. 37–49.
[24] Colligan KJ. Material flow behavior during friction stir welding of aluminum. Weld Res Suppl 1999:229–37.
[25] Schneider JA, Nunes AC. Characterization of plastic flow and resulting microtextures in a friction stir weld. Metall Mater Trans B 2004;35:777–83.
[26] Properties and selection: nonferrous alloys and special-purpose Materials. vol. 2, Metals Handbook, 10th ed. ASM International; 1990. p. 294.
[27] Zhang Z, Xiao BL, Ma ZY. Hardness recovery mechanism in the heat-affected zone during long-term natural aging and its influence on the mechanical properties and fracture behavior of friction stir welded 2024Al-T351 joints. Acta Mater 2014;73:227–39.
[28] Xu W, Liu J, Zhu H, Fu L. Influence of welding parameters and tool pin profile on microstructure and mechanical properties along the thickness in a friction stir welded aluminum alloy. Mater Des 2013;47:599–606.
[29] Bussu G, Irving PE. The role of residual stress and heat affected zone properties on fatigue crack propagation in friction stir welded 2024-T351 aluminium joints. Int J Fatigue 2003;25:77–88.
[30] Radisavljevic I, Zivkovic A, Radovic N, Grabulov V. Influence of FSW parameters on formation quality and mechanical properties of Al 2024-T351 butt welded joints. Trans Nonferr Metal Soc China 2013;23:3525–39.
[31] Mahoney MW, Rhodes CG, Flintoff JG, Spurling RA, Bingel WH. Properties of Friction-Stir-Welded 7075 T651 Aluminum. Metall Mater Trans A 1998;29:1955–64.

Influence of friction stir welding parameters on the mechanical performance of 25%SiC/2124Al composite joints conducted with an un-threaded WC-Co tool

F. Cioffi[1], J. Ibáñez[1], R. Fernández[1], D. Verdera[2], and G. González-Doncel[1]

[1] Centro Nacional de Investigaciones Metalúrgicas (CENIM) C.S.I.C., Av. de Gregorio del Amo 8, E-28040 Madrid, Spain.

[2] Centro Tecnológico AIMEN, C. Relva 27, E-36410 O Porriño, Spain.

Trabajo preparado para enviar a una revista Científica para su publicación

Abstract

Friction Stir Welding (FSW) is a very promising technique for joining metal matrix composites (MMCs), but in comparison with aluminum alloys, for which this technique is most widespread, many difficulties arise from the presence of the non-deformable reinforcing particles. The most important one is the severe wear occurring in conventional tools. To avoid this problem an un-threaded hard tool (WC-Co) can be used but the condition parameter window shrinks. In this research, we have joined successfully 8mm thick plates of 25%SiC/2124Al composite by FSW using an un-threaded WC-Co tool in which wear was barely appreciated. Using appropriate welding parameters (rotation speed, advancing speed and tool off-set), a joint efficiency ($100*UTS_{joint}/UTS_{BaseMaterial}$) of up to 97% was reached revealing an optimal mechanical performance of these welds.

KEYWORDS: Metal-matrix composites (MMCs); Microstructure; Mechanical properties; Friction Stir Welding

1. Introduction

Joining of metal matrix composites is one of the processes to be improved in order to increase the applications of these materials, whose good mechanical properties have been known for several years [1]. Friction Stir Welding (FSW) is a promising alternative to traditional fusion welding techniques [2-4], but since its invention in the 1990s it has mainly been focused on monolithic alloys: firstly, light alloys like aluminum alloys [5] and more recently, harder materials [6-8].

Many of the publications regarding FSW of MMCs have focused on one of the main obstacles to be overcome: the tool wear phenomenon. For example, a average wear rate in steel tool of about 0.5%/cm at rotation speeds in the range 1000-2000 rpm is obtained on welding 6061-20%Al_2O_3 [9], and about 5-30% during welding Al359-20%SiC composite after only 1.5 m of welding distance [10-11]. It was also found in these two investigations that tool wear virtually disappeared once the initially threaded tool turned into a smooth one (i.e., the wear process was concentrated on the tool threads). More recently, Prater et al. [12] completed a modeling and experimental work on welds conducted on Al359-20%SiC composite with a trivex^{TM} un-threaded tool. They found that wear was strongly dependent on the processing parameters, but was lower than in the above studies with threaded tools [9- 12]. As a final example, it is worth mentioning the comparative study of the wear of threaded and un-threaded tools conducted during welding AC4A-30vol%SiCp composite [13]. A significant wear decrease was found on the un-threaded tool with respect the threaded one.

Tool wear not only reduces the lifetime of the FSW tool but can also deteriorate the properties of the welds due to the addition of wear debris into the welds. Obviously, overcoming this difficulty is crucial from an industrial standpoint if FSW is to be implemented in the fabrication of MMCs components on a massive scale. This problem is less critical for aluminum alloys, where the use of hard steel tools guarantees the reproducibility of the process since the tool profile integrity is maintained for several meters of weld [14]. Furthermore, the tool profiles in these cases have been becoming increasingly more complex, as reviewed by Rai et al. in [15]. In their review, these authors examine the tool material and geometry used for welding aluminum alloys and other alloys. Very complex tool profiles are included in this work. At the same time, the parameters window for welding aluminum alloys has been expanding. This is a consequence of the better material transport caused by these complex tool profiles. As a result, nowadays one can choose among dozens of tool materials and profiles and a wide range of welding parameters.

On the contrary, the tool material and welding parameters window for the case of MMCs, in particular when the amount of reinforcing particles is 15% in vol. or more, is still quite small. Most of the published studies, like those mentioned above, have used steel tools, but despite that sound joints are usually obtained, tool wear is always unavoidable irrespectively of tool geometry and FSW conditions. To overcome this problem, Wang et al. [16] used an "ultra hard material" for the un-threaded pin tool to FSW six mm thick plates of Al2009-15%vol.SiCp composite, and they stated that "almost no wearing occurred during FSW". In this study, however, a T4 post-heat treatment had to be conducted to nearly recover the strength of the base material. In a more recent study of the present authors [17], a threaded pin tool fabricated from MP159 superalloy was used to weld a 15 mm thick plate of Al25%SiC/2124Al composite, the same material of the present investigation. Very severe pin tool wear occurred. Finally, few studies utilize WC-Co or cermet tools to weld MMCs with high content of ceramic reinforcement. As it was mentioned previously, Liu et al. [13] obtained a better wear resistance with a un-threaded WC-Co pin tool in comparison to a threaded one upon welding AC4A+30vol%SiCp composite. However, the microstructure and mechanical properties of the resulting joints are not reported. Very recently, these same authors reported defect free FSW joints obtained in AC4A+30vol%SiCp composite joints conducted by FSW with only the threaded WC-Co tool [18]. Finally, Ni et al. [19] studied the tensile properties of Al2009+17vol%SiCp composite joints obtained with a cermet pin tool with a triangular tip and no threads. However, the tool wear characteristics in these two studies are not given.

In summary, publications accounting for joints carried out on MMCs with a high volume fraction of SiCp (15% or more) with good mechanical properties and minimal or no tool wear are virtually nonexistent. From the above studies, however, it seems that a reasonable approach to avoid tool wear during FSW of MMCs is to use hard material tools with smooth profiles. The drawback is that such tools will negatively affect the material transport and, therefore, the formation of the joint, in two ways:

1) The absence of threads diminishes the volume swept by the tool, in other words, less material is transported [14].
2) Hard tool materials are most likely to have "sliding" contact conditions with the composite than "sticking" ones [4]. This circumstance leads to limited material transport because the tool is less effective in dragging the composite around it.

The limited material transport makes it difficult the realization of sound welds. This is reflected in a small parameter window, restricted to low rotation speed, *w*, and low advancing speed, *v* [20].

The purpose of this research is to study the weldability of thick plates of a high quality powder metallurgical MMC with a high content of small ceramic particles by FSW, using an un-threaded WC-Co tool to minimize the wear. As it will be shown, experiments under different conditions have been made until sound welds with optimal mechanical properties are obtained. Contrary to the strategy usually adopted when FSW composites with a high content of reinforcement using hard WC-Co tools, we progressively decreased *w* to reduce the wear. This is consistent with the decrease in effective tool wear with decreasing *w* observed in Al6061-20vol%Al2O3 [9,12]. The achievements found are discussed in the context of similar studies on FSW of composites. It is shown for the first time the possibility to weld successfully thick plates of MMCs with high volume fraction of reinforcement; with hardly any tool wear, no detectable defects, and high joint efficiencies.

2. Material and experimental procedures

The MMC used in this study, 25%SiC/2124Al, was fabricated by Aerospace Metal Composites, AMC, UK, by a powder metallurgy route, using a AA2124 aerospace grade aluminum alloy as matrix and 25% by volume of ultra-fine silicon carbide particles (2-3 μm) as reinforcement [21]. The 260x90x8 mm^3 plates used for the welds were electro-discharge cut from a 420X260x90 mm^3 block naturally aged after high temperature forging (T1 condition). The plates were friction stir welded in the as received condition.

The welds were carried out at AIMEN, Porriño, Spain, making use of a PDS-4 Intelligent Stir FSW machine from MTS (model 100-183-869C, ISTIR PDS). This machine is instrumented to accurately measure, control and monitoring the key process parameters. In particular, the forge (or vertical load) between the shoulder and the workpieces, F_z, is measured using two custom MTS load cells, and the torque on the spindle, *T*, using pressure transducers mounted on the inlet and outlet of the motor. This possibility allows a direct calculation of the heat input, *H*, for the different *w* and *v* values. By contrary, in other works which employ adapted conventional mills (typically used in machining) *H* must be calculated from more indirect procedures [22]. The one piece WC-Co tool had a tapered conical pin (which included three flat faces at 120˚) and a concave shoulder. The shoulder diameter, pin diameter, and length were 25, 7.2-6.35 and 7.6mm, respectively. A total of eight joints, denoted as W1 to W8, were carried out using different heat input conditions varying *w*, *v*, and tool off-set, Table 1. The rest of the conditions remained constant: 1.5˚ of tilt angle, position control (7.7 mm penetration), clockwise rotation, and steel backing plate. Conventional pre-weld cleaning of butt surfaces for welds W4-W8 was conducted. The tool pin wear after all welds were made was calculated

from high magnification pictures on which detailed measurements of the pin reduction were conducted [9-11,13,23]. As it will be shown, unappreciable tool wear occurred.

Weld code	Rotation speed, *w* (rpm)	Advancing speed, *v* (mm/min)	Weld pitch, *v/w* (mm/rev)	Vertical force, *F*, (kN)	Average torque, T (Nm)†	Heat input‡, *H* (kJ/mm)	Friction coefficient‡‡, *μ*	UTS (MPa)*	Fracture location (nº of samples)	Joint efficiency (%)	Remarks on the SZ microstructure
W1	400	30	0.075	7.55	63	0.87	0.87	-	-	-	Large tunnel defects and superficial pores
W2	450	30	0.067	8.24	59	0.88	0.75	-	-	-	Smaller tunnel defects than in W1
W3	400	20	0.050	12.97	67	1.34	0.54	291	Boundary (2)	78	No tunnel defect but depressed volumes or voids at the boundary
W4	400	20	0.050	14.15	70	1.39	0.52	-	-	-	Fine and continuous boundary, occasionally interrupted by voids
W5	400	20	0.050	13.43	68	1.36	0.54	-	-	-	Mixture of sections with voids and clean areas at the boundary
W6	450	20	0.044	14.27	62	1.37	0.46	316	Boundary (3)	85	Small voids at the boundary
W7	400	15	0.038	14.41	65	1.72	0.47	359	HAZ (3)	97	Smaller voids than in W6 and very homogeneous SiCp distribution at the SZ
W8**	400	15	0.038	17.64	72	1.92	0.43	352	HAZ (3)	95	No detectable defects and very homogeneous SiCp distribution at the SZ

Table 1. Welding parameters, heat input, friction coefficient, and mechanical properties of the joints conducted for the study (The UTS of the base material is 371 MPa).

† Average torque value. This value fluctuates in an interval of +/-2Nm for every weld.
‡ Heat input, H, is calculated from equation (1)
‡‡ Friction coefficient, μ, is calculated using equation (2)
* Average value of the tests conducted for each weld.
** A tool off-set of -1.5mm into the retreating side, measured as the distance from the tool axis to the butt line, was used.

As mentioned in the Introduction, the main strategy followed in this research consisted on using low *w* values with the aim of minimizing the tool wear. This is expected since the lower the rotation speed the less is the total composite surface per second which frictions against the pin tool. Table 2 summarizes the results from previous investigations and the FSW conditions to obtain joints in MMCs with a high content of SiCp in which the pin tool was fabricated from ultra-hard material.

reference	Material	*w*, rpm	*V*, mm/min	Travel distance, mm	pin	Wear reported
[19]	AC4A+30vol%SiC	2000	25-150	1700	threaded, WC-Co	appreciable
[9]	AC4A+30vol%SiC	2000	25-200	1300	un-threaded, WC-Co	slight
		1500-2000	25-150	1300	threaded, WC-Co	appreciable
[15]	AA2009+17vol%SiC	1000	50	-	un-threaded, Cermet	-
Present work	AA2124+25vol%SiC	400	15	1800	un-threaded, WC-Co	minimal

Table 2. Data from the literature in which MMCs with high content of reinforcement are joined by FSW using tools fabricated from hard material. Welding conditions and wear detected in joints are summarized.

Transverse metallographic sections were prepared in every weld: They were ground and polished using diamond paste up to 1 μm, for microstructural study under the optical (OM) and scanning electron microscope (SEM).

Dog-bone tensile samples, with 75 mm gauge length and 12.5 mm width, were machined from some of the welds (W3-W8), perpendicular to the welding direction so that all the different microstructural zones could be evaluated. For comparative purposes, dog-bone tensile samples were machined from the base material. Tensile tests to fracture were performed at $5x10^{-4}$ s^{-1} using a universal tensile test machine.

3. Results

Besides the welding conditions (including *T* and F_z), Table 1 summarizes the microstructure of the stir zone, SZ, and the mechanical properties of the joints conducted in the present work. As it can be seen, sound welds, free of defects and with attractive mechanical properties, are obtained for welds W7 and W8. For these welds, *w* and *v* were of 400 rpm and 15 mm/min, respectively, values which are considerably lower than those used in other works, Table 2.

The presence of different type of defects, ranging from tunnel defects and pores in the upper surface in W1 and W2 to small pores and discontinuities in the SZ of W3-W6, were virtually eliminated in these two joints. The *H* values are obtained from the common expression relating this parameter with *T* (which is measured directly by the FSW machine), *w*, and *v* [24],

$$H = T\,\frac{w}{v} \tag{1}$$

A general description of the microstructure of joints W3 and W8 (conducted under different heat input values, Table 1) is shown in Fig. 1. A clear line or boundary, which goes from the top to the bottom surfaces and corresponds to the original contact surface of the plates before welding, is seen in the SZ of W3. The detail of the micrograph, Fig. 1a) reveals that it is defined by voids (similar voids, but smaller, were still appreciated in W7). These voids were virtually eliminated in W8, resulting in a boundary practically indiscernible from the surrounding microstructure, Fig. 1b). Furthermore, and as it is commonly observed in composite joints obtained by FSW, a more homogeneous distribution of the reinforcing particles is obtained in the SZ with respect to the BM. This is seen when comparing Fig. 1 a) and b), which correspond to the SZ of W3 and W8, respectively, with Fig. 1c) and d), which correspond to the HAZs of the same joints. In addition, it is also seen that a pronounced coarsening of the precipitates (the white particles) occurs in the HAZ of W8, Fig. 1d). This is due to the overaging underwent by the composite matrix as a consequence of the severe FSW conditions and high *H*, Table 1.

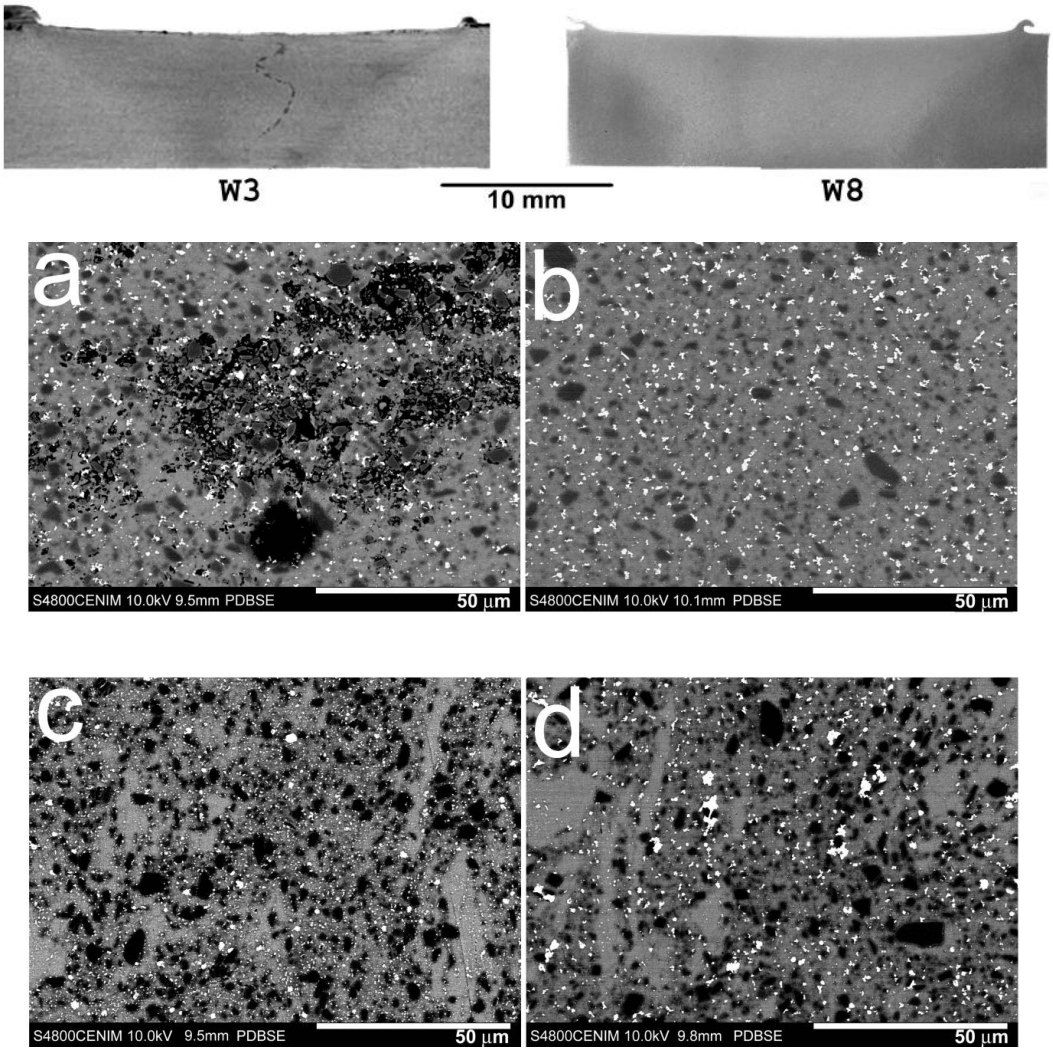

Figure 1.- General overview of welds W3 and W8 and details of, a) pores in the boundary of the SZ of W3, b) homogeneous distribution of reinforcement in the SZ of W8, c) distribution of reinforcement and small precipitates in the HAZ of W3, and d) distribution of the reinforcement and large precipitates in the HAZ of W8.

The unappreciable wear observed after completion of all the welds (a total of some 186 cm) of the present research can be seen from Fig. 2, where the pin at the beginning and at the end of the experiment is shown. A comparative evaluation of the tool wear of the present study and that obtained by other researchers [8] using a tool fabricated from the same material can be seen from the plot of Fig. 3. As can be seen, the tool wear obtained in this research is significantly smaller than that reported previously, Table 2.

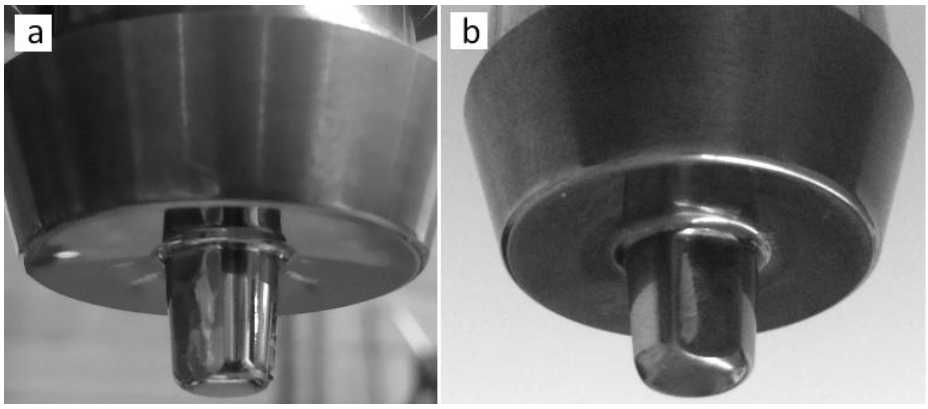

Figure 2. FSW tool used in this study: (a) before and (b) after conducting all the welds. No wear is appreciated after the welds were made.

Finally, it is worth remarking that fracture in the joints W3 and W6, which led to a tensile strength of 291 and 316 MPa, respectively, occurred at the boundary, revealing that this was the weakest region of each of these joints. Despite this, a significant average joint efficiency of 78% in W3 and 85% in W6 was obtained. In W7 and W8, however, fracture occurred at the heat affected zone, HAZ, indicating that the strength of the boundary was improved with respect to the previous joints. A remarkable joint efficiency of 97 and 95%, respectively, was reached in these cases.

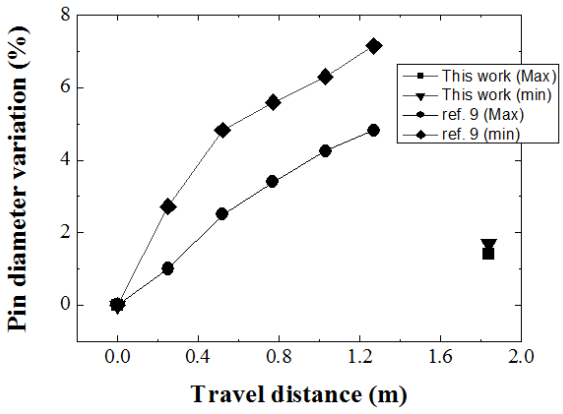

Figure 3. Comparative evolution of tool wear (maximum and minimum diameter of pin) in the present study with respect that reported by other researchers [9] using a tool fabricated from the same material.

4.- Discussion

As it can be seen from Table 1, sound joints of 8 mm thick plates of 25%SiC/2124Al composite can be obtained by FSW. In agreement with [8], where the FSW of several composites is reviewed, the welding parameters in MMCs with high volume fraction of reinforcement must

be limited to high heat-input conditions to evade the low ductility of these composites. In other words, tunnels and superficial pores are avoided if sufficient heat input is reached. However, excessive *H* can be also detrimental for FSW joints, in agreement with [25], where an optimal *H* value in joints conducted on Al6061-10%SiCp composite is found around *H*=1040 J mm^{-1}. Above this value, the ultimate tensile strength (UTS) decreases. It should be emphasized the restricted welding conditions window found in the present investigation that leads to sound welds: Only reducing *w* and *v* down to 400 rpm and 15 mm/min, respectively, and including a -1.5 mm off-set into the retreating side, a weld with no visible defects in the SZ and joint efficiency of 95% has been reached. A very homogeneous distribution of the reinforcement and the typical refined microstructure is also obtained, Fig. 1, as a result of dynamic recrystallization [10,20]. Cracking of the large SiC particles due to strong stirring was very occasionally observed.

The UTS as a function of *H* is represented in the plot of Fig. 4. The increase revealed (joints W3, W6 and W7) is due to the defects present at the boundary, which evolve with the FSW parameters. As seen from the Remarks column of Table 1, increasing *H* leads to a diminution of the boundary defects (tunnel defects, large voids, small voids, no voids). The presence of these defects in W3 and W6 accounts for the fact that fracture occurs at the boundary region (revealing also that mixing in this region is not completed) and their progressive disappearance increases the tensile strength (and joint efficiency). On the contrary, the defects in the SZ of welds W7 and W8 play a secondary role since fracture was located in the HAZ. The strength of this zone should decrease with an increase of *H* due to a more severe overaging of the matrix alloy. Although the strength of welds W7 and W8 is practically identical, the above explanation is in line with the slight decrease reported (from 359 MPa in W7 to 352 MPa in W8). In summary, increasing *H* leads to an increase in UTS when the fracture is dominated by the defects in the SZ (from W3 to W6). But when the fracture is dominated by the overaging of the HAZ, further increasing *H* would lead to a decrease in UTS, as could be inferred from welds W7 and W8.

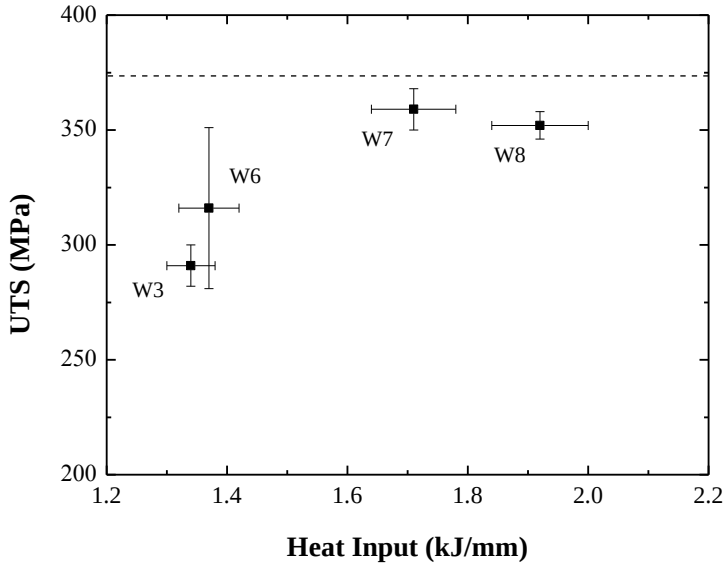

Figure 4. UTS *vs*. heat input, *H,* per turn. The error bars correspond to the standard deviation. The dotted line represents the UTS of the base material (371 MPa).

It is generally agreed that the processes and the variables involved in a FSW operation, such as the energy generated during joining and/or the torque required by the tool, must be analyzed in the frame of the stick-slip phenomena [4,24,26-27]. Both, stick and slip, must occur during the FSW process, but a balance among them can be fixed according with the specific "system"; namely, tool shape/material, workpieces properties, FSW conditions, etc. As stated in the introduction, the achievement of sound welds in MMCs (in particular, with high content of ceramic particles) and limited tool wear requires the use of hard tool materials and smooth shapes. This approach implies, as a drawback, that material transport is reduced and that slipping conditions predominate over sticking ones; i.e., the FSW process can be analyzed assuming that little sticking occurs during joining. This is, in agreement with other works [28], supported by the presence of a lazy, as it appears clearly in some of the present welds: see W3 in Figure 3. Finally, it is worth noting that, despite the low w values used, the average weld pitch resulting from the welding conditions of this investigation is very low, Table 1. In fact, this value is typically well below the usual ones used to FSW similar composites, as can be seen from the revisions of Ni et al., [19] and Wang et al., [8]. A low weld pitch, in connection with the observation of the lazy in the *nugget*, supports further a limited material transport (minimal sticking conditions), and a predominance of sliding conditions over sticking ones. According to the above hypothesis, the torque of welds W1-W8, Table 1, can be explained on the basis of the frictional forces between the tool and the workpiece and by the different F_z

values, necessary in each case to keep the tool at the same depth (position control). In agreement with [27], the total torque, T_{tot}, can be expressed in terms of the frictional forces according with the following relationship,

$$T_{tot} = T_s + T_p = 2 F_z \mu \left(\frac{R_1}{3} + h\frac{R_2^2}{R_1^2}\right) \quad (2)$$

where T_s and T_p are the shoulder and pin contributions to the torque, respectively, μ the friction coefficient between the tool and the workpieces, R_1 and R_2 the shoulder and pin radius, respectively, and *h* the length of the pin. The first term of this equation, related to the shoulder contribution, is, in fact, similar to the torque proposed by Midling et al. [29] for the case of friction welding of metals and Frigaard et al [30] for friction stir welding, where pure sliding is considered.

It is also assumed in equation (2) that the tool shoulder is flat and that the tool and the workpieces undergo a uniform constant stress, $\sigma_z = \sigma_r = \sigma$ (where σ_z is the vertical stress and σ_r the lateral stress between the pin surface and workpiece). This assumption, however, may be appropriate from the point of view of energetic considerations and heat flow calculations, in accordance with [31], but it is unacceptable from the standpoint of determining the plastic flow of the workpieces around the pin, as could be inferred, for example, from [32]. Uniform σ is incompatible with transport of material from the pin front towards the back region: This transport (and the accompanying pin advancing motion) must require a significant radial stress gradient with the angle θ; *i.e.*, with respect the transverse pin motion direction; namely, between $\theta = 0$ (front edge) and $\theta = \pi$ (back edge) such that $\sigma_r(0) > \sigma_r(\pi)$. The variation of this stress term with θ, $\sigma_r(\theta)$, is, in summary, responsible of composite matrix shear deformation, material transport, and crucial to understand the plastic flow of the composite matrix in the SZ. An estimation of σ_r as a function of θ requires, at least, knowledge of the advancing stress, σ_x, offered by the workpieces during transverse tool motion. This analysis is, however, beyond the scope of this investigation.

On the other hand, the differences in the microstructure of W7 and W8 joints can be understood on the basis of the non symmetrical nature of the FSW process and the variation of the radial stress term with θ, $\sigma_r(\theta)$, as above explained. As a consequence, the plastic flow in the metallic matrix varies with θ. This implies that a tool off-set makes that the region corresponding to the contact surface of the plates flows differently. As a consequence, the defects associated with this surface (boundary region of the SZ) also depend on the tool off-set. In fact, for a tool off-set of 1.5mm into the retreating side, these defects virtually disappear in W8. The increase in *H* from W7 to W8 through the observed increase in F_z, Table

1, should be also taken into account when considering the above changes. Since the welds were conducted under position control, it seems that including a tool off-set in the FSW process requires an increase in pressure between tool and workpieces to conduct the joint. The subsequent increase in frictional forces and temperature facilitates further plastic deformation of the alloy matrix of the composite during FSW and an easier disappearance of the voids associated with the boundary. In summary, an off-set, as a welding parameter in FSW operations, is important not only in dissimilar joints [33] but also in similar welds. This accounts for the strong non-symmetrical nature of FSW process. However, a correlation between an off-set and an increase in *H* (through an increase in F_z) is, at the moment, difficult to understand and further investigation would be needed to account for this effect.

Equation (2) should be taken cautiously, not only because of the assumption of uniform and constant σ between tool and workpieces but also because of other factors, such as workpieces butt surfaces preparation, the initial pressure between them, temperature of backing plate before welding, and others (e.g., the fact that μ between workpieces-shoulder and workpieces-pin could differ from each other, and/or that μ could be θ dependent) are not usually taken into consideration in the calculations, but they also may alter the correlation between T, μ, and Fz. Also inherent errors in the experiment and a different handling of the different welds should also be considered. It would, therefore, be more appropriate to define μ as an average friction coefficient equation (4) should not be taken strictly rigorous.

From the data of T and Fz, Table 1, an average value of the coefficient μ can be obtained using equation (2). Again, the validity of this value must take into consideration the above limitations. The resulting values are also summarized in Table 1. It is noticeable the large μ values at low heat inputs and also that this coefficient decreases with an increase of H. In spite of the restrictions mentioned, μ values in welds W7 and W8 are very similar to those reported for similar and dissimilar welds of aluminum alloys (see, for example, Table III in [30] and figure 9 of [24]). A comparison with the case of other composites is, unfortunately, not possible since, to the best of these authors´ knowledge, there are no published studies on FSW of MMCs including μ data obtained from the experiments.

The variation of μ with H is better appreciated in the plot of Fig. 5, and can be interpreted as a decrease of μ with temperature since an increase in H is related to an increase of the temperature during the FSW operation. Although a decrease of μ with temperature has been reported in several studies [24,34-36], there is not a conclusive explanation for this trend yet. In some cases it has been related to local melting of the matrix alloy due to rapid heating

above the eutectic temperature, before re-solutioning of the precipitates, as reported in 6082-T6 aluminium alloy and A357-13vol%SiC composite [29]. For our case, however, this is unlikely due to the low v used in the welds, which allows for a re-solution of the precipitates during the FSW operations. The large values of μ obtained at low heat inputs are also in agreement with previous investigations on the FSW of 7020-T6 alloy [37]. Finally, it is worth remarking that for calculating the average friction coefficient values, equation (2), it was assumed that the shoulder was flat. However, if the angle between workpiece and shoulder surfaces (of about 7°) is also taken into account, an additional term in equation (2) should be also included [27]. This would decrease the μ values obtained in this investigation by about 10%.

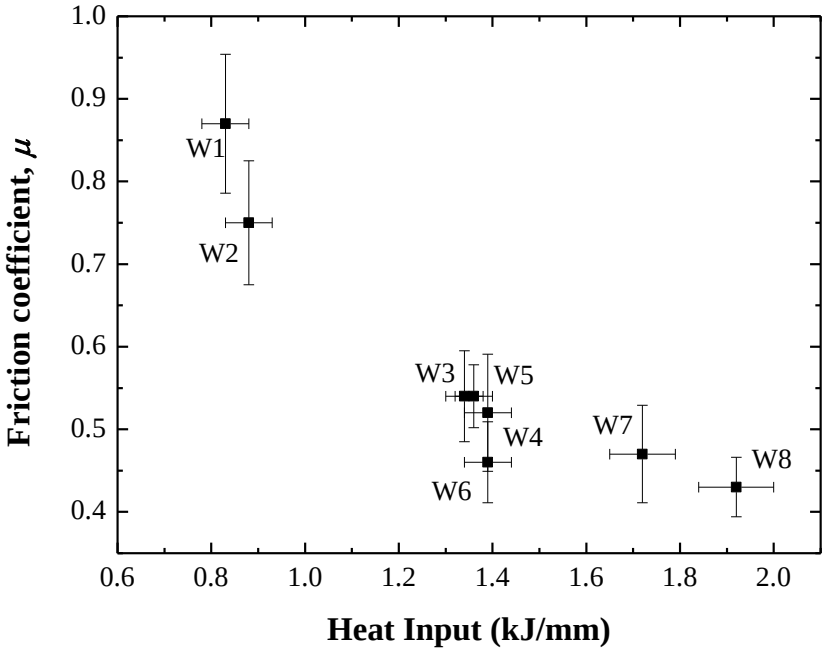

Figure 5. Variation of the average friction coefficient, μ, with heat input, *H*. The contribution of shoulder and pin is taken into account in the calculation.

4. Summary and Conclusions

In the present work, 8 mm thick plates of MMC with a high volume fraction of reinforcement, 25%SiC/2124Al, have been successfully joined by FSW using an un-threaded WC-Co tool in which unappreciable tool wear occurred. The present results reveal the importance of the heat input on the final mechanical performance of the composite welds, as well as the need of a deeper analysis on the FSW parameters dependence of the friction coefficient. Clearly, such study will throw further insight on the underlying deformation mechanisms involved during FSW of these composites. This analysis is under progress and will be the subject of a future publication.

The following are the main conclusions that can be drawn from this study:

- The severe tool wear caused by MMCs can be avoided by using an un-threaded WC-Co un-threaded tool. Appropriate FSW conditions to obtain sound welds without macroscopic defects (tunnel and superficial pores) and microscopic defects (oxides and voids in the boundary) have been found in the low (*v, w*) range.
- Remarkably high joint efficiencies ($100*UTS_{joint}/UTS_{BaseMaterial}$), well above 90%, have been obtained under the appropriate welding conditions.
- A tool off-set, as a welding parameter in FSW operations, is important not only in dissimilar joints but also in similar welds since it can be used to eliminate defects in the SZ. This accounts for the strong non-symmetrical nature of FSW process.

Acknowledgements

Support from Projects MAT-05-0527, MAT-09-09545, and MAT13-48483-C2-2-P from MICINN, and PIE 200960I076 from C.S.I.C., Spain, is gratefully acknowledged. The support of PhD grant BES-2010-030247 for one of the authors (F.C.) from MINECO is acknowledged.

References

1. Chawla KK (1993) Structure and properties of composites. VCH Publishers Inc, New York

2. Ma ZY (2008) Friction stir processing technology: a review. Metall Mater Trans A 39:642-658

3. Nandan R, DebRoy T and Bhadeshia HKDH (2008) Recent advances in friction-stir welding Process, weldment structure and properties. Progress in Materials Science 53:980–1023

4. Mishra RS and Ma ZY (2005) Friction stir welding and processing. Mater Sci Eng R 50:1-78

5. Threadgill PL, Leonard AJ, Shercliff HR and Withers PJ (2009) Friction stir welding of aluminium alloys. Int Mat Rev 54:49-93

6. Storjohann D, Barabash OM, Babu SS, David SA, Sklad PS and Bloom EE (2005) Fusion and friction stir welding of aluminum-metal-matrix composites. Metall Mater Trans A 36:3237-3247

7. Çam G (2011) Friction stir welded structural materials: beyond Al-alloys. Int Mater Rev 56:1-48

8. Wang D, Xiao BL, Ni DR and Ma ZY (2014) Friction stir welding of discontinuously reinforced aluminum matrix composites: a review. Acta Metall Sin (Engl Lett) 27:816-824

9. Prado RA, Murr LE, Shindo DJ and Soto KF (2001) Tool wear in friction-stir welding of aluminum alloy 6061 + 20% Al2O3: a preliminary study. Scr Mater 45:75-80

10. Fernandez GJ and Murr LE (2004) Characterization of tool wear and weld optimization in the friction-stir welding of cast aluminum 359+20% SiC metal-matrix composite. Mater Charact 52:65-75

11. Shindo DJ, Rivera AR and Murr LE (2002) Shape optimization for tool wear in the frictionstir welding of cast AI359-20% SiC MMC. J Mater Sci 37:4999-5005

12. Prater TJ, Strauss AM, Cook GE, Machemehl C, Sutton P and Cox CD (2010) Statistical modeling and prediction of wear in friction stir welding of a metal matrix composite (Al 359/SiC/20p). J Manuf Tech Res 2:1-13 13. Liu HJ, Fujii H and Nogi K (2004) Wear behavior

13. Liu HJ, Fujii H and Nogi K (2004) Wear behavior of hard alloy tools in the friction stir welding of AC4A + 30 vol.% SiCp aluminum matrix composite. Proceedings of the Fifth International Conference on Friction Stir Welding Sept 14–16 (Metz, France), TWI.

14. Christian B (2007) CHAPTER 2: Friction stir tooling: Tool materials and designs. Friction Stir Welding and Processing. ASM international

15. Rai R, De A, Bhadeshia HKDH and DebRoy T (2011) Review: friction stir welding tools. Sci Technol Weld Join 16(4):325-342

16. Wang D, Xiao BL, Wang QZ and Ma ZY (2013) Friction stir welding of SiCp/2009Al composite plate. Mater Des 47:243-247

17. Cioffi F, Fernández R, Gesto D, Rey P, Verdera D and González-Doncel G (2013) Microstructure and mechanical properties of 2124/25%SiCp composite joints obtained by friction stir welding. Compos A 54:117-123

18. Liu HJ, Hu Y, Zhao Y and Fujii H (2015) Microstructure and mechanical properties of friction stir welded AC4A + 30 vol.%SiCp composite. Mater Des 65:385-400

19. Ni DR, Chen DL, Wang D, Xiao BL and Ma ZY (2014) Tensile properties and strain-hardening behaviour of friction stir welded SiCp/AA2009 composite joints. Mater Sci Eng A 608:1-10

20. Bozkurt Y (2011) Weldability of metal matrix composites plates by friction stir welding at low welding parameters. Mater Tech 45:407-412

21. Materion, SupremEX® AMC217XE, accessed 14 August 2014 http://materion.com/Products/CompositesCompoundsCeramics/MetalMatrixComposites/AluminumSiliconCarbide/SupremEX%20AMC225XE.aspx

22. Pew JW, Nelson TW and Sorensen CD (2007) Torque based weld power model for friction stir welding. Sci Technol Weld Join 12:341-347

23. Liu HJ, Feng JC, Fujii H and Nogi K (2005) Wear characteristics of a WC–Co tool in friction stir welding of AC4A+30vol.% SiCp composite. Int J Mach Tools Manuf 45:1635-1639

24. Peel MJ, Steuwer A, Withers PJ, Dickerson T, Shi Q and Shercliff H (2006) Dissimilar friction stir welds in AA5083-AA6082. Part I: process parameter effects on thermal history and weld properties. Metall Mater Trans A 37:2183-2193

25. Periyasamy P, Mohan B and Balasubramanian V (2012) Effect of heat input on mechanical and metallurgical properties of friction stir welded AA6061-10% SiCp MMCs. J Mater Eng Perform 21:2417-2428

26. Neto DM and P. Neto P (2013) Numerical modeling of friction stir welding process: A literature review. Int J Adv Manuf Technol 65:115-126

27. Schmidt H, Hattel J and Wert J (2004) An analytical model for the heat generation in friction stir welding. Modelling Simul Mater Sci Eng 12:143-157

28. Oosterkamp A, Oosterkamp LD and Nordeide A (2004) Kissing bond phenomena in solidstate welds of aluminum alloys. Weld J 83:225S-231S

29. Midling OT, Grong Ø (1994) A process model for friction welding of Al–Mg–Si alloys and AlSiC metal matrix composites. Acta Metall Mater 42:1595-1609

30. Frigaard Ø, Grong Ø and Middling OT(2001) A process model for friction stir welding of age hardening aluminum alloys. Metall Mater Trans A 32:1189-1200

31. Hamilton C, Dymer S and Sommers A (2008) A thermal model of friction stir welding in aluminum alloys. Int J Mach Tools Manuf 48:1120-1130

32. Kumar R, Singh K and Pandey S (2012) Process forces and heat input as function of process parameters in AA5083 friction stir welds. Trans Nonferrous Met Soc China 22:288-298

33. Cioffi F, Ibáñez J, Fernández R and González-Doncel G (2015) The effect of lateral off-set on the tensile strength and fracture of dissimilar friction stir welds, 2024Al alloy and 17%SiC/2124Al composite. Mater Des 65:438-446

34. Chen CM and Kovacevic R (2003) Finite element modeling of friction stir welding-thermal and thermomechanical analysis. Int J of Mach Tools Manuf 43:1319-1326

35. Prasanna P, Rao BS and Rao GKM (2010) Finite element modeling for maximum temperature in friction stir welding and its validation. Int J Adv Manuf Technol 51:925-933

36. Kang SW and Jang BS (2014) Comparison of friction stir welding heat transfer analysis methods and parametric study on unspecified input variables. J Mech Sci Technol 28:4233-4246

37. Kumar K, Kalyan C, Kailas SV and Srivatsan TS (2009) An investigation of friction during friction stir welding of metallic materials. Mater Manuf Proc 24:438-445

Available online at www.sciencedirect.com

ScienceDirect

Acta Materialia 74 (2014) 189–199

Acta MATERIALIA

www.elsevier.com/locate/actamat

Analysis of the unstressed lattice spacing, d_0, for the determination of the residual stress in a friction stir welded plate of an age-hardenable aluminum alloy – Use of equilibrium conditions and a genetic algorithm

F. Cioffi [a], J.I. Hidalgo [b], R. Fernández [a], T. Pirling [c], B. Fernández [a], D. Gesto [d], I. Puente Orench [c,e], P. Rey [d], G. González-Doncel [a,*]

[a] Dept. of Physical Metallurgy, Centro Nacional de Investigaciones Metalúrgicas, CENIM, C.S.I.C., Av. de Gregorio del Amo 8, 28040 Madrid, Spain
[b] Dept. de Arquitectura de Computadores y Automática, Universidad Complutense de Madrid, 28040 Madrid, Spain
[c] Diffraction Group, Institut Laue-Langevin, ILL, BP 156, F-38042 Grenoble Cedex 9, France
[d] Centro Tecnológico AIMEN, C. Relva 27, E-36410 O Porriño, Spain
[e] Instituto de Ciencia de Materiales de Aragón, C.S.I.C.-Universidad de Zaragoza, Cl Pedro Cerbuna 12, 50009 Zaragoza, Spain

Received 25 March 2014; accepted 16 April 2014
Available online 14 May 2014

Abstract

Procedures based on equilibrium conditions (stress and bending moment) have been used to obtain an unstressed lattice spacing, d_0, as a crucial requirement for calculating the residual stress (RS) profile across a joint conducted on a 10 mm thick plate of age-hardenable AA2024 alloy by friction stir welding (FSW). Two procedures have been used that take advantage of neutron diffraction measurements. First, equilibrium conditions were imposed on sections parallel to the weld so that a constant d_0 value corresponding to the base material region could be calculated analytically. Second, balance conditions were imposed on a section transverse to the weld. Then, using the data and a genetic algorithm, suitable d_0 values for the different regions of the weld have been found. For several reasons, the comb method has proved to be inappropriate for RS determination in the case of age-hardenable alloys. However, the equilibrium conditions, together with the genetic algorithm, has been shown to be very suitable for determining RS profiles in FSW joints of these alloys, where inherent microstructural variations of d_0 across the weld are expected.

Keywords: Residual stress; Genetic algorithms; Neutron diffraction; Aluminum alloys; Friction stir welding (FSW)

1. Introduction

Probably the most critical issue for the determination of the residual stress (RS) state of a given sample/component by diffraction methods (usually X-rays or neutrons) is the availability of an accurate and reliable value of the unstressed lattice spacing, d_0 [1–4]. It is well known that the procedure requires the determination of the spacing, d_{hkl}, of a given crystallographic hkl plane in the stressed sample using Bragg's law, $2d_{hkl}\sin\theta = \lambda$, where θ is the Bragg's angle and λ is the wavelength of the incident beam. Then, by using the formula

$$\varepsilon = \frac{d_{hkl} - d_0}{d_0} \quad (1)$$

the elastic strain, ε, in a given gauge volume is calculated in the same way as macroscopic strains are obtained in

* Corresponding author. Tel.: +34 91 5538900x337; fax: +34 915347425.
E-mail address: ggd@cenim.csic.es (G. González-Doncel).

conventional mechanical testing with the help of a suitable extensometer. Direct use of the generalized Hooke's law of elasticity, namely,

$$\sigma_i = \frac{E}{(1+v)(1-2v)}[(1-v)\varepsilon_i + v(\varepsilon_j + \varepsilon_k)] \quad (2)$$

where σ_i is the i component of the stress tensor, related to the three strain components, ε_i, ε_j and ε_k, E is the elastic modulus and v is the Poisson's ratio, provides the stress state in the same way as a load cell measures applied loads in a testing machine. The attractiveness of using neutrons (or X-rays) is that a triaxial stress state can be evaluated in a non-destructive way. The data obtained can then be compared with the predictions derived from elaborated finite element codes or proposed models for subsequent assessment.

The crucial issue that makes the need for a very precise value of d_0 is that small fluctuations or experimental errors in the peak position can lead to huge variations of the calculated strain and resulting stress. For example, a variation of a few 10^{-14} m (or 10^{-4} Å) in the value of d_0 (or d), say 2×10^{-14} m, can lead to a variation in the stress of the order of 10 MPa for the case of aluminum alloys. The stiffer the material, the wider the variation (titanium, steel, etc.).

Usually, a guaranteed d_0 value is obtained from powder of the same material, provided that the powder does not hold any macroscopic stress. For this purpose, powder with a particle microstructure similar to that of the sample on which the RS is to be measured is required. In the case of many age-hardenable aluminum alloys, it is thus important that both the powder and the sample have undergone the same temperature cycle to avoid the well-known strong influence of the precipitation state on the lattice spacing [5].

However, in many real cases, such as welds of these aluminum alloys, the above procedure is impractical since the temperature cycle undergone by the material is not known. Rather, it differs across the welded region, i.e. different microstructures can be found across the weld. Such variations make it impossible in practice to apply the powder method to determine d_0. In cases like these, the so-called "comb" sample method is used [3,6–10]. This method consists in sectioning the weld into small pieces or coupons so that the macroscopic RS(M-RS) is relieved. The peak positions obtained in each piece before and after sectioning can then be compared and the M-RS profile calculated, provided that the microstructures in the different pieces are not modified by the cutting operation. To ensure that the RS is relieved after sectioning, it is necessary for the dimensions of each piece to be significantly smaller than the initial sample size or the "wavelength" of the M-RS to be determined. For practical purposes, the different pieces are not separated from each other; instead, they are kept together in the form of a comb, in which each tooth keeps the specific orientation and d_0 value at that portion of the original weld with respect to a given coordinate system [6].

There are, however, several limitations to the comb method. First, one has to take into account the procedure itself. The measurements must first be conducted on the stressed sample. Then the comb must be machined out to conduct further measurements for the d_0 determination. In this process, two set of measurements must be carried out, in two separate experiments. This implies a different configuration of the instrument, which can significantly modify the positions of the diffracted peaks. To avoid these inconveniences, it is common to extract a comb piece from the sample under study, so that both the sample and the comb can be studied in the frame of the same round of measurements using the same experimental set up [11]. This operation nevertheless inevitably leads to an alteration of the initial RS state to be studied. Alternatively, one can prepare two welds under identical conditions such that a similar RS state is assumed in both cases: one of the welds would be used to measure the lattice spacing across the weld and the second one to extract a comb to be used as the unstrained reference. Both samples could be measured during the same experiment. Even in this case, it is possible that the precipitation and solid solution state differ from one weld to the other. As has been shown [5], very small variations in Cu content greatly modify the lattice spacing of aluminum and, as mentioned above, it is unlikely that the temperature cycle undergone in both welds is identical. For example, a slight difference in the temperature of the backing plate in contact with the plates between the first and second friction stir welding (FSW) experiments can lead to different cooling cycles. Therefore, the possibility that the same "microstructural" gradient across the weld is obtained in both experiments is minimal. This makes the use of a reference comb extracted from a replica weld risky, even when the welding parameters are ostensibly the same.

Furthermore, several other considerations should be born in mind when using the comb method. Ganguly et al. [2] suggest that a retained macrostress along the direction of the maximum dimension of the teeth is still present in the comb sample and, to use the sample as a stress-free reference sample, the M-RS should first be determined. They propose, in agreement with Ref. [3], to measure near the tooth's end using the $\sin^2\psi$ method. They also found that inter-granular strains were retained along the transverse direction of the comb teeth. Hughes et al. [3] scanned along the teeth of a comb specimen machined out from a 100 mm diameter quenched nickel superalloy cylinder. Measurements were conducted on several teeth for the strain direction parallel to the long tooth dimension and for a perpendicular direction. They found no variation along almost the whole length of a tooth for the perpendicular strain direction, but found significant disparity along the teeth for the parallel direction. It was also found that there was convergence in data for the parallel direction at all tooth ends, and that the value coincided with the value seen for the direction perpendicular to the teeth.

In summary, the comb method may be of interest from a scientific point of view as it gives further understanding of the RS evolution/relaxation upon sample sectioning and/or machining. It is, however, undesirable from an engineering or practical approach, when the RS state of "real" components is sought. As a consequence of the sample sectioning to obtain the comb, the diffraction method becomes unattractive as it turns into a destructive technique. Nobody considers machining out a comb from a crucial component of an expensive device to study its RS state, particularly if it is to be used in service . Alternative procedures which provide reliable d_0 data to determine the RS state in real components such as welds of age-hardenable Al alloys, e.g. 2xxx, are therefore desirable.

In the present study, the RS state resulting from a joint conducted in an AA2024 plate by FSW has been analyzed, making use of neutron diffraction data and equilibrium conditions (stress and bending moment) to obtain d_0. FSW is an excellent method for joining aluminum alloys in many industrial uses [12] and, as in other welding techniques, residual stresses are developed, affecting component performance. Two methods have been used to obtain d_0: first, equilibrium conditions have been imposed on sections parallel to the weld so that a d_0 value corresponding to the microstructure of the base material region can be calculated. Second, the same conditions were imposed on a cross-section transverse to the weld. An analytical solution is not possible here because d_0 values vary across the weld, i.e. a large number of variables is involved. The different d_0 values across the weld were obtained using a genetic algorithm (GA), which is a simplified evolutionary algorithm (EA). Such a method is able to handle problems in which many variables and possible solutions are involved. EAs operate in the field of evolutionary computation, which emerged in the late 1960s, when the possibility of incorporating the natural mechanisms of selection and survival, in accordance with Darwinian evolution, was proposed to solve artificial intelligence problems [13]. An important factor of natural selection is the appearance of small variations, which are both random and directionless in phenotypes. These variations, usually referred to as mutations, can survive the selection process if they prove their value in the environment of the species. The capacity of these search and optimization algorithms has recently been extended to solve very different problems in materials science [14]. For example, a GA has been used together with a finite element code to simulate the FSW process of aluminum alloys 6005A-T6 and 2024-T3 [15].

2. Materials and experimental procedure

The aluminum alloy used in this investigation was AA2024 in the form of a 10 mm thick plate, supplied by Alustock in a T351 condition. In this condition the material is solution treated, quenched, stress relieved by 1.5–2% stretching and naturally aged. In its naturally aged condition, the alloy exhibits high ductility crack resistance and high fracture toughness. For this investigation, two $296 \times 150\ mm^2$ pieces were cut in order to perform a butt weld, of about 250 mm in length.

The weld was made with no additional mechanical/chemical preparation of the plates butt surfaces: just the usual finishing from the mill was made to eliminate defects from the cuts. The welding experiment was conducted at AIMEN (Porriño, Spain), making use of a PDS-4 Intelligent Stir FSW machine from MTS. The welding conditions were: 400 rpm rotational speed and 100 mm min^{-1} advancing speed. The tilt angle was 1.5°. A two-piece fix tool with a threaded pin (7.62 mm long) which included three ground flats was used. The shoulder diameter was slightly more than 20 mm while the pin diameter varied from 7.95 to 6.35 mm. The internal face of the shoulder was not flat, but inclined by 7° to create a conical surface. The shoulder and the pin were made of H13 steel (48 HRc) and MP159 alloy, respectively.

To investigate the RS state across the weld, d_{311} (where the sub-index denotes the crystallographic plane) was extracted from neutron diffraction experiments at three different depths: −2.5, −5 and −7.5 mm from the surface on which the tool pin entered the plate (top surface), denoted hereafter as the front, center and back regions. The region measured covered up to ±85 mm on both sides from the center of the weld, in the transverse direction of the plate. In this way, a complete scan across the weld, including the nugget, the thermomechanically affected zone (TMAZ), the heat-affected zone (HAZ) and the base material (BM) was performed. Since the plate was not sectioned, it is guaranteed that no modification of the M-RS had occurred.

Furthermore, measurements of d_{311} across two different longitudinal sections, located 52 and 120 mm from the center of the weld, on the retreating side, at five locations along the plate and at six depths, namely −1.2, −2.7, −4.2, −5.7, −7.2 and −8.7 mm, were conducted. Fig. 1 is a scheme of the welded plate showing the location across the weld where the M-RS state was studied and the two longitudinal sections on which d_{311} measurements for the three principal directions were carried out. As seen in the figure, both sections correspond to the base material where

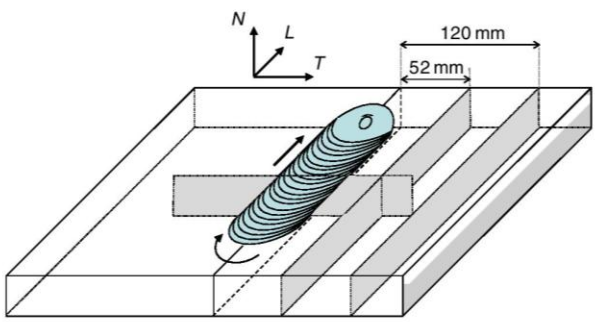

Fig. 1. (a) Scheme of the welded plate showing the location on which the RS state was studied and the two longitudinal sections on which d_{311} measurements were conducted. Directions T, L and N of the reference system coincide with axes X, Y and Z, respectively.

microstructural variations are insignificant. Measurements were made on two different sections to ensure the reproducibility of the results. A Cartesian reference system was adopted whereby the origin is located at the center of the welded plate, on the top surface, and the axes coincide with the longitudinal (rolling, L), transverse (T) and normal (N) directions of the plate (Fig. 1). Due to the limited beam time allocated for this kind of experiment and the typically long time required to obtain reasonable peak signals by neutron diffraction, only measurements for the principal directions were possible. Finally, $\sin^2\Psi$ scans (with Ψ the angle between the scattering vector and the N direction) were conducted at different locations of the weld to ensure that the sample reference system is a principal direction one.

After the neutron diffraction experiment, the plate was used to study the microstructure of the plate and the different zones of the weld. Conventional metallographic procedures were used to examine the microstructure by optical microscopy. Texture measurements were conducted by the Schulz reflection method using laboratory X-rays, as described elsewhere [16].

The d_{311} measurements were performed on the SALSA diffractometer of the ILL (Institute Laue Langevin, Grenoble, France). This instrument is most suitable for measuring RS in real components used in engineering, with a hexapod that can hold, move and rotate large and heavy samples (up to some 1000 kg) with high precision (5 μm) [17]. Fig. 2a shows a general overview of the instrument with the AA2024 welded plate mounted on the holder, and Fig. 2b shows the details of the plate studied. Further details of this diffractometer are provided in Refs. [17,18]. The wavelength of the neutron beam was $\lambda = 1.699$ Å, selected by a double-focusing silicon bent crystal monochromator. The Al(311) was used because it represents the bulk behavior of the material well and is little affected by crystallographic texture [19]. The resulting Bragg angle for the diffracted peak used was around $2\theta = 88°$. The scattering plane, defined by the incident and diffracted beams, lies in the horizontal plane of the instrument. The elastic modulus used for the RS calculations was taken as the average between the tension and compression values (72.4 and 73.8 GPa, respectively), and the Poisson ratio was 0.33 [20].

Due to the limited rotations of the hexapod and the sample shape, the measurements were made in two steps. The plate, placed in a vertical position, was measured under two configurations: first, with the weld in the vertical direction so that a 90° rotation about a vertical axis (perpendicular to the scattering plane) allowed for the measurement in the N and T directions; and second, with the weld located horizontally, in which case the 90° rotation about the same vertical axes makes it possible to determine the d_{311} values for the L and N directions. Two different gauge volumes were used to optimize the beam time allocated for this experiment. For the first case (with the weld in the vertical position), a gauge volume of $2 \times 2 \times 24\ \text{mm}^3$, where the longest direction coincided with the vertical one (rolling direction), was used. It was possible to use such a large gauge volume because the microstructural variation along the weld and corresponding RS state is minimal. For the second case, a smaller gauge volume, of $2 \times 2 \times 2\ \text{mm}^3$, was used to avoid possible microstructural gradients and RS variations inside the gauge volume. The gauge volumes were defined by radial focusing collimators made of Gd-coated Mylar foils.

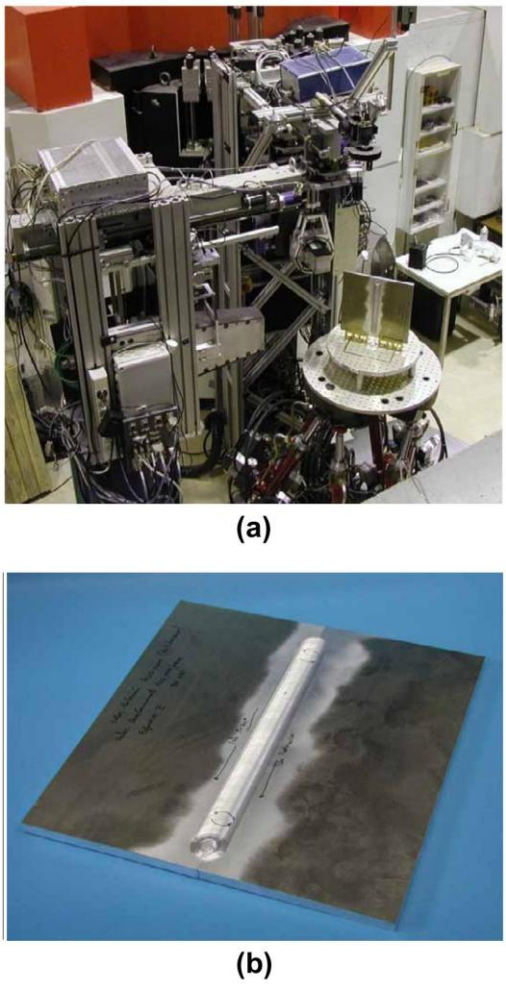

Fig. 2. Experimental set-up of the SALSA instrument, showing (a) the AA2024 welded plate mounted on the hexapod and (b) the welded plate used for RS determination. The welding line is parallel to the rolling direction.

3. Experimental results

3.1. Microstructure

The resulting microstructure of the weld is shown from the transverse metallographic section in Fig. 3. In this figure, the microstructures of the different regions developed

during FSW are clearly discernible: in the nugget, or recrystallized region, an even distribution of small equiaxed grains, of about 5 μm, is seen. The boundary between the nugget and the TMAZ is very sharp on the advancing side, but becomes more diffuse in the retreating one, which reveals the non-symmetrical nature of the FSW process. The microstructure developed on the TMAZs results from the combined effect of temperature and deformation. This leads to elongated grains in the direction of the material flow and an overaged, coarse, precipitation. The microstructure of the HAZ is characterized by the same grain structure as that of the base material: a bimodal distribution, with average grain sizes of 30 and 110 μm. This microstructure results from the cold rolling process undergone by the original plates. Additionally, the temperatures reached in these zones are insufficiently high to cause resolution, but still high enough to cause substantial overaging of the parent-metal precipitates [21,22].

Despite attempts to determine clear pole figures of the BM in the outer and inner regions of the plate being unsuccessful (the grain size was too large for the gauge volume used), differences between the resulting texture in these two regions were evident. The development of a through-thickness texture gradient is commonly observed in rolled aluminum alloys [23]. The presence of a texture gradient suggests that not only does the inter-granular RS vary through the plate thickness, but also that the usual approximation of plane stress conditions for RS calculation is not recommended.

3.2. Neutron diffraction measurements

The results of the d_{311} values obtained across the welded plate for the three components L, N and T, and at the three depths front, center and back, are summarized in the plots of Fig. 4. For any component, the shape of the profile does not vary substantially with plate depth. Also, the profiles of the L component are M-shaped, in agreement with other investigations [7,24–26], with a total variation of $\Delta d_{311} \approx 0.0025$ Å, which corresponds to some 2450 μ-strains. The d_{311} value remains nearly constant in regions away from the weld, but increases rapidly to a maximum as the weld is approached, then decreases to a minimum at the center (nugget) of the weld ($X = 0$). The N and T components, however, are W-shaped, and the total variation in d_{311} is slightly smaller than for the L component: the total

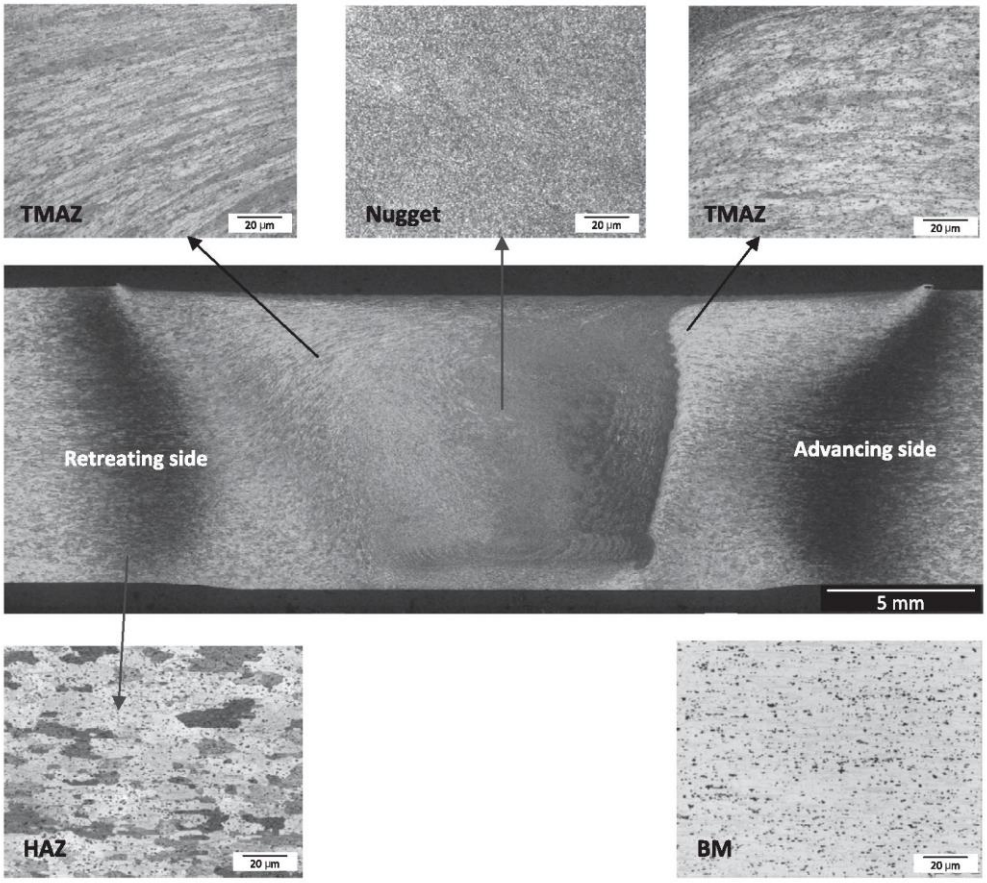

Fig. 3. Transverse metallographic section of the weld showing the microstructure developed in the different regions.

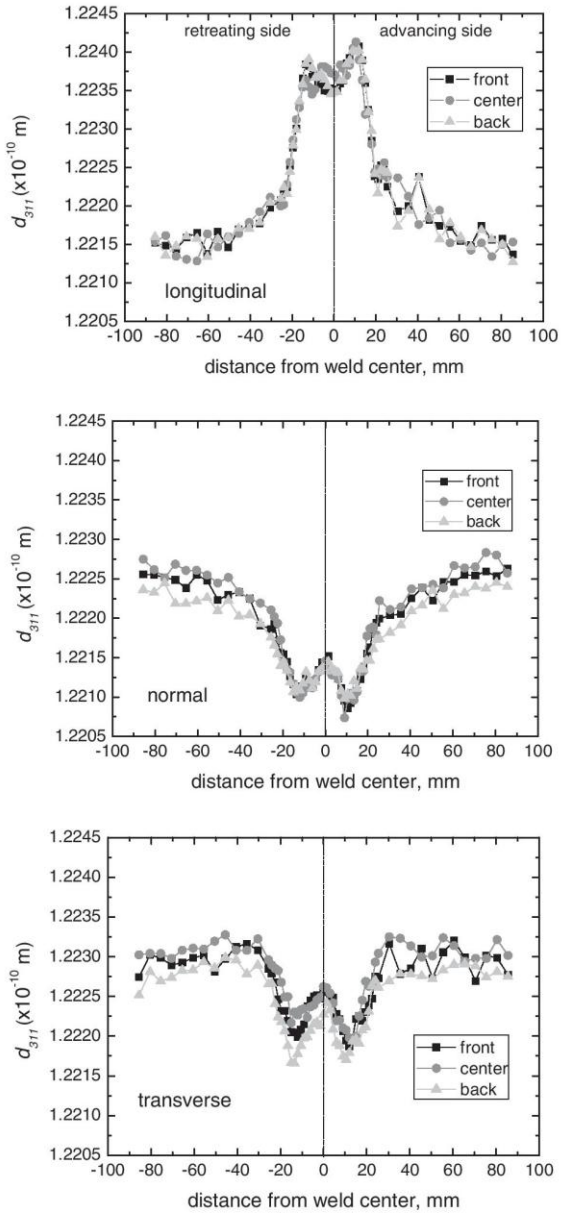

Fig. 4. Inter-planar distance data, d_{311}, as a function of distance from the center of the weld, at three different depths, front, center and back, for three directions, L, N and T. The error is $\sim\pm0.0007$ Å.

variation corresponds to about 1800 and 1500 μ-strains for the N and T components, respectively. These profiles are, again, commonly observed in FSW of aluminum alloys [25]. The significant d_{311} variation across the weld for the N component should be attributed not only to the microstructural changes caused by the FSW process [5], but also to the presence of an RS. This confirms that a biaxial stress approach is not valid here, as suggested above.

The results of the d_{311} values in the longitudinal sections at $X = 52$ mm, for the three directions (L, N and T) and at different plate depths, are summarized in the plot of Fig. 5. The close values obtained for the different depths suggest that the through-thickness gradient is not relevant. It can also be seen that the d_{311} variation along L is very smooth. No significant differences between the profiles obtained at $X = 52$ mm and $X = 120$ mm (not shown in this figure) were noted.

The $\sin^2\Psi$ scans led to reasonable linear 2θ dependences, which confirm that the coordinate reference system selected – that of the rolled plate – is a system of principal axes. For the sake of simplicity, plots of these data are not presented.

4. The genetic algorithm

A GA works with a population of individuals, whereby each individual represents a potential solution to a problem. The basic idea is to evolve the initial randomly generated population (or representations of solutions), forcing it into a repeated process of selection, crossover and mutation. Each cycle or process gives rise to a new generation. The objective is to find the individual that, over a certain number of generations, best approaches the optimal solution. As follows, a multi-objective genetic algorithm has been implemented to obtain d_0 profiles across the weld which minimizes both the sum of the longitudinal stresses and the bending moments in the transverse section, according to a protocol described in this section.

Using the smallest distance between neutron diffraction measurement points, the whole transverse section of the welded plate was divided into 181 zones. The actual measurements made in the regions away from the weld were more spread out than in regions close to the nugget, and the very extreme regions were not scanned since the time available for the experiment at SALSA had to be optimized. Since these regions were not affected by the FSW process, it was assumed that their d_{311} values were similar (the average of the measurements made in the base material). In principle, the procedure was as follows: each zone was specified by nine parameters, corresponding to the three depths (front, center and back) and the three components of the stress (L, N and T). Therefore, a chromosome (string of numbers representing the solution) composed of $181 \times 9 = 1629$ genes (positions) was used. The first nine genes represent the parameters for the first zone, i.e. $d_{0L\mathrm{Front}}$, $d_{0T\mathrm{Front}}$, $d_{0N\mathrm{Front}}$, $d_{0L\mathrm{Center}}$, $d_{0T\mathrm{Center}}$, $d_{0N\mathrm{Center}}$, $d_{0L\mathrm{Back}}$, $d_{0T\mathrm{Back}}$ and $d_{0N\mathrm{Back}}$), the next nine the parameters for the second one and so on. For the purpose of the present research, however, it was assumed that no anisotropic effect on the d_0 value exists, i.e. the same d_0 value is obtained irrespectively of the sample direction. This is in agreement with the results of other investigations on age-hardenable 2xxx (and also 7xxx) aluminum alloys [2,6,27]. Therefore, the final chromosome was composed of 543 genes. A randomly generated set of solutions, or a set of strings of numbers, was used as the starting point. Finally, a population size of 8000 individuals, 2000 generations, 0.1% mutation probability and 80% crossover probability was used in the present analysis.

5. Discussion

As mentioned in the introduction section, the comb method does not provide a reliable reference for the case of age-hardenable aluminum alloys. Besides the argued reasons, it is important to emphasize the additional effect of the microscopic (inter-granular) residual stress state resulting from the cold rolling process. It has been argued that, despite the machining operation aimed at relieving the stresses in the comb samples, relaxation of the microscopic inter-granular stress (m-RS) is not possible [2,3,27]. This is because the comb teeth are typically significantly larger than the grain size. The presence of a m-RS is revealed as different lattice spacing values in the L, N and T directions: a circumstance that is an obstacle for the determination of a reliable d_0 value from a comb sample for the subsequent RS measurements. Procedures based on equilibrium conditions of macrostresses [28] were therefore used to calculate appropriate d_0 values for RS determination.

On the basis that the AA2024 alloy can be considered a single-phase material, like all 2xxx alloys, the contribution of second-phase particles and the required stress equilibrium with them are ignored in the analysis. Therefore, it is assumed that the measurements conducted correspond to actual macroscopic stresses, as assumed in other works [4–6,29].

The use of equilibrium conditions is a very rigorous procedure, which furthermore avoids the tedious operations and approximations involved in the comb method. It is surprising, however, that it has not been exploited more widely in the past [30,31]. The condition of equilibrium implies that, on any section of the component, S, the total force perpendicular to it and the bending moment of the in-section forces with respect to the neutral plane, N, should be zero. For the present case, a plate in which one of the dimensions, Z, is significantly smaller than the other two dimensions, X and Y (Fig. 1), bending is possible only about an in-plane axis. In these circumstances, the equations describing this equilibrium in a general form are integrals [28], which can be substituted by summations since only discrete measurements were taken in the experiment. Therefore, the equilibrium is given by

$$\sum \sigma_{\perp} \Delta S|_S = 0 \tag{3}$$

and for the bending moment, M,

$$\sum M|_S = \sum \sigma_T \Delta S Z_n|_S = 0 \tag{4}$$

where Z_n refers to the distance from the neutral plane of the plate.

Local equilibrium within the plate should also be satisfied. To apply this condition, however, a description of the stress variation along the three spatial directions is needed. Since measurements on specific sections of the plate were conducted, stress variations in only two directions are possible. Therefore the above condition cannot be applied.

As mentioned above, two different approaches are presented here. First, taking advantage of the measurements conducted on the longitudinal sections (retreating side), at $X = 52$ mm and $X = 120$ mm (Fig. 5), balance conditions are imposed to seek a constant d_0 corresponding to the BM. Secondly, equilibrium is applied to the transverse section, across the weld, where a variation in the unstressed lattice parameter is expected due to the aging nature of the AA2024 alloy.

5.1. Equilibrium on longitudinal sections of the plate

In this case, equilibrium, in accordance with Eq. (3), should be found for σ_T. Using Eqs. (1) and (2), this must be

$$\sum \frac{E}{(1+\nu)(1-2\nu)} \left[(1-\nu)\frac{d_T - d_0}{d_0} + \nu\left(\frac{d_N - d_0}{d_0} + \frac{d_L - d_0}{d_0}\right)\right] \Delta S\Big|_{X=52,120} = 0 \tag{5}$$

Since a unique value of d_0 is sought, an analytical solution of Eq. (5) is possible. Solving for the two sections, this is found to be $d_0 = 1.22228$ Å at $X = 52$ mm and $d_0 = 1.22232$ Å at $X = 120$ mm. The small difference between these values accounts for their validity. Their soundness is further supported by imposing the equilibrium of the bending moment, as dictated by Eq. (4). For this case, Eq. (4), as applied to the longitudinal sections, turns into

$$\sum \frac{E}{(1+\nu)(1-2\nu)} \left[(1-\nu)\frac{d_L - d_0}{d_0} + \nu\left(\frac{d_N - d_0}{d_0} + \frac{d_T - d_0}{d_0}\right)\right] \Delta S Z_n\Big|_{X=52,120} = 0 \tag{6}$$

Using the average d_0 value resulting from those obtained at $X = 52$ mm and $X = 120$ mm of 1.22230 Å, it is found that the total bending moment, M, for these two sections is -110.8 Nm at $X = 52$ mm and -22.3 Nm at $X = 120$ mm. The values are not null, but are reasonably low considering that a discrete summation of data, obtained from the experimental results, has been made, rather than the integral of a continuous description of the stress. It should be borne in mind that it is not analytically possible to find a unique solution which satisfies both Eqs. (5) and (6) simultaneously. It is also worth mentioning that this unstressed lattice parameter is not influenced by the presence of a microscopic inter-granular stress, usually revealed in comb samples [2,3,27]. This microstress, with a much smaller "wavelength" than that of the macroscopic stress, overlaps the latter, but does not modify its profile through the sample and must be self-equilibrating.

The average d_0, together with the d_{311} data of Fig. 4 and Eqs. (1) and (2), were used as a first approximation to obtain the RS profiles across the weld. The results obtained are shown in the plots of Fig. 6, where the RS profiles for the L, N and T components at the three depths are presented. As can be seen, profiles similar to those obtained

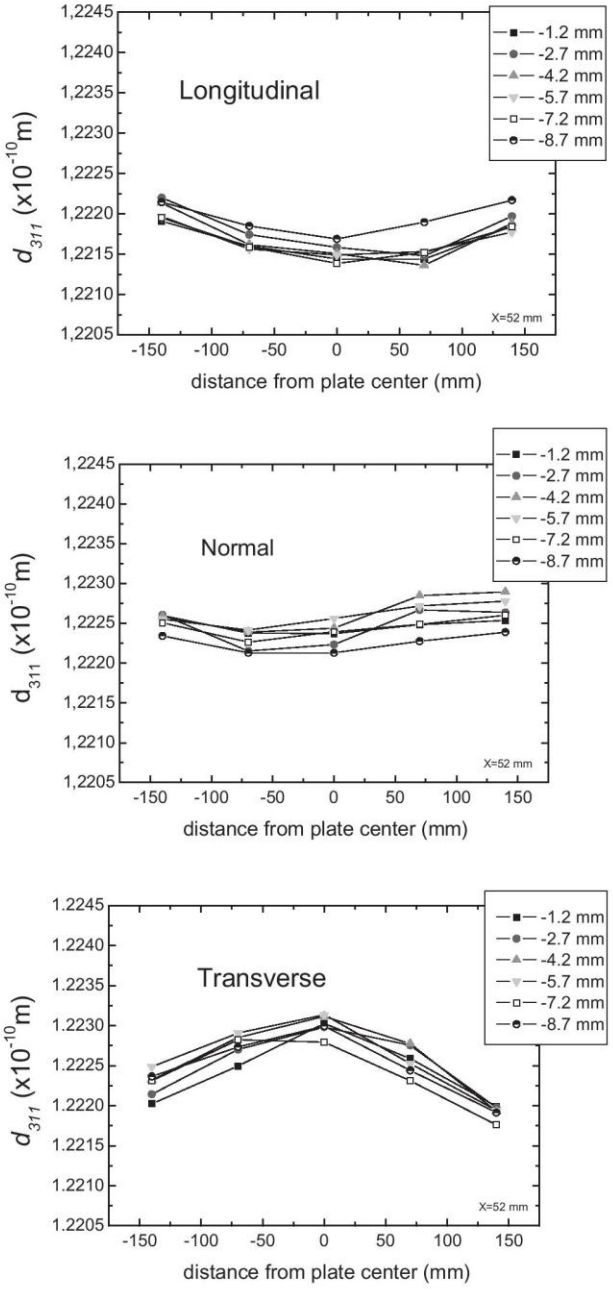

Fig. 5. Inter-planar distance data, d_{311}, for the L, N and T directions in the section at $X = 52$ mm, parallel to the welding line and at different plate depths (error is of about $\sim\pm 0.0007$ Å).

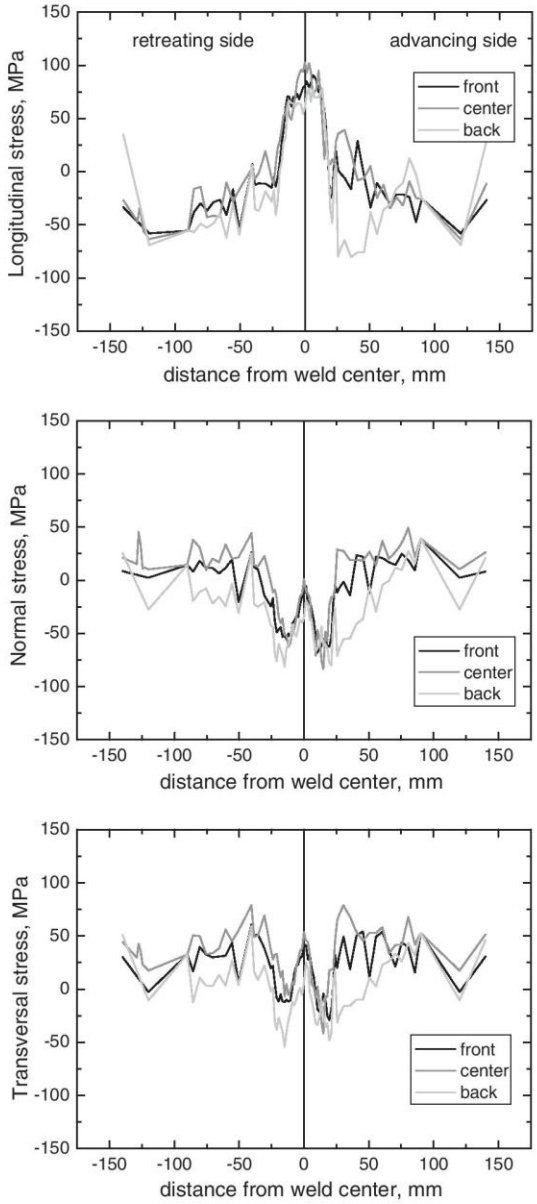

Fig. 6. Residual stress profiles of the L, N and T components across the weld calculated with a constant d_0 value obtained from the equilibrium conditions in the longitudinal sections of the plate at $X = 52$ mm and $X = 120$ mm. The maximum error is $\sim\pm 10$ MPa).

in other research works are obtained [6,18,29]: the stress in the L direction shows the largest absolute value (positive) and is similar for the three depths.

With this value, it is possible to determine if the L component of the stress for the section perpendicular to the weld also satisfies the balance condition. The total stress calculated is above 10,300 MPa and the bending moment

d_0 across the weld, nugget, TMAZ and HAZ regions is not taken into account in this calculation.

5.2. Equilibrium on a transverse section of the plate using a genetic algorithm

Despite the above method producing a reasonable RS profile (Fig. 6), equilibrium across the weld is not reached. For a rigorous description of the RS state, it is therefore necessary to take into account that d_0 is not constant

can be considered valid. In contrast, the nugget, the TMAZ and the HAZ undergo microstructural changes produced by the welding process which affect the unstrained lattice spacing considerably. The use of the equilibrium condition on a section with a variable d_0 implies a great number of unknown quantities, which cannot be calculated by an analytical method such as the one used in the previous section.

For this case, the implementation of EAs can be of great help due to their capacity to handle problems in which a large number of unknown quantities are to be determined. In the present study, we pursue a string of d_0 values which vary in the welded region as a consequence of the severe thermomechanical process introduced by the FSW. Here, it is important to note the restrictions imposed on the possible d_0 values in the different weld regions: they should lie between the maximum and minimum d values given by the plots in Fig. 4. This restriction is correct under two assumptions: (i) the possible hydrostatic stress component is negligible; and (ii) the inter-granular stress is also insignificant. The first assumption is supported in principle by the fact that welds do not lead to significant hydrostatic stress, as revealed by the RS profiles obtained in previous investigations [11,29,32]; the second is supported by the results obtained from comb measurements in published investigations [2,3,27].

To obtain the best set of d_0 values for each one of the 181 zones after the iterative procedure of the GA, Eqs. (3) and (4) should be employed using the different chromosomes and the experimental data of Fig. 4 (the searching process was simplified by using only eight intervals in the welded region and the constant d_0 value calculated in Section 5.1 for the BM). The iterative procedure was repeated 30 times to ensure the reproducibility of the final result. The GA was implemented and run in Java, using an Intel core i-5, 4 GB RAM memory running under Windows 7. The average total execution time for a population of 1000 individuals and 500 generations over 30 runs was about 100 s and the average evaluation time of one individual was nearly 0.2 ms. A progressive decay of the total stress as a function of the number of iterations was obtained, which supports the validity and uniqueness of the result. It is worth mentioning that once full convergence was reached no further change in the final result (string of d_0 values) was required by the GA. The average of the 30 solutions resulting from the GA is summarized in Fig. 7, where the d_0 profile across the weld is shown. The highest values are obtained in the BM, whereas in the HAZ, TMAZ and nugget a clear drop is evident. In summary, a W-type profile in the welded region is obtained, where the minimum is reached near the TMAZ zones and the maximum occurs in the nugget region.

The d_0 values provided by the GA (Fig. 7) are consistent with the precipitation state in the BM, HAZ, TMAZ and nugget, in agreement with other works [33]. Considering that the plates were in a T351 state before welding, the lattice spacing must be increased by the coherent precipitates (S′). The temperature rise in the HAZ and TMAZ zones modifies the initial precipitation state to an overaged one (mainly incoherent coarse S precipitates). In these conditions, the lattice spacing is "relaxed" to its lowest value. Finally, the FSW-induced recrystallization process modifies the microstructure, leading to grain boundary S precipitates and a fine dispersion of coherent precipitates inside grains. This microstructure results in intermediate lattice spacing. Therefore the d_0 profile across the weld is expected to have a W shape, which somewhat agrees with the result shown in Fig. 7. It is also seen that the d_0 profiles across the plate (front, center and back) differ from each other, which is an indication that the friction occurring mainly on the top surface induces a through-thickness gradient of the thermomechanical process.

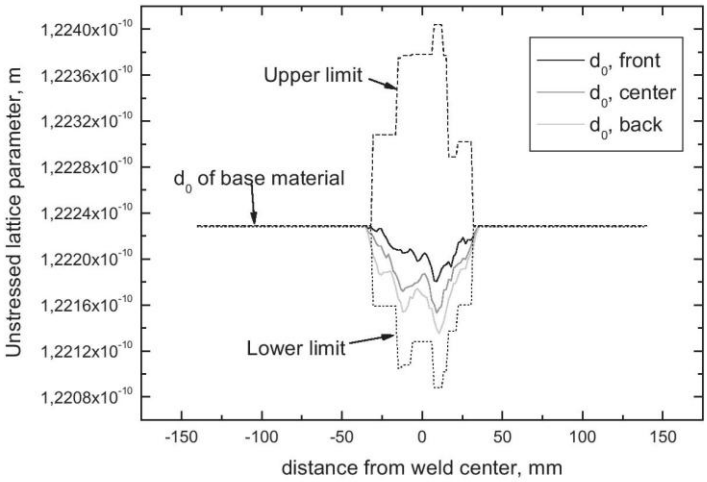

Fig. 7. Profiles of the unstressed d_0 values (front, center, and back regions) calculated from the equilibrium conditions imposed to the transverse section of the weld using the GA. The upper and lower d_{311} values used by the GA are included.

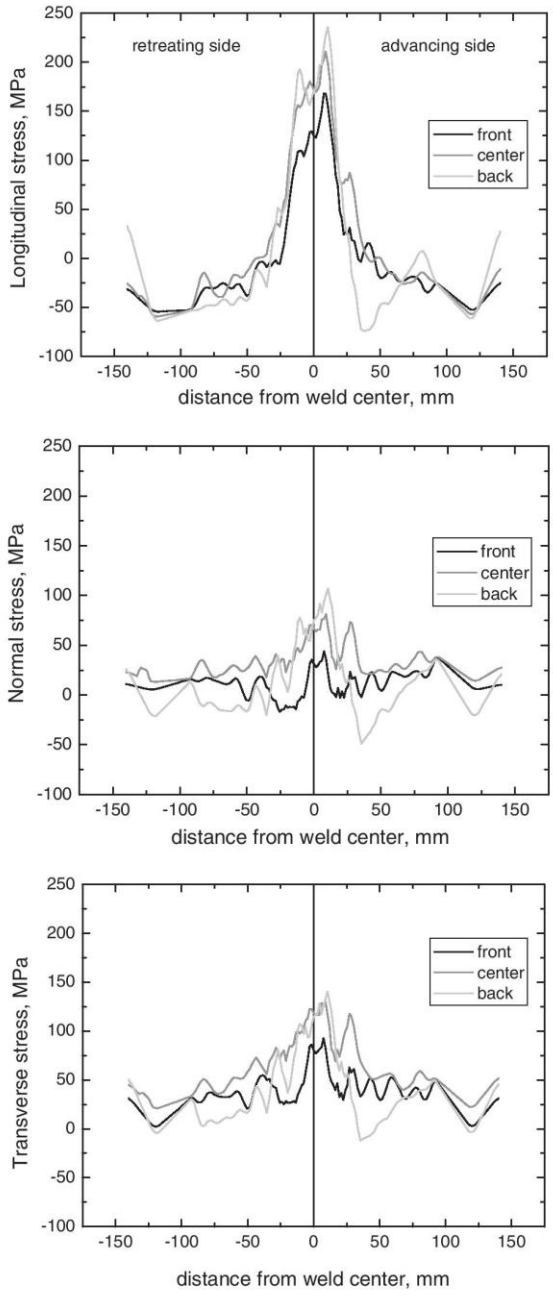

Fig. 8. Residual stress profiles across the weld calculated using the unstressed d_0 values resulting from the GA (data of Fig. 7).

The final RS profiles calculated using the d_0 values given in Fig. 7 are shown in Fig. 8. The profiles resemble an M shape for the longitudinal component and a W shape for the transverse and normal components, as reported elsewhere [4,25,34–36]. The highest tensional RS was found in the longitudinal component, in agreement with previous studies [10,26,35], and reached about 74% of the yield strength of the BM, which exceeds the 20–70% range reported in Ref. [25]. The asymmetry of the FSW process is also reflected in the RS profile, the maximum being located in the TMAZ of the advancing side. Depending on the material and the welding parameters, the location of the maximum RS has been reported as being in the HAZ [4,25,26] or the TMAZ [10,34,35]. The profiles corresponding to the back region (Fig. 8) showed the highest RS levels, which decay progressively, first in the center and then in the front region. The latter region shows the smoothest RS profile. This trend is more evident in the T and N components, and is consistent with the idea that the macroscopic RS generated by FSW is greatest in the back region, where the temperature reached is not as high as in the front region, where partial RS relaxation may have occurred.

When comparing the RS profiles of Figs. 6 and 8, it can be seen that the maximum stress is higher in the second case. In other words, the RS obtained using a constant d_0 value underestimates the actual RS state in the plate, as obtained from the GA. Not taking this difference into account in engineering design could lead to dramatic consequences during the weld's service.

6. Summary

In this research, an analysis of the d_0 value needed to calculate the M-RS across a weld conducted by FSW on AA2024 plates has been made. The comb method usually employed to obtain an unstressed reference is criticized for several reasons: the first disadvantage of this method lies in the fact that the sample/component on which the RS is of interest must be sectioned. On the other hand, if the comb is machined from a "twin" weld, it is likely that minimal and uncontrolled variations in the precipitation state of age-hardenable alloys (in particular, alloys of the 2xxx series, where small variations of Cu in solid solution lead to large changes in the lattice spacing) will distort the real unstressed reference. Finally, the possible presence of inter-granular stresses resulting from the manufacture process (e.g. rolling) not relieved in the comb can further complicate the determination of a reliable d_0 value. As an alternative to the comb method, two procedures based on equilibrium principles have been used to calculate a suitable unstressed reference. The first one makes use of a constant d_0 value calculated from the equilibrium conditions applied to longitudinal sections, parallel to the weld. Here, an analytical solution can be derived, given that a single d_0 value – that corresponding to the base material – is the unknown variable. The unstressed lattice parameter obtained is not affected by the inter-granular stress since it must self-equilibrate: it overlaps the profile of the M-RS. Since a constant d_0 is used, the RS obtained across the weld (the L component) and the bending moment are not equilibrated, despite the profile being reasonably similar to those obtained in previous studies. The second procedure uses a genetic algorithm to find the equilibrium across the weld (transverse section). In this case, application of the analytical method used in the longitudinal section is not possible as d_0 varies through the weld

due to the presence of different microstructural regions which have undergone different thermomechanical cycles. The only requirement imposed on the GA is to minimize the summation of stresses perpendicular to the section under study and the bending moment about an axis parallel to the weld. With this method, d_0 values for the different regions, namely, the nugget, the TMAZ and the HAZ, are selected from values which range within the interval given by the maximum and minimum values measured in each region. With the resulting d_0 profile, a final RS state across the weld is obtained, where the d_0 oscillations due to the microstructural variations in the weld are taken into account. The RS obtained (the L component) with the constant d_0 value underestimates the calculated RS resulting from the GA.

Acknowledgments

Support from Projects MAT-05-0527 and MAT-09-09545 from MICINN, and PIE 200960I076 from C.S.I.C., Spain, is gratefully acknowledged. Financial help from the ILL to conduct the neutron diffraction measurements on SALSA, experiments 1-02-6 and 1-02-10, is recognized. Support from Spanish Government Grants TIN 2008-00508 and MEC CONSOLIDER CSD00C-07-20811 and from Spanish MINECO (projects MAT2011-23455 and MAT2011-25991) is also acknowledged by J.I.H. and I.P.O., respectively.

References

[1] Altenkirch J, Peel MJ, Steuwer A, Withers PJ. J Strain Anal Eng Des 2011;46(46):651–62.
[2] Ganguly S, Edwards L, Fitzpatrick ME. Mater Sci Eng A 2011;528:1226–32.
[3] Hughes DJ, James MN, Hattingh DG, Webster PJ. J Neutron Res 2003;11(4):289–93.
[4] Prime MB, Gnäupel-Herold T, Baumann JA, Lederich RJ, Bowden DM, Sebring RJ. Acta Mater 2006;54(15):4013–21.
[5] Steuwer A, Dumont M, Peel M, Preuss M, Withers JP. Acta Mater 2007;55:4111–20.
[6] Altenkirch J, Steuwer A, Peel M, Richards DG, Withers PJ. Mater Sci Eng A 2008;488(16–2):4.
[7] Lombard H, Hattingh DG, Steuwer A, James MN. Mater Sci Eng A 2009;501:119–24.
[8] Florea RS, Hubbard CR, Solanki KN, Bammann DJ, Whittington WR, Marin EB. J Mater Proc Technol 2012;212:2358–70.
[9] Pratihar S, Stelmukh V, Hutchings MT, Fitzpatrick ME, Stuhr U, Edwards L. Mater Sci Eng A 2006;437:46–53.
[10] Woo W, Em V, Hubbard CR, Lee H, Park KS. Mater Sci Eng A 2011;528:8021–7.
[11] Sutton MA, Reynolds AP, Wang D-Q, Hubbard CR. J Eng Mater Technol 2002;124:215–21.
[12] Mishra RS, Ma ZY. Mater Sci Eng R 2005;50:1–78.
[13] Holland JH. JACM 1962;9:279–314.
[14] Li B, Lin J, Yao X. Int J Mech Sci 2002;44:987–1002.
[15] De Vuyst T, D' Alvise L, Simar A, de Meester B, Pierret S. Weld World 2005;49:47–55.
[16] Pérez-Prado MT, Cristina MC, Ruano OA, González-Doncel G. Mater Sci Eng A 1998;244:216–23.
[17] Bruno G, Pirling T, Withers PJ, Hutta W, Rowe S. J Neutron Res 2003;11:235–9.
[18] James MN, Webster PJ, Hughes DJ, Chen Z, Ratel N, Ting SP, et al. Mater Sci Eng A 2006;427:16–26.
[19] Bruno G, Fernández R, González-Doncel G. Mater Sci Eng A 2004;382:188–97.
[20] ASMHandbook, vol. 2. Properties and Selection; Nonferrous Alloys and Special-Purpose Materials, 10th ed. Materials Park, OH: ASM International; 1990.
[21] Bussu G, Irving PE. Int J Fatigue 2003;25:77–88.
[22] Fratini L, Pasta S, Reynolds AP. Int J Fatigue 2009;31:495–500.
[23] Peréz-Prado MT, Cristina MC, Torralba M, Ruano OA, González-Doncel G. Scripta Mater 1996;36:1455–60.
[24] Peel M, Steuwer A, Preuss M, Withers PJ. Acta Mater 2003;51:4791–801.
[25] Woo W, Feng Z, Wang XL, David SA. Sci Technol Weld Join 2011;16:23–32.
[26] Dalle Donne C, Lima E, Wegener J, Pyzalla A, Buslaps T. In: Proceedings of the 3rd international symposium on friction stir welding. Kobe; September 2001.
[27] Ganguly S, Fitzpatrick ME, Edwards L. Metall Mater Trans A 2006;37:411–20.
[28] Noyan IC, Cohen JB. Residual stress; measurements by diffraction and interpretation. New York: Springer Verlag; 1987.
[29] Linton VM, Ripley MI. Acta Mater 2008;56:4319–27.
[30] Withers PJ, Preuss M, Steuwer A, Pang WL. J Appl Crystallogr 2007;40:891–904.
[31] Ferreira-Barragáns S, Fernández R, Fernández-Castrillo P, González-Doncel G. J Alloy Compd 2012;523:94–101.
[32] Reynolds AP, Wei Tang, Gnaupel-Herold T, Prask H. Scripta Mater 2003;48:1289–94.
[33] Genevois C, Deschamps A, Denquin A, Doisneau-cottignies B. Acta Mater 2005;53:2447–58.
[34] Masubuchi K. Analysis of welded structures: residual stresses, distortion, and their consequences. New York: Pergamon Press; 1980.
[35] Hatamleh O, Rivero IV, Maredia A. Metall Mater Trans A 2008;39:2867–74.
[36] Buffa G, Fratini L, Pasta S. Invited paper at ICRS-8 8th international conference on residual stresses. Denver Marriott Tech Center Hotel, Denver, CO; 2008.

4. DISCUSIÓN INTEGRADORA

Esta discusión se divide en dos secciones: en la primera, se analiza el conjunto de conocimientos actuales de la técnica de FSW junto con las estrategias para la eliminación de defectos habitualmente utilizadas en aleaciones de aluminio. A partir de este análisis, se cuestiona la aplicabilidad de dichos conocimientos a los materiales compuestos de este trabajo. Además, se analizan las diferencias entre las solicitaciones que sufre la herramienta en ambos casos. En la segunda sección, se presentan algunas consideraciones específicas de la soldadura por FSW de materiales compuestos.

4.1. Análisis del conocimiento actual sobre la técnica de FSW en aleaciones de aluminio. Aplicabilidad a compuestos con alto contenido de refuerzo

Como se explicó en la introducción, la utilización más extensa de la soldadura por FSW se concentra en las aleaciones de aluminio [32]. Para las que existe el mayor número de publicaciones científicas, patentes y avances tecnológicos [18]. Este conocimiento se utiliza como punto de partida para encontrar las condiciones adecuadas que permitan unir satisfactoriamente materiales compuestos con alta carga de refuerzo. Se puede considerar que las aleaciones de aluminio constituyen una versión simplificada, sin partículas de refuerzo, del material compuesto. Sin embargo, la puesta en práctica de todo este conocimiento no es inmediata ni directa.

Como se detalló en la sección 1.1.1, existen diferencias importantes en las propiedades de los materiales compuestos y las aleaciones de aluminio. En concreto, las diferencias en ductilidad y conductividad térmica, tendrán una influencia importante en el proceso de soldadura por FSW de MMCs puesto que se trata de un proceso de deformación plástica severa a alta temperatura. A modo de comparación, en la Figura 22 se muestran los resultados de ensayos de tracción uniaxial a temperatura ambiente del material compuesto 25%SiC/2124Al y la aleación 2024Al, ambos en estado T6. Se puede observar que el compuesto alcanza una mayor resistencia que la aleación monolítica, al tiempo que su ductilidad es casi un 50% inferior.

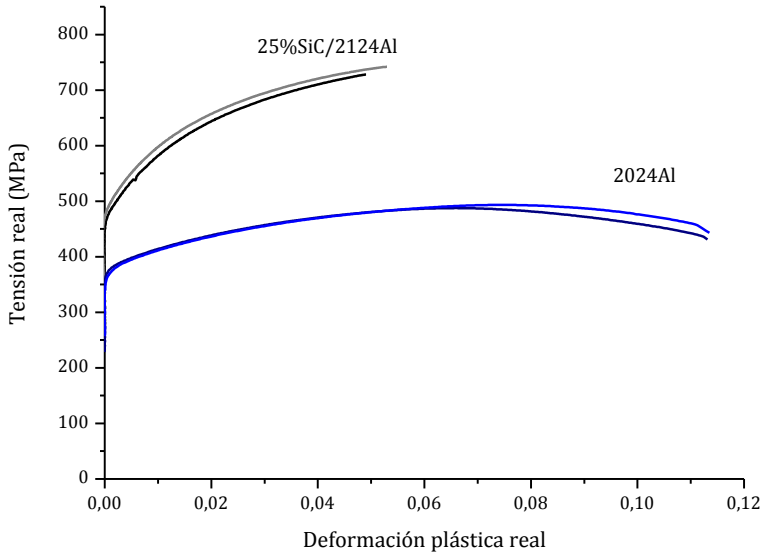

Figura 22. Curvas Tensión real vs. Deformación plástica real para material compuesto y aleación en estado T6.

Los resultados de los ensayos de tracción descritos sirven para dar una idea de la diferencia de comportamiento mecánico existente entre el compuesto y su correspondiente aleación de aluminio. Sin embargo, no representan la respuesta de estos materiales frente a las solicitaciones que impone el proceso de FSW. Para evaluar la aplicabilidad del proceso de FSW, es más adecuado estudiar el comportamiento del material en el rango de condiciones del proceso: alta temperatura y alta velocidad de deformación. En general, es extremadamente difícil establecer las condiciones bajo las que se deforma el material durante el proceso de FSW, ya que éstas dependen del campo de temperaturas y del flujo de material, que a su vez están condicionados por muchas variables del proceso. Entre ellas se encuentran la velocidad de rotación y avance de la herramienta, el esfuerzo de forja, la forma de la herramienta y material del que está fabricada, factores geométricos (espesor del material a soldar, configuración de la soldadura), material del soporte o "backing plate" y condiciones del ambiente. Probablemente sea el gran número de variables que intervienen en el proceso, la razón por la que en la literatura no se ha llegado a un consenso sobre las condiciones de velocidad de deformación y esfuerzo que sufre el material durante el mismo. En general se acepta que la temperatura alcanzada se encuentra en el intervalo correspondiente a los procesos de trabajado en caliente (hasta $0.8T_m$, donde T_m es la temperatura de fusión del material). Sin embargo, existe todavía mucha discrepancia sobre la velocidad de deformación en unas condiciones específicas de soldadura por FSW y para un material dado. En la literatura, se han publicado valores tan dispares como 10 y 1000 s^{-1} [42].

Los ensayos de torsión permiten evaluar la respuesta del material a temperaturas similares a las encontradas en el proceso de FSW y a altas velocidades de deformación. Por ello se consideran ensayos muy adecuados para caracterizar el comportamiento del material en las condiciones del proceso de FSW, a pesar de que imponen un estado de tensiones diferente del que sufre el material durante esta soldadura. En torsión pura (ensayo de torsión) la componente hidrostática de la tensión puede considerarse nula; sólo se imponen tensiones de cizalla sobre la muestra. En cambio, en el proceso de FSW tanto los esfuerzos de forja que impone el hombro de la herramienta, como las restricciones que aplica el material circundante (firmemente sujeto y frío), hacen que la componente hidrostática de la tensión no pueda considerarse nula. Otro aspecto a considerar en el análisis de los resultados es que en los ensayos de torsión no se alcanzan velocidades de deformación tan altas como las reportadas para el proceso de FSW.

En la Figura 23 se comparan resultados de ensayos de torsión en la aleación 2024Al recogidos de la literatura [125] y ensayos que hemos realizado en el compuesto 25%SiC/2124Al. En estos últimos se seleccionó un rango de temperaturas parecido al del proceso de FSW y dos velocidades de deformación, entre ellas la máxima permitida por el equipo disponible ($5s^{-1}$).

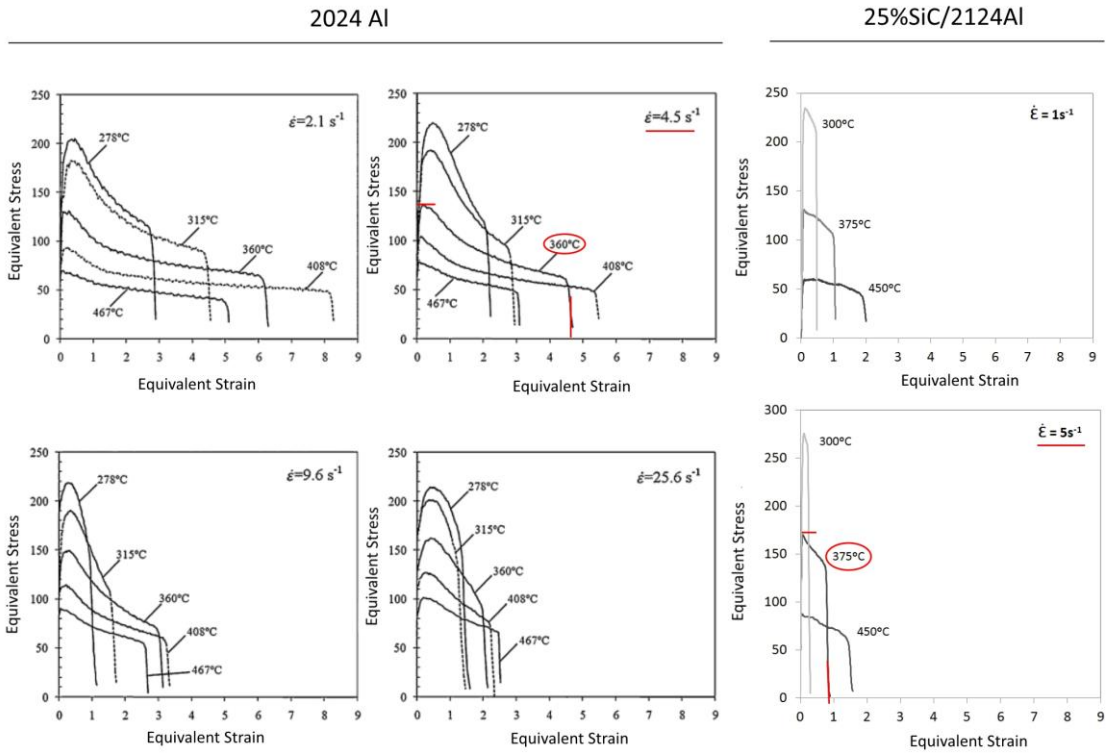

Figura 23. Resultados de ensayos de torsión para la aleación 2024Al [125] y el material compuesto 25%SiC/2124Al.

El material compuesto presenta mayor resistencia y menor ductilidad que la aleación en las condiciones estudiadas. Para condiciones similares de temperatura y velocidad de deformación, resultados marcados en rojo en la Figura 23, la tensión equivalente [126] máxima en el compuesto es un 25% mayor que en la aleación y la ductilidad 5 veces menor. Este resultado debe ser analizado teniendo en cuenta que el proceso de FSW está basado en un mecanismo de deformación severa, siendo necesario por tanto un alto grado de ductilidad en el material a soldar. Desde este punto de vista, en el caso de los compuestos estudiados, parece adecuado incrementar todo lo posible la temperatura de proceso (sin llegar a fundir) y disminuir la velocidad de deformación para acercarse a los niveles de ductilidad del aluminio.

Las propiedades térmicas del material compuesto 25%SiC/2124Al y la aleación 2024Al se muestran en la Tabla 4 [4, 127].

	2024Al	25%SiC/2124Al
Thermal conductivity [W/m°C]	121	150
Thermal expansion coefficient [ppm/°C]	24.7	15.5
Heat capacity [J/g °C]	0.875	0.836

Tabla 4. Propiedades térmicas.

En los aspectos relacionados con las características térmicas de los materiales, existen dos diferencias principales entre el material compuesto y la aleación que forma su matriz:

- El coeficiente de expansión térmica es menor en el compuesto por la adición de partículas con un coeficiente de expansión térmica 6 veces menor al de la aleación. Su efecto se discutirá más adelante.
- La conductividad térmica es más alta en el compuesto. Ello provoca que el calor generado por fricción y deformación se distribuya más rápidamente al material circundante. Esta característica es beneficiosa para algunos aspectos del proceso. Por ejemplo, el tiempo a la máxima temperatura de soldeo es menor, con lo que el estado de precipitación en aleaciones termotratables se modifica en menor medida. Al mismo tiempo, es perjudicial porque disminuye la eficiencia energética del proceso.

Es necesario tener en cuenta estas diferencias a la hora de aplicar al caso de los MMC el conocimiento que se utiliza para soldar mediante el proceso de FSW aleaciones de aluminio.

A continuación, se discutirá porqué en algunos aspectos del proceso de FSW el conocimiento referente a las aleaciones de aluminio no puede ser aplicado a los compuestos con alta carga de refuerzo.

4.1.1. Elección de herramientas

Como se explicó en la introducción, las herramientas son un componente clave en las soldaduras por FSW. Éstas determinan el flujo del material y condicionan los parámetros de soldadura. Desde los comienzos de la técnica se dedicaron grandes esfuerzos al diseño de las herramientas [128]. Hoy en día se ha llegado al consenso de que aquellas herramientas con formas más complejas consiguen un flujo de material que favorece su mezcla, lo que permite ampliar la ventana de parámetros en la que se obtienen buenas soldaduras [79, 80].

Las herramientas de formas complejas incluyen roscas, canaletas curvas y facetas en el punzón y muescas de distintas formas en el hombro. En la Figura 24 se muestran algunos ejemplos de este tipo de herramientas.

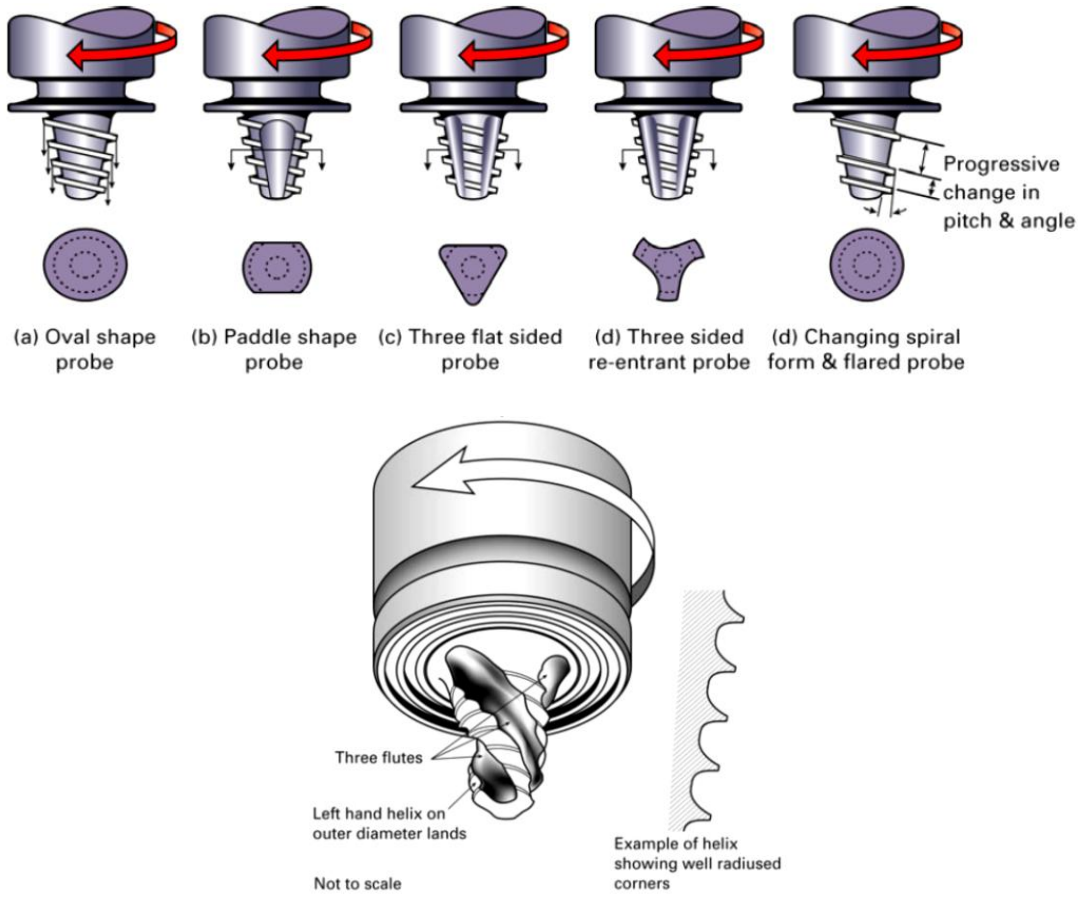

Figura 24. Herramientas de formas complejas. Variantes de los punzones tipo Whorl™ (arriba). Punzón MX-Triflute™ (abajo) [129].

A su vez, en lo que a materiales se refiere, las herramientas fabricadas en acero y tratadas térmicamente son las utilizadas con mayor frecuencia por su facilidad de mecanizado y su bajo coste. Sin embargo, para las condiciones más exigentes se recomiendan herramientas de superaleaciones, como la MP159, por su mayor tenacidad y resistencia a altas temperaturas.

En la mayoría de los trabajos publicados sobre FSW en compuestos de matriz metálica [114, 117, 119-124, 130-136] se utilizan herramientas roscadas de acero y chapas de material compuesto de espesores medios, como se muestra en la revisión de la Tabla 5. El material utilizado en este trabajo es de mayor espesor y/o mayor contenido de refuerzo que los encontrados en los antecedentes publicados.

Material	Espesor (mm)	Material del punzón	Forma del punzón	Referencia
6061Al/20%Al_2O_3	5 y 6	Acero para herramientas termotratado (62 HRC)	cilíndrico roscado	[120, 121]
Al 359 + 20% SiC	4	Acero para herramientas termotratado (62 HRC)	cilíndrico roscado	[117]
Al 359 + 20% SiC	4	Acero para herramientas termotratado	cilíndrico roscado	[114]
Al + 10%wt. TiB_2	6	Acero de alto C y alto Cr (60-62 HRC)	cílindrico cuadrado, cónico cuadrado, cilíndrico hexagonal, cónico hexagonal, cilíndrico octogonal, cónico octogonal	[130]
Al + 15%wt. Mg_2Si	6	Acero H13	cónico roscado	[119]
6061Al/3-7%TiC	6	Acero de alto C y alto Cr	cílindrico cuadrado, cónico cuadrado, cilíndrico hexagonal, cónico hexagonal, cónico octogonal	[131]
2009Al/15%SiC	8	Acero para herramientas endurecido	cilíndrico roscado	[132]
Al-Si alloy/30%SiC	6	WC-Co	cilíndrico roscado	[124]
6061Al/20%Al_2O_3	7	Acero reforzado con 30%TiC	cónico roscado	[134]
2124/25%SiC	6	Acero recubierto con TiAlN	cónico roscado	[122]
6063/13,5%B_4C	4,5	Acero AISI 4340	cónico roscado	[135]
7075/10%Al_2O_3	7	ferro-titanit	cónico roscado	[133]
2009Al/15%SiC	6	Acero para herramientas endurecido	cilíndrico	[123]
6061Al/10%SiC	6	Acero rápido	cilíndrico roscado	[136]

Tabla 5. Resumen de distintas herramientas utilizadas para soldar MMC mediante FSW.

En este trabajo se han utilizado varias herramientas, cuyas características se han ido modificando de manera sucesiva para adecuarse a las exigencias de la soldadura de los materiales estudiados. En primer lugar, como punto de partida, se utilizó una herramienta cuyo desempeño en uniones de 2024Al había sido muy satisfactorio. Esta consta de dos piezas, con hombro de acero H13 para herramientas y punzón de MP159, Figura 25.

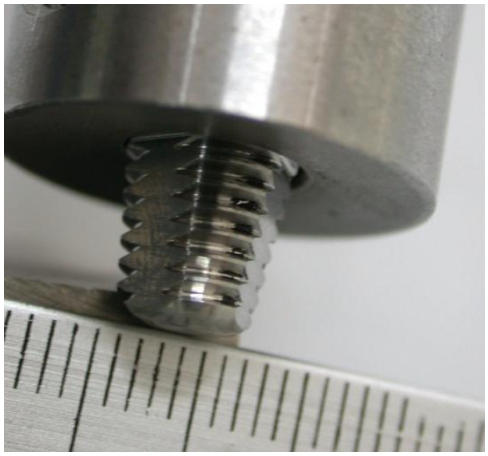

Figura 25. Herramienta de punzón roscado y facetado de aleación MP159.

La aleación MP159 se caracteriza por su ultra alta resistencia mecánica (UTS_{Tamb}=2070 MPa, $UTS_{650°C}$=1500 MPa), alta tenacidad y buena resistencia a la corrosión a altas temperaturas [137], su composición química se muestra en la Tabla 6.

Elemento	Ni	Co	Cr	Fe	Mo	Ti	Nb	Al
% m/m	25.5	37.5	19.0	9.0	7.0	3.0	0.6	0.2

Tabla 6. Composición química nominal de la aleación MP159.

El hombro de la herramienta es liso y cóncavo. El punzón tronco-cónico contiene una rosca y tres facetas con 120° entre ellas.

Si bien esta herramienta permitió lograr una soldadura en material 25%SiC/2124Al de 15mm de espesor en dos pasadas (una por cada cara), sin defecto túnel, el desgaste producido durante el proceso fue excesivo. Para evaluarlo, se realizaron a continuación pasadas sucesivas en chapas de 8 mm de espesor del mismo material compuesto y se estudió cualitativamente el desgaste. El aspecto de la herramienta al finalizar cada una de las 8 pasadas se muestra en la Figura 26.

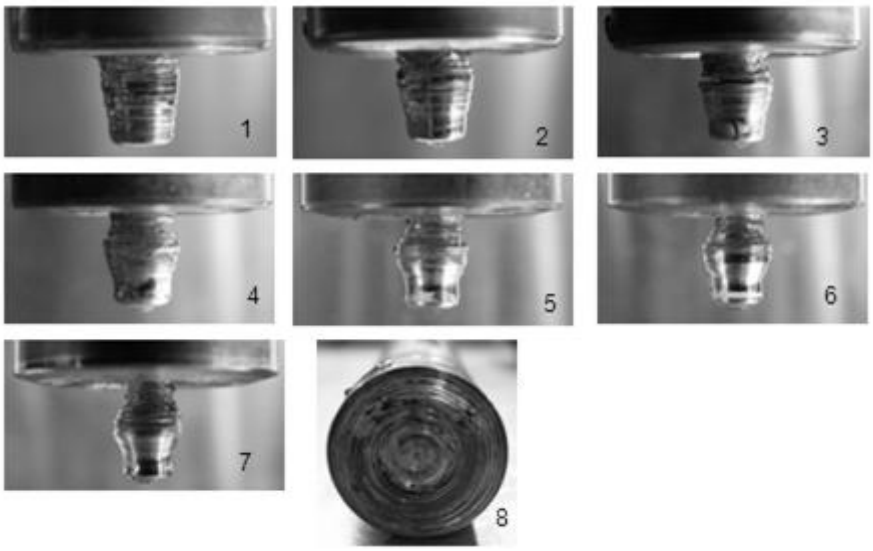

Figura 26. Aspecto de la herramienta al finalizar cada pasada de 220 mm de largo en 25%SiC/2124Al a 700 rpm y 75 mm/min.

Como se observa, primero se desgastan rápidamente las aristas agudas de la rosca. A continuación se desgasta la zona próxima al hombro donde se alcanzan las temperaturas más elevadas [84]. Finalmente, al comenzar el avance de la octava pasada, la sección del punzón se encontraba ya muy reducida. Ello unido a los severos esfuerzos del comienzo de la soldadura, en las que el material circundante aún se encuentra frío, llevaron a la rotura del punzón. Se habían completado en total menos de 3 metros de soldaduras en material 25%SiC/2124Al.

El gran desgaste que producen los compuestos con alta carga de refuerzo en las herramientas introduce diversos inconvenientes al proceso de FSW, que se resumen en los siguientes puntos:

- la herramienta deja de ser «no consumible» con los perjuicios económicos que eso conlleva;
- el proceso pierde su reproducibilidad ya que la forma y/o dimensiones de la herramienta cambia constantemente, lo cual equivale a cambiar de perfil de herramienta en cada soldadura (e incluso durante una misma soldadura);
- el material desgastado de la herramienta se deposita dentro de la soldadura alterando su composición y propiedades, principalmente mecánicas y frente a la corrosión [132].

En relación a este último punto, se estudió la distribución del material desgastado de la herramienta dentro de la unión. Para ello se realizaron análisis químicos mediante Espectrocopía de emisión óptica de descarga luminiscente en distintas zonas de secciones

transversales de las chapas soldadas. Los resultados se recogen en la Tabla 7. Los mayores contenidos de Cr, Ni y Co, indican que el material que se desprende del punzón se deposita en el lado de avance de la zona batida. Esta región coincide con la del material proveniente de la corriente de vórtice del modelo de flujo de Nunes [24] que, como se explicó en la sección 1.2.2.1, contiene el material que entra en contacto con el punzón.

Pasada	**Posición con respecto al centro de la unión (mm)**	**Composición química (%m/m)**		
		Cr	Ni	Co
7	3.05 (A)	0.6	0.82	>0.7
	-5.95 (R)	*	*	*
	-12.85 (R)	*	*	*
2	4.4 (A)	0.12	0.16	0.22
	-1.3 (R)	*	*	*
	-5.6 (R)	*	*	*
Concentración nominal en la aleación MP159		19	25.5	37.5

(A) lado de avance, (R) lado de retroceso, * contenido por debajo del límite detectable por la técnica.

Tabla 7. Presencia del material desgastado proveniente de la herramienta en función de la posición con respecto al centro de la unión.

Por todo lo anterior, hay que evitar el desgaste de la herramienta [138] para conseguir buenas soldaduras por FSW en materiales compuestos. Una manera de minimizar el desgaste consiste en seleccionar herramientas con las siguientes características:

a) fabricadas en material duro (WC-Co, compuestos con TiC, etc.) [124]
b) de forma simple, sin aristas agudas (roscas y muescas profundas) [117, 120, 121, 132].

Esta fue la estrategia adoptada para realizar las siguientes soldaduras recogidas en esta Tesis.

En definitiva, a la hora de seleccionar la herramienta adecuada para soldar por FSW un compuesto con alta carga de refuerzo cerámico no es aconsejable seguir las pautas dictadas para las aleaciones de aluminio. Es decir, en lugar de formas complejas que mejoran la mezcla, se deben utilizar herramientas sin aristas agudas para evitar el desgaste. Por esta misma razón, se deben sustituir los aceros para herramientas y las superaleaciones base níquel o cobalto por materiales más duros de naturaleza cerámica.

4.1.2. Solicitaciones críticas sobre la herramienta

Los mayores esfuerzos que se producen durante el proceso de FSW suelen encontrarse en la etapa de penetración de la herramienta en el material aún frío [139, 140]. Estos esfuerzos de compresión son mayores al soldar materiales compuestos por su mayor dureza en comparación con las aleaciones de aluminio. Además, la ausencia de roscas dificulta aún más la penetración.

Sin embargo, cuando se utilizan herramientas de WC-Co o similar, como las utilizadas en este trabajo, la etapa más crítica no es la penetración, sino el comienzo del avance. Estos materiales, de naturaleza casi cerámica, poseen una alta resistencia a esfuerzos de compresión, pero no a solicitaciones de tracción o flexión. Su baja tenacidad lleva a roturas repentinas y catastróficas. Por lo tanto, la etapa más crítica para estas herramientas no es la penetración, donde los esfuerzos son principalmente de compresión, sino el comienzo del avance, ya que entonces los esfuerzos de flexión son máximos debido a que el material alrededor de la herramienta aún se encuentra frío y su resistencia al flujo plástico es máxima.

A continuación se describe la experiencia recogida durante el desarrollo del presente trabajo en relación al comportamiento de las herramientas de WC-Co en soldaduras de materiales compuestos. Cinco de las nueve herramientas de WC-Co utilizadas se rompieron: tres de ellas al comenzar el avance de uniones de compuesto 25%SiC/2124Al, una antes de completar la penetración en su primer uso y otra al comenzar el avance de una soldadura en aleación 2024Al. El aspecto de las herramientas rotas se muestra en la Figura 27.

Figura 27. Herramientas de FSW de WC-Co que se fracturaron durante su utilización en el desarrollo del presente trabajo. Se puede observar que en todos los casos la fractura del punzón fue completa.

Por lo tanto, es importante minimizar los esfuerzos de flexión sobre las herramientas cerámicas al soldar compuestos. Esto se logra utilizando tiempos de espera (desde que acaba la penetración del pin y el hombro entra en contacto con el material hasta que comienza el avance) largos y velocidades de avance bajas en comparación con los habitualmente utilizados en aleaciones de aluminio. De este modo, el material alcanza una

temperatura de trabajo suficiente para disminuir la resistencia al flujo plástico y minimizar los esfuerzos de flexión sobre la herramienta al comenzar el avance.

4.1.3. Ajuste de los parámetros de proceso para la eliminación de defectos

La elección de parámetros y su relación con la aparición de defectos, la microestructura y las propiedades mecánicas, son los principales temas de estudio en uniones por FSW. Es muy difícil predecir cuáles serán los parámetros correctos para realizar una soldadura a partir de la información disponible en la literatura. Esto se debe a que existen muchas variables que intervienen en el proceso: la herramienta (su forma, tamaño y material), el material a soldar (dimensiones, propiedades mecánicas y térmicas, resistencia a la corrosión y al desgaste), cuestiones geométricas (soldadura a tope, a solape, circular, por puntos, etc.), las características del soporte o «*backing plate*», etc. Por lo tanto, es muy difícil encontrar en la literatura un antecedente que coincida con el sistema que se desea soldar y utilizarlo para decidir las condiciones del proceso.

Se suele comenzar por una combinación de parámetros medios (velocidad de avance: 75-125 mm/min, velocidad de rotación: 300-700 rpm) [42, 74, 141]. A continuación, se ajustan las variables del proceso siguiendo los procedimientos ya establecidos para la eliminación de defectos. Es decir, aunque las condiciones de partida y los sistemas sean distintos (herramienta, material, etc.), se utilizan las mismas estrategias para eliminar cierto tipo de defecto [142, 143]. Por ejemplo, una gran rebaba en la superficie superior de la soldadura se suele asociar a una penetración excesiva de la herramienta, por lo tanto, se recomienda disminuirla para solucionarlo [144].

En nuestro caso, el defecto más frecuente es el llamado «defecto túnel» o «*wormhole*»: un orificio interno continuo que se extiende a lo largo de la soldadura. Éste sólo puede detectarse mediante radiografía o seccionando la unión, aunque en ocasiones, se intuye su presencia observando el orificio de salida de la herramienta. Este tipo de defecto se ha clasificado en uniones de aleaciones de aluminio como un «defecto frío», es decir, se produce cuando el aporte energético no ha sido suficiente [145-147]. Para aumentar la temperatura del proceso, se recomienda aumentar la velocidad de rotación, w, y/o disminuir la velocidad de avance, v [146]. Desde un punto de vista económico, es preferible aumentar la velocidad de rotación para no ralentizar el proceso. Por lo tanto, esta estrategia es la que se utiliza más frecuentemente en aleaciones de aluminio [42]. En la Figura 28 se pueden observar secciones transversales de soldaduras en aleaciones de

aluminio, en las que se destaca la aparición de defectos túnel según sean las velocidades de avance y rotación.

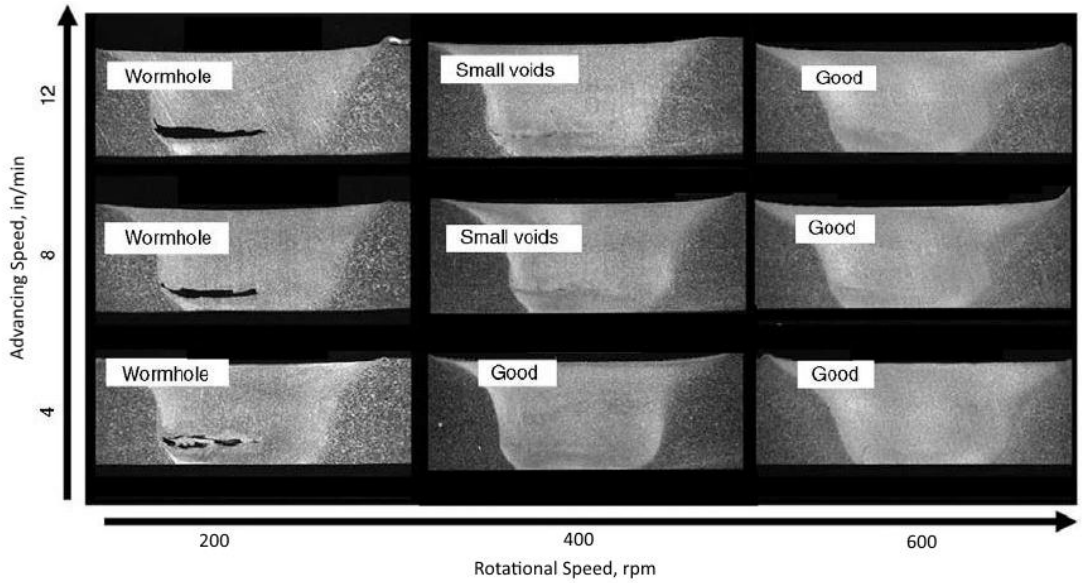

Figura 28. Secciones transversales de uniones realizadas por FSW en aleaciones de aluminio [42]. Se observa que el defecto túnel aparece cuando la velocidad de rotación es baja y la de avance alta.

La aparición de defectos túnel depende de las características del sistema (material + herramienta) y de las condiciones de soldadura. Los sistemas estudiados en este trabajo se resumen en la Tabla 8.

	Material	Espesor (mm)	Herramienta					
			Material	L_p*	D_p*	D_h*	Punzón	Imagen
s1	25%SiC/2124Al	15	Acero (hombro) MP159 (punzón)	7.6	7.95-6.35	20	Roscado y facetado	
s2	25%SiC/2124Al	8	WC-Co	6.8	9-8	19	Liso	
s3	17%SiC/2124Al – 2024Al	8						
s4	25%SiC/2124Al	8	WC-Co	7.6	7.2-6.35	25	Facetado	
s5	2024Al	10	Acero (hombro) MP159 (punzón)	9	7.95-6.35	20	Roscado y facetado	

*L_p: longitud del punzón, D_p y D_h: diámetro del punzón y del hombro, respectivamente. Magnitudes en mm.

Tabla 8. Características de los sistemas estudiados en este trabajo.

En la Figura 29 se resumen las uniones que presentaron defecto túnel (símbolos vacíos) y aquellas que no (símbolos llenos) en función de las condiciones de velocidad de rotación y de avance utilizadas para cada sistema. Se puede observar cómo las condiciones que para un sistema resultan en uniones con defecto túnel, en otro sistema pueden resultar en lo contrario (400 rpm - 30 mm/min, 250rpm - 30mm/min, 400 rpm - 100 mm/min). Esto se debe a que el cambio de herramienta y/o material hace que las condiciones de soldadura idóneas también cambien.

En el primer sistema estudiado (s1) que utiliza una herramienta roscada de MP159, Tabla 8, el aumento de la velocidad de rotación *w* (la estrategia usualmente utilizada en aleaciones de aluminio) logró eliminar el defecto túnel. En cambio, al utilizar herramientas no roscadas (s2-s4) se observó que aumentar *w* no lo elimina.

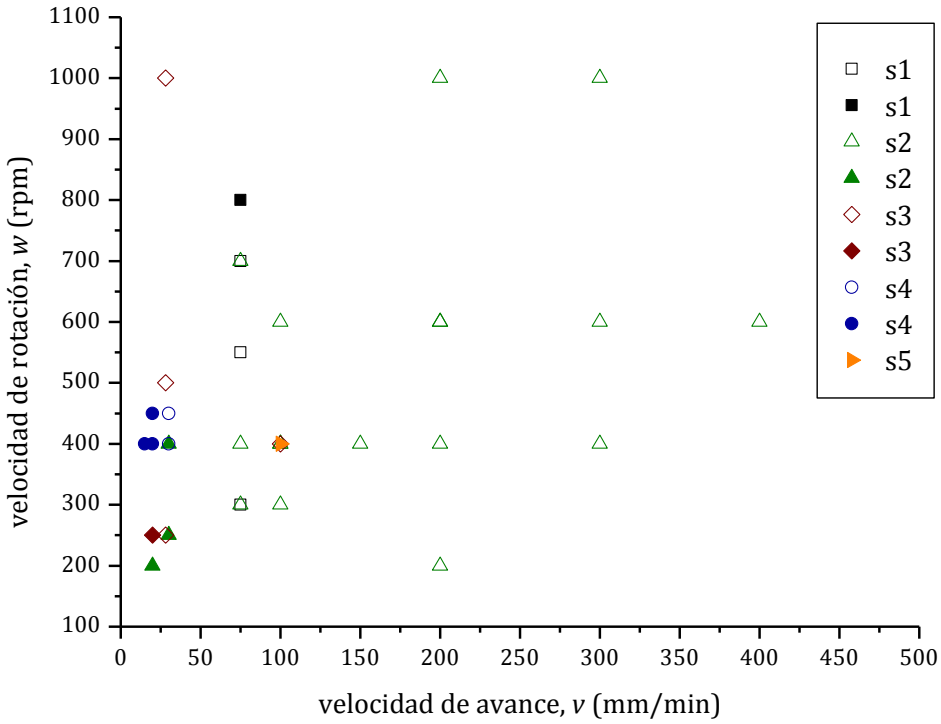

Figura 29. Aparición de defecto túnel en función de las condiciones de soldadura (w, v) para los distintos sistemas estudiados. Los símbolos vacíos corresponden a uniones con defecto túnel y los llenos a uniones sin defectos volumétricos.

Después de numerosas pruebas, se concluyó que para evitar su aparición es necesario aumentar la temperatura del proceso, utilizando velocidades de avance y rotación bajas. En sistemas en los que la herramienta es de forma simple y hecha de un material de dureza elevada (similar a la de las partículas de refuerzo), al aumentar la velocidad de

rotación el transporte de material se vuelve menos eficiente y no se logra eliminar el defecto túnel. En la sección 4.2.2.1, se explicará el porqué de este resultado. Esto difiere de la estrategia normalmente utilizada en aleaciones de aluminio.

En la Figura 30 se muestran secciones transversales de uniones correspondientes al sistema s2. Se puede comprobar que el defecto túnel aparece en aquellas uniones con mayores velocidades de rotación y de avance, marcadas con rectángulos rojos.

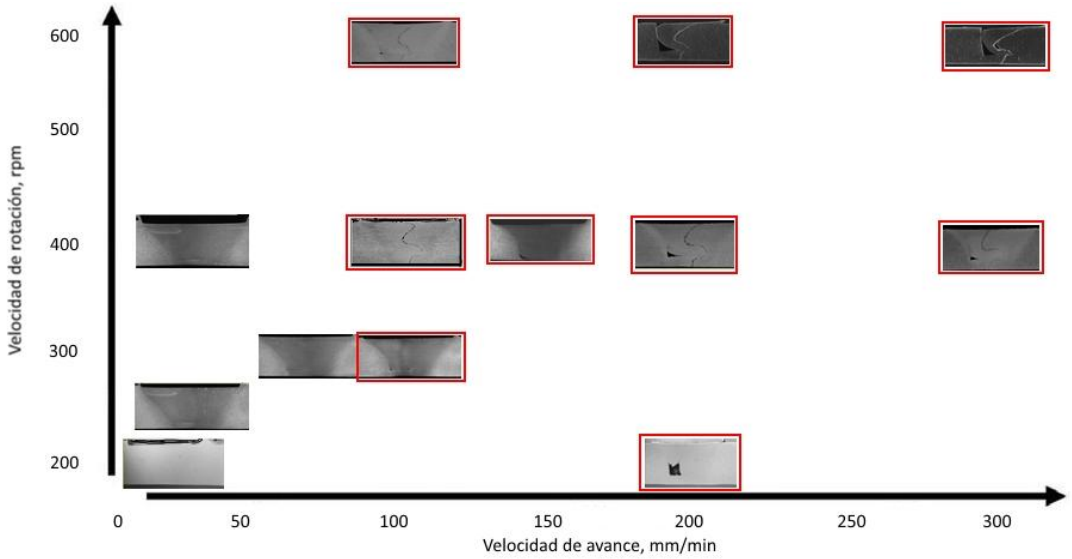

Figura 30. Macrografías de secciones transversales a soldaduras en compuesto 25%SiC/2124Al (s2) para distintas velocidades de rotación y de avance.

Otros defectos que se han encontrado en las uniones de compuesto con 25% de SiC, fueron huecos y/o trazas de óxidos en la zona correspondiente a las superficies de contacto de las chapas o «frontera».

En aleaciones de aluminio se han reportado dos tipos de defectos relacionados con esta zona de la unión, ejemplos de los mismos se muestran en la Figura 31:

- «*kissing bond*» o «*root flaw*», Figura 31 a), las superficies quedan en contacto pero no llegan a unirse;
- «*lazy s*», «*oxide alignment*», «*zig-zag line*» o «*joint line remnant*», Figura 31 a) y b), una línea en forma de zigzag en la que quedan atrapados óxidos provenientes de las superficies laterales de las chapas.

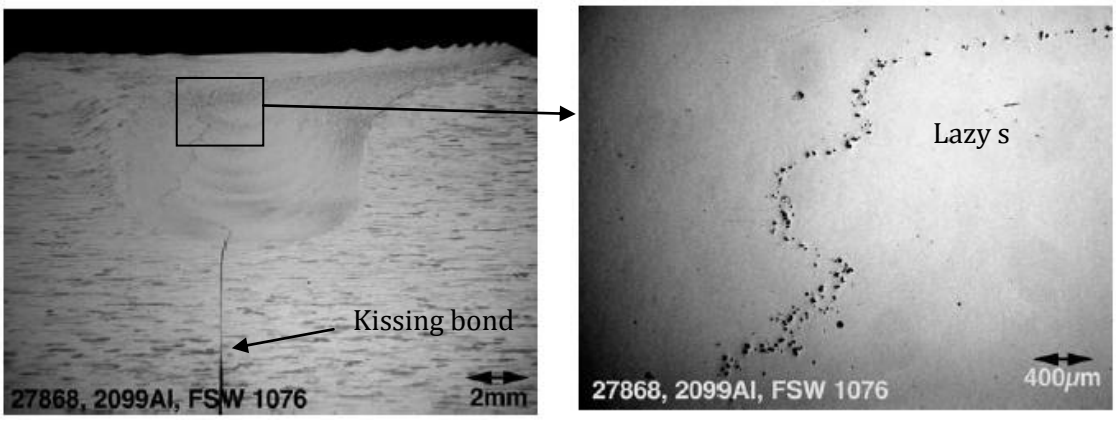

Figura 31. Defectos asociados a la zona de frontera [74]. Se ve el defecto llamado «*lazy s*» formando un zig-zag en la zona batida (ampliación a la derecha) y el llamado «*kissing bond*» en la parte inferior de la soldadura.

La terminología asociada a estos defectos se emplea en la literatura de forma confusa y muchas veces se superpone [142, 148, 149]. Al igual que los defectos túnel, son considerados de naturaleza fría. En el caso del «*lazy s*», la causa es una baja velocidad de rotación [142] y el «*kissing bond*» se debe a una penetración insuficiente de la herramienta [31]. Ambos defectos provocan una disminución de las propiedades mecánicas en uniones de aleaciones de aluminio [150, 151].

Para evitar estos defectos en aleaciones de aluminio se aconseja limpiar las superficies laterales [32, 152-155], aumentar la penetración de la herramienta (en el caso del «*kissing bond*») [148, 155] y mejorar la mezcla [152, 156, 157]. En la Figura 32 se muestra la aparición de «*kissing bond*» y/o «*zig-zag line*» en función de las condiciones de velocidad de avance y rotación en uniones de aleación de aluminio [148]. Se puede observar que a medida que disminuye la velocidad de rotación y aumenta la de avance (flecha en la Figura 32), aparece en primer lugar la «*zig-zag line*» y luego, además el «*kissing bond*».

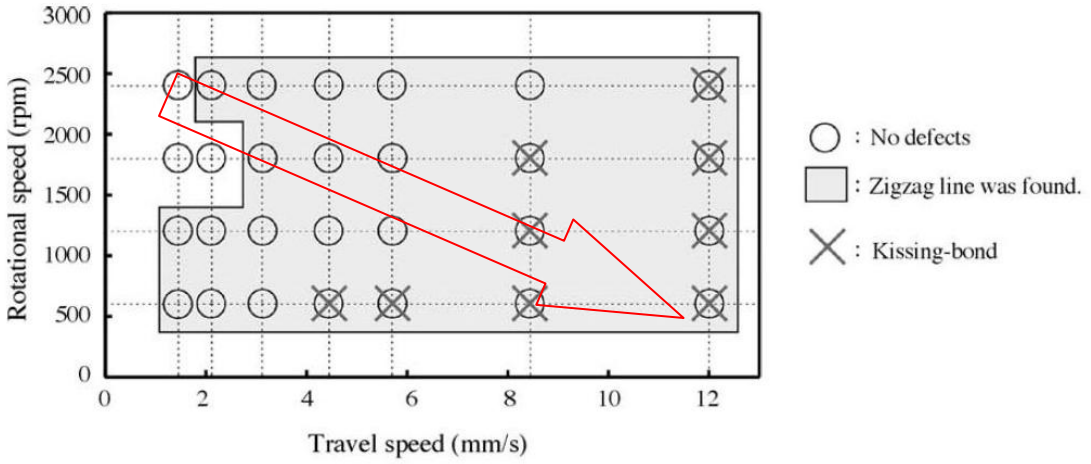

Figura 32. Aparición de distintos defectos en uniones de 1050Al en función de las velocidades de rotación y avance utilizadas en el proceso FSW [148].

Los defectos encontrados en las uniones de este trabajo en materiales compuestos guardan cierta similitud con los reportados en la literatura para aleaciones de aluminio, pero son sin duda diferentes. Mientras que en las uniones de aleación de aluminio los «*kissing bond*» sólo se forman en la parte inferior de la soldadura, donde no alcanza a penetrar la herramienta; en nuestro caso, aparecieron en casi todo el espesor. En la Figura 33 se muestra un ejemplo de estos defectos a los que llamamos defectos de frontera.

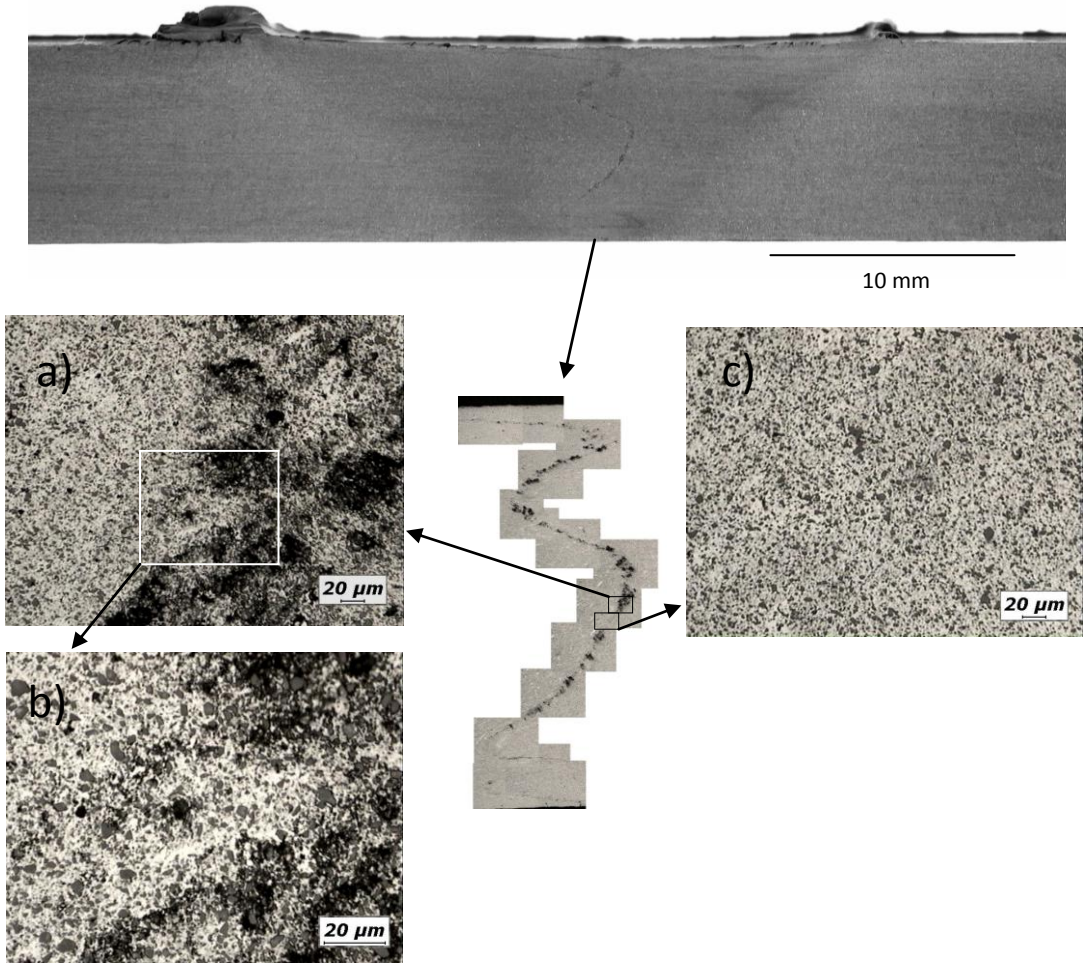

Figura 33. Imágenes obtenidas por microscopía óptica en una sección transversal a una unión por FSW en el compuesto 25%SiC/2124Al. Se muestra en detalle la microestructura del defecto de frontera que se produce en la zona batida en todo el espesor de la soldadura.

Para evitar o eliminar estos defectos, cuando se utilizan herramientas roscadas, el aumento de velocidad de rotación permite un mejor mezclado. De este modo, se rompen las capas de óxido que se forman en las superficies de las chapas antes de soldar, y los óxidos se dispersan dentro de la zona batida y minimizando su efecto perjudicial.

En nuestro caso, estas estrategias no son suficientes para eliminar los defectos. Por un lado, al utilizar herramientas lisas aumentar la velocidad de rotación no mejora prácticamente la mezcla. Y por otro, aumentar la penetración de la herramienta no logra eliminar los huecos que aparecen en la frontera, ya que estos se extienden en todo el espesor de la unión y no solo en la parte inferior. Por lo tanto, fue necesario estudiar nuevos métodos de eliminación de estos defectos para el caso de compuestos con alta carga de refuerzo en los que no se recomienda utilizar herramientas roscadas. Estos métodos se centraron en aumentar la mezcla en la zona batida, para que los óxidos se dispersen y las superficies de las chapas se unan completamente (sin dejar huecos). Esto se logró mediante una serie de pautas que consisten en:

- aplicar una limpieza mecánica a las superficies laterales de las chapas antes de soldar para minimizar la presencia de óxidos,
- aumentar el aporte calorífico (H): de este modo se aumenta la temperatura del material y este se reblandece,
- disminuir el cociente entre las velocidades de avance, v, y rotación, w, denominado «*weld pitch*» (v/w): de este modo la cantidad de material que se transporta en cada giro es menor,
- utilizar un desplazamiento lateral de la herramienta (off-set) hacia el lado de retroceso: así se aprovecha la asimetría del flujo de material, para someter al material que forma la frontera a mayores deformaciones.

En la Figura 34 se muestran los resultados de la aplicación de las pautas descritas en uniones de compuesto 25%SiC/2124Al utilizando una herramienta lisa de WC-Co (sistema s4). Se puede observar cómo el tamaño de los huecos que forman el defecto de frontera disminuye progresivamente hasta desaparecer.

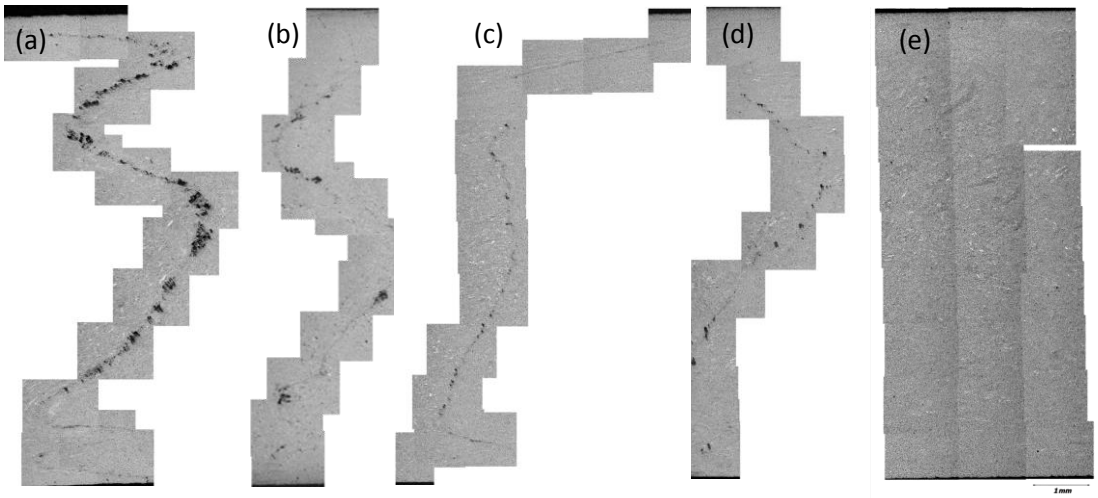

Figura 34. Evolución de los defectos de frontera en uniones por FSW de compuesto 25%SiC/2124Al con herramienta lisa de WC-Co (sistema s4). Superposición de imágenes obtenidas por microscopía óptica. Las estrategias utilizadas para progresivamente disminuir el tamaño de estos defectos fueron las siguientes: De (a) a (b) se incluyó la limpieza mecánica de las superficies laterales de las chapas antes de soldar. De (b) a (c) se aumento la velocidad de rotación. De (c) a (d) se disminuyó la velocidad de avance. Y de (d) a (e) se utilizó un desplazamiento lateral de la herramienta hacia el lado de retroceso.

Se puede concluir que los conocimientos previos encontrados en la literatura son útiles para la identificación de defectos y sus posibles causas. Pero las estrategias para evitarlos o eliminarlos no suelen ser aplicables a compuestos con alta carga de refuerzo. Por lo tanto, ha sido de suma importancia el desarrollo de estrategias específicas para la eliminación de los defectos más frecuentes en la soldadura por FSW de compuestos de este tipo.

4.2. Consideraciones adicionales del proceso de FSW en materiales compuestos

Como se ha detallado a lo largo de la sección anterior, el proceso de FSW en los MMC con alta carga de refuerzo presenta dificultades propias que difieren de las de aleaciones de aluminio. Uno de las aportaciones del presente trabajo de tesis consiste en la determinación de estas dificultades específicas y el planteamiento de un estudio que permita superarlas.

En las secciones posteriores de esta Tesis se ha realizado una división entre las dificultades derivadas del carácter termotratable de la matriz del compuesto y aquellas derivadas de la presencia de partículas de refuerzo.

4.2.1. Consideraciones derivadas del carácter termotratable de la matriz

Las aleaciones estudiadas en este trabajo, ya sea como matriz de compuestos o como materiales monolíticos, son termotratables. Es decir, endurecen por precipitación mediante tratamiento térmico. Por lo tanto, el ciclo térmico introducido por el proceso de FSW provocará cambios en el estado de precipitación de los materiales empleados en las uniones realizadas. Esta característica aumenta la complejidad de la caracterización de las mismas, especialmente en lo que refiere a microestructura, propiedades mecánicas y tensiones residuales.

Las aleaciones que se han estudiado en este trabajo son de la serie 2XXX, cuyas composiciones químicas se detallan en la Tabla 9. Su principal elemento de aleación es el cobre, seguido por el magnesio. Debido a su alta resistencia mecánica y a la fatiga, son ampliamente utilizadas en el sector aeroespacial.

Aleación	%	Si	Fe	Cu	Mn	Mg	Cr	Zn	Ti	Zr+Bi	Otros	Al
2024	Mín.			3.80	0.30	1.20						
	Máx.	0.50	0.50	4.90	0.90	1.80	0.10	0.25	0.15	0.20	0.15	resto
2124	Mín.			3.80	0.30	1.20						
	Máx.	0.20	0.30	4.90	0.90	1.80	0.10	0.25	0.15	0.20	0.15	resto

Tabla 9. Composición química de las aleaciones de aluminio 2024 y 2124.

La composición química es prácticamente igual en ambas, sólo difieren en los contenidos máximos de elementos considerados impurezas como silicio y hierro, que son menores en 2124Al. A la hora de comparar su comportamiento durante en proceso de FSW se desprecian dichas diferencias.

4.2.1.1. Evolución de la precipitación debido al ciclo térmico producido por el proceso de FSW

En este trabajo se soldaron materiales en distintos estados de precipitación inicial: T6, T351 y T1. El primero corresponde a un tratamiento térmico de solubilización, temple y envejecimiento hasta alcanzar el máximo de dureza. El segundo, a un tratamiento de solubilización, trabajado en frío por estiramiento y envejecimiento natural. Por último, el estado T1 se corresponde con un envejecimiento natural desde las temperaturas de forja en caliente. Estos tres estados son de gran interés, ya sea por poseer la mayor resistencia (T6), por ser el de mayor aplicación industrial (T351) o por ser el más económico (T1).

Durante el proceso de FSW se alcanzan temperaturas elevadas en las que la difusión es significativa. En la mayoría de los casos, esto implica que la precipitación evoluciona desde su estado de partida (T1, T351 ó T6) hacia uno más cercano al equilibrio, es decir sobreenvejecido. El grado de sobreenvejecimiento depende del tiempo que se encuentra el material a una temperatura dada. Puesto que la distribución de temperaturas en el proceso de FSW no es uniforme, el estado de precipitación final del material y su respuesta mecánica, tampoco lo son. En resumen, el carácter no uniforme del ciclo térmico del proceso de FSW se transmite a la respuesta mecánica de la unión. Por lo tanto, para evaluar dicha respuesta, es necesario estudiar la soldadura como un todo, constituido por una variedad de materiales puestos en serie [158, 159]. La resistencia final de la unión vendrá dada por la resistencia de su sección más débil.

Añadidos a los efectos del sobreenvejecimiento, existen otros factores que afectan a la resistencia de la unión: defectos macroscópicos (disminución del espesor, exceso de rebaba, defecto túnel, porosidad en la superficie, etc.), defectos microscópicos (poros, «*kissing bond*», óxidos, etc.) y/o cambios microestructurales (cambios en la estructura de grano, rotura partículas de refuerzo, tensiones residuales, etc.).

En las uniones ensayadas, los defectos túnel han llegado a disminuir en un 25% la resistencia a rotura en tracción de la unión con respecto al material base (25%SiC/2124Al T1). En el mismo material, los defectos microscópicos en la zona de la frontera produjeron pérdidas de resistencia entre 15 y 22%. Su efecto perjudicial es llamativamente grande si se compara con el de los defectos túnel. A modo de ejemplo, en la Figura 35 se muestran macrografías de uniones del mismo material: una con defecto túnel y otra con defectos microscópicos en la frontera, cuyas eficiencias de junta resultan muy similares. Esto se debe a que, si bien cada poro es pequeño, la superficie total que pueden cubrir es comparable con la de un defecto túnel y, por lo tanto, la pérdida de resistencia que provocan también lo es.

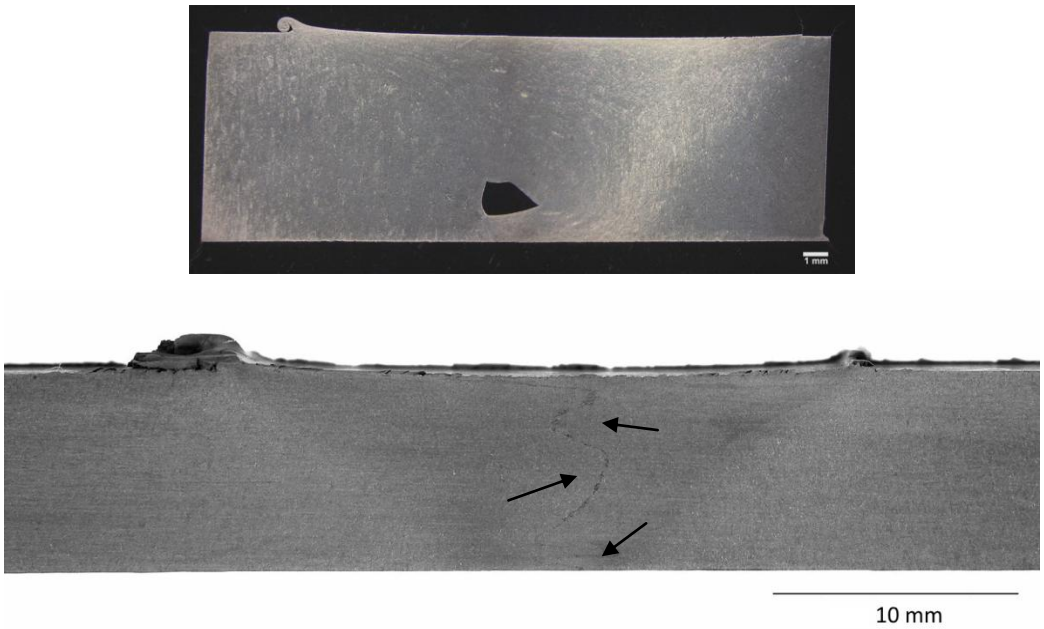

Figura 35. Macrografías de uniones realizadas por FSW en 25%SiC/2124Al T1. Arriba: A pesar del defecto túnel la eficiencia de junta resultó del 77%. Abajo: La presencia de poros y óxidos en la frontera (señalado con flechas) hizo que la eficiencia de junta fuera del 78%.

Estos son ejemplos de lo difícil que resulta predecir la perdida de resistencia que cierto defecto puede provocar en una unión. En la gráfica de la Figura 36 se compara la resistencia de uniones en compuesto 25%SiC/2124Al de 8mm de espesor en estado T1 con respecto al material base, considerando el efecto de defectos túnel, defectos microscópicos en la zona de la frontera y el estado de precipitación sobreenvejecido.

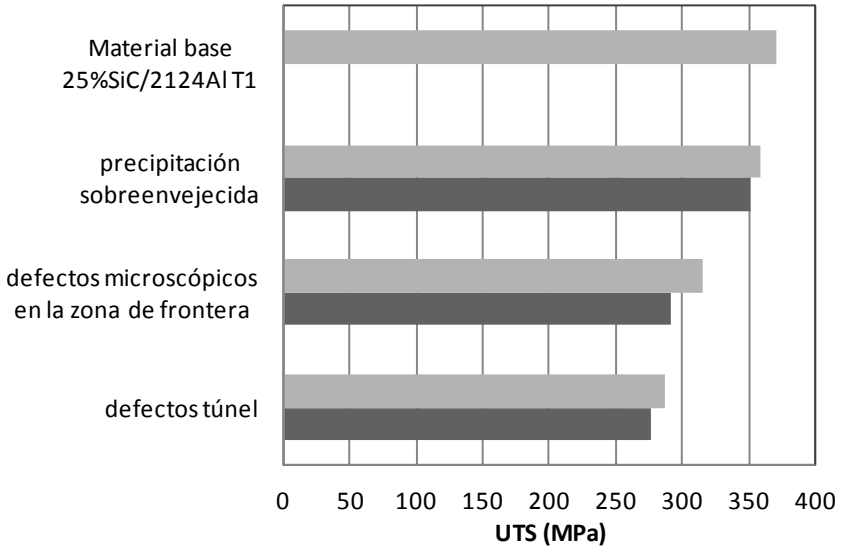

Figura 36. Efecto de distintos factores en la resistencia a la tracción de uniones realizadas por FSW en 25%SiC/2124Al -T1.

La pérdida de resistencia que provoca la precipitación sobreenvejecida es de poca importancia comparada con la que provocan los defectos micro y macroscópicos. Pero se debe tener en cuenta que este resultado es debido a que el estado de precipitación de partida en las uniones de la Figura 36 es un estado de por sí sobreenvejecido (T1).
Si comparamos la resistencia de la zona batida de uniones del mismo compuesto pero esta vez realizadas en estado T6, Figura 37, vemos que la pérdida de resistencia debida a los cambios microestructurales es más importante (entre 29 y 38%). Además, la magnitud del cambio depende del proceso termomecánico que impone la soldadura por FSW en la porción ensayada de la unión. En este caso, a mayor velocidad de rotación, mayor aporte térmico y mayor pérdida de resistencia.

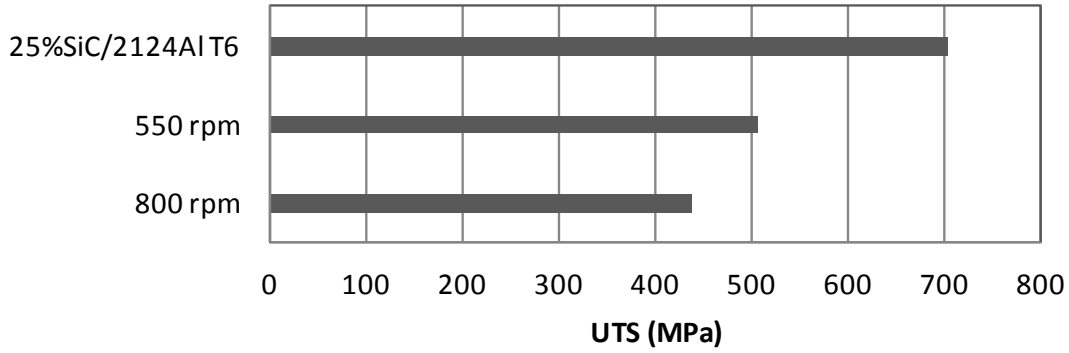

Figura 37. Resistencia a la tracción del compuesto 25%SiC/2124Al-T6 y de soldaduras realizadas sobre dicho material por FSW con distinta velocidad de rotación.

En resumen, el ciclo térmico que introduce el proceso de FSW provoca una respuesta mecánica no uniforme en los componentes soldados de materiales termotratables. El efecto del sobreenvejecimiento en la resistencia de la unión dependerá del estado de precipitación inicial y de la severidad del proceso termomecánico. En algunos casos esta pérdida de resistencia es comparable a la que introducen factores macroscópicos, como la presencia de defectos túnel.

4.2.1.2. Tensiones residuales: la dificultad de establecer el parámetro d_0

El diseño estructural de componentes con soldaduras requiere de una caracterización completa de su comportamiento mecánico. Uno de los aspectos a tener en cuenta es la presencia de tensiones residuales. Éstas se generan durante el enfriamiento del material debido a las restricciones que impone el anclaje mecánico de las chapas y a las diferencias en velocidad de enfriamiento dentro del material [160]. La distribución de tensiones es muy compleja en soldaduras por FSW debido a que la temperatura no es uniforme en la

pieza, el proceso es asimétrico, la fuente de calor se mueve durante el mismo, etc. Una dificultad añadida en la determinación de tensiones residuales en estas soldaduras es la relacionada con tener un material con distinta microestructura según la posición. Este hecho complica considerablemente el cálculo del valor de referencia del espaciado interplanar sin tensiones, d_0.

Como aproximación al problema de la determinación de tensiones residuales en soldaduras por FSW en MMC, se abordó una versión simplificada del mismo sin partículas de refuerzo pero que considera el efecto del estado de precipitación. Es decir, se estudió una unión realizada por la técnica de FSW en chapas de la aleación que actúa como matriz del compuesto, 2024Al. Se propuso un método para superar las dificultades que el carácter termotratable de algunas aleaciones de aluminio presenta a la hora de determinar el espaciado interplanar sin tensiones, d_0. Conocer este espaciado es imprescindible para el cálculo de tensiones residuales por métodos de difracción.

En aleaciones de aluminio termotratables, como la 2024Al, el valor de d_0 depende principalmente del porcentaje y naturaleza de los átomos de elementos aleantes que se encuentran en solución sólida en el material [161], o dicho de otro modo, es función del estado de precipitación del material. Como se muestra en la Figura 38, ciertos átomos afectan en mayor medida que otros el valor del espaciado interplanar para un mismo porcentaje en solución sólida. Además, mientras que el magnesio expande la red por ejemplo, el cobre la contrae.

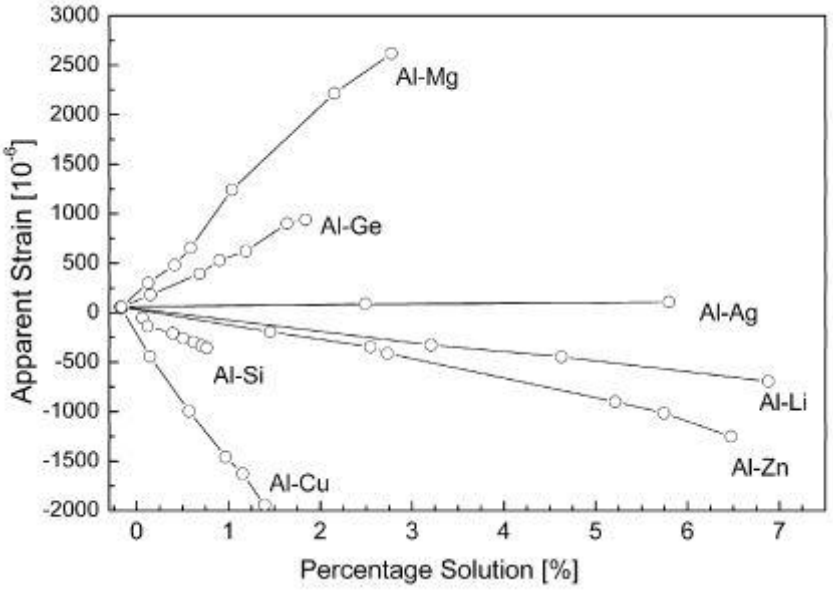

Figura 38. Variación del espaciado interplanar, representado como una deformación aparente, en función del contenido de distintos solutos (% at.) en aluminio [161].

En el caso de soldaduras, el porcentaje de átomos en solución sólida cambia a través de la unión ya que el ciclo térmico no es uniforme en el material. Por lo tanto, d_0 cambia punto a punto en la soldadura. Esto hace que el cálculo de tensiones residuales sea una tarea muy compleja.

El método planteado en este trabajo para el cálculo del parámetro d_0, se basa en la imposición de las condiciones de equilibrio de la mecánica; es decir, la suma de tensiones y momentos en una sección cualquiera del sólido deben ser nulos. La aplicación de estas condiciones en el caso de aleaciones envejecibles no puede realizarse de manera analítica al variar el parámetro d_0 en cada punto de la sección. Mediante el uso de algoritmos evolutivos, es posible encontrar el perfil de espaciado interplanar a través de la unión que permite conseguir el equilibrio en dicha sección del sólido. Es decir, se evita determinar experimentalmente el parámetro d_0, que puede ser una fuente de error importante en la determinación del perfil de tensiones residuales [162]. Además, como se muestra en la publicación incluida en el Anexo 1, el método permite imponer distintas aproximaciones, o condiciones de contorno, y llegar a resultados realistas de forma robusta para cada uno de los escenarios que surgen de estas aproximaciones. De este modo se demuestra la versatilidad de los algoritmos evolutivos para encontrar soluciones a problemas complejos.

Si bien los valores de macrotensiones residuales obtenidos en el trabajo no son trasladables a las uniones de compuestos, el método es válido y aplicable a soldaduras de estos materiales.

A las tensiones residuales macroscópicas se superpondrán, las tensiones microscópicas características de estos materiales compuestos. De ellas se hablará en la sección 4.2.2.3.

En resumen, la determinación de tensiones residuales en soldaduras de materiales termotratables, requiere un método que permita determinar de manera fiable el valor del parámetro de red de referencia, d_0. La aplicación del método propuesto en este trabajo a uniones de MMC supone un avance importante en la caracterización del estado de tensiones residuales de dichas uniones en materiales termotratables.

4.2.2. Consideraciones derivadas de la presencia de partículas

Como se detalló en la introducción, la principal motivación para aplicar la técnica de FSW a los compuestos de este trabajo es que estos materiales se consideran no soldables por técnicas tradicionales. En las soldaduras en las que se produce fusión, la matriz líquida

reacciona con las partículas formando carburos en la superficie de las mismas [163, 164], lo que fragiliza la intercara y empeora las propiedades mecánicas [115, 118].
En esta sección se analizan las dificultades que introduce la presencia de partículas de refuerzo en el proceso de soldadura por FSW y en la caracterización microestructural de las uniones resultantes.

4.2.2.1. Utilización de herramientas no roscadas de WC-Co

Una de las primeras dificultades que se presentaron al soldar los MMC por FSW fue el desgaste de las herramientas. Trabajos anteriores se han centrado en estudiar los fenómenos de desgaste en herramientas de acero [114, 120, 121, 132] y WC-Co [124, 165, 166]. Sin embargo, un enfoque práctico del problema consiste en definir estrategias que eviten el desgaste. En particular, el uso de herramientas no roscadas de WC-Co ha logrado superar el problema de desgaste al soldar materiales compuestos con refuerzo de SiC. A pesar de este éxito, es imprescindible estudiar las consecuencias de utilizar este tipo de herramientas, en otros aspectos del proceso como por ejemplo, el flujo de material.
Por un lado, las herramientas de formas simples producen menos mezcla que las de perfiles complejos [167], reduciendo la ventana de parámetros que permite obtener buenas uniones [62]. Y por otro, la alta dureza del WC-Co hace que las condiciones de contacto entre la superficie de la herramienta y el material a soldar, sean menos favorables para el transporte de material (deslizamiento > arrastre) [168]. Estos dos factores disminuyen el flujo del material, crucial para este tipo de soldadura [169-171].
La fuerza de rozamiento (F_k), en la superficie de contacto entre la herramienta y el material circundante, determina la deformación (y el transporte) del mismo. Cuando el valor de la fuerza de rozamiento es suficientemente alto, el material alrededor del punzón se deforma y se mueve siguiendo el giro de la herramienta. De este modo, el material que se encuentra delante del punzón en el lado de avance es deformado y arrastrado contra el material en el lado de retroceso, pasa alrededor de la herramienta por el lado de retroceso y, continuando con el giro, rellena el espacio dejado por el punzón al avanzar. De este modo se obtiene una unión sin defectos volumétricos. En el caso contrario, el hueco que se forma por el paso de la herramienta no se rellena completamente, dando lugar al defecto túnel.
La magnitud de la fuerza de rozamiento depende del coeficiente de rozamiento dinámico del sistema (μ_k) y de la fuerza de contacto normal a la superficie (**N**):

$$F_k = \mu_k N \quad (1)$$

Para aumentar F_k lo suficiente como para deformar plásticamente el material y transportarlo según la dirección tangencial de la superficie del punzón, se puede aumentar N y/o aumentar μ_k. Lo primero implicaría un mayor nivel de esfuerzos sobre la herramienta. Esto no es recomendable ya que, como se explicó en la sección 4.1.2, estas herramientas poseen baja resistencia a la flexión. Por lo tanto, para mejorar el transporte del material alrededor de la herramienta, hay que aumentar μ_k cuyo valor depende de muchos factores del sistema [172]. A continuación se describen los más importantes:

1. El acabado superficial de los materiales en contacto (herramienta y material compuesto). El área de contacto depende de la rugosidad de estas superficies: a mayor rugosidad mayor μ_k [173].

2. La dureza de los materiales en contacto (que a su vez dependen de la temperatura): cuanta mayor diferencia de dureza entre la herramienta y el compuesto, mayor es μ_k. A nivel microscópico, esto equivale a que las rugosidades del material más duro se «incrusten» en el más blando, aumentando la magnitud de μ_k.

3. La naturaleza química de los materiales. De esto depende que se formen enlaces entre los materiales y se produzca adherencia (microsoldaduras en los puntos de contacto). La adherencia entre materiales es mayor según la siguiente secuencia: metal/metal > metal/cerámico > cerámico/cerámico [174, 175].
4. La velocidad de deslizamiento de las superficies: a menor velocidad mayor μ_k.

A tenor de los factores anteriores, es de esperar que en los sistemas estudiados en este trabajo el valor de μ_k sea relativamente bajo por las siguientes razones:

- La superficie de la herramienta es muy lisa.
- La diferencia de dureza entre la herramienta ($H_{knoopWC\text{-}Co}$ = 1600-1900) y la matriz del compuesto ($H_{knoop2124Al}$ = 140-160) es grande. Pero debido al alto porcentaje (17-25%) de pequeñas partículas de refuerzo, una porción importante de la superficie del compuesto la cubren partículas de SiC ($H_{knoopSiC}$ = 2480) con las que la diferencia de dureza es menor [176].
- Es poco probable que se produzcan condiciones de adherencia ya que la herramienta es cerámica. Por lo tanto, no existe contacto metal/metal. En el

contacto metal/cerámico puede producirse adherencia, aunque ésta es más probable con óxidos cerámicos (Ej.: Al – Al_2O_3) que con WC-Co.

Para un sistema (herramienta + material) dado, la rugosidad de la herramienta y la naturaleza química de los materiales en contacto están determinados. En cambio, existen variables del sistema tribológico que se pueden modificar para aumentar μ_k. Éstas tienen que ver con la dureza de los materiales y la velocidad de deslizamiento. La velocidad de deslizamiento entre las superficies (material/herramienta) será proporcional a la velocidad de rotación del punzón y a su diámetro. Por un lado, se puede aumentar la temperatura del sistema para que la dureza de matriz de aluminio disminuya y de este modo, incrementar la diferencia de dureza con la herramienta. Para ello se debe aumentar el aporte calorífico, *H* [177]:

$$\mathrm{H} = \mathrm{T}\,\frac{\mathrm{w}}{\mathrm{v}} \qquad (2)$$

Dónde *T* es el torque medio, *w* es la velocidad de rotación y *v* la velocidad de avance. Por lo tanto, para aumentar *H* se puede aumentar *w* y/o disminuir *v*. Por otro lado, la velocidad de deslizamiento en la superficie de contacto herramienta/material se puede minimizar disminuyendo *w*. Finalmente, se deduce que para aumentar la temperatura del sistema a la vez que se minimiza la velocidad de deslizamiento, se deben mantener *w* y *v* bajas.

En la Figura 39 se resumen las condiciones que resultaron en uniones sin defecto túnel en los sistemas estudiados. Se puede observar que en las uniones realizadas con herramientas lisas de WC-Co (sistemas s2 a s4 de la Tabla 8) sólo se logra evitar el defecto túnel en la región de *w* y *v* bajos. En cambio, en los sistemas con herramientas roscadas de MP159 (sistemas s1 y s5 de la Tabla 8), se consigue con valores de *w* y *v* mayores.

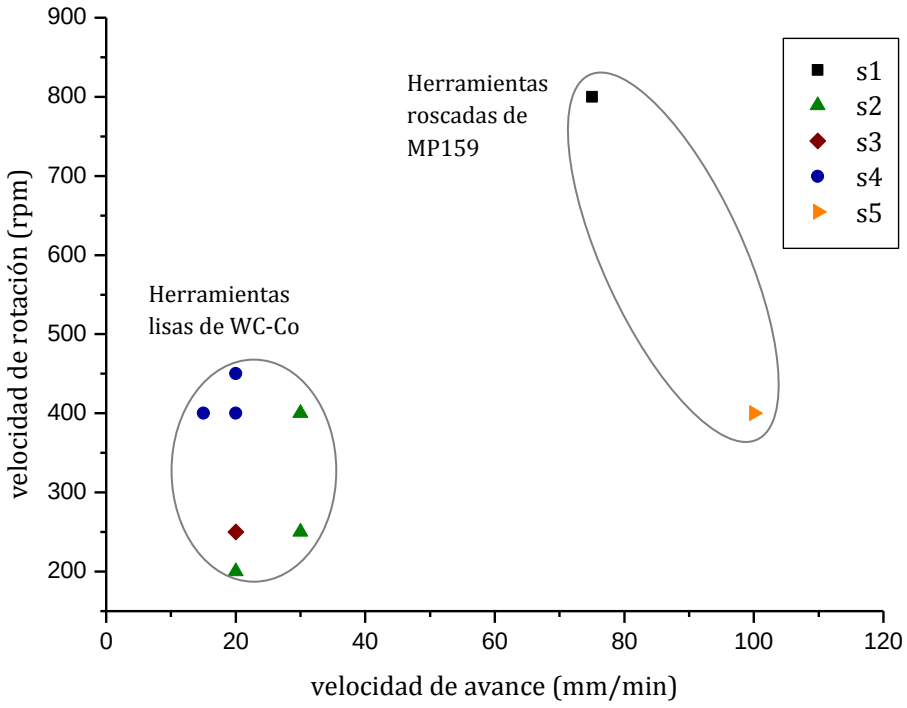

Figura 39. Velocidad de rotación vs. velocidad de avance para uniones sin defecto túnel en los distintos sistemas de la Tabla 8.

En resumen, la utilización de herramientas de WC-Co resistentes al desgaste para soldar MMC conlleva fuerzas de rozamiento bajas en comparación con los sistemas formados por herramientas de acero y aleaciones de aluminio. Las bajas fuerzas de rozamiento disminuyen el transporte de material alrededor de la herramienta durante el proceso. Por lo tanto, se deben utilizar velocidades de avance y rotación bajas en comparación con las utilizadas habitualmente en aleaciones de aluminio. Para, de este modo, promover un aumento en la fuerza de rozamiento, suficiente para poder deformar plásticamente y transportar el material circundante, y así lograr uniones sin defectos volumétricos.

Con el objetivo de cuantificar el coeficiente de fricción se utilizaron los datos recogidos por el máquina de soldadura por FSW para las uniones del sistema s4 y la siguiente ecuación [178]:

$$T_{tot} = T_s + T_p = 2\,F_z\,\mu\left(\frac{R_1}{3} + h\frac{R_2^2}{R_1^2}\right) \quad (3)$$

Donde T_{tot} es el torque total, T_s y T_s las contribuciones al torque correspondientes al hombro y al punzón de la herramienta respectivamente, F_z la fuerza vertical, μ el coeficiente de fricción, R_1 y R_2 el radio del hombro y del punzón respectivamente y h la altura del punzón.

Esta ecuación considera el hombro plano y el punzón cilíndrico sin pérdida de generalidad. Además, se considera que la totalidad del torque es empleado en superar la

fuerza de fricción que ofrece el material en contacto con la herramienta. Esta aproximación se ha utilizado exitosamente en muchos casos [178-180] para simulaciones del flujo térmico, cálculos de temperaturas máximas del proceso, etc. Sin embargo, no logra explicar la formación de defectos volumétricos u otras características del proceso ligadas al flujo de material [181]. En un intento por representar los fenómenos que ocurren en la superficie de contacto herramienta/material, Schmidt et al. [182] propusieron un modelo que separa la fricción en «deslizamiento» y «adherencia», representado por la ecuación (4). Su primer término corresponde al caso en el que la velocidad de las superficies en contacto es distinta, es decir hay deslizamiento entre la herramienta y el material, y el esfuerzo de contacto viene dado por el esfuerzo de fricción. El segundo término, en cambio, corresponde al caso en el que la superficie del material se mueve a la velocidad de la superficie de la herramienta, es decir están adheridas y, por lo tanto, se produce transporte. Aquí el esfuerzo de contacto es igual al esfuerzo necesario para deformar plásticamente el material. Por último, se propone que ambos fenómenos conviven en las soldaduras por FSW en distintas proporciones, cuantificadas mediante el parámetro δ que indica la proporción de adherencia (considerado igual en todas las superficies de contacto).

$$T_{tot} = \delta\, T_{adh} + (1-\delta) T_{fr} = \frac{2}{3}\pi \left[\delta \frac{\sigma_{ys}}{\sqrt{3}} + (1-\delta)\mu\sigma_z\right] \times (R_1^3 + 3R_2^2 h) \qquad (4)$$

Donde T_{adh} y T_{fr} son las contribuciones al torque correspondientes al fenómeno de «adherencia» y «fricción deslizamiento» respectivamente, σ_{ys} el límite elástico del material compuesto y σ_z el esfuerzo vertical.

Esta nueva aproximación al problema supone un paso adelante en la explicación del fenómeno que ocurre en la superficie de contacto del material con la herramienta, a costa de introducir una nueva variable desconocida y difícilmente medible (δ). Si analizamos el sistema de datos (uniones de s4), considerando una proporción de adherencia del 0.5 (lo que equivale a decir que la mitad de la superficie sufre adherencia y podría interpretarse como que la mitad del material en el frente de la herramienta se transporta hacia la parte de atrás de la misma) se obtienen valores de μ entre 0,14 y 0,30. Es decir, valores más pequeños y con una variación menor que cuando se calculan sin tener en cuenta la adherencia (0,43-0,87).

Abordar el fenómeno de fricción como una combinación de deslizamiento y adherencia permite una mejor comprensión del fenómeno que ocurre localmente en la superficie de contacto material/herramienta. Y de este modo es posible separar conceptualmente y sin olvidar que son fenómenos acoplados e interdependientes, la parte térmica o de calentamiento (deslizamiento), de la parte de transporte o flujo de material (adherencia).

4.2.2.2. Incremento de la resistencia al flujo plástico

Como se mencionó en la sección 4.1, los MMCs presentan una mayor resistencia al flujo plástico que las aleaciones sin reforzar, tanto a temperatura ambiente como a las del proceso de FSW. Esto supone una dificultad para la realización de procesos de deformación severa como la soldadura por FSW.

La mayor resistencia al flujo plástico que posee el compuesto tiene dos contribuciones fundamentales. Por un lado, la contribución debida al mecanismo de transferencia de carga [183]. En los materiales compuestos se genera una tensión de tracción en el refuerzo que es consecuencia de la tensión de cizalla presente en la intercara matriz-refuerzo cuando el material se encuentra sometido a una tensión externa. La tensión de cizalla en la intercara debe estar, por tanto, en equilibrio con la de tracción en el refuerzo σ_f, obteniéndose:

$$\sigma_f = \frac{2\tau_i}{r}(L - x) \tag{5}$$

donde τ_i es la tensión de cizalla aplicada al refuerzo, *x* indica la posición a lo largo de la fibra/partícula, 2*L* es la longitud de la misma y *r* su radio. Además de esta tensión de cizalla, existe una contribución de la tensión normal aplicada en los extremos [183-186]. Esta contribución es tanto más importante, cuanto menor es la relación de aspecto de las partículas de refuerzo. La transferencia de carga alcanza su máximo valor cuando la tensión en la matriz que rodea a la partícula de refuerzo llega al valor del límite elástico, σ_{my}, alcanzándose el siguiente valor de tensión en la fibra/particula, σ_f:

$$\sigma_f = \sigma_{my} f(1 + s/2) \tag{6}$$

donde *f* es la fracción en volumen de refuerzo y *s* es la relación de aspecto.

El límite elástico del compuesto, σ_{yc}, predicho bajo carga uniaxial y como consecuencia de la transferencia de carga considerando la contribución de los extremos de las partículas está dado por la siguiente expresión,

$$\sigma_{yc} = \sigma_{yM} \cdot \mathrm{R} \tag{7}$$

$$\text{donde } \mathrm{R} = \left[f_M + f_I \int_{-L}^{L} \left(\frac{E_I}{E_M} - \left(\frac{E_I}{E_M} - \frac{E_M^*}{E_M} \right) \cosh\left(\frac{nz}{r_0} \right) \operatorname{sech}(ns) \right) dz \right] \tag{8}$$

con (*-L> z >L*) y σ_{yM} es el valor del límite elástico de la matriz

$$\text{y} \qquad E_M^* = \frac{E_I(1-sech(ns))+E_M}{2-sech(ns)} \tag{9}$$

$$n = \left(\frac{2E_M}{E_I(1+\nu_M)Ln(1/f_I)} \right) \tag{10}$$

E_M y E_I son, respectivamente, el módulo elástico de la matriz y del refuerzo, s la relación de aspecto del refuerzo ($s=L/r_0$, r_0 el radio del refuerzo cilíndrico de longitud $2L$), ν_M es el coeficiente de Poisson de la matriz y f_M y f_I las fracciones en volumen de la matriz y el refuerzo respectivamente. La descripción de este modelo supone el refuerzo homogéneamente distribuido y alineado, lo cual representa una buena aproximación para el material de este trabajo.

A partir de estas expresiones es posible calcular la parte de la tensión aplicada al material que no es efectiva para producir deformación porque se ha transferido el refuerzo cerámico. En nuestro caso esa contribución es del 40% según los resultados del modelo de transferencia de carga. Este resultado está en consonancia con la diferencia de resistencia mecánica entre el material compuesto y su aleación de referencia, Figura 22.

Por otro lado, existe una segunda contribución al aumento de límite elástico de la aleación que está relacionada con las modificaciones microestructurales que se introducen en la aleación metálica por la adición de partículas, $\Delta R_{p,C}$, [187]. Estas contribuciones se pueden describir mediante el siguiente modelo micromecánico [188, 189]:

$$\Delta R_{p,C} = \Delta\sigma_{KG} + \Delta\sigma_{KF} + \Delta\sigma_{\alpha} + \Delta\sigma_{SKG} \tag{11}$$

Los términos primero y cuarto de la ecuación corresponden a la influencia de los cambios en tamaño de grano y subgrano respectivamente, análogos a Hall-Petch, (por ejemplo debidos a la recristalización durante el tratamiento termomecánico del material compuesto). El segundo término corresponde al endurecimiento por deformación que introducen las partículas en la matriz del compuesto. Por último, el tercer término corresponde al aumento en el límite elástico introducido por las dislocaciones geométricamente necesarias inducidas durante el enfriamiento por la diferencia en coeficientes de expansión entre la matriz y el refuerzo.

En las gráficas de la Figura 40 se describen las aportaciones de cada uno de los mecanismos descritos en el modelo micromecánico descrito en la ecuación (11). Se puede observar que para el mismo volumen de refuerzo, las partículas de tamaño pequeño contribuyen en mayor medida al endurecimiento que las partículas grandes [190].

Además, dependiendo del tamaño de las partículas de SiC un mecanismo de refuerzo prevalecerá sobre los otros.

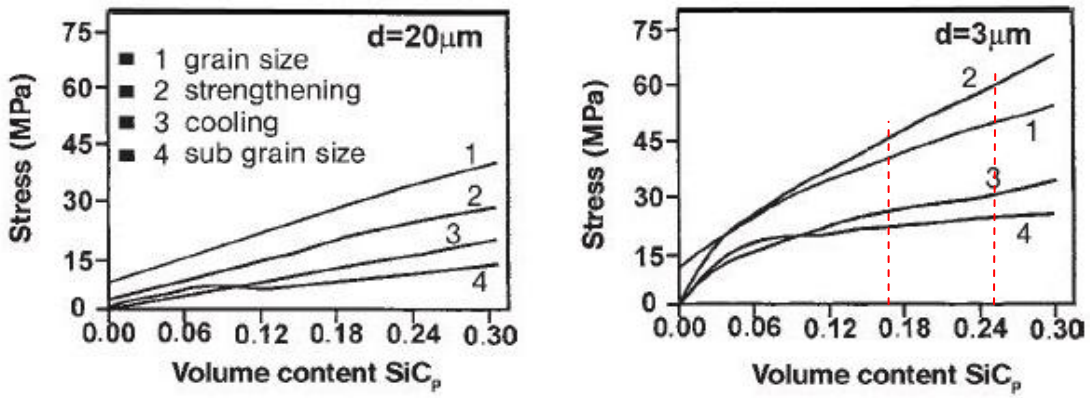

Figura 40. Contribución de cada mecanismo al límite elástico, calculado a partir del modelo micromecánico anterior para aleaciones de aluminio en función del contenido de SiC para tamaños medios de partícula de 20 μm y 3μm [188]. Las líneas rojas discontinuas corresponden a los contenidos de refuerzo de los compuestos estudiados en este trabajo.

Según esta descripción, la mayor aportación al límite elástico en los compuestos de este trabajo corresponde al endurecimiento por deformación, seguido por la disminución del tamaño de grano. En el compuesto 25%SiC/2124Al-T6, la suma de estos dos mecanismos de endurecimiento equivaldría a un 32% del límite elástico de la matriz.

4.2.2.3. Tensiones residuales microscópicas

Entre los diferentes cambios microestructurales introducidos al material compuesto por el ciclo termomecánico asociado al proceso de FSW se encuentran las tensiones residuales. En la sección 4.2.1.2 se abordó el problema de la determinación de las tensiones residuales macroscópicas en uniones realizadas por FSW en materiales termotratables monolíticos. Al incorporar partículas al material, además de tensiones residuales macroscópicas se generan tensiones microscópicas (de tracción en la matriz y compresión en las partículas). Estas son consecuencia de la gran diferencia (6:1) entre los coeficientes de expansión térmica de la matriz de aluminio y el refuerzo de SiC.

El proceso de FSW es un proceso termomecánico similar a la forja o la extrusión, pero a diferencia de estos conformados, induce un fuerte gradiente de temperaturas en el material que al enfriarse se traduce en un complejo perfil de tensiones residuales. Por lo tanto, es importante el estudio de las tensiones residuales macro- y microscópicas características del proceso de soldadura por FSW. Además, a la hora de realizar cálculos estructurales, las tensiones residuales macroscópicas deben ser tenidas en cuenta [97].

Existen dos procedimientos principales para calcular las tensiones microscópicas asociadas a las presencia de refuerzo en un material compuesto. Un primer método consiste en calcular la totalidad de las tensiones (macroscópicas + microscópicas) sobre el material, y posteriormente separar analíticamente sus contribuciones [191]. Otro método, consiste en eliminar o relajar las tensiones macroscópicas del material compuesto y de una aleación de referencia sin tensiones microscópicas asociadas a partículas de refuerzo, para medir experimentalmente las tensiones microscópicas.

En este trabajo se optó por el segundo método para determinar las tensiones microscópicas asociadas a la presencia de partículas en uniones realizadas por FSW en el material compuesto 2124Al/25%SiC. Para ello se extrajeron muestras peine de forma transversal a soldaduras del material compuesto y de aleación 2024Al. Luego se realizaron medidas de difracción en ambas muestras y se compararon los resultados. Cada púa de las muestras tipo peine debe ser pequeña para no retener tensiones macroscópicas [192, 193], pero de mayor tamaño que la variación de las tensiones microscópicas (del orden del espaciado entre partículas). En la Figura 41, se muestra el resultado de las medidas realizadas por difracción de radiación sincrotrón en dichas muestras.

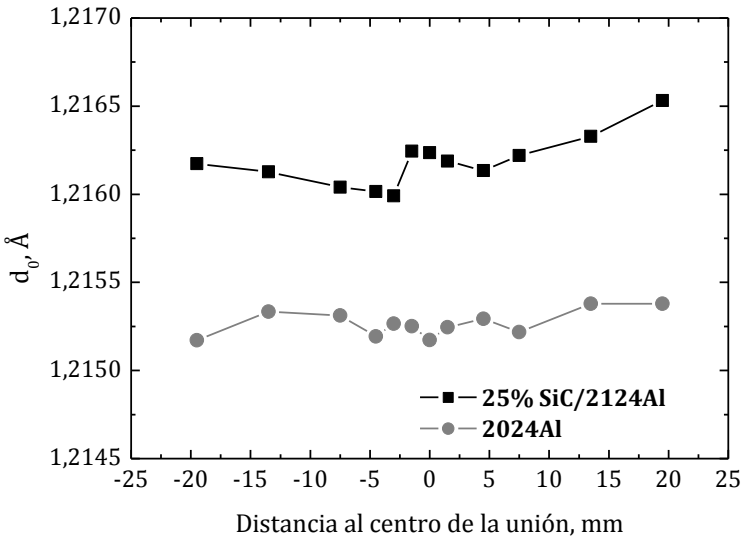

Figura 41. Perfiles de espaciado interplanar medidos utilizando radiación sincrotrón sobre muestras tipo peine extraídas de chapones soldados por FSW.

La diferencia entre el espaciado interplanar, d_{311}, de la matriz en el compuesto y la aleación, indican que en la matriz del compuesto existen tensiones microscópicas asociadas a la presencia de partículas cerámicas. El hecho de que el valor de espaciado interplanar, d_{311}, sea mayor en el compuesto que en la aleación da cuenta del carácter

positivo (de tracción) de dichas tensiones en la matriz metálica. Estas tensiones tienen un valor medio de 50 MPa, lo que equivale a un 15% del límite elástico de la aleación, que representa una contribución importante en comparación con las tensiones descritas en la Figura 40.

Estás mismas tensiones son las que se ponen de manifiesto al comparar la respuesta del material compuesto en ensayos de tracción y compresión [194, 195] y que siguen presentes incluso en la zona batida del compuesto soldado por FSW.

4.2.2.4. Caracterización microestructural

Como todo proceso termomecánico, la soldadura por FSW introduce cambios microestructurales en el material soldado. Estos cambios han sido objeto de numerosos estudios [32, 62, 74, 196, 197] en distintos materiales. En la sección 1.2.2.3 se detallaron las características de las distintas zonas microestructurales que se desarrollan en uniones de aleaciones de aluminio. La misma nomenclatura se adopta para el resto de materiales. Pero en el caso de los MMC con alta carga de partículas, la delimitación de las zonas es muchas veces compleja y requiere de métodos complementarios a la metalografía óptica, especialmente si las partículas de refuerzo son pequeñas. Por este motivo se utilizan técnicas de caracterización alternativas para delimitar las zonas microestructurales. Por ejemplo, se realizan perfiles de dureza en un corte transversal a la soldadura para identificar el límite entre la HAZ y el MB. Éste se asocia con el punto en que la dureza se aparta del valor del MB.

En los compuestos estudiados en este trabajo, el alto contenido (17 y 25% en volumen) de partículas pequeñas, entre 2 y 3 μm, provoca que la distancia entre partículas también sea pequeña (del orden de micras). Debido a esto, no es posible distinguir los bordes de grano de la matriz del material compuesto mediante microscopía óptica y muy difícilmente por SEM. Por lo tanto, no ha sido posible caracterizar la microestructura de la zona batida que típicamente es de granos finos equiaxiales en las uniones de aleaciones de aluminio por FSW. En cambio, en la zona central de la unión, se observa que la distribución de las partículas de refuerzo es más homogénea que en el MB. Un ejemplo de este fenómeno para el compuesto 25%SiC/2124Al se muestra en la Figura 42. Este aumento de la homogeneidad en la zona batida, ha sido observado en la mayoría de los estudios de soldadura por FSW de MMC [112, 113, 115, 122, 123]. Por lo tanto, éste puede considerarse uno de los cambios microestructurales característicos de las uniones por FSW en los MMC, como lo es el afino de grano en aleaciones de aluminio.

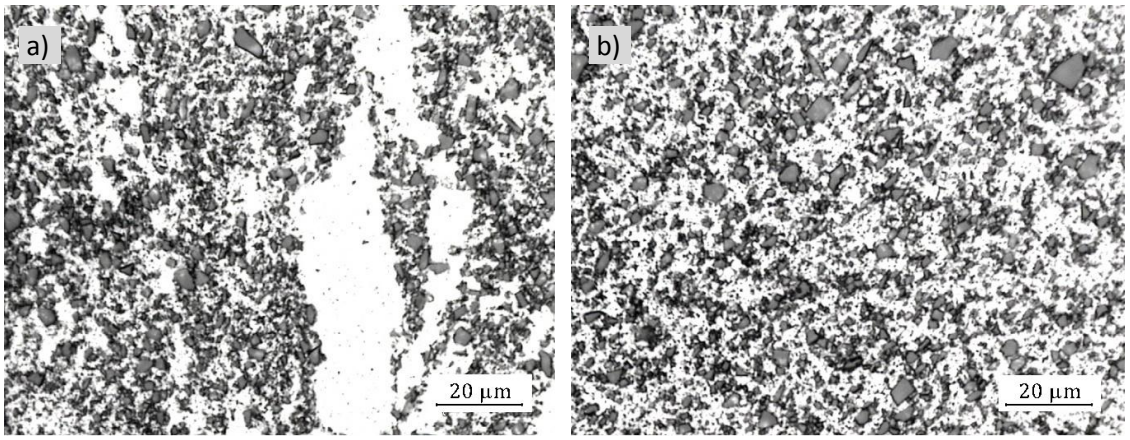

Figura 42. Micrografías ópticas en una sección transversal de una soldadura realizada por FSW: a) material base 25%SiC/2124Al-T6 y b) zona central de la unión. Se puede observar como la distribución de partículas se vuelve más homogénea debido al proceso de deformación severa.

Otro de los cambios asociados con la zona batida de las uniones de MMC que ha sido reportado en la literatura, es la fractura de las partículas de refuerzo [112, 122, 133, 134, 198-200]. En estos trabajos se sugiere que la disminución del tamaño de partícula medida en la zona batida se debe la fractura de esquinas y bordes, y raramente a una rotura de la partícula de origen en varios fragmentos de menor tamaño [199]. Este fenómeno se asocia a causas diversas. En algunos casos, la rotura se asoció a zonas de aglomeración de partículas, que durante la deformación del material eran comprimidas entre sí y por esta razón se fracturaban [133, 134]. Y en otros, se asoció a la dificultad de las partículas de mayor tamaño (mayores a 10 µm) [112, 200, 201] para acomodar la deformación de la matriz circundante. En las uniones de este trabajo, se observaron sólo casos puntuales de rotura de partículas, lo cual se debe a su buena distribución (sin aglomeraciones) y su tamaño pequeño (bastante menor a 10 µm).

La fractura de las partículas de refuerzo en la zona batida depende de la microestructura del material base (tamaño y distribución del refuerzo). Por lo tanto, no es una característica generalizable a todas las uniones por FSW de compuestos.

En resumen, las partículas de refuerzo dificultan la caracterización microestructural de las uniones realizadas por FSW en materiales compuestos. Tanto más cuanto menor sea su tamaño y mayor el contenido en volumen; es decir, cuanto menor sea la distancia entre ellas. Esta característica no impide aplicar la nomenclatura de zonas microestructurales que se utiliza en el resto de materiales. Simplemente, hace que la determinación de estas zonas requiera de un mayor esfuerzo experimental.

5. CONCLUSIONES

Las conclusiones más importantes de la presente Tesis doctoral son las siguientes:

1.- La presencia de partículas de refuerzo en el material compuesto, condiciona de manera muy importante el proceso de soldadura mediante FSW, inhabilitando la aplicación directa de muchos de los conocimientos establecidos en aleaciones de aluminio.

2.- La ventana de parámetros de soldadura en la que se consiguen soldar materiales compuestos de matriz aluminio con alta carga de refuerzo, utilizando herramientas lisas y duras que no sufren desgaste, es muy estrecha en comparación con la de las aleaciones de aluminio. Esta ventana se encuentra a velocidades de rotación y avance bajas.

3.- A pesar de ello, es posible soldar estos materiales mediante FSW de manera reproducible y fiable, obteniendo uniones con buena resistencia a la tracción. También es posible unirlos a aleaciones de aluminio monolíticas (uniones disimilares).

4.- El carácter termotratable de la matriz de estos materiales compuestos afecta al comportamiento mecánico de las uniones realizadas por FSW y dificulta el cálculo de su estado de tensiones residuales. Por lo tanto, será un factor clave a tener en cuenta en la optimización del comportamiento mecánico de estas uniones.

6. BIBLIOGRAFÍA

1. Techtrends, *Metal matrix composites: technology and industrial applications*. 1990: Innovation 128.
2. DEFENSE, D.O., *Composite Materials Handbook*. 2002, MIL-HDBK-17-3F), EUA.
3. Kainer, K.U., *Basics of Metal Matrix Composites*, in *Metal Matrix Composites*. 2006, Wiley-VCH Verlag GmbH & Co. KGaA. p. 1-54.
4. Materion. *AMC225XE PARTICLE REINFORCED ALUMINUM ALLOY*. [cited 2014 Novemver 27th]; manufacturer material datasheet]. Available from: http://materion.com/~/media/Files/PDFs/Aerospace%20Metal%20Composites/Materion%20AMC%20225XE%202012.pdf.
5. Magagnin, L., *Engineered Metal Matrix Composites: Forming Methods, Material Properties and Industrial Applications*. 2013: Nova.
6. Kaczmar, J.W., K. Pietrzak, and W. Włosiński, *The production and application of metal matrix composite materials.* Journal of Materials Processing Technology, 2000. **106**(1–3): p. 58-67.
7. Ibrahim, I.A., F.A. Mohamed, and E.J. Lavernia, *Particulate reinforced metal matrix composites — a review.* Journal of Materials Science, 1991. **26**(5): p. 1137-1156.
8. Miracle, D.B., *Metal matrix composites – From science to technological significance.* Composites Science and Technology, 2005. **65**(15–16): p. 2526-2540.
9. Kainer, K.U., *Metal Matrix Composites: Custom-made Materials for Automotive and Aerospace Engineering*. 2006: Wiley.
10. Allison, J. and G. Cole, *Metal-matrix composites in the automotive industry: Opportunities and challenges.* JOM, 1993. **45**(1): p. 19-24.
11. brakes, T.f.-C., *Discontinuously Reinforced Aluminum Has Come of Age.*
12. *Assessment of Metal Matrix Composites for Innovations*. Available from: http://mmc-assess.tuwien.ac.at/mmc/cat/Applications.html.
13. Rawal, S., *Metal-Matrix Composites for Space Applications.* JOM, 2001. **53**(4): p. 14-17.
14. CeramTec. *New concepts for metal/ceramic composites*. Available from: http://extranet.spk-tools.com/products/metal-matrix-composites/.
15. Composites, M.-M.M. *METALLIC COMPOSITES FOR THE 21st CENTURY*. Available from: http://www.mc21inc.com/.
16. Prasad, S.V. and R. Asthana, *Aluminum Metal-Matrix Composites for Automotive Applications: Tribological Considerations.* Tribology Letters, 2004. **17**(3): p. 445-453.
17. W.M. Thomas, E.D.N., J.C. Needham, M.G. Murch, P. Templesmith, and C.J. Dawes, *Friction Stir Butt Welding*, TWI, Editor. 1991: Great Britain.
18. I. J. Smith, D.D.R.L., *Paper no. 2007-01-1707*, in *7th Syposium on Friction Stir Welding*. 2008, TWI: Awaji Island, Japan.
19. Santos, T.G., R.M. Miranda, and P. Vilaça, *Friction Stir Welding assisted by electrical Joule effect.* Journal of Materials Processing Technology, 2014. **214**(10): p. 2127-2133.
20. Kumari, K., S.K. Pal, and S.B. Singh, *Friction Stir Welding by using Counter-rotating Twin Tool.* Journal of Materials Processing Technology, (0).
21. Li, J.Q. and H.J. Liu, *Characteristics of the reverse dual-rotation friction stir welding conducted on 2219-T6 aluminum alloy.* Materials & Design, 2013. **45**(0): p. 148-154.
22. NASA, *Three New Technologies Enhance Friction Stir Welding*, in *Technology*.
23. Krishnan, K.N., *On the formation of onion rings in friction stir welds.* Materials Science and Engineering: A, 2002. **327**(2): p. 246-251.
24. Guerra, M., et al., *Flow patterns during friction stir welding.* Materials Characterization, 2002. **49**(2): p. 95-101.

25. M.W. Mahoney, C.G.R., J.G. Flintoff, R.A. Spurling, and W.H. Bingel, *Properties of Friction-Stir-Welded 7075 T651 Aluminum.* Metallurgical and Materials Transactions A, 1998. **29A**: p. 1955-1964.
26. Flores, O.V., et al., *Microstructural Issues in a Friction-Stir-Welded Aluminum Alloy.* Scripta Materialia, 1998. **38**(5): p. 703-708.
27. Gibson, B.T., et al., *Friction stir welding: Process, automation, and control.* Journal of Manufacturing Processes, 2014. **16**(1): p. 56-73.
28. *Auto-Adjustable Pin Tool for FSW*. Publications and Successes [cited 2014; Available from: https://techtran.msfc.nasa.gov/successes/auto-adj-pin-top-fsw.php.
29. Wang, K.-s., et al., *Underwater friction stir welding of ultrafine grained 2017 aluminum alloy.* Journal of Central South University, 2012. **19**(8): p. 2081-2085.
30. De Backer, J., G. Bolmsjö, and A.-K. Christiansson, *Temperature control of robotic friction stir welding using the thermoelectric effect.* The International Journal of Advanced Manufacturing Technology, 2014. **70**(1-4): p. 375-383.
31. Lohwasser, D. and Z. Chen, *Friction Stir Welding: From Basics to Applications*. 2009: Elsevier Science.
32. Threadgill, P.L., et al., *Friction stir welding of aluminium alloys.* International Materials Reviews, 2009. **54**(2): p. 49-93.
33. T. Kawasaki, T.M., S. Todori, H. Takai, M. Ezumi and Y. Ina. in *2nd Int. Symp. on 'Friction stir welding'*. 2000. Gothenburg, Sweden.
34. *'Recent trends in ship technologies"*. 2007, https://nippon.zaidan.info/seikabutsu/2006/00382/contents/0002.htm: Japan
35. Ray, J., *Delta 4 fleet goes from 'Medium' to 'Heavy'*, in *Spaceflight now*. 2002: http://www.spaceflightnow.com/delta/delta4/021112delta4/.
36. Johnsen, M.R., *Friction stir welding takes off at boeing.* Welding Journal, 1999. **78**: p. 35-39.
37. Roberts, D.J.W.a.R.W. in *Aerospace automated fastening*. 1998. Long Beach, CA, USA: SAE.
38. *Mazda Furai Concept and New Mazda RX-8 to Make World Debut at 2008 North American International Auto Show*, in *http://www.mazda.com/publicity/release/2007/200712/071212.html*. 2007.
39. http://www.apple.com/es/imac/design/. 11 de septiembre de 2014].
40. Threadgill, R.J.a.P.L., *Progress in friction stir welding of aluminium and steel for marine applications*, in *RINA Conference: Advanced Marine Materials: Technology and Applications*. 2003, Royal Institution of Naval Architects.
41. S. W. Kallee, J.D., E. D. Nicholas. *Railway Manufacturers Implement Friction Stir Welding*. Welding Journal [cited 2014 15 de septiembre]; Available from: http://www.aws.org/wj/oct02/feature.html.
42. Mishra, R.S. and M.W. Mahoney, *Friction Stir Welding and Processing*. 2007: ASM International.
43. Holroyd. *Friction stir welding applications and uses*. 2013 [cited 2014; Available from: http://www.holroyd.com/blog/friction-stir-welding-applications/.
44. *http://www.i-car.com/html_pages/technical_information/advantage/advantage_online_archives/2003/071403.shtml*. [cited 2014 16 de Agosto].
45. Zhang, H., et al., *Defects formation procedure and mathematic model for defect free friction stir welding of magnesium alloy.* Materials & Design, 2006. **27**(9): p. 805-809.
46. Zhang, H., *16 - Friction stir welding of magnesium alloys*, in *Welding and Joining of Magnesium Alloys*, L. Liu, Editor. 2010, Woodhead Publishing. p. 274-305.

47. Lin, J.-W., H.-C. Chang, and M.-H. Wu, *Comparison of mechanical properties of pure copper welded using friction stir welding and tungsten inert gas welding.* Journal of Manufacturing Processes, 2014. **16**(2): p. 296-304.
48. Sun, Y.F. and H. Fujii, *Investigation of the welding parameter dependent microstructure and mechanical properties of friction stir welded pure copper.* Materials Science and Engineering: A, 2010. **527**(26): p. 6879-6886.
49. Liu, H.-j. and L. Zhou, *Microstructural zones and tensile characteristics of friction stir welded joint of TC4 titanium alloy.* Transactions of Nonferrous Metals Society of China, 2010. **20**(10): p. 1873-1878.
50. Esmaily, M., et al., *Microstructural characterization and formation of α' martensite phase in Ti–6Al–4V alloy butt joints produced by friction stir and gas tungsten arc welding processes.* Materials & Design, 2013. **47**(0): p. 143-150.
51. Cho, H.-H., et al., *Three-dimensional numerical and experimental investigation on friction stir welding processes of ferritic stainless steel.* Acta Materialia, 2013. **61**(7): p. 2649-2661.
52. Saeid, T., et al., *On the formation of grain structure during friction stir welding of duplex stainless steel.* Materials Science and Engineering: A, 2010. **527**(24–25): p. 6484-6488.
53. Jeon, J., et al., *Friction stir spot welding of single-crystal austenitic stainless steel.* Acta Materialia, 2011. **59**(20): p. 7439-7449.
54. Ambroziak, A., *Investigations of the friction welding of Incoloy MA 956 alloy.* Archives of Civil and Mechanical Engineering, 2010. **10**(2): p. 5-13.
55. Song, K.H., W.Y. Kim, and K. Nakata, *Evaluation of microstructures and mechanical properties of friction stir welded lap joints of Inconel 600/SS 400.* Materials & Design, 2012. **35**(0): p. 126-132.
56. Song, K.H. and K. Nakata, *Microstructural and mechanical properties of friction-stir-welded and post-heat-treated Inconel 718 alloy.* Journal of Alloys and Compounds, 2010. **505**(1): p. 144-150.
57. Chen, Y.-h., Q. Ni, and L.-m. Ke, *Interface characteristic of friction stir welding lap joints of Ti/Al dissimilar alloys.* Transactions of Nonferrous Metals Society of China, 2012. **22**(2): p. 299-304.
58. Coelho, R.S., et al., *Friction-stir dissimilar welding of aluminium alloy to high strength steels: Mechanical properties and their relation to microstructure.* Materials Science and Engineering: A, 2012. **556**(0): p. 175-183.
59. Kwon, Y.J., I. Shigematsu, and N. Saito, *Dissimilar friction stir welding between magnesium and aluminum alloys.* Materials Letters, 2008. **62**(23): p. 3827-3829.
60. Li, X.-w., et al., *Microstructure and mechanical properties of dissimilar pure copper/1350 aluminum alloy butt joints by friction stir welding.* Transactions of Nonferrous Metals Society of China, 2012. **22**(6): p. 1298-1306.
61. Sadeesh, P., et al., *Studies on Friction Stir Welding of AA 2024 and AA 6061 Dissimilar Metals.* Procedia Engineering, 2014. **75**(0): p. 145-149.
62. Çam, G., *Friction stir welded structural materials: beyond Al-alloys.* International Materials Reviews, 2011. **56**(1): p. 1-48.
63. Sued, M.K., et al., *Design features for bobbin friction stir welding tools: Development of a conceptual model linking the underlying physics to the production process.* Materials & Design, 2014. **54**(0): p. 632-643.
64. Wan, L., et al., *Effect of self-support friction stir welding on microstructure and microhardness of 6082-T6 aluminum alloy joint.* Materials & Design, 2014. **55**(0): p. 197-203.

65. Schneider, J.A. and A.C. Nunes, Jr., *Characterization of plastic flow and resulting microtextures in a friction stir weld.* Metallurgical and Materials Transactions B, 2004. **35**(4): p. 777-783.
66. Arbegast, W.J., *A flow-partitioned deformation zone model for defect formation during friction stir welding.* Scripta Materialia, 2008. **58**(5): p. 372-376.
67. Schneider, J., R. Beshears, and A.C. Nunes Jr, *Interfacial sticking and slipping in the friction stir welding process.* Materials Science and Engineering: A, 2006. **435–436**(0): p. 297-304.
68. Ying Li, L.E.M.a.J.C.M., *Solid-state flow visualization in the friction stir weldinf of 2024 Al to 6061 Al* Scripta Materialia, 1999. **40**(9): p. 1041–1046.
69. Murr, L.E., et al., *Intercalation vortices and related microstructural features in the friction-stir welding of dissimilar metals.* Material Research Innovations, 1998. **2**(3): p. 150-163.
70. Colligan, K.J., *Material Flow Behavior during Friction Stir Welding of Aluminum.* Welding research supplement, 1999: p. 229-237.
71. Seidel, T.U. and A.P. Reynolds, *Visualization of the material flow in AA2195 friction-stir welds using a marker insert technique.* Metallurgical and Materials Transactions A, 2001. **32**(11): p. 2879-2884.
72. B. London, M.M., W. Bingel, M. Calabrese, R.H. Bossi, D. Waldron, *Material Flow in Friction Stir Welding Monitored with Al-SiC and Al-W Composite Markers*, in *2nd Friction stir welding and processing Conference* W. TMS , Pa., Editor. 2003. p. 10.
73. J.R. Sanders, J.A.S., and A.C. Nunes, Jr., *Tracing Material Flow Paths in Friction Stir Welds*, in *Materials Science and Technology*, TMS, Editor. 2005: Pittsburgh,PA.
74. Mishra, R.S. and Z.Y. Ma, *Friction stir welding and processing.* Materials Science and Engineering: R: Reports, 2005. **50**(1-2): p. 1-78.
75. Seidel, T. and A. Reynolds, *Two-dimensional friction stir welding process model based on fluid mechanics.* Science and Technology of Welding & Joining, 2003. **8**(3): p. 175-183.
76. Colegrove, P.A. and H.R. Shercliff, *3-Dimensional CFD modelling of flow round a threaded friction stir welding tool profile.* Journal of Materials Processing Technology, 2005. **169**(2): p. 320-327.
77. Reynolds, A., *Visualisation of material flow in autogenous friction stir welds.* Science and technology of welding & joining, 2000. **5**(2): p. 120-124.
78. S. M. Dörfler, W.G., *Advanced modeling of friction stir welding - improved material model for aluminum alloys and modeling of different materials with different properties by using the level set method*, in *COMSOL Conference*. 2008: Hannover.
79. Rai, R., et al., *Review: friction stir welding tools.* Science and Technology of Welding and Joining, 2011. **16**(4): p. 325-342.
80. Limited, C.M. and T. Cambridge, *ADVANCES IN TOOLING MATERIALS FOR FRICTION.*
81. He, X., F. Gu, and A. Ball, *A review of numerical analysis of friction stir welding.* Progress in Materials Science, 2014. **65**: p. 1-66.
82. Shercliff, M.J.R.a.H.R., *Analytical Modeling of Microstructure Development in Friction Stir Welding*, in *First International Symposium on Friction Stir Welding*. 1999: thousand Oaks, CA.
83. Chao, Y.J., X. Qi, and W. Tang, *Heat Transfer in Friction Stir Welding—Experimental and Numerical Studies.* Journal of Manufacturing Science and Engineering, 2003. **125**(1): p. 138.
84. Tang, W., et al., *Heat Input and Temperature Distribution in Friction Stir Welding.* Journal of Materials Processing & Manufacturing Science, 1998. **7**(2): p. 163-172.

85. Feng, J.E.G.a.Z., *Heat Flow Model for Friction Stir Welding of Aluminum Alloys,*. J. Mater. Process. Manuf. Sci., 1998. **7**: p. 185-194.
86. M. Song, R.K., *Numerical and experimental study of the heat transfer process in friction stir welding.* Proceedings of the Institution of Mechanical Engineers, Part B, 2003. **217**: p. 73-85.
87. Cioffi, F., *Estudio de la microestructura, las propiedades mecánicas y las tensiones residuales en un chapón de aleación AA7075 soldado por Friction Stir Welding*, in *Metalurgia Física*. 2012, Universidad Carlos III de Madrid: Madrid, España.
88. Myhr, O.R. and Ø. Grong, *Modelling of non-isothermal transformations in alloys containing a particle distribution.* Acta Materialia, 2000. **48**(7): p. 1605-1615.
89. Myhr, O.R. and Ø. Grong, *Process modelling applied to 6082-T6 aluminium weldments—II. Applications of model.* Acta Metallurgica et Materialia, 1991. **39**(11): p. 2703-2708.
90. Myhr, O.R., Ø. Grong, and S.J. Andersen, *Modelling of the age hardening behaviour of Al–Mg–Si alloys.* Acta Materialia, 2001. **49**(1): p. 65-75.
91. Myhr, O.R., et al., *Modelling of the microstructure and strength evolution in Al–Mg–Si alloys during multistage thermal processing.* Acta Materialia, 2004. **52**(17): p. 4997-5008.
92. Derry, C.G. and J.D. Robson, *Characterisation and modelling of toughness in 6013-T6 aerospace aluminium alloy friction stir welds.* Materials Science and Engineering: A, 2008. **490**(1–2): p. 328-334.
93. Mochizuki, M., et al., *Fracture toughness of structural aluminium alloy thick plate joints by friction stir welding.* Science and Technology of Welding and Joining, 2006. **11**(3): p. 366-370.
94. Withers, P.J. and H.K.D.H. Bhadeshia, *Residual stress. Part 1 – Measurement techniques.* Materials Science and Technology, 2001. **17**(4): p. 355-365.
95. Veqter. *Residual Stress measurement: overview*. [cited 2014; Available from: http://www.veqter.co.uk/residual-stress-measurement/overview.
96. Torben, L., *Interpretation and Analysis of Lattice Strain Data*, in *Introduction to the Characterization of Residual Stress by Neutron Diffraction*. 2005, CRC Press. p. 203-262.
97. Woo, W., et al., *Neutron diffraction measurements of residual stresses in friction stir welding: a review.* Science and Technology of Welding and Joining, 2011. **16**(1): p. 23-32.
98. Altenkirch, J., et al., *The effect of tensioning and sectioning on residual stresses in aluminium AA7749 friction stir welds.* Materials Science and Engineering: A, 2008. **488**(1–2): p. 16-24.
99. Prime, M.B., et al., *Residual stress measurements in a thick, dissimilar aluminum alloy friction stir weld.* Acta Materialia, 2006. **54**(15): p. 4013-4021.
100. Ericsson, M. and R. Sandström, *Influence of welding speed on the fatigue of friction stir welds, and comparison with MIG and TIG.* International Journal of Fatigue, 2003. **25**(12): p. 1379-1387.
101. P.M.G.P. Moreira, A.M.P.d.J., A.S. Ribeiro, *Assessment of the Fatigue Behaviour of Friction Stir Welded Joints: Aluminium Alloy 6082-T6.* Key Engineering Materials 2007. **348-349**: p. 209-212.
102. M Ericsson, R.S., J Hagström, *Fatigue of friction stir welded AlMgSi-alloy 6082*, in *2nd Int Symp on Friction stir welding*. 2000: Gothenburg
103. John, R., K.V. Jata, and K. Sadananda, *Residual stress effects on near-threshold fatigue crack growth in friction stir welds in aerospace alloys.* International Journal of Fatigue, 2003. **25**(9–11): p. 939-948.

104. Ni, D.R., et al., *Residual stresses and high cycle fatigue properties of friction stir welded SiCp/AA2009 composites.* International Journal of Fatigue, 2013. **55**(0): p. 64-73.
105. Pouget, G. and A.P. Reynolds, *Residual stress and microstructure effects on fatigue crack growth in AA2050 friction stir welds.* International Journal of Fatigue, 2008. **30**(3): p. 463-472.
106. Tra, T.H., M. Okazaki, and K. Suzuki, *Fatigue crack propagation behavior in friction stir welding of AA6063-T5: Roles of residual stress and microstructure.* International Journal of Fatigue, 2012. **43**(0): p. 23-29.
107. James, M.N., D.G. Hattingh, and G.R. Bradley, *Weld tool travel speed effects on fatigue life of friction stir welds in 5083 aluminium.* International Journal of Fatigue, 2003. **25**(12): p. 1389-1398.
108. Park, I.-D., et al., *Structural considerations in friction welding of hybrid Al2O3-reinforced aluminum composites.* Transactions of Nonferrous Metals Society of China, 2011. **21, Supplement 1**(0): p. s42-s46.
109. Srinivasan, M., et al., *Feasibility of joining AZ31B magnesium metal matrix composite by friction welding.* Materials & Design, 2011. **32**(3): p. 1672-1676.
110. Thomas, W.M., E. D. Nicholas, and S. W. Kallee, *Friction based technologies for joining and processing*, in *TMS Friction Stir Welding and Processing Conference*, T. Ltd, Editor. 2001: Indianapolis.
111. M.B.D. Ellis, M.F.G.a.P.D.T., *Joining Aluminium Based MMCs.* Materials World, 1994. **2**(8): p. 415-17.
112. Amirizad, M., et al., *Evaluation of microstructure and mechanical properties in friction stir welded A356+15%SiCp cast composite.* Materials Letters, 2006. **60**(4): p. 565-568.
113. Bozkurt, Y., *Weldability of metal matrix composites by friction stir welding at low welding parameters.* Materials and technology, 2011. **45**(5): p. 407-412.
114. D. J. Shindo, A.R.R., L. E. Murr, *Shape optimization for tool wear in the friction-stir welding of cast AI359-20% SiC MMC.* Journal of materials science, 2002. **37**: p. 4999 - 5005.
115. D. Storjohann, O.M.B., S.S. Babu, S.A. David, P.S. Skald, and E.E. Bloom, *Fusion and Friction Stir Welding of Aluminum-Metal-Matrix Composites.* Metalurgical and Materials Transactions A, 2005. **36A**: p. 3237-3247.
116. Guo, J., et al., *Joining of AA1100–16 vol.-%B4C metal matrix composite using laser welding and friction stir welding.* Canadian Metallurgical Quarterly, 2012. **51**(3): p. 277-283.
117. Fernandez, G.J. and L.E. Murr, *Characterization of tool wear and weld optimization in the friction-stir welding of cast aluminum 359+20% SiC metal-matrix composite.* Materials Characterization, 2004. **52**(1): p. 65-75.
118. J.A. Lee, R.W.C., and J. Ding, *Friction Stir Welding for Aluminum Metal Matrix Composites (MMC's).* NASA report, 1999.
119. Nami, H., et al., *Microstructure and mechanical properties of friction stir welded Al/Mg2Si metal matrix cast composite.* Materials & Design, 2011. **32**(2): p. 976-983.
120. Prado, R.A., et al., *Tool wear in the friction-stir welding of aluminum alloy 6061 + 20% Al2O3: a preliminary study.* Scripta Materialia, 2001. **45**: p. 75-80.
121. Prado, R.A., et al., *Self-optimization in tool wear for friction-stir welding of Al 6061+20% Al2O3 MMC.* Materials Science and Engineering: A, 2003. **349**(1-2): p. 156-165.
122. Uzun, H., *Friction stir welding of SiC particulate reinforced AA2124 aluminium alloy matrix composite.* Materials & Design, 2007. **28**(5): p. 1440-1446.
123. Wang, D., et al., *Friction stir welding of SiCp/2009Al composite plate.* Materials & Design, 2013. **47**: p. 243-247.

124. Liu, H.J., et al., *Wear characteristics of a WC–Co tool in friction stir welding of AC4A+30vol%SiCp composite.* International Journal of Machine Tools and Manufacture, 2005. **45**(14): p. 1635-1639.
125. Cepeda-Jiménez, C.M., et al., *Study of hot deformation of an Al–Cu–Mg alloy using processing maps and microstructural characterization.* Materials Science and Engineering: A, 2012. **552**(0): p. 530-539.
126. Higdon, A., *5.3 Torsional shearing formula in "Mechanics of materials"*. 1985: Wiley.
127. Cverna, F. and A.S.M.I.M.P.D. Committee, *ASM Ready Reference: Thermal properties of metals*. 2002: ASM International.
128. Thomas, W.M., K.I. Johnson, and C.S. Wiesner, *Friction Stir Welding – Recent Developments in Tool and Process Technologies.* Advanced Engineering Materials, 2003. **5**(7): p. 485-490.
129. W.M. Thomas, D.G.S., I.M. Norris, and R. de Frias, *Friction Stir Welding-Tools and Developments*, in *FSW Seminar*. 2002: OPporto, Portugal.
130. Vijay, S.J. and N. Murugan, *Influence of tool pin profile on the metallurgical and mechanical properties of friction stir welded Al-10 wt.% TiB2 metal matrix composite.* Materials & Design, 2010. **31**(7): p. 3585-3589.
131. Gopalakrishnan, S. and N. Murugan, *Prediction of tensile strength of friction stir welded aluminium matrix TiCp particulate reinforced composite.* Materials & Design, 2011. **32**(1): p. 462-467.
132. Feng, A.H. and Z.Y. Ma, *Formation of Cu2FeAl7 phase in friction-stir-welded SiCp/Al–Cu–Mg composite.* Scripta Materialia, 2007. **57**(12): p. 1113-1116.
133. Ceschini, L., et al., *Effect of friction stir welding on microstructure, tensile and fatigue properties of the AA7005/10vol.%Al2O3p composite.* Composites Science and Technology, 2007. **67**(3–4): p. 605-615.
134. Ceschini, L., et al., *Microstructure, tensile and fatigue properties of AA6061/20vol.%Al2O3p friction stir welded joints.* Composites Part A: Applied Science and Manufacturing, 2007. **38**(4): p. 1200-1210.
135. Chen, X.G., et al., *Microstructure and mechanical properties of friction stir welded AA6063–B4C metal matrix composites.* Materials Science and Engineering: A, 2009. **518**(1–2): p. 174-184.
136. Periyasamy, P., et al., *Multi-objective optimization of friction stir welding parameters using desirability approach to join Al/SiCp metal matrix composites.* Transactions of Nonferrous Metals Society of China, 2013. **23**(4): p. 942-955.
137. *MP159 alloy*, L.S.S. Company, Editor. 2007.
138. Devanathan, C. and A.S. Babu, *Friction Stir Welding of Metal Matrix Composite Using Coated Tool.* Procedia Materials Science, 2014. **6**(0): p. 1470-1475.
139. Trimble, D., J. Monaghan, and G.E. O'Donnell, *Force generation during friction stir welding of AA2024-T3.* CIRP Annals - Manufacturing Technology, 2012. **61**(1): p. 9-12.
140. Su, H., et al., *Simultaneous measurement of tool torque, traverse force and axial force in friction stir welding.* Journal of Manufacturing Processes, 2013. **15**(4): p. 495-500.
141. Colligan, K.J., *2 - The friction stir welding process: an overview*, in *Friction Stir Welding*, D. Lohwasser and Z. Chen, Editors. 2010, Woodhead Publishing. p. 15-41.
142. Sharma, C., D.K. Dwivedi, and P. Kumar, *Effect of welding parameters on microstructure and mechanical properties of friction stir welded joints of AA7039 aluminum alloy.* Materials & Design, 2012. **36**: p. 379-390.
143. Chen, H.-B., et al., *The investigation of typical welding defects for 5456 aluminum alloy friction stir welds.* Materials Science and Engineering: A, 2006. **433**(1–2): p. 64-69.
144. R. Zettler, T.V., M. Schmucker, *9 - Effects and defects of friction stir welds*, in *Friction Stir Welding: From Basics to Applications*, Z.C. D. Lohwasser, Editor. 2010.

145. Arbegast, W.J., *13 - Application of Friction Stir Welding and Related Technologies*, in *Friction Stir Welding and Processing*, M.W.M. R.S. Mishra, Editor. 2007, ASM International.
146. Sato, Y., M. Urata, and H. Kokawa, *Parameters controlling microstructure and hardness during friction-stir welding of precipitation-hardenable aluminum alloy 6063.* Metallurgical and Materials Transactions A, 2002. **33**(3): p. 625-635.
147. Balasubramanian, V., *Relationship between base metal properties and friction stir welding process parameters.* Materials Science and Engineering: A, 2008. **480**(1–2): p. 397-403.
148. Sato, Y.S., et al., *Characteristics of the kissing-bond in friction stir welded Al alloy 1050.* Materials Science and Engineering: A, 2005. **405**(1-2): p. 333-338.
149. Al-Jarrah, J.A., et al., *Welding equality and mechanical properties of aluminum alloys joints prepared by friction stir welding.* Materials & Design, 2014. **56**: p. 929-936.
150. Di, S., et al., *The influence of zigzag-curve defect on the fatigue properties of friction stir welds in 7075-T6 Al alloy.* Materials Chemistry and Physics, 2007. **104**(2-3): p. 244-248.
151. Zhou, C., X. Yang, and G. Luan, *Effect of oxide array on the fatigue property of friction stir welds.* Scripta Materialia, 2006. **54**(8): p. 1515-1520.
152. Okamura, H., et al., *Behaviour of oxides during friction stir welding of aluminium alloy and their effect on its mechanical properties.* Welding International, 2002. **16**(4): p. 266-275.
153. Hou, X., et al., *Influences of joint geometry on defects and mechanical properties of friction stir welded AA6061-T4 T-joints.* Materials & Design, 2014. **53**: p. 106-117.
154. Zhao, Y., et al., *Defects and tensile properties of 6013 aluminum alloy T-joints by friction stir welding.* Materials & Design, 2014. **57**: p. 146-155.
155. Leonard, A. and S. Lockyer. *Flaws in friction stir welds*.
156. A. OOSTERKAMP, L.D.O., AND A. NORDEIDE, *'Kissing Bond' Phenomena in Solid-State Welds of Aluminum Alloys.* Supplement to the Welding Journal, 2004: p. 225-231.
157. Cui, L., et al., *Characteristics of defects and tensile behaviors on friction stir welded AA6061-T4 T-joints.* Materials Science and Engineering: A, 2012. **543**: p. 58-68.
158. Lockwood, W. and A. Reynolds, *Simulation of the global response of a friction stir weld using local constitutive behavior.* Materials Science and Engineering: A, 2003. **339**(1): p. 35-42.
159. Lockwood, W.D., B. Tomaz, and A. Reynolds, *Mechanical response of friction stir welded AA2024: experiment and modeling.* Materials Science and Engineering: A, 2002. **323**(1): p. 348-353.
160. Noyan, I.C. and J.B. Cohen, *Residual stress: measurement by diffraction and interpretation*. 1987: Springer.
161. Steuwer, A., et al., *The variation of the unstrained lattice parameter in an AA7010 friction stir weld.* Acta Materialia, 2007. **55**(12): p. 4111-4120.
162. Ganguly, S., L. Edwards, and M.E. Fitzpatrick, *Problems in using a comb sample as a stress-free reference for the determination of welding residual stress by diffraction.* Materials Science and Engineering: A, 2011. **528**(3): p. 1226-1232.
163. Guo, J., P. Gougeon, and X.G. Chen, *Study on laser welding of AA1100-16 vol.% B4C metal–matrix composites.* Composites Part B: Engineering, 2012. **43**(5): p. 2400-2408.
164. Lei, Y.-c., et al., *In-situ weld-alloying plasma arc welding of SiCp/Al MMC.* Transactions of Nonferrous Metals Society of China, 2007. **17**(2): p. 313-317.
165. Liu, H., et al., *Microstructure and mechanical properties of friction stir welded AC4A+ 30vol.% SiCp composite.* Materials & Design, 2015. **65**: p. 395-400.

166. Liu, H.J., H. Fujii, and K. Nogi. *Wear behaviour of hard alloy tools in the friction stir welding of AC4A+30vol.%SiCp aluminum matrix composite*. in *5th; International Symposium, Friction stir welding* 2004. Metz, France.
167. Lorrain, O., et al., *Understanding the material flow path of friction stir welding process using unthreaded tools.* Journal of Materials Processing Technology, 2010. **210**(4): p. 603-609.
168. Schneider, J.A., *3 - Temperature Distribution and Resulting Metal Flow*, in *Friction Stir Welding and Processing*, M.W.M. R.S. Mishra, Editor. 2007, ASM International. p. 36-49.
169. Park, H.S., *Basal Plane Texture and Flow Pattern in Friction Stir Weld of a Magnesium Alloy.* Materials Science and Engineering: A, 2003.
170. Sato, Y., et al., *Microtexture in the friction-stir weld of an aluminum alloy.* Metallurgical and Materials Transactions A, 2001. **32**(4): p. 941-948.
171. Field, D., et al., *Heterogeneity of crystallographic texture in friction stir welds of aluminum.* Metallurgical and Materials Transactions A, 2001. **32**(11): p. 2869-2877.
172. Stachowiak, G.W. and A.W. Batchelor, *1 - Introduction*, in *Engineering Tribology (Third Edition)*, G.W.S.W. Batchelor, Editor. 2006, Butterworth-Heinemann: Burlington. p. 1-9.
173. Stachowiak, G.W. and A.W. Batchelor, *10 - Fundamentals of Contact Between Solids*, in *Engineering Tribology (Third Edition)*, G.W.S.W. Batchelor, Editor. 2006, Butterworth-Heinemann: Burlington. p. 461-499.
174. Stachowiak, G.W. and A.W. Batchelor, *12 - Adhesion and Adhesive Wear*, in *Engineering Tribology (Third Edition)*, G.W.S.W. Batchelor, Editor. 2006, Butterworth-Heinemann: Burlington. p. 553-572.
175. Buckley, D., *Surface Effects in Adhesion, Friction, Wear and Lubrication.* 1983.
176. Somiya, S., *Handbook of Advanced Ceramics: Materials, Applications, Processing, and Properties*. 2013: Elsevier Science.
177. *Heat input*. The Welding Institute: UK. p. 1-7.
178. Hamilton, C., S. Dymek, and A. Sommers, *A thermal model of friction stir welding in aluminum alloys.* International Journal of Machine Tools and Manufacture, 2008. **48**(10): p. 1120-1130.
179. Kang, S.-W. and B.-S. Jang, *Comparison of friction stir welding heat transfer analysis methods and parametric study on unspecified input variables.* Journal of Mechanical Science and Technology, 2014. **28**(10): p. 4233-4246.
180. Peel, M.J., et al., *Dissimilar friction stir welds in AA5083-AA6082. Part I: Process parameter effects on thermal history and weld properties.* Metallurgical and Materials Transactions A, 2006. **37**(7): p. 2183-2193.
181. Kumar, K., et al., *An Investigation of Friction During Friction Stir Welding of Metallic Materials.* Materials and Manufacturing Processes, 2009. **24**(4): p. 438-445.
182. Schmidt, H., J. Hattel, and J. Wert, *An analytical model for the heat generation in friction stir welding.* Modelling and Simulation in Materials Science and Engineering, 2004. **12**(1): p. 143.
183. Nardone, V.C. and K.M. Prewo, *On the strength of discontinuous silicon carbide reinforced aluminum composites.* Scripta Metallurgica, 1986. **20**(1): p. 43-48.
184. Piggott, M.R., *5 - Reinforcement Processes*, in *Load-Bearing Fibre Composites*, M.R. Piggott, Editor. 1980, Pergamon. p. 83-99.
185. Hsueh, C.-H., *Elastic load transfer from partially embedded axially loaded fibre to matrix.* Journal of Materials Science Letters, 1988. **7**(5): p. 497-500.
186. Starink, M.J.a.S., S., *Shear lag models for discontinuous composites: fibre end stresses and weak interface layers.* Materials Science and Engineering A, 1999. **2**: p. 270-277.

187. Llorca, J. and C. Gonzalez, *Microstructural factors controlling the strength and ductility of particle-reinforced metal-matrix composites.* Journal of the Mechanics and Physics of Solids, 1998. **46**(1): p. 1-28.
188. F. J. Humphreys, A.B., M. R. Djazeb. *The microstructure and strength of particulate metal-matrix composites*. in *12th Risø Int. Symp. on Materials Science, Metal-Matrix Composites – Processing, Microstructure and Properties*. 1991. Roskilde, USA.
189. Humphreys, F.J. *Deformation and annealing mechanisms in discontinuously reinforced metal-matrix composites*. in *9th Risø Int. Symp. on Mechanical and Physical Behavior of Metallic and Ceramic Composites*. 1988. Roskilde, USA.
190. Kiser, M.T., F.W. Zok, and D.S. Wilkinson, *Plastic flow and fracture of a particulate metal matrix composite.* Acta Materialia, 1996. **44**(9): p. 3465-3476.
191. Hauk, V., *Definition of macro- and microstresses and their separation*, in *Structural and Residual Stress Analysis by Nondestructive Methods: Evaluation - Application - Assessment*. 1997, Elsevier Science.
192. Paradowska, A., et al., *Investigation of reference samples for residual strain measurements in a welded specimen by neutron and synchrotron X-ray diffraction.* Physica B: Condensed Matter, 2006. **385–386, Part 2**(0): p. 904-907.
193. Jiang, W., et al., *Neutron diffraction and finite element modeling to study the weld residual stress relaxation induced by cutting.* Materials & Design, 2013. **51**(0): p. 415-420.
194. Bruno, G., R. Fernández, and G. González-Doncel, *Gauge volume effects in residual stress determination by neutron diffraction: The strength differential effect in metal matrix composites.* Materials Science and Engineering: A, 2006. **437**(1): p. 100-108.
195. Meijer, G., F. Ellyin, and Z. Xia, *Aspects of residual thermal stress/strain in particle reinforced metal matrix composites.* Composites Part B: Engineering, 2000. **31**(1): p. 29-37.
196. Nandan, R., T. DebRoy, and H.K.D.H. Bhadeshia, *Recent advances in friction-stir welding – Process, weldment structure and properties.* Progress in Materials Science, 2008. **53**(6): p. 980-1023.
197. Simar, A., et al., *Integrated modeling of friction stir welding of 6xxx series Al alloys: Process, microstructure and properties.* Progress in Materials Science, 2012. **57**(1): p. 95-183.
198. Feng, A.H., B.L. Xiao, and Z.Y. Ma, *Effect of microstructural evolution on mechanical properties of friction stir welded AA2009/SiCp composite.* Composites Science and Technology, 2008. **68**(9): p. 2141-2148.
199. Baxter, S.C. and A.P. Reynolds, *Characterization of Reinforcing Particle Size Distribution in a Friction Stir Welded Al-SiC Extrusion*, in *Lightweight Alloys for Aerospace Application*. 2001, John Wiley & Sons, Inc. p. 283-293.
200. Marzoli, L.M., et al., *Friction stir welding of an AA6061/Al2O3/20p reinforced alloy.* Composites Science and Technology, 2006. **66**(2): p. 363-371.
201. Cavaliere, P., et al., *Friction Stir Welding of Ceramic Particle Reinforced Aluminium Based Metal Matrix Composites.* Applied Composite Materials, 2004. **11**(4): p. 247-258.

7. ANEXO 1

Applied Soft Computing 40 (2016) 429–438

Contents lists available at ScienceDirect

Applied Soft Computing

journal homepage: www.elsevier.com/locate/asoc

Using evolutionary algorithms to determine the residual stress profile across welds of age-hardenable aluminum alloys

J. Ignacio Hidalgo [a,*], Ricardo Fernández [b], J. Manuel Colmenar [c], Florencia Cioffi [b], José L. Risco-Martín [a], Gaspar González-Doncel [b]

[a] Adaptive and Bioinspired System Group, Universidad Complutense de Madrid, Calle del Profesor José García Santesmases 9, 28040 Madrid, Spain
[b] Department of Physical Metallurgy, Centro Nacional de Investigaciones Metalúrgicas, CENIM, C.S.I.C., Av. de Gregorio del Amo 8, 28040 Madrid, Spain
[c] Universidad Rey Juan Carlos, Calle Tulipán, 28933 Móstoles, Spain

ARTICLE INFO

Article history:
Received 11 February 2015
Received in revised form
17 September 2015
Accepted 1 November 2015
Available online 2 December 2015

Keywords:
Multi-objective evolutionary algorithm
Real world application
Residual stress determination

ABSTRACT

This paper presents an evolutionary based method to obtain the un-stressed lattice spacing, d_0, required to calculate the residual stress profile across a weld of an age-hardenable aluminum alloy, *AA*2024. Due to the age-hardening nature of this alloy, the d_0 value depends on the heat treatment. In the case of welds, the heat treatment imposed by the welding operation differs significantly depending on the distance to the center of the joint. This implies that a variation of d_0 across the weld is expected, a circumstances which limits the possibilities of conventional analytical methods to determine the required d_0 profile. The interest of the paper is, therefore, two-fold: First, to demonstrate that the application of an evolutionary algorithm solves a problem not addressed in the literature such as the determination of the required data to calculate the residual stress state across a weld. Second, to show the robustness of the approximation used, which allows obtaining solutions for different constraints of the problem. Our results confirm the capacity of evolutionary computation to reach realistic solutions under three different scenarios of the initial conditions and the available experimental data.

1. Introduction

Aluminium Alloys (*AA*) are used in a plethora of industrial processes. For example, alloys of the *AA2xxx* series are commonly used in aircraft structures. In many applications, AAs need to be welded, a process which is difficult to control using common fusion welding techniques in comparison to other metals, such as steels. This is due in part to the high thermal conductivity of aluminum. As an alternative to conventional methods, Friction Stir Welding (FSW) [1,2] has proven to solve most of the difficulties associated with the joining of aluminum alloys [3–5].

However, the development of a Residual Stress (RS) is, as in other welding procedures, inherent to this joining operation. In FSW the existence of a RS is mainly due to the non-homogeneous nature of the severe plastic deformation phenomenon involved and the heat generated during the welding process. The FSW process also involves significant changes in the microstructure and the mechanical properties of the material. There are various methods for determining residual stresses in a component. We can use destructive techniques, such as "hole drilling", sectioning or indentation, and nondestructive techniques, such as those based on X-ray and neutron diffraction [6]. These diffraction techniques use the lattice spacing as an atomic probe to measure elastic deformations. By comparing the lattice spacing in the stressed and un-stressed condition, one can determine, first, the elastic deformation and, then, the associated stress using well established linear elasticity theory equations and tabulated elastic constants. One of the advantages of the diffraction techniques is that the full triaxial stress state inside a component can be investigated if one takes advantage of the high penetrating capacity of neutrons and (hard) X-rays [7,8].

As it will be shown, the crucial factor to determine the RS state by these methods is the availability of a reliable un-stressed lattice spacing value, d_0. When a unique constant, d_0 value is sought, conventional analytical procedures can be applied to determine the residual stress state. For the case of age-hardening AA2xxx series alloys, however, d_0 is strongly dependent on the amount of atoms in solid solution (such as copper atoms) and, in turn, on the heat treatment imposed to the component. If the heat treatment is uniform through the sample, a constant d_0 is expected, and the RS calculation is straightforward. But for the case of welds the heat treatment varies dramatically across the weld and, as a consequence, a variation of d_0 should be taken into account. For these cases, conventional analytical procedures are no longer applicable [9,10].

Recently, evolutionary algorithms (EAs) have been applied for solving optimization, modeling and identification problems [11–14]. The present investigation addresses the capacity and robustness of EAs to solve the above difficulty. Several scenarios, depending on the initial constraints imposed by the experimental data available from neutron diffraction experiment, are discussed. Specifically, the unstressed lattice spacing variation under the three scenarios and the resulting RS profile across the weld are obtained. The use of EAs, applied to current used methods to determine residual stress fields, is very appropriate when d_0 value is not constant. We solve this optimization problem using a Multi-Objective Evolutionary Algorithm (MOEA). The nature of the problem, where the values for a set of parameters have to be found, allows for a direct encoding of these parameters within a chromosome as in other problems [15]. In summary, the motivation of this research relies on the need of alternative methods to conventional analytical ones in order to find the required information (in this case, the d_0 values) to calculate the residual stress profile across welds of age-hardening Al alloys.

* Corresponding author. Tel.: +34 913947537; fax: +34 913847527.
E-mail address: hidalgo@ucm.es (J. Ignacio Hidalgo).

We have found that the experimental results are metallurgically consistent, allowing the characterization of the residual stress state of the weld.

The main contributions of the present work are the following:

- We present a method for obtaining the distribution of d_0 parameter, based on a MOEA, under different measurement scenarios.
- We use for the first time the capacity of EAs to calculate the residual stress across a weld of 2024 alloy using neutron diffraction data of the lattice spacing variations.
- We analyze the robustness of the proposed MOEA.

The rest of the paper is organized as follows. A description of the problem is made in Section 2. Section 3 describes the metallurgical experimental details. Section 4 gives the details of the evolutionary algorithm implementation. Section5 presents the experimental results in terms of both the metallurgical solution and the convergence and robustness of the evolutionary approach. Finally, Section 6 summarizes the conclusions of this work.

2. Problem description

Any forming process used in the industry (rolling, extrusion, welding, deep drawing, etc.) for the fabrication of components leads to the development of a RS which extends over the resulting component. This is because, generally, these procedures are non-homogeneous in nature and the development of a RS is inherent to non-homogeneous dimensional changes of bodies (due to deformation, thermal effects, or both). Because this RS varies throughout the whole piece, it is usually referred to as a macroscopic stress, M-RS, to distinguish it from the microscopic stresses, m-RS, inherent to the material microstructure [16]. Understanding the development of M-RSs and their magnitude is of great importance in structural engineering because it is a key factor in the design of structural components. Disregarding this stress may be critical and the cause of component rupture at stress levels below that at which failure would be expected from the applied stresses alone. As mentioned above, several techniques have been developed in the past decades aimed at determining this stress.

Probably, the most successful ones among them are those which make use of the diffraction phenomenon. Given the crystallographic nature of most engineering materials (metals), diffraction allows determining with high precision, lattice spacing values, d_{hkl}. In this way, an expansion or contraction of the given lattice spacing is identified with an elastic strain and, associated to it through the linear elasticity theory, the corresponding internal stress. Determining this expansion/contraction of the lattice spacing with respect to a relaxed value, d^0_{hkl}, is, hence, the core of the diffraction methods to calculate internal (and residual) stresses in structural materials and components. The use of diffraction methods implies the use of Bragg's law,

$$2 \cdot d_{hkl} \cdot \sin(\theta) = \lambda \tag{1}$$

where θ is the Bragg's angle and λ the wavelength of the incident beam. Bragg's law allows determining d_{hkl} for different spatial directions. Then, by using the formula,

$$\epsilon = \frac{d_{hkl} - d^0_{hkl}}{d^0_{hkl}} \tag{2}$$

the elastic strain, ϵ, can be calculated in the same way as macroscopic strains are obtained in conventional mechanical testing with the help of a suitable extensometer. Then, direct use of the generalized Hookes law of elasticity, namely,

$$\sigma_i = \frac{E}{(1+\nu)\cdot(1-2\nu)} \cdot [(1-\nu)\epsilon_i + \nu(\epsilon_j + \epsilon_k)] \tag{3}$$

where σ_i is the i component of the stress tensor, related to the three strain components, ϵ_i, ϵ_j andϵ_k, E the elastic modulus, and ν the Poisson's ratio provides the stress state of the component under study.

Formerly, when only standard laboratory X-rays were available, determining the residual stress in components was limited to the near surface region where a bi-axial stress state should be assumed. Under this approximation, the extra calculation of an un-stressed spacing value is not needed since it can be obtained from the fact that the normal stress component is null.

More recently, however, the availability of high penetration capacity of neutrons and synchrotron X-rays has allowed calculating the full tri-axial residual stress state inside materials. In these cases, the extra calculation of an un-stressed lattice spacing value is required. In fact, it is very likely that the most critical issue and a key factor for the determination of this M-RS is, precisely, the availability of an accurate and reliable value of d^0_{hkl}. This is because small fluctuations or experimental errors in this parameter (and of d_{hkl} itself) can lead to huge variations of the calculated strain and the resulting stress. For example, a variation of some few 10^{-14} m (or 10^{-3} Å) in the value of d^0_{hkl}, say 2×10^{-14} m, can lead to a variation of the stress in the order of 10 MPa for the case of aluminum alloys. This variation increases with an increase of materials stiffness, e.g., titanium or steels. As a consequence, the development of reliable methods to determine d^0_{hkl} has been the subject of many efforts. A detailed description of these methods can be found in [17,18]. Here, a brief description of the main ones namely, the powder method, the sample sectioning method, and the use of the equilibrium conditions is given.

2.1. Powder method

Powder of the same material under study guarantees a macroscopic un-stressed reference since powder is always free of long range stresses. Furthermore, powder is susceptible to undergo a heat treatment if necessary: it is known that the lattice spacing can be strongly affected by the amount of solid solution elements and, hence, of the precipitation state. This is the case of some age-hardening aluminum alloys. These aluminum alloys, such as those of the 2*xxx* and 7*xxx* series, widely employed in the aeronautical an aerospace industries, have the particularity that their mechanical properties are strongly dependent on the thermal history, i.e., their precipitation state. Hence, if powder is to be used as reference for d^0_{hkl} determination in components fabricated from one of these alloys, one must be sure that the heat treatment undergone by the alloy powder is the same as that of the component under study. This task is, however, virtually impossible in some cases, for example in welds, where the specific thermal cycle imposed during this process is not known. Furthermore, it may change dramatically across the weld. This implies that the powder method cannot be recommended as a way to determine d^0_{hkl} in complex cases such as in welds of age hardening alloys.

2.2. Sample sectioning in small pieces or combs

In the same manner as powder particles do not hold a M-RS, a sample that is cut into small pieces relieves its M-RS. In this way, one can section the sample (or a twin replica if it is not possible to section the sample) such that the size of the pieces is smaller than the expected residual stress variation: The larger the stress gradient or the shorter its range, the smaller the piece dimension to ensure stress relaxation. The use of these small pieces, cut from different parts of the sample, allows determining the specific d^0_{hkl} value at the corresponding sample position and avoids errors associated with compositional changes or precipitation variations resulting from possible heat treatments. When large number of pieces are required, as in the case of welds, they can be organized by using "comb" samples. These are samples where the different stress relaxed pieces are maintained together and, hence, "recall" their specific coordinates with respect to those in the original component

from which the comb was extracted. Furthermore the exact thermal cycle undergone at each "tooth" in the case of a weld, is kept. This guarantees, in principle, that a reliable d^0_{hkl} at each location is available regardless that this un-stressed lattice spacing varies through the component.

There are, however, several limitations to the comb method. First one is the procedure itself. Since the comb must be machined out for the d^0_{hkl} measurements (after conducting the measurements on the stressed sample), two rounds of neutron diffraction measurements must be carried out in separate experiments. This implies different configuration of the instrument in the two experiments, which can affect the positions of the diffracted peaks appreciably. To avoid this, it is common to extract a comb piece from the sample under study, so that both the sample and the comb can be studied in the frame of the same round of measurements using the same experimental set up [19]. In this case, however, an alteration of the RS state to be studied may occur.

Instead, one can prepare two welds such that a similar RS state results in both cases: one of the welds would be used to measure the lattice spacing across the weld and the second one to extract the comb sample. Both the weld and the comb could be measured during the same experiment. Even in this case it is possible that the precipitation and solid solution state differ from one weld to the other. As reported in [20], very small variations in *Cu* contents greatly modify the lattice spacing of aluminum. Since it is unlikely that the temperature cycle undergone in both welds is identical (due, for example, to a slight difference in the temperature of the backing plate), the possibility to obtain the same microstructural gradient across the weld in both experiments is minimal. This makes the use of a reference comb extracted from a replica weld risky, even when the welding parameters are ostensibly the same.

2.3. Equilibrium conditions

A not sufficiently exploited method which avoids the extra experimental work required by the above two methods to determine d^0_{hkl} employs a fully mathematical procedure which makes use of well known principles of Mechanics: These principles are the equilibrium conditions of stresses and bending moments [21,22]. According to these principles, the total force perpendicular to any sample section of a solid and the total bending moment of the in-section forces must be null. They are mathematically expressed as:

$$\int \sigma_{\perp} dS = 0 \tag{4}$$

where subindex $\perp$ refers to the normal stress component to section S and for the bending moments, M,

$$\int_S M dS = 0 \tag{5}$$

The use of this method avoids, as mentioned, the tediousness and inaccuracies associated with the handling of powders or sample sectioning to obtain an experimental d^0_{hkl} value. On the contrary, it requires many measurements of d_{hkl} at different locations on selected sample sections to apply Eqs. (4) and (5) with rigor. In this manner, an analytical solution can be obtained as long as d^0_{hkl} remains constant throughout the measured section. However, as we mentioned above, this is not true in many real cases, such as in welds of age hardenable aluminum alloys, where a measurable variation of d^0_{hkl} across the weld is expected. Such a problem cannot be solved analytically by using Eqs. (4) and (5) due to the large number of variables involved. For cases like this, EAs have proven their capacity to arrive to satisfactory solutions [23,24]. In a recent paper [25], an EA has been used to deduce the M-RS profile across a weld conducted between two 10 mm thick plates of AA2024 aluminum alloy, a typical aerospace aluminum alloy with elevated mechanical properties. In the present research a detailed description of the EA used to determine the d^0_{hkl} profile on the basis of neutron diffraction data and in the context of the equilibrium conditions method is made. Furthermore, the results obtained by the EA under three different scenarios or approximations of the possible d^0_{hkl}, according to the different microstructural zones of the weld, are presented.

3. Metallurgical experimental procedures

The aluminum alloy investigated, *AA2024*, is a typical aerospace alloy also used in other applications. It contains *Cu* atoms as the main alloying element. *Cu* atoms combine with *Al* ones leading to precipitates which, under appropriate heat treatments, are semi-coherent with the aluminum lattice. In fact, the strong precipitate-dislocation interaction is the final responsible of the excellent mechanical properties of the alloy. Further information of this alloy, the welding procedure used, the metallographical preparation employed to study the different parts of the weld and the details of the experimental set-up for the neutron diffraction measurements are described in [25]. Here, a brief description of these methods is reported.

The two plates of the alloy, of dimensions $10 \times 296 \times 150\,mm^3$, were butt welded using the PDS-4 Intelligent Stir FSW machine of the AIMEN Technology Center at Porriño, Spain (http://www.aimen.es/). The RS state across the weld was investigated by measuring, first, the lattice spacing of the 311 planes, d_{311}, using neutron diffraction and applying the Braggs law, Eq. (1). Fig. 1 shows the geometry of the welded plate mounted on SALSA diffractometer at the ILL (Institute Laue-Langevin) for the neutron diffraction measurements. In Fig. 2 the geometry of the diffraction phenomenon is shown (incident and diffracted beams and the gauge volume generated, where the lattice spacing in the sample is measured).

These measurements were made at three different depths of the plate: −2.5, −5 and −7.5 mm from the top surface, denoted hereafter as *Front*, *Center* and *Back* zones, respectively. The distance across the weld covered by the measurements extended up to ±85 mm on both sides from the center of the weld. In this way, all regions of the weld, namely the *nugget*, the thermomechanically affected zone *(TMAZ)*, the heat-affected zone *(HAZ)*, and the base material *(BM)*, were covered by the neutron diffraction measurements. Fig. 3 is a scheme of the plate showing the section across the weld where the neutron diffraction measurements were conducted at the three depths (marked as dotted lines in the section).

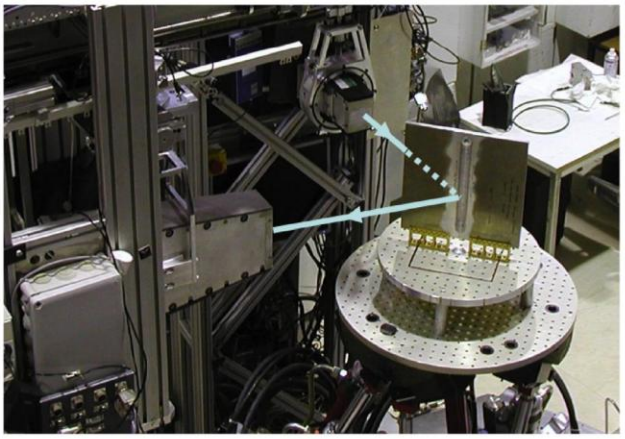

Fig. 1. The AA2024 welded plate (the welding line is in the vertical direction) mounted on the hexapod holder of SALSA instrument at the ILL showing the incoming and diffracted neutron beams.

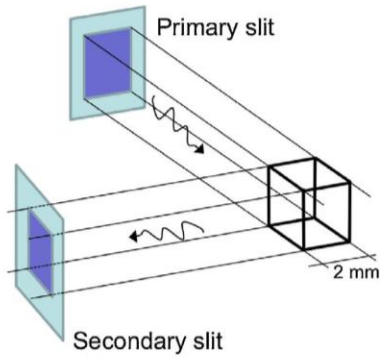

Fig. 2. Scheme of the geometry of the diffraction experiment to determine lattice spacing values (for the 311 planes), showing primary and secondary slits which define the gauge volume ($2 \times 2 \times 2\,mm^3$) in which measurements were made.

After the neutron diffraction measurements, conventional metallographic procedures were used to examine the microstructure of the different regions by optical microscopy after sectioning the welded plate suitability. Finally, hardness measurements were conducted on the cross-section to evaluate the mechanical properties of the different regions across the weld: nugget, TMAZ, HAZ and BM. These measurements were also useful to determine the dimensions of the different regions. The measurements were conducted using a Micromaterials^{TM} nanotest 600 instrumented indenter. Constant displacement mode was used to complete a profile located at the central region, through-the-thickness, along the transverse section of the plate. A 5 μm depth indentation, maintaining 1 mm distance between successive indentations, was used. In this way, a hardness profile covering a total distance of 120 mm was obtained.

4. Evolutionary algorithm

As stated in Section 2.3, we look for a combination of d^0_{hkl} values across the weld, or a d^0_{hkl} profile, that minimizes both, the sum of the longitudinal stresses and the bending moments in a transverse section, S, of the welded plate (Eqs. (4) and (5)). Thus, we are dealing with a bi-objective problem. Under these conditions, we have selected NSGA-II (Non-dominated Sorting Genetic Algorithm II), a well-known MOEA, to solve this problem [26]. In a nutshell, NSGA-II is a fast and elitist MOEA based on a non-dominated sorting approach. NSGA-II is an evolution of NSGA which obtains very good results solving problems with up to three objectives [27,28].

Besides the algorithm, solving a problem under an evolutionary approach requires additional elements. The first one is the definition of a fitness function, which establishes the quality of the candidate solutions in relation to a given objective of the problem. The fitness function guides the search across the space of solutions. Second, a codification of the candidate solutions (also called individuals) must be defined. The codification consists on selecting how each individual is represented into the algorithm. Finally, given that we use a genetic algorithm, the genetic operators must be selected and configured.

4.1. Fitness function

Given a set of z zones in section S of the welded plate and a set of measurements of d_{311} for each one of the z zones, we can define the matrix D as:

$$D = \begin{pmatrix} d_{311}^{\text{Front}}[0] & d_{311}^{\text{Front}}[1] & \cdots & d_{311}^{\text{Front}}[z-1] & d_{311}^{\text{Front}}[z] \\ d_{311}^{\text{Center}}[0] & d_{311}^{\text{Center}}[1] & \cdots & d_{311}^{\text{Center}}[z-1] & d_{311}^{\text{Center}}[z] \\ d_{311}^{\text{Back}}[0] & d_{311}^{\text{Back}}[1] & \cdots & d_{311}^{\text{Back}}[z-1] & d_{311}^{\text{Back}}[z] \end{pmatrix}$$

where $d_{311}^{\text{Front}}[i]$, $d_{311}^{\text{Center}}[i]$, $d_{311}^{\text{Back}}[i]$ is the d_{311} measurement on zone i resulting from the neutron diffraction experiment.

The objective is to find a set of $d_i^{0L_j}$ across the weld, which minimizes F_1 and F_2 simultaneously, where

$$F_1 = T_{L_{\text{Front}}} + T_{L_{\text{Center}}} + T_{L_{\text{Back}}} \quad (6)$$

$$F_2 = M_{\text{Front}} + M_{\text{Back}} \quad (7)$$

where T and M denote stress and bending moment, respectively, subindexes Front, Center, and Back, the corresponding region

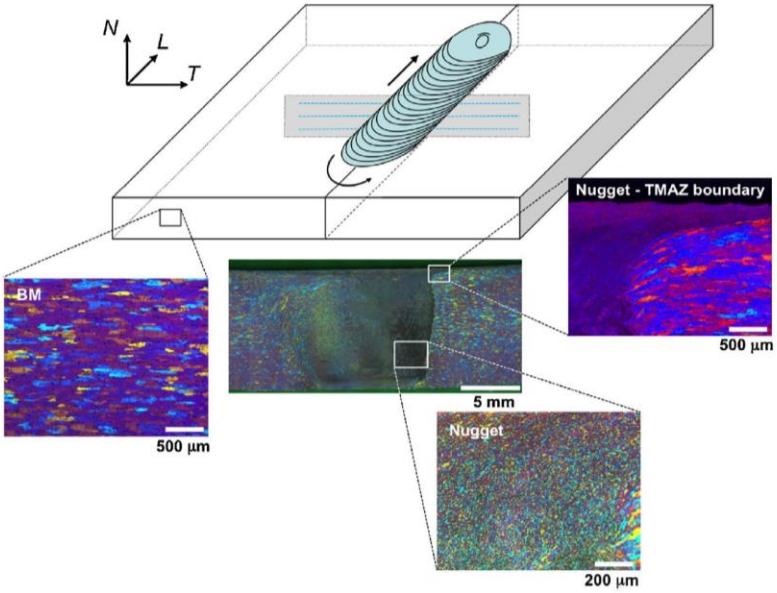

Fig. 3. Scheme of the welded plate showing the section on which the neutron diffraction measurements were made (along the three dotted lines marked in blue in this section). Reference system, denoted by the longitudinal, L, transverse, T, and normal, N, directions of the aluminum alloy plate is also shown. The micrographs of the different regions in the weld, showing the corresponding microstructure together with that of the initial microstructure, BM, are also detailed. (For interpretation of the references to color in this figure legend, the reader is referred to the web version of the article.)

in section S, and subindex L longitudinal stress. F_2 can be also expressed in terms of $T_{N_{\text{Front}}}$ and $T_{N_{\text{Back}}}$. Since M_{Front} and M_{Back} are the bending moments at a distance f of the neutral line[1], and considering that

$$M_{\text{Front}} = T_{N_{\text{Front}}} \cdot f \tag{8}$$

$$M_{\text{Back}} = T_{N_{\text{Back}}} \cdot (-f) \tag{9}$$

we can express Eq. (7) as:

$$F_2 = T_{\text{Front}} \cdot f - T_{\text{Back}} \cdot f \tag{10}$$

or

$$F_2 = T_{N_{\text{Front}}} - T_{N_{\text{Back}}} \tag{11}$$

since f affects both terms of the right side in Eq. (10). The T values are given by Eqs. (12)–(16).

$$T_{\text{Front}} = \sum_{i=0}^{z} \left[(C_1 + C_2) \cdot \frac{d_{311}^{\text{Front}}[i] - d_i^{0L_{\text{Front}}}}{d_i^{0L_{\text{Front}}}} + C_2 \cdot \left(\frac{d_{311}^{\text{Center}}[i] - d_i^{0L_{\text{Front}}}}{d_i^{0L_{\text{Front}}}} + \frac{d_{311}^{\text{Back}}[i] - d_i^{0L_{\text{Front}}}}{d_i^{0L_{\text{Front}}}} \right) \right] \tag{12}$$

$$T_{\text{Center}} = \sum_{i=0}^{z} \left[(C_1 + C_2) \cdot \frac{d_{311}^{\text{Center}}[i] - d_i^{0L_{\text{Center}}}}{d_i^{0L_{\text{Center}}}} + C_2 \cdot \left(\frac{d_{311}^{\text{Front}}[i] - d_i^{0L_{\text{Center}}}}{d_i^{0L_{\text{Center}}}} + \frac{d_{311}^{\text{Back}}[i] - d_i^{0L_{\text{Center}}}}{d_i^{0L_{\text{Center}}}} \right) \right] \tag{13}$$

$$T_{\text{Back}} = \sum_{i=0}^{z} \left[(C_1 + C_2) \cdot \frac{d_{311}^{\text{Back}}[i] - d_i^{0L_{\text{Back}}}}{d_i^{0L_{\text{Back}}}} + C_2 \cdot \left(\frac{d_{311}^{\text{Center}}[i] - d_i^{0L_{\text{Back}}}}{d_i^{0L_{\text{Back}}}} + \frac{d_{311}^{\text{Front}}[i] - d_i^{0L_{\text{Back}}}}{d_i^{0L_{\text{Back}}}} \right) \right] \tag{14}$$

C_1 and C_2 being derived from Eqs. (15) and (16), which are functions of the elastic modulus, E (7200 for aluminum) and the Poissons ratio, ν (0.33 for aluminum):

$$C_1 = \frac{E}{(1+\nu)} \tag{15}$$

$$C_2 = \frac{E \cdot (1-2\nu)}{(1+\nu) \cdot (1-2\nu)} \tag{16}$$

4.2. Individual representation

As it will be explained in Section 4.4, we will study three different scenarios depending on the data available. Nevertheless, we will use the same codification for all three cases since the unique difference is the number of parameters that describe each scenario. Using the smallest distance between measurement points, the whole transverse section of the welded plate was divided into a number of zones. Depending on the number of zones, we will be on a different scenario.

Each zone is specified by three parameters, corresponding to the three depths (Front, Center and Back), and the three components of the stress (L, N and T). Although we need to identify nine parameters, it was assumed that no anisotropic effect on the d_0 value exists, i.e. the same d_0 value must result irrespective of the sample direction or:

$$d_{311}^{0L_{\text{Front}}} = d_{311}^{0T_{\text{Front}}} = d_{311}^{0N_{\text{Front}}} \tag{17}$$

$$d_{311}^{0L_{\text{Center}}} = d_{311}^{0T_{\text{Center}}} = d_{311}^{0N_{\text{Center}}} \tag{18}$$

$$d_{311}^{0L_{\text{Back}}} = d_{311}^{0T_{\text{Back}}} = d_{311}^{0N_{\text{Back}}} \tag{19}$$

From the data of neutron diffraction we know that $d_{zone_i}^0$ must lie between two limits,

$$1.22 \cdot 10^{-15} < d_{zone_i}^0 < 1.23 \cdot 10^{-15}$$

In order to limit the number of possible solutions we have restricted the number of decimals used to express the values of $d_{0_i} \cdot 10^{-15}$ to five digits. This limit also fits with the precision of our measures. So we look for values of d_{0_i} that verify the following condition:

$$1.22000 \cdot 10^{-15} < d_{zone_i}^0 < 1.22999 \cdot 10^{-15}$$

Now the encoding of the individuals is direct. A chromosome is composed by $3 \cdot z$ genes. The first three values of the chomosome represent the parameters for the first zone, i.e. $d_{zone_0}^{0L_{\text{Front}}}$, $d_{zone_0}^{0L_{\text{Center}}}$ and $d_{zone_0}^{0L_{\text{Back}}}$, the next three the parameters for the second one, and so on. In order to decode the actual value of $d_{zone_i}^0$ from an individual, we use Eq. (20):

$$d_{zone_i}^0 = (1.22 + gene * 10^{-5}) * 10^{-15} \tag{20}$$

For example, if we assume that we have measured $d_{zone_i}^{0L_{\text{Front}}}$, $d_{zone_i}^{0L_{\text{Center}}}$ and $d_{zone_i}^{0L_{\text{Back}}}$ in five zones, we will have $0 \le i \le 4$. Thus, we will represent a solution by 15 genes (5 for *Center*, 5 for *Front* and 5 for *Back*), or fifteen $d_i^{0L_j}$ values, corresponding to $0 \le i \le 4$ and $j \in \{\text{Front, Center, Back}\}$. Table 1 shows, as an example, the decoding of individual:

$$22 - 189 - 123 - 132 - 23 - 23 - 14 - 111 - 122 - 230 - 230 - 230 - 39 - 36 - 45$$

4.3. Genetic operators

In order to avoid the random bias, we have executed 30 runs of the NSGA-II evolutionary algorithm for each scenario. The genetic operators configuration that we have considered for all runs is the following:

Table 1
Example of decoding for five zones of individual: 22 – 189 – 123 – 132 – 23 – 23 – 14 – 111 – 122 – 230 – 230 – 230 – 39 – 36 – 45.

Gene	Zone	Parameter	Value
22	0	$d_{zone0}^{0L_{\text{Front}}}$	1.22022×10^{-15}
189	0	$d_{zone0}^{0L_{\text{Front}}}$	1.22189×10^{-15}
123	0	$d_{zone0}^{0L_{\text{Back}}}$	1.22123×10^{-15}
132	1	$d_{zone1}^{0L_{\text{Front}}}$	1.22132×10^{-15}
23	1	$d_{zone1}^{0L_{\text{Front}}}$	1.22023×10^{-15}
23	1	$d_{zone1}^{0L_{\text{Back}}}$	1.22023×10^{-15}
14	2	$d_{zone2}^{0L_{\text{Front}}}$	1.22014×10^{-15}
111	2	$d_{zone2}^{0L_{\text{Front}}}$	1.22111×10^{-15}
122	2	$d_{zone2}^{0L_{\text{Back}}}$	1.22122×10^{-15}
230	3	$d_{zone3}^{0L_{\text{Front}}}$	1.22230×10^{-15}
230	3	$d_{zone3}^{0L_{\text{Front}}}$	1.22230×10^{-15}
230	3	$d_{zone3}^{0L_{\text{Back}}}$	1.22230×10^{-15}
39	4	$d_{zone4}^{0L_{\text{Front}}}$	1.22039×10^{-15}
36	4	$d_{zone4}^{0L_{\text{Front}}}$	1.22036×10^{-15}
45	4	$d_{zone4}^{0L_{\text{Back}}}$	1.22045×10^{-15}

[1] The neutral line is the position of the Center, and f is the Front-Center distance, which is the same as that of the Center-Back distance.

- Initial population: randomly generated.
- Population size: 1000 individuals.
- Stop criterion: 10,000 as maximum number of generations.
- Mutation probability: 0.1.
- Crossover probability: 0.8.
- Selection: tournament of two individuals.

4.4. Scenarios

The following are the three possible scenarios considered in the present research. In each one, a potential space of solutions is considered depending on the microstructure of the weld and the different microstructural zones in section *S*.

4.4.1. Scenario 1

A first case considers the least restrictive condition for potential d^0_{hkl} values across the weld. In this case, the possible d^0_{hkl} values are "selected" by the evolutionary algorithm from the absolute maximum and minimum d values measured in the neutron diffraction experiment. Then, we have to let the EA search into the whole space, seeking for a solution which meets the equilibrium of stresses, i.e. which minimizes F_1. In this case a single objective approach is considered.

4.4.2. Scenario 2

An improved scenario considers the application of Eq. (7) considering every individual measurement position across the transverse section. In this case, it is not needed to determine the dimensions of the microstructural zones. We have 181 homogeneously distributed measurements. In this situation it is possible to establish the maximum and minimum values of d^0_{hkl} for every of these locations as individual limits for the $d_i^{0L_j}$ parameter in each location. This allows us reducing the size of the searching space and thus, to make a faster and more effective search.

4.4.3. Scenario 3

In this case we will consider two possibilities. The first one is Scenario 3a, in which the dimensions of the different microstructural zones in the transverse section, from the weld to the base material, are known. In this situation it is possible to fix precisely, the maximum and minimum d values for every specific microstructural zone. This allows us to reduce the size of the search space and thus, to make an even faster and more effective search. From theoretical considerations of the balance, it is known that the values of $d_i^{0L_j}$ should be between the maximum and minimum values of the lattice spacing, d_{311}.

The second case, Scenario 3b, is an upgraded version of Scenario 3a. Here, the value of d^0_{hkl} in the base material is also known. This single value can be calculated experimentally from measurements conducted on longitudinal sections of the base material plate (perpendicular to the transverse section). Here, the welded region is, thus, avoided.

5. Results

Once we have explained our problem formulation and the proposed EA, let us analyze the experimental results. First, we will analyze the metallurgical results, showing that the approach proposed in this paper is an absolutely new approach in the field of materials. Finally, we also analyze the results in terms of performance and robustness of the MOEA we have used.

5.1. Metallurgical results

The results of the neutron diffraction measurements are summarized in the plots of Fig. 4, where the lattice spacing of the 311 crystallographic planes is shown as a function of the distance from the center of the weld for the three depths. As seen, a significant variation of d_{311} across the weld results, but the shape of the profiles does not vary substantially with depth. The profiles of the *L* component are M-shaped whereas it is W-shaped for the *N* and *T* components. Furthermore, the total variation of d_{311} across the weld is larger for the *L* component than for the *N* and *T* ones. These profiles are commonly observed in FSW of aluminum alloys [29]. The significant d_{311} variation observed across the weld should be attributed not only to variations of the solid solution caused in the FSW process, but also to the presence of a RS.

The microstructure of the different zones of the weld, nugget, TMAZ, HAZ, and BM is shown in the macro- and micrographs of Fig. 3. As it can be seen, the microstructure of the different regions

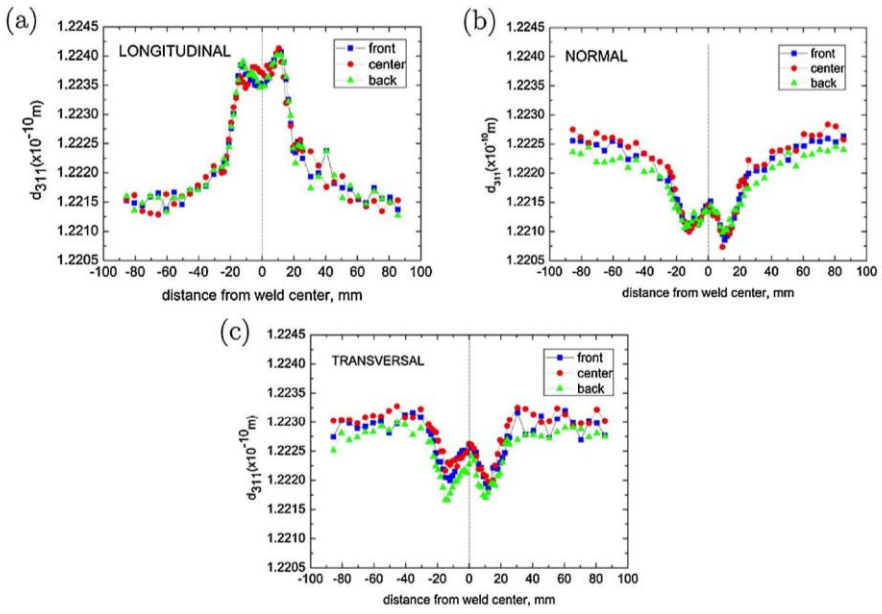

Fig. 4. 311 Inter-planar distance data as a function of distance from the center of the weld, for three directions, longitudinal (*L*), normal (*N*) and transversal (*T*).

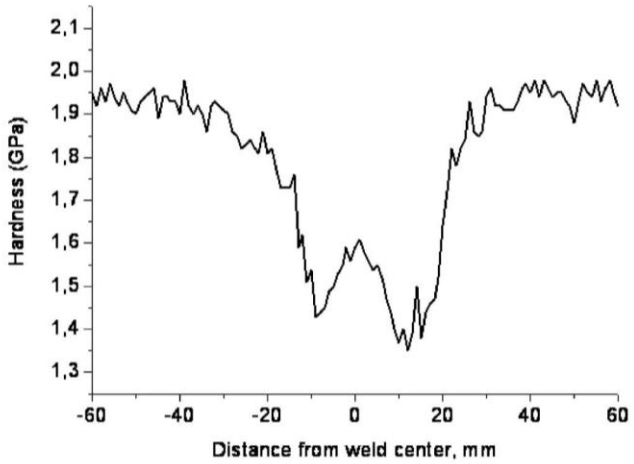

Fig. 5. Hardness profile across the weld. The error is of ±0.1 GPa.

differs dramatically from each one. The nugget is characterized by a very homogeneous, equiaxed, and small grain size, of about 5 μm. This is a result of the full recrystallization phenomenon of the original microstructure; the original microstructure corresponds to that of the micrograph of the BM in this figure. Here, the grains are elongated, with the smallest dimension coincident with the normal direction, *N* in Fig. 3. This microstructure is a consequence of the original cold rolling process. In the HAZ, no significant difference with respect to the microstructure in the BM is appreciated. A modification of the precipitation state due to the heating cycle, however, occurs which modifies the mechanical properties of the alloy. Finally, a deformed structure of the initially elongated grains in the TMAZ caused by the pin is appreciated. The grains do not lose their original entity revealing that recrystallization of new grains has not occurred in this zone.

The results of the hardness measurements are illustrated in the plot of Fig. 5. As it can be seen, the highest hardness values are obtained in the BM, whereas a clear drop is found mainly in the HAZ region. In particular, a W-type profile in the welded region is obtained, where the minimum is reached near the TMAZ zones and the maximum occurs in the nugget region. This variation is related with the different precipitation state of the different microstructural zones.

The temperature rise in the HAZ and TMAZ zones modifies the initial precipitation state to an overaged one. In this precipitation state, large incoherent precipitates are formed, which allows the lattice spacing to be relaxed with respect to the base material. In the nugget region, the recrystallization process induced by the severe deformation phenomenon leads to grain boundary precipitates and a fine dispersion of coherent precipitates inside the grains. This microstructure results in an intermediate lattice spacing value.

The d^0_{hkl} profile across the weld, directly related with the precipitation state, is expected to have a W shape. The good agreement between harness values and the results of d_0 values (normalized data) resulting from scenario 3b is shown in Fig. 6. To evaluate the

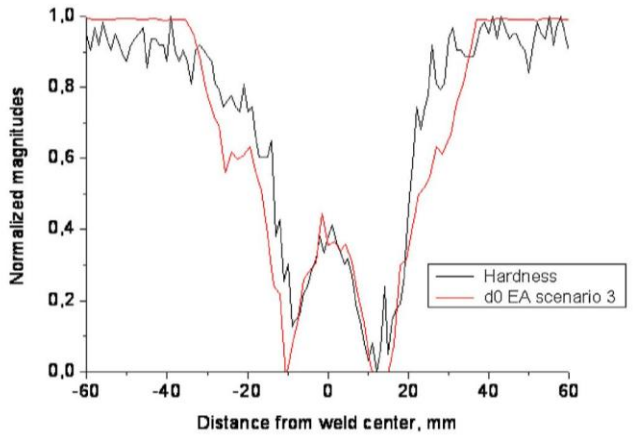

Fig. 6. Comparison of the normalized values [0,1] of experimental hardness and EA d_0 prediction.

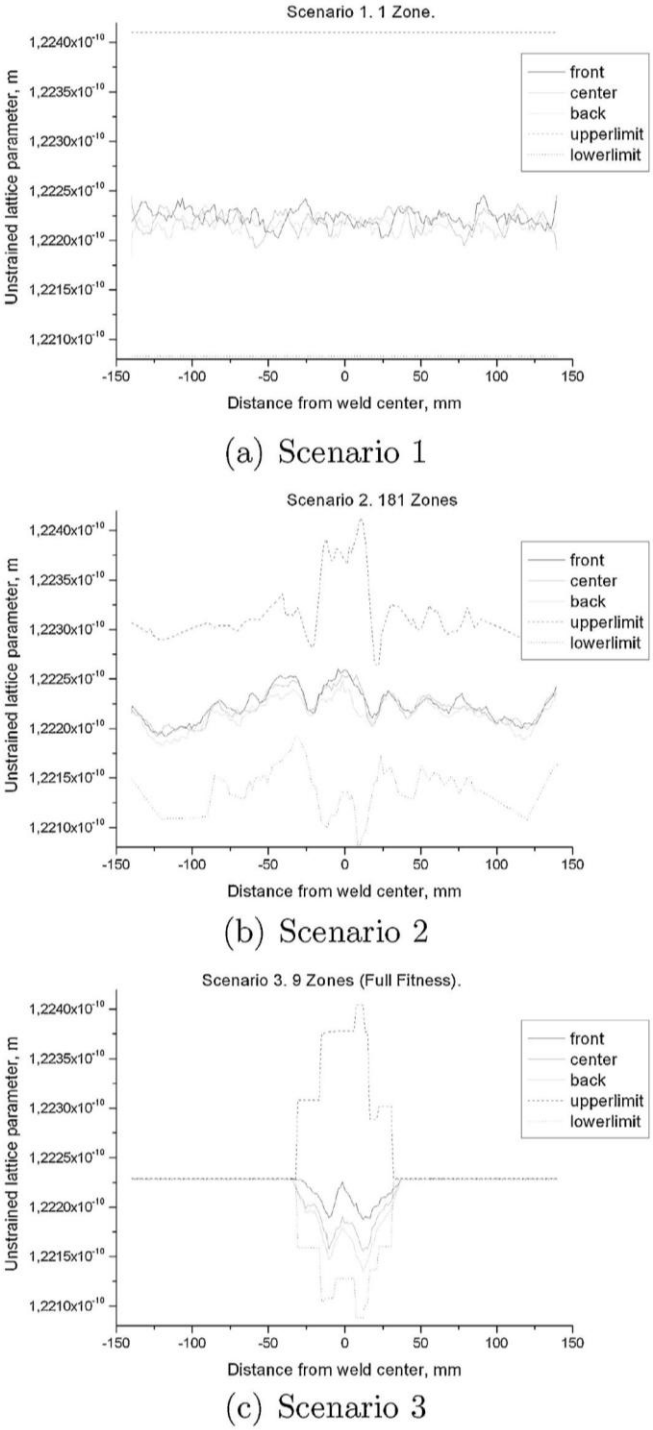

Fig. 7. Profiles of the transverse unstressed d_0 values (Front, Center, and Back) calculated using the MOEA from the equilibrium conditions.

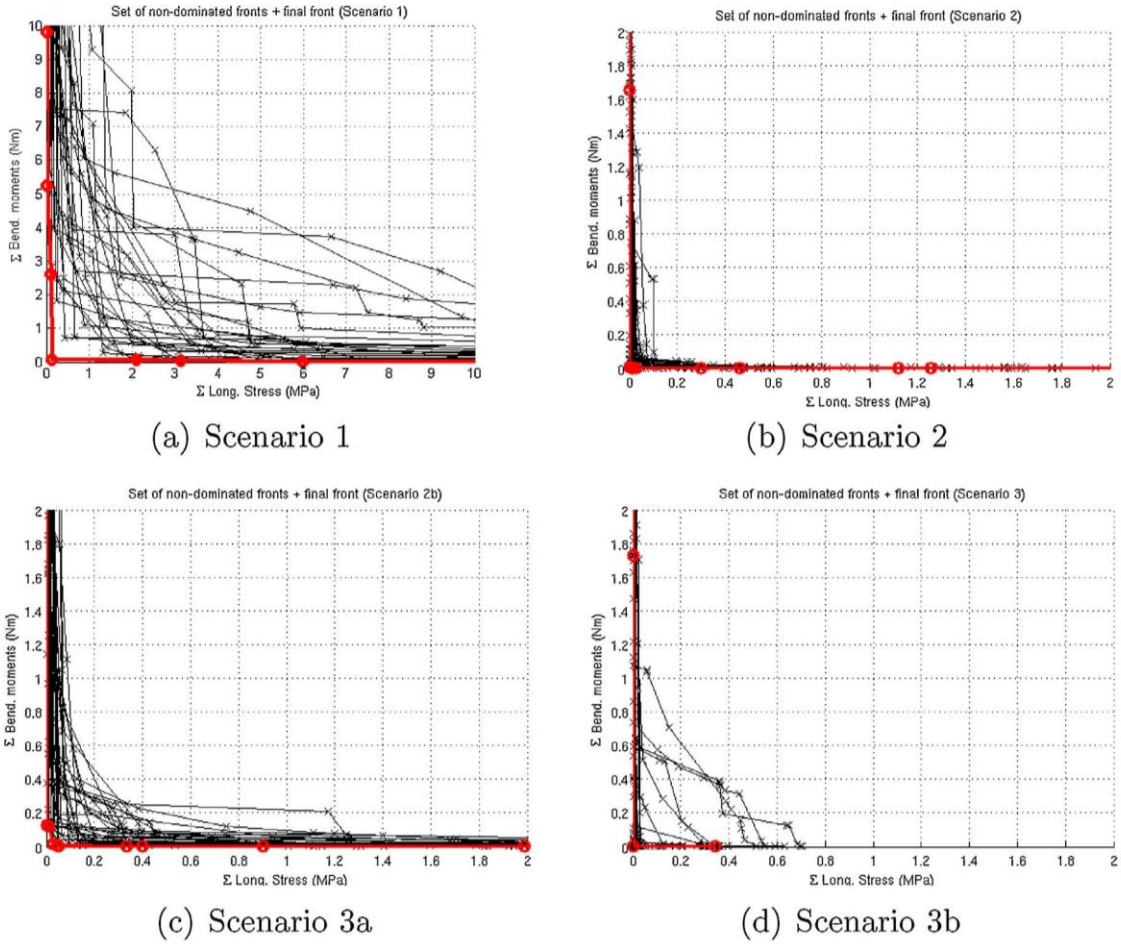

Fig. 8. Pareto front for the four different Scenarios. All the Pareto Fronts located close to the origin are covered by our EA.

predictive capacity in the different scenarios, the hardness profile (Fig. 6) must be compared to the EA d^0_{hkl} predictions. To this aim, Fig. 7 shows the predictions obtained with the values given by the EA on the different scenarios. At a first sight it is seen that the results provided by the EA in scenarios 1 and 2 do not adjust with the experimental hardness profile. However, the results obtained in Scenario 3 are consistent with the W shape and the precipitation state in the BM, HAZ, TMAZ, and nugget. Fig. 6 is a plot of normalized data of d_0 and hardness measurements to compare both sets of data. As seen, an excellent correlation for the variation of both magnitudes is obtained. This reveals the expected connection between the precipitation state, associated with the relaxed lattice spacing value, and the mechanical properties of the alloy.

5.2. Evolutionary algorithm analysis

In this section we are going to analyze the performance and the robustness of the evolutionary approach.

5.2.1. Performance

As explained above, we are dealing with a multi-objective problem. Although this is not the subject of this paper, it must be borne in mind that a MOEA approach leads to a set of solutions, called Pareto Set (PS). Since we have two objectives, we will obtain a set of non-dominated solutions that form this PS. In addition, we must also have in mind that evolutionary algorithms are stochastic in nature (non deterministic), so we will need to conduct several runs of the algorithm to avoid the random bias of the experiments. The performance analysis of MOEAs is not a trivial issue.

There are several metrics that allow the obtention of a numerical classification of the final solutions when comparing different algorithms. One of this metrics is the hypervolume of the Pareto front [30]. The hypervolume indicator, *HV*, is a measure of the quality of the set, according to a reference point. In this work we are proposing a method for solving a real-world problem. Thus, our intention

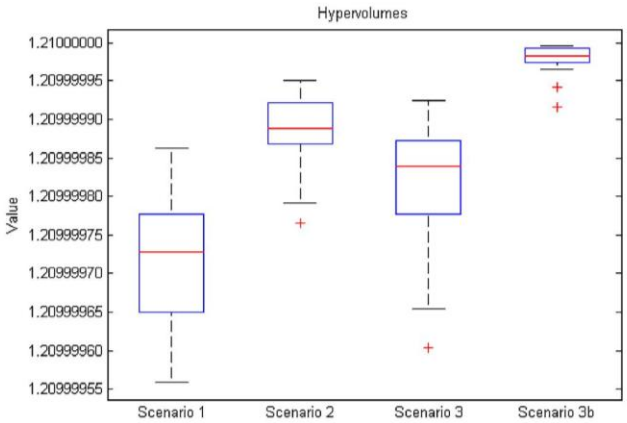

Fig. 9. Hypervolume indicator *HV* for the different scenarios. All the values belong to the interval [1.210, 1.219].

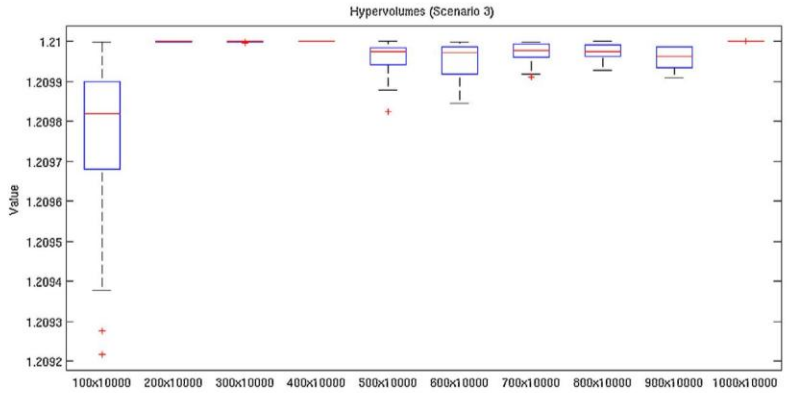

Fig. 10. *HV* for the different number of individuals when solving Scenario 3.

was not to explore different MOEA approaches. On the contrary, our contribution is to use a MOEA, and NSGA-II gives us satisfactory results; therefore a deeper study is not necessary at this point. However, we will use *HV* in Section 5.2.2 to show the robustness of our approach for different configurations of the algorithm over Scenario 3.

According to Zitzler, Deb and Thiele [31], there are three aspects to be considered when evaluating a Pareto front obtained with a multi-objective approach:

1. The distance to the Pareto-optimal set, which is the best (optimal) Pareto front. In our problem, the unreachable optimal Pareto front will be composed by only one point.
2. The distribution of the solutions along the Pareto front. Usually we look for a front as spreaded as possible and with a uniform distribution of the solutions along the front.
3. The number of elements of the PS. The more number of solutions within the PS, the better.

In most real-world problems, several conflicting objectives exist, and solutions are positioned along the Pareto front. Although we could say that the goal is to minimize (or maximize) two objectives simultaneously (and therefore the optimal solution is (0,0)), this point is usually unreachable in practice.

Therefore, to check the quality of the solutions we must observe what happens to the sum of normal forces in the region near the origin, let us say 10 MPa. Something similar can be considered for the bending moments. In other words:

$$0 < F_1 < 10\,\text{MPa}$$

$$0 < F_2 < 10\,\text{MPa m}$$

Moreover, by analyzing the Pareto Front obtained with NSGA-II we can observe that the front obtained with the EA covers all the meaningful points. Fig. 8 shows plots of the Pareto fronts obtained for the four different scenarios. Each plot in this figure depicts the fronts after 30 runs. The red line shows the Pareto front obtained when selecting only the non-dominated solutions of all the 30 runs. As we can see, we cover all the Pareto fronts in the area close to the origin which is the optimal point for all the scenarios.

5.2.2. Robustness

Fig. 9 shows the values of the hypervolume indicator *HV* for the different scenarios. All the values belong to the interval [1.210, 1.219] which gives us an idea of the robustness of the EA, since all the obtained non-dominated fronts are very similar in quality, in terms of the approximation to the optimal set. The greater the indicator value, the better the non-dominated front.

The algorithm needed an average of 64.9 s to run 1000 generations with 300 individuals when solving Scenario 3b. Those results are for a Intel i5 © processor with 8 GB of RAM memory running under OSX. As we can see also in Fig. 10, the *HV* for the different number of individuals is also similar and we can reduce the number of individuals up to 200 individuals.

6. Summary and conclusions

In this research an evolutionary algorithm has been developed and proposed to investigate the un-stressed lattice spacing, d_0, needed to calculate the macroscopic residual stress across a weld conducted on plates of aerospace aluminum alloy *AA2024*. Due to the dependence of the lattice spacing on the amount of solid solution atoms and the variation of solid solution atoms across the weld (of mainly Cu and Mg atoms in 2xxx alloys), a continuous change of d_0 is expected. This is because the thermal history across the weld differs dramatically depending on the distance to the center of the weld. In other words, the d_0 value is no longer constant across the weld. This circumstance derives in that the usual analytical procedures to calculate the residual stress profile across the weld cannot be used. The evolutionary algorithm developed in this work, in the context of equilibrium conditions of stresses, has proven the capacity of these searching procedures to obtain a satisfactory solution. Four possible scenarios, each one considering different restrictions of the searching space, have been investigated, and the following are the main conclusions obtained in this work:

- Our method covers all the Pareto fronts in the area close to the origin which is the optimal point for all the scenarios.
- The evolutionary approach is very robust since all the obtained non-dominated fronts of solutions are very similar in quality and very close to the optimal point. The experience obtained with the fine tuning of the algorithm will be useful for other task of the supporting projects. In particular to the multi-objective modeling of glucose profiles.
- The results obtained in Scenario 3 are consistent with the W shape and the precipitation state in the BM, HAZ, TMAZ, and nugget, which proves the expected connection between the precipitation state, associated with the relaxed lattice spacing value, and the mechanical properties of the alloy.

Acknowledgements

Support from Projects MAT-09-09545 from MICINN and MAT2014-55415-C3-1-R from MINECO, Spain is gratefully acknowledged. Financial help from the ILL to conduct the neutron diffraction measurements on SALSA, experiments 1-02-6 and

1-02-10 is recognized. Support from Spanish Government Grant TIN 2008-00508 and TIN2014-54806-R, Spain is also acknowledged by J.I.H. and J.M.C. We appreciate the work on the friction stir welding experiments and the metallographical preparation, conducted at AIMEN technological Center, Spain. Bruno Fernández de la Figuera helped us in the initial stages of this research.

References

[1] W. Thomas, E. Nicholas, J. Needham, M. Murch, P. Temple-Smith, C. Dawes, Friction stir butt welding, *gb* patent 9125978.8, (1991).
[2] W. Thomas, E. Nicholas, J. Needham, M. Murch, P. Temple-Smith, C. Dawes, Friction stir butt welding, us patent 5,460,317, (1995).
[3] J. Ouyang, R. Kovacevic, Material flow and microstructure in the friction stir butt welds of the same and dissimilar aluminum alloys, J. Mater. Eng. Perform. 11 (1) (2002) 51–63.
[4] M. Mahoney, C. Rhodes, J. Flintoff, W. Bingel, R. Spurling, Properties of friction-stir-welded 7075 t651 aluminum, Metall. Mater. Trans. A 29 (7) (1998) 1955–1964.
[5] R.S. Mishra, Z. Ma, Friction stir welding and processing, Mater. Sci. Eng.: R: Rep. 50 (1) (2005) 1–78.
[6] P. Withers, H. Bhadeshia, Residual stress. Part 2 – nature and origins, Mater. Sci. Technol. 17 (4) (2001) 366–375.
[7] C.J. Dawes, W.M. Thomas, Friction stir process welds aluminium alloys, Weld. J. 41 (5) (1996).
[8] K.A.O.T. Midling, E. Morley, Joining of aluminium constructions by friction stir welding, new and alternative materials for the transportation industries, in: Proceedings of the 27th International Symposium on Automotive Technology and Automation, 1994.
[9] B. Chaparro, S. Thuillier, L. Menezes, P.-Y. Manach, J. Fernandes, Material parameters identification: gradient-based, genetic and hybrid optimization algorithms, Comput. Mater. Sci. 44 (2) (2008) 339–346.
[10] R. Sharma, R. Saha, S. Nandy, S.P. Bhattacharyya, P. Chaudhury, Computation of molecular electronic structure by genetic algorithm, Mater. Manuf. Process. 24 (2) (2009) 155–161.
[11] A. Sorsa, K. Leiviskä, S. Santa-aho, T. Lepistö, Quantitative prediction of residual stress and hardness in case-hardened steel based on the barkhausen noise measurement, Ndt & E Int. 46 (2012) 100–106.
[12] M.K. Rausch, E. Kuhl, On the effect of prestrain and residual stress in thin biological membranes, J. Mech. Phys. Solids 61 (9) (2013) 1955–1969.
[13] S.K. Karak, S. Chatterjee, S. Bandopadhyay, Mathematical modelling of the physical and mechanical properties of nano-y 2 o 3 dispersed ferritic alloys using evolutionary algorithm-based neural network, Powder Technol. 274 (2015) 217–226.
[14] F. Jafarian, H. Amirabadi, J. Sadri, Experimental measurement and optimization of tensile residual stress in turning process of inconel718 superalloy, Measurement 63 (2015) 1–10.
[15] D. Cuesta, J.L. Risco-Martin, J.L. Ayala, J.I. Hidalgo, 3d thermal-aware floorplanner using a moea approximation, Integr. VLSI J. 46 (1) (2013) 10–21.
[16] M. Fitzpatrick, P. Withers, A. Baczmanski, M. Hutchings, R. Levy, M. Ceretti, A. Lodini, Changes in the misfit stresses in an al/sicp metal matrix composite under plastic strain, Acta Mater. 50 (5) (2002) 1031–1040.
[17] P.J. Withers, M. Preuss, A. Steuwer, J.W.L. Pang, Methods for obtaining the strain-free lattice parameter when using diffraction to determine residual stress, J. Appl. Crystallogr. 40 (5) (2007) 891–904.
[18] M. Rogante, The stress-free reference sample: the problem of the determination of the interplanar distance d_0, Phys. B: Condens. Matter 276–278 (0) (2000) 202–203.
[19] M. Sutton, A. Reynolds, D.-Q. Wang, C. Hubbard, A study of residual stresses and microstructure in 2024 – t3 aluminum friction stir butt welds, J. Eng. Mater. Technol. Trans. ASME 124 (2) (2002) 215–221.
[20] A. Steuwer, M. Dumont, M. Peel, M. Preuss, P. Withers, The variation of the unstrained lattice parameter in an {AA7010} friction stir weld, Acta Mater. 55 (12) (2007) 4111–4120.
[21] I.C. Noyan, J.B. Cohen, Residual Stress. Measurements by Diffraction and Interpretation, Springer-Verlag, New York Inc., New York, NY, 1986.
[22] R. Winholtz, A. Krawitz, The effect of assuming the principal directions in neutron diffraction measurement of stress tensors, Mater. Sci. Eng. A 205 (1) (1996) 257–258.
[23] Y. Maldonado, O. Castillo, P. Melin, A multi-objective optimization of type-2 fuzzy control speed in {FPGAs}, Appl. Soft Comput. 24 (2014) 1164–1174, http://dx.doi.org/10.1016/j.asoc.2014.04.041 http://www.sciencedirect.com/science/article/pii/S1568494614002208.
[24] A. Melendez, O. Castillo, P. Melin, Genetic optimization of interval type-2 fuzzy reactive controllers for mobile robots, in: Joint IFSA World Congress and NAFIPS Annual Meeting (IFSA/NAFIPS), IEEE, 2013, pp. 1418–1422.
[25] F. Cioffi, J. Hidalgo, R. Fernández, T. Pirling, B. Fernández, D. Gesto, I.P. Orench, P. Rey, G. González-Doncel, Analysis of the unstressed lattice spacing, d_0, for the determination of the residual stress in a friction stir welded plate of an age-hardenable aluminum alloy: use of equilibrium conditions and a genetic algorithm, Acta Mater. 74 (0) (2014) 189–199.
[26] K. Deb, A. Pratap, S. Agarwal, T. Meyarivan, A fast and elitist multiobjective genetic algorithm: NSGA-II, IEEE Trans. Evolut. Comput. 6 (2) (2002) 182–197.
[27] K. Deb, Multi-Objective Optimization Using Evolutionary Algorithms, Vol. 16, John Wiley & Sons, 2001.
[28] C. Coello, Evolutionary Algorithms for Solving Multi-Objective Problems, Kluwer, 2002.
[29] W. Woo, Z. Feng, X. Wang, S.A. David, Neutron diffraction measurements of residual stresses in friction stir welding: a review, Sci. Technol. Weld. Join. 16 (1) (2011) 23–32.
[30] E. Zitzler, Evolutionary Algorithms for Multiobjective Optimization: Methods and Applications, Ph.D. thesis, Swiss Federal Institute of Technology (ETH), 1999.
[31] E. Zitzler, K. Deb, L. Thiele, Comparison of multiobjective evolutionary algorithms: empirical results, Evolut. Comput. 8 (2) (2000) 173–195.